Formation and properties of epitaxial CdSe/ZnSe quantum dots

Conventional molecular beam epitaxy and related techniques

Dissertation zur Erlangung des
naturwissenschaftlichen Doktorgrades der
Bayerischen Julius-Maximilians-Universität
Würzburg

15 83

vorgelegt von
Suddhasatta Mahapatra
aus Kharagpur, Indien

Würzburg, 2007

Eingereicht am: 16.10.2007

bei der Fakultät für Physik und Astronomie

Gutachter der Dissertation:

1. Gutachter: Professor Dr. K. Brunner

2. Gutachter: Priv. Doz. Dr. L. Worschech

3. Gutachter: Professor Dr. H. Hinrichsen

Prüfer in Promotionskolloquium:

1. Prüfer: Professor Dr. K. Brunner

2. Prüfer: Priv. Doz. Dr. L. Worschech

3. Prüfer: Professor Dr. H. Hinrichsen

Tag der Promotionskolloquiums: 16.01.2008

Doktorurkunde ausgehändigt am:

Declaration

I hereby declare that the matter embodied in this thesis titled "Formation and properties of epitaxial CdSe/ZnSe quantum dots: Conventional MBE and related techniques" is the result of investigations carried out by me in the chair of "Experimentelle Physik 3" (Prof. L. W. Molenkamp), Physikalisches Institut, Julius-Maximilians-Universität, D97074 Würzburg, under the guidance of Prof. K. Brunner.

In keeping with the general practice of reporting scientific observations, due acknowledgements have been made whenever work of other investigators have been cited or described in this thesis. Any omission, which might have occurred by oversight or error in judgment, is regretted.

Suddhasatta Mahapatra

Summary

Over the last decade, epitaxially self-assembled quantum dots (QDs) based on II-VI semiconductor heterosystems have attracted considerable research interest due to their potential in developing (opto)electronic devices with improved or completely new functionalities. The wide bandgap II-VI semiconductors are attractive due to their band-to-band optical transition in the much-coveted blue-green region of the electromagnetic spectrum. In particular, self-assembly of CdSe/ZnSe(001) QDs, has been investigated in the past for possible applications in blue-green lasers and light emitting diodes and very recently, to realize visible single photon sources.

Albeit of high technological import, epitaxial self-assembly of CdSe/ZnSe QDs is non-trivial and still not clearly understood. The origin and attributes of these QDs appear to be significantly different from those of their well-established III-V and group-IV counterparts. For III-V and group-IV heterosystems, QD-formation is assigned to the Stranski Krastanow (SK) transition, wherein elastic relaxation of misfit strain leads to the formation of coherent three-dimensional (3D) islands, from a supercritically strained two-dimensional (2D) epilayer. Unfortunately, this phenomenon is inconspicuous for the CdSe/ZnSe heterosystem. Well-defined 3D islands, as characteristic of most III-V and group-IV heterosystems, are not readily formed in conventional molecular beam epitaxial (MBE) growth of CdSe on ZnSe. Consequently, several alternative approaches have been adopted to induce/enhance formation of QDs. This thesis systematically investigates three such alternative approaches, along with conventional MBE, with emphasis on the formation-mechanism of QDs, and optimization of their morphological and optical attributes.

In accordance with several previous investigations it is shown here that no distinct 3D islands are formed in MBE growth of CdSe on ZnSe. The surface of the CdSe layer represents a rough 2D layer, characterized by a dense array of shallow (<1nm) abutting mounds, elongated and weakly oriented in the [110] direction. In capped samples, the CdSe deposit forms an inhomogeneous CdZnSe quantum well (QW)-like structure. This ternary QW consists of local Cd-rich inclusions, which confine excitons three-dimensionally, and act as QDs. The density of such QDs is very high (~ 10^{12} cm^{-2}). The QDs defined by the composition inhomogeneities of the CdZnSe QW presumably originate from the shallow mounds of the uncapped CdSe surface. In this work, it is shown that these shallow mounds are formed due to multilayer growth of CdSe at the chosen growth temperature (T_G = 300 °C).

While CdSe heteroepitaxy occurs in the multilayer-mode at T_G = 300 °C, a reentrant recovery of the layer-by-layer mode is reported in this thesis, for growth at T_G < ~ 240 °C. The recovery of the layer-by-layer growth at low T_G is assigned to the breakdown of the Ehrlich Schwoebel barrier at the step edges, due to which adatom "down-climb" is reestablished.

By a technique wherein a CdSe layer is grown at a low temperature (T_G = 230 °C) and subsequently annealed at a significantly higher temperature (T_A =310 °C), tiny but distinct 3D islands are formed. In this work, the fundamental mechanism underlying the formation of these islands is reported. While the CdSe deposit forms a quasi-two-dimensional (quasi-2D) layer at T_G = 230 °C, subsequent annealing at T_A = 310 °C results in a thermally activated "up-climb" of adatoms onto two-dimensional clusters (or precursors) and concomitant nucleation of 3D islands. The areal density of QDs, achieved by this technique, is at least an order of magnitude lower than that typical for conventional MBE growth. It is demonstrated that further reduction is possible by appropriately delaying the temperature ramp-up to T_A.

In the second variant technique, formation of large and distinct islands is demonstrated by deposition of amorphous selenium (*a*-Se) onto a 2D CdSe epilayer at room temperature and its subsequent desorption at a higher temperature (T_D = 230 °C). Albeit the self-assembled islands are large, they are severely truncated during subsequent capping with ZnSe, presumably due to segregation of Cd and Zn-alloying of the islands. The segregation phenomenon is analyzed in this work and correlated to the optical properties of the QDs. Additionally, very distinct vertical correlation of QDs in QD-superlattices, wherein the first QD-layer is grown by this technique and the subsequent ones by migration enhanced epitaxy (MEE), is reported.

The process steps of the third variant technique, developed in course of this work, are very similar to those of the previous one-the only alteration being the substitution of selenium with tellurium as the cap-forming-material. The substitution leads not only to large alteration of the morphological and optical attributes of the QDs, but also to formation of unique self-assembled island-patterns. Oriented dashes, straight and buckled chains of islands, and aligned island-pairs are formed, depending on the thickness of the Te-cap layer. The islands are partially alloyed with Te and emit luminescence at very low energies (down to 1.7 eV at room temperature). Unlike the *a*-Se cap layer in the previous method, the Te cap layer undergoes (poly)crystallization during temperature ramp-up (from room temperature to T_D) for desorption. Here, it is shown that the self-assembled patterns of the island-ensembles are determined by the pattern of the grain boundaries of the polycrystalline Te layer. Based on an understanding of the mechanism of pattern formation, a simple and "clean" method for controlled positioning of individual QDs and QD-based extended nanostructures, is proposed in this work.

To conclude, the studies carried out in the framework of this thesis provide not only a deeper insight into the microscopic processes governing the heteroepitaxial self-assembly of CdSe/ZnSe(001) QDs, but also concrete approaches to achieve, optimize, and control several technologically-important features of QD-ensembles. Reduction and control of QD-areal-density, pronounced vertical correlation of distinctly-defined QDs in QD-superlattices, and self-assembly of QD-based extended structures, as demonstrated in this work, might turn out to be beneficial for envisioned applications in information-, and communication-technologies.

Zusammenfassung

Epitaktisches, selbstorganisiertes Wachstum von Quantenpunkten (engl.: quantum dots, QDs) auf der Basis von II-VI Halbleiterheterosystemen hat im Verlauf des letzten Jahrzehnts wegen ihres Potentials zur Entwicklung (opto-)elektronischer Bauteile mit verbesserten oder grundlegend neuen Eigenschaften beträchtliches wissenschaftliches Interesse auf sich gezogen. II-VI Halbleiter mit breiter Bandlücke sind wegen ihres optischen Band-zu-Band Übergangs im blau-grünen Bereich des elektromagnetischen Spektrums von großem Interesse. Bisher wurde insbesondere die Selbstorganisation von CdSe/ZnSe(001) QDs im Hinblick auf ihre mögliche Verwendung in blau-grünen Lasern und lichtemittierenden Dioden untersucht, vor kurzem auch die Verwirklichung von Einzelphotonenquellen im sichtbaren Bereicht.

Trotz ihrer großen technologischen Bedeutung ist die nichttriviale epitaktische Selbstorganisation von CdSe/ZnSe QDs noch immer nicht vollständig verstanden. Die Ursachen und Merkmale dieser QDs scheinen sich deutlich von ihren wohletablierten III-V und IV-IV Gegenstücken zu unterscheiden. Für III-V und IV-IV Heterosysteme wird die QD-Formation dem Stranski-Krastanow (SK) Übergang zugeordnet, bei dem, ausgehend von einer hochverspannten zweidimensionalen (2D) Epitaxieschicht, die elastische Relaxation von durch Gitterfehlanpassung hervorgerufener Verspannung zur Formation von kohärenten dreidimensionalen (3D) Inseln führt. Im Falle des CdSe/ZnSe Heterosystems ist es noch unklar ob das SK-Modell die Formation von QDs zutreffend beschreibt. Beim konventionellen Wachstum durch Molekularstrahlepitaxie (engl.: molecular beam epitaxy, MBE) von CdSe auf ZnSe kommt es nicht zur Bildung von gut definierten 3D Inseln, wie es für die meisten III-V und IV-IV Heterosysteme charakteristisch ist. Infolgedessen wurden mehrere alternative Herangehensweisen eingesetzt, um die Formation der QDs anzuregen bzw. zu verbessern. Diese Doktorarbeit beschreibt die systematische Untersuchung dreier solcher alternativer Ansätze im Zusammenspiel mit konventioneller MBE. Der Schwerpunkt liegt auf dem Formationsmechanismus der QDs und Optimierung ihrer morphologischen und optischen Eigenschaften.

In Übereinstimmung mit früheren Untersuchungen wird gezeigt, dass beim MBE Wachstum von CdSe auf ZnSe keine Bildung ausgeprägter, dreidimensionaler Inseln stattfindet. Die Oberfläche der CdSe-Schicht stellt eine rauhe 2D Schicht dar, gekennzeichnet durch ein dichte Anordnung flacher (<1nm), aneinander angrenzender Hügel, die mit ihrer gestreckte Form annähernd entlang der [110] Richtung orientiert sind. In bedeckten Proben bildet die CdSe-Ablagerung eine inhomogene CdZnSe Quantentrog- (engl.: quantum well, QW) änliche Struktur. Dieser ternäre QW enthält lokale Cd-reiche Einschlüsse, die die Bewegung von Exzitonen in drei Dimensionen einschränken und als QDs fungieren. Die Dichte solcher QDs ist sehr hoch (~ 10^{12} cm^{-2}). Die QDs, definiert durch Inhomogenitäten in der Zusammensetzung des CdZnSe-QW, haben ihren Ursprung vermutlich in den flachen Hügeln der unbedeckten CdSe-

Oberfläche. In dieser Arbeit wird gezeigt, dass diese Hügel aufgrund des multilayer Wachstums des CdSe bei der gewählten Wachstumstemperatur (T_G = 300°C) gebildet werden.

Während epitaktisches Wachstum von CdSe bei T_G = 300 °C im mulitlayer Modus geschieht, wird in dieser Arbeit die unerwartete Wiederherstellung des layer-by-layer Schichtwachstums bei T_G <~ 240 °C beschrieben. Die Wiederherstellung des layer-by-layer Modus bei niedrigem T_G wird dem Zusammenbruch der Ehrlich-Schwoebel-Barriere an den Stufengrenzen zugeschrieben, wodurch der „down-climb" von Adatomen wiederhergestellt wird.

Mit einer Methode, bei der eine CdSe-Schicht bei niedriger Temperatur (T_G = 230 °C) gewachsen und anschießend bei signifikant höherer Temperatur (T_A = 310 °C) getempert wird, kommt es zur Bildung winziger aber ausgeprägter 3D Inseln. In dieser Arbeit wird der Mechanismus, der der Bildung dieser Inseln zugrunde liegt, beschrieben. Während die CdSe-Ablagerung eine quasi-zweidimensionale (quasi-2D) Schicht bei T_G = 230 °C bildet, führt das darauffolgende Tempern bei T_A = 310 °C zu einem thermisch aktivierten „up-climb" von Adatomen auf zweidimensionale Cluster (oder Vorgänger, engl.: precursor), bei gleichzeitiger Nukleation von 3D Inseln. Die Flächendichte von QDs, die mit dieser Methode erreicht werden kann, ist mindestens eine Größenordung geringer als für konventionelles MBE Wachstum typisch ist. Es wird demonstriert, dass eine weitere Verringerung möglich ist, indem der Temperaturanstieg auf T_A entsprechend verzögert wird.

In einer zweiten Variante wird die Bildung großer und ausgeprägter Inseln durch Aufbringen einer amorphen Selenschicht (α-Se) auf eine 2D CdSe-Epischicht bei Raumtemperatur und anschließender Desorption bei höherer Temperatur (T_D = 230 °C) demonstriert. Obwohl die selbstorganisierten Inseln groß sind, werden sie durch nachträgliches Bedecken mit ZnSe stark abgeflacht, was vermutlich durch Segregation von Cd und Legieren der Inseln mit Zn hervorgerufen wird. Das Segregationsphänomen sowie sein Zusammenhang mit den optischen Eigenschaften der QDs wird in dieser Arbeit untersucht. Weiterhin wird die stark ausgeprägte vertikale Korrelation von QDs in QD-Übergittern beschrieben, in welchen die erste QD-Schicht mit dieser Methode gewachsen wurde. Darauffolgende Schichten werden duch migration enhanced epitaxy (MEE) aufgebracht.

Die Prozessschritte der dritten im Rahmen dieser Arbeit entwickelten Variante sind denen der eben beschriebenen sehr ähnlich. Die einzige Abwandlung besteht in der Substitution von Selen mit Tellur als bedeckendes Material. Jedoch führt diese Variation nicht nur zu beträchtlicher Veränderung der morphologischen und optischen Eigenschaften der QDs, sondern auch zur Bildung einzigartiger Muster von selbstorganisierten Inseln. Abhängig von der Dicke der Tellurbedeckung kommt es zur Bildung orientierter „dashes", gerader und gebogener Ketten von Inseln und ausgerichteter Inselpaare. Die Inseln sind teilweise mit Tellur legiert und strahlen Lumineszenz in einem sehr niedrigen Energiebereich ab (bis hinunter zu 1.7 eV bei Raumtemperatur). Im Gegensatz zur α-Se Bedeckung der vorherigen Methode kommt es in der Te-Schicht zu Polykristallisierung während der

Temperaturerhöhung (von Raumtemperatur zu T_D) zur Desorption. Es wird gezeigt, dass die selbstorganisierten Muster der Inseln durch die Verteilung der Korngrenzen der polykristallinen Te-Schicht bestimmt werden. Basierend auf dem Verständnis des Mechanismus der Musterbildung wird in dieser Arbeit eine einfache und „saubere" Methode für die kontrollierte Positionierung individueller QDs und QD-basierter, ausgedehnter Nanostrukturen vorgeschlagen.

Zusammenfassend kann gesagt werden, dass die Studien, die im Rahmen dieser Doktorarbeit durchgeführt wurden, nicht nur einen tieferen Einblick in die grundlegenden mikroskopischen Prozesse, die die heteroepitaktische Selbstorganisation von CdSe/ZnSe(001) QDs bestimmen, liefern, sondern auch konkrete Methoden zur Herstellung, Optimierung und Kontrolle von QD-Ensemblen mit verschiedenen technologisch wichtigen Eigenschaften. Es wird erwartet, dass in dieser Arbeit demonstrierte Phänomene, wie Verringerung und Kontrolle der Fächendichte der QDs, ausgeprägte vertikale Korrelation von klar definierten QDs in QD-Übergittern und Selbstorganisation von ausgedehnten QD-basierten Strukturen, einen hilfreichen Einfluss auf die Entwicklung zukünftiger Anwendungen in Informations- und Kommunikationstechnologie haben werden.

Acknowledgements

The work presented in this thesis is a result of cooperation, guidance, inspiration, and encouragement of several people. I wish I make justice in giving due credit to all of them.

First and foremost, I sincerely thank my research supervisor Prof. Dr. Karl Brunner, who offered me the position to work on this topic. It has been an excellent learning experience working together with him. I have immensely benefited from his profound knowledge and experience on the subject. I wish to thank him also for allowing utmost freedom to carry out all "wild" experiments that came to my mind. He has provided a very conducive ambient for scientific research and has been patient and encouraging throughout. My thanks are due to him for his critical supervision and constructive suggestions, which helped me improve my analytical aptitude. I take this opportunity to wish him lots of success in all his future scientific endeavors.

I thank Prof. Dr. Laurens Molenkamp for allowing me to work in the chair of "Experimentelle Physik 3" (EP3). I sincerely believe that the liberal work-ambient within EP3, under his management, is exemplary.

I consider myself fortunate to have had the guidance of Professor Dr. Grzegorz Karczewski, Polish Academy of Sciences, Warsaw. His wealth of novel research ideas, immense enthusiasm, and an always-jovial demeanour is certainly what I will treasure.

Dr. Claus Schumacher introduced me to the real world of molecular beam epitaxy (MBE), patiently walking me through the intricate details of the gigantic MBE-cluster of EP3, and showing me how to tame it. He has been an excellent tutor, who taught me the "art of growing good crystals" and how to keep cool and cope with Murphy's Law[†]. I thank Claus sincerely for his support and cooperation, and for being always friendly, even in critical situations. Dr. Timo Schallenberg and Dr. Peter Grabs have also been equally cooperative and also extremely helpful with their experience in MBE. I acknowledge the support and cooperation of Dr. Gisela M Schott and Dr. Taras Slobodskyy for the same.

I gratefully acknowledge the contributions of several people from different research groups, with whom we collaborated in the context of this thesis work. Dr. Georgy V Astakhov and Tobias Kiessling, from the Optical Spectroscopy group led by Prof. Dr. Wolfgang Ossau, have carried out a substantial part of the photoluminescence (PL) measurements. Similar measurements, along with micro- and time-resolved PL, have been performed by Emanuela Margapoti, Johannes Renner, and Thomas Schmidt, from the II-VI Spectroscopy group (Technische Physik (Prof. Dr. Alfred Forchel), Universität Würzburg) led by PD Dr. Lukas Worschech. Utz Bass has performed the Raman spectroscopic measurements, discussed in this work. I thank him and Prof. Dr. Jean Geurts for the Raman studies. Dr. Tanja Borzenko has carried out scanning tunneling microscopy and e-beam lithography of some of the samples. Markus Klein and Dr. Azzedine Bendounan, from the group of Prof. Dr. Friedrich Th. Reinert (Experimentelle Physik 2, Universität Würzburg), have done the x-ray photoelectron spectroscopic

---

[†] For information on Murphy's Law, refer to http://en.wikipedia.org/wiki/Murphy's_law

measurements and analysis. Transmission electron microscopy (TEM) has been carried out by Dr. Catherine Bougerol, CEA/DRFMC/SP2M 17, rue des martyrs, Fr-3804, Grenoble. I deeply appreciate her contribution in measurement and analysis of the TEM data. Isabella Gierz and PD Dr. Christian Kumpf (Experimentelle Physik 2, (Prof. Dr. Eberhard Umbach)) performed the glancing incidence x-ray diffraction measurements and a major part of the analysis.

I deeply appreciate the cooperation and assistance of my present and previous colleagues. Most of the experimental work presented in chapter 7 has been done by Fabian Eschenbach, in the framework of his Diplom work. His diligence and strong resolve has made the work possible within a rather short period of time. Andreas Benkert and Jan Wenisch have been extremely helpful with their comments and suggestions. I have learnt a great deal from discussions with both of them, on topics within and outside the world of Physics. Also, some of the samples discussed in Chapter 4 have been grown by Andreas and his co-workers. Lars Ebel and Alexander Frey have also been friendly and cooperative.

No work presented in this thesis would be possible without the valuable technical assistance of Anita Gebhardt, Petra Wolf-Müller, Alfred Schönteich, and Volkmar Hock. In the world of MBE, Alfred has answers to all problems which do or don’t arise. Volkmar has been particularly helpful in developing processes related to fabrication of mesas and metallization of samples for electrical contacts. Anita and Petra have always had enough time to do the preparatory work, even if the request came in the last minute. Rainer Brauner has been helpful with his assistance in the mechanical workshop.

I would also like to thank Anja Brück-Poirier, the secretary of EP3, for her help assistance, and cooperation in official and administrative matters. She deserves special thanks for being always jovial and affable.

Several colleagues, within EP3 have helped in different ways, which have directly or indirectly contributed to the making of this thesis. I thank all my colleagues of EP3, especially Dr. Charles Becker, PD Dr. Georg Schmidt, Dr. Charles Gould, Dr. Ralph Scheibner, and Dr. Idriss Chado. I thank Tobias, Timo, Claus, Jan, and Alex for proof-reading parts of this thesis and previous manuscripts.

The last four years have been rich with experience, incurring several new friends and acquaintances, who have, in varying degrees and in numerous contexts, helped me by their myriad contributions, suggestions, and timely distractions. To Emanuela, I express my heartfelt gratitude, for showing me the pristine beauty in small and simple aspects of life. My special thanks are due to Elisa, Alessandra, Juilee, Dhananjay, Timo, Zoi, Alonso, and Claus. I am thankful also to Utz, Markus, Marta (Italy), Marta (Spain), Armin, Pamela, Geoffrey, Petra, Christian, Lucia, Antje, Daniel, Karin, Teresa, Axel, Francesco, Romain, Peter (Bach), Peter (Grabs), Andreas, Surojit, Klaus, Michael (Lentze), and Michael (Leufgen).

Last but no the least, I am deeply thankful to my family and friends in India, who have been encouraging, patient, and affectionate throughout.

Contents

Introduction

1

On the technology roadmap of the semiconductor industry, the invention of molecular beam epitaxy, in the 1960s, undoubtedly represents a very important landmark. Aside from enabling feature-size reduction of conventional semiconductor devices, particularly transistors, the invention brought a totally new class of structures to existence– the *low-dimensional quantum heterostructures*. While charge carriers of a bulk semiconductor are itinerant in nature, in quantum heterostructures, they are arrested in one, two, or all three dimensions. More appropriately, the low-dimensionality of quantum heterostructures results in *quantization* of energy states, and thereby, in "confinement" of charge carriers. Engineering of quantum heterostructures began in earnest during the early 1970s, when the first two-dimensional "quantum wells" were fabricated. Since then, over the last three-and-a-half decades, semiconductor research has taken on, quite literally, new dimensions [Reed93]. Today, conduction band electrons, valence band holes, or excitons (bound electron-hole pairs) are routinely confined to planes (quantum wells), lines (quantum wires), or mathematical points-the *quantum dots*.

Mathematical points are however abstract constructs. To comprehend how quantum dots are realized in practice, it is helpful to consider the de Broglie wavelength, λ, of a charge carrier in a semiconductor crystal. λ is related to the effective mass of the charge carrier, m^*, and the absolute temperature, T, by the equation

$$\lambda = \frac{h}{\sqrt{2m^* k_B T}} \quad (1.1),$$

where h and k_B are the Planck's and Boltzmann constant, respectively. The de Broglie wavelength defines the length-scale below which quantum phenomena start to appear. In typical semiconductors, with m^* value ~10% of the free electron mass, λ turns out to be ~ 20 nm, at T = 300 K. Therefore, by creating potential traps with all three dimensions measuring in the scale of a few nanometers, charge carriers of a semiconductor crystal can be confined to completely quantized energy-states. In the state-of-art semiconductor technology, such traps are easily created either by application of appropriate electric fields to carrier gases or by embedding nano-size structures of a low-bandgap semiconductor within the matrix of a larger-bandgap semiconductor. Such *nanostructures*, which allow three-dimensional (3D) quantum confinement of charge carriers, represent the real quantum dots.

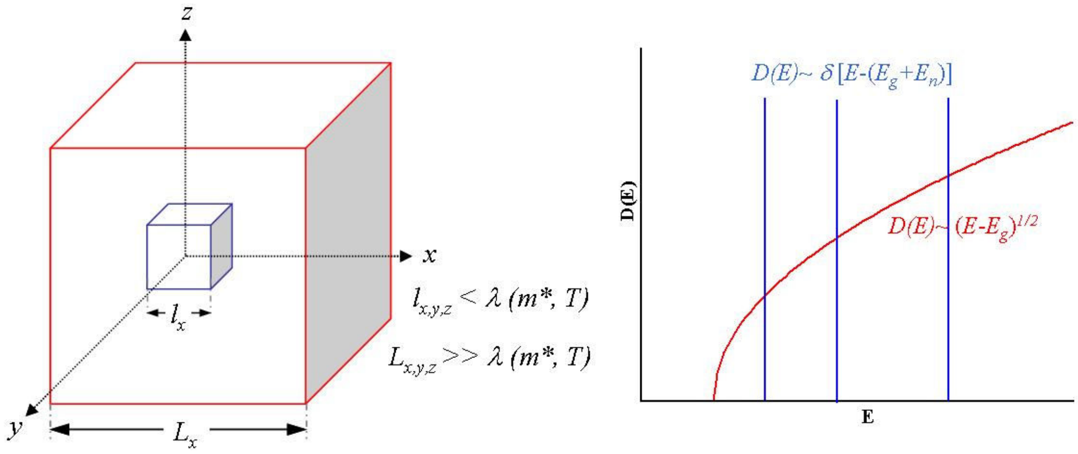

FIG. 1.1: The electronic density of states as a function of the energy of charge carriers residing within a macroscopic semiconductor crystal (the red box), and a QD (the blue box).

The quantum confinement effect is best visualized by comparing the density of electronic states of a macroscopic semiconductor crystal to that of a quantum dot (QD). Figure 1.1 depicts the comparison pictorially. For a macroscopic semiconductor crystal of dimensions $L_{x,y,z} >> \lambda(m^*, T)$, the density of states, D(E), shows a parabolic (and continuous) dependence on the energy of the carriers, E. Within a QD, of dimensions $l_{x,y,z} < \lambda(m^*, T)$, D(E) is composed of discrete δ-functions, with non-zero values corresponding to the quantized states. Due to this discreteness of the electronic states, charge carriers confined within QDs, lose their itinerancy.

In effect, the quantization phenomenon in QDs is similar to that of an isolated atom. Being confined to the attractive Coulomb potential of the nucleus, electrons of an isolated atom occupy quantized energy states, similar to charge carriers trapped in QDs. Due to this similarity of quantum confinement, QDs are often dubbed as "artificial atoms". However, the two systems have certain subtle, but important, differences. In contrast to atoms, the confinement potential in QDs does not necessarily show spherical symmetry. Additionally, the confined charge carriers do not reside in free space, but in the semiconductor host crystal. The QD host material, in particular its band structure, does therefore play an important role for all QD-properties. Typical energy scales, for example, are of the order of 10 eV in atoms, but of the order of ~ 10 meV in QDs. Finally, in contrast to atoms, the energy spectrum of a QD can be tuned by controlling the geometrical size, shape, and the strength of the confinement potential. This important feature allows QDs to be manipulated and engineered to meet the requirements of practical applications.

Fabrication of nanostructures for 3D confinement of charge carriers began in the early 1980s [Reed86]. Broadly, the efforts may be classified as those relying on chemical routes to synthesize nano-size semiconductor crystallites [Murray93] and those based on *epitaxial* growth and processing of semiconductor *heterostructures*. Within the second class, initial endeavors focused on lithographic patterning and etching of quantum wells (QWs) [Reed86]. Related techniques include selective intermixing of QWs [Werner89], and use of stressors [Kash88]. Nanostructures are also fabricated by manipulating atoms with a scanning probe microscope (SPM) [Eigler90]. Alternatively, the SPM tip is used as a stylus or pen to "write" nanoscale structures [Minne98]. QDs (confining only one type of carriers) are also created by application of modulated electric fields to two-dimensional (2D) carrier gases [Sikorski89].

Of all techniques, the one that has proven over the last one-and-a-half decades to be the most advantageous route to fabricate large ensembles of quantum dots (QDs) exploits the elegant concept of *self-assembly*, during heteroepitaxial growth of semiconductors. In heteroepitaxial self-assembly, nanoscale 3D features (often called "islands") of one semiconducting material are *spontaneously* formed on the substrate of another. Thus, it has been justly termed as the *"Nature's Way"* [Madhukar95] to produce QDs. The success of this way lies in a fortunate coincidence in the variation of two fundamental physical properties of the majority of technologically-important semiconducting materials. Within each of group-IV, III-V, and II-VI semiconductor-families, the bandgap energy of a material is lower, larger its lattice constant is. This is seen in the Fig. 1.2, for some of the important semiconductors, belonging to all three families [Faschinger99]. Due to this trend, several combinations of semiconductors naturally fulfill two essential conditions, imperative for heteroepitaxial self-assembly of QDs: i) an energetic condition under which the QDs have to be formed of a material of lower bandgap, embedded in a material of higher bandgap (such that confining potentials are defined by the difference in the bandgaps), and ii) a epitaxial-growth condition wherein the QD-forming material needs to have a larger lattice constant than that of the host-material in which the QDs are embedded. This condition is necessary since island formation in heteroepitaxy is driven by release of compressive strain, which builds up during heteroepitaxial growth (This is addressed to in further detail in Chapter 2).[†] In Fig. 1.2, the solid lines connecting some of materials indicate to the further possibility of realizing alloyed systems, wherein the bandgaps and the lattice constants can be continuously tuned between the end values.

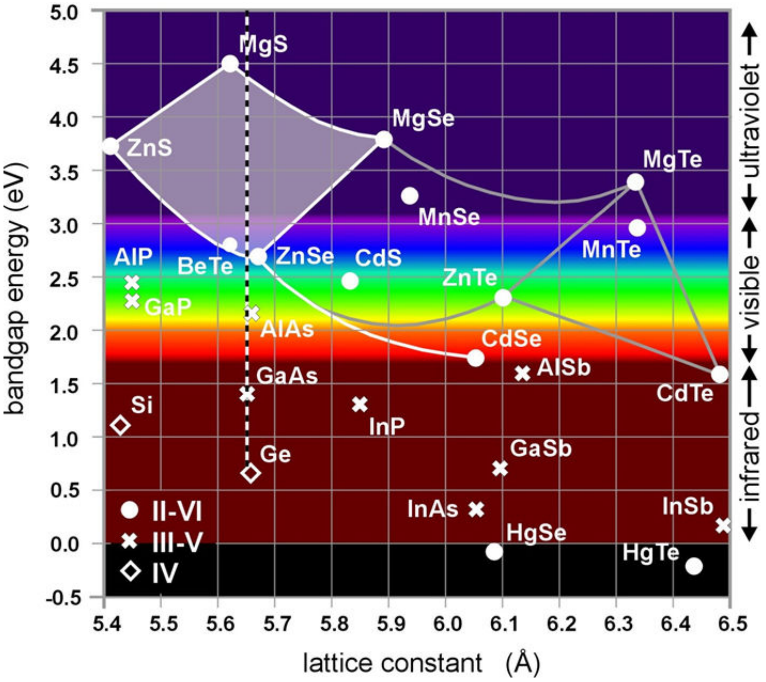

Fig. 1.2: Band gap energy versus lattice constant for several group-IV, III-V, and II-VI semiconductors. The solid curves connecting selected binary compounds represent the complete range of the possible ternary alloy compositions. Adopted from [Faschinger99]

For many reasons, self-assembly stands out as the technique of choice for fabrication of QDs. Firstly, involving merely epitaxial growth by well established techniques, the process is attractive in terms of technical simplicity and cost- and time-economy. Since epitaxial growth is carried out in ultra-high-vacuum (UHV), self-assembled QDs are free of contamination from the atmospheric ambient. Self-assembly involves neither any chemical processing (as required in lithographic techniques) nor any precise deposition of metal electrodes (as required for QDs defined by modulated electric fields). Above all, self-assembled QDs are small (down to diameters of 10 nm) and crystallographically coherent (defect-free). These advantages make self-assembled QDs the most attractive candidate for design of practical devices.

[†] Though claimed by some theoretical works [Korutcheva00], island-formation has been observed experimentally also for heteroepitaxial growth under tensile strain.

For different combinations of semiconductors, belonging to the group-IV, III-V, IV-VI, and II-VI families, self-assembled QDs have been successfully grown and investigated. The systems which have been studied most widely are InAs QDs on GaAs(001) substrates and Ge QDs on Si (001) substrates (see Fig. 1.2). The range of applications, either already realized or envisaged, using self assembled QDs, is also large. Several opto-electronic devices have been developed, primarily using InAs/GaAs(001) QDs. These include low-threshold, high differential gain, laser diodes, emitting at 1.1-1.3 μm at room temperature [Huffaker98, Heinrichsdorff97], resonant cavity photodiodes operating at wavelengths around 1.2-1.3 μm [Campbell97, Baklenov98], and normal incidence infrared photodetectors [Phillips98]. An ideal QD-laser, consisting of an ensemble of equi-sized QDs, is theoretically predicted to have ultra-low, temperature-independent, threshold current density and high material and differential gain. Size homogeneity of QDs is also important for applications in detection devices. However, a complete uniformity of sizes for self-assembled QDs is not straightforward to achieve, though considerable improvements have been recently made.

Schemes of memory devices using QDs have also been demonstrated. Electrical detection of charge storage in self assembled QDs has been reported by Finley et al. [Finley98]. A charge storage time of 22 mins (8 hours) was found at 200 K (140 K). Lundstrom et al. demonstrated the possibility of using confined excitons within InAs/GaAs(001) QDs for storage and retrieval of information by optical methods [Lundstrom99]. Currently, tremendous research efforts have been directed towards exploiting the 3D quantum confinement properties of QDs in realizing schemes for generation of non classical light, i.e. single and entangled photon sources [Michler00, Yuan00, Santori01, Zwiller01, Santori02, Santori04], and the basic building blocks of quantum computers-the qubits [Loss98, Imamoglu99]. Such devices would revolutionize the next-generation communication and information technologies.

Over the last decade, the wide-band-gap II-VI combinations, CdSe/ZnSe(001) and CdTe/ZnTe(001), have also attracted considerable research interest in the context of epitaxial self-assembly of QDs. The II-VI combinations are attractive due to their band-to-band optical transition in the much-coveted blue-green region of the electromagnetic spectrum (see Fig. 1.2). Albeit initially envisaged for blue-green lasers and light emitting diodes, the II-VI QDs have proven to be promising candidates for novel applications, such as visible single photon sources operating at room temperature [Aichele04]. However, unlike the prototypical InAs/GaAs(001) and Ge/Si(001) systems, self-assembly of II-VI QDs is not straightforward and is still not completely understood.

The outline of this thesis

This thesis primarily deals with the epitaxial self-assembly, ordering, and properties of CdSe/ZnSe(001) QDs. Molecular beam epitaxy (MBE) has been used as the epitaxial growth technique to fabricate QD-ensembles. Apart from conventional MBE growth, three other variant techniques have been studied in this work. The topography of uncapped CdSe surfaces, and the morphology, chemical composition, crystallographic, and confinement properties of the QDs have been investigated by several characterization tools like, reflection high energy electron diffraction (RHEED), high resolution x-ray diffraction and interferometry (HRXRD and XRI), atomic force microscopy (AFM), transmission electron microscopy (TEM), resonant Raman spectroscopy (RRS), x-ray photoelectron spectroscopy (XPS), and photoluminescence (PL) spectroscopy. Based on a systematic analysis and correlation of the results of these characterization techniques, this thesis investigates the attributes and formation mechanism of CdSe/ZnSe QDs, self-assembled in the four studied techniques. The thesis is organized as follows:

Chapter 2 introduces in detail the phenomenon of heteroepitaxial self-assembly of QDs and related nanostructures. Both, thermodynamics and kinetics of QD-self-assembly are presented, along with other issues related to practical realization of QD-ensembles, like intermixing, segregation, capping etc. Vertical and lateral ordering of QDs is also discussed in this chapter. Finally, the energy levels and exciton confinement in QDs is presented briefly.

Chapter 3 deals with the details of the tools and techniques used for fabrication and characterization of different samples.

Chapter 4 addresses to the growth of homoepitaxial GaAs buffers on GaAs(100) substrates and subsequent heteroepitaxy of ZnSe. These steps preceded the deposition of the CdSe layer and an understanding of their details was crucial for optimization of the subsequent QD-self assembly.

Chapter 5 is the first of the four chapters presenting QD-self assembly by different techniques. In this chapter, the properties of QDs, formed in conventional MBE growth of CdSe (at a growth temperature of 300 °C) on ZnSe(001) surfaces, are presented first. The mechanism of QD-formation is analyzed next. Finally, some characteristic features of CdSe/ZnSe (001) heteroepitaxy are discussed.

Chapter 6 deals with the self-assembly of CdSe/ZnSe(001) QDs by a technique combining low temperature MBE growth of CdSe (at 230 °C) and subsequent in-situ annealing at a significantly higher temperature (310 °C). Primarily, the mechanism of QD-formation by this technique has been investigated in this work, based on an analysis of the different attributes of the QDs. A method to control the areal density of QDs, self-assembled by this technique, is also demonstrated in this chapter.

Chapter 7 presents self-assembly of CdSe/ZnSe(001) QDs by the second variant technique, wherein, QD-formation is induced by deposition of amorphous selenium onto an epitaxially strained CdSe layer and its subsequent desorption. The properties of the QDs formed by this technique are discussed in the first part of this chapter. The second part deals with growth and positional ordering of QDs in QD-superlattices. For the QD-superlattices, the first layer of QDs was grown by this technique, while the subsequent layers by migration enhanced epitaxy (MEE) (refer to section 3.1, Fig. 3.3), an alternative of conventional MBE.

Chapter 8 addresses to a technique similar to that of Chapter 7, the only difference being in the fact that instead of amorphous selenium, amorphous tellurium is used to induce self assembly of CdSe/ZnSe(001) QDs. A key feature of this approach is the formation of patterned ensembles of QDs. In this chapter, the morphology, composition and optical properties of these QDs, and the mechanism of pattern formation by this technique are discussed in detail. An approach for controlled positioning of QDs and QD-based nanostructures is also presented.

Chapter 9 concludes the main results of this thesis and provides possible future directions of research in the field of CdSe/ZnSe(001) QD self assembly.

Epitaxial quantum dots: Self-assembly, ordering, and exciton confinement

2

This chapter provides a general introduction to self-assembly, ordering, and confinement properties of epitaxial QDs. In the first two sections, self-assembly of QDs is discussed from a thermodynamic standpoint. Section three deals with the kinetics of heteroepitaxy in general, and of QD-self-assembly, in particular. Different issues associated with practical fabrication of self-assembled QDs are detailed in the fourth and the fifth sections, followed by a discussion on the vertical and lateral ordering of self-assembled QDs, in section seven. The eighth section is devoted to epitaxial QDs of the CdSe/ZnSe(001) heterosystem, which is the primary topic of this thesis. The final section deals in brief with the energy levels of confined excitons in epitaxial QDs.

2.1 ***Heteroepitaxy and the Stranski-Krastanow transition***

The term *epitaxy*, introduced by Royer in 1928 [Royer1928], refers to the growth of a crystalline layer upon (*epi)* a crystalline substrate, where the orientation of the substrate imposes an order (*taxis*) on the orientation of the deposit layer. If the substrate and the deposit are identical, the growth process is known as *homoepitaxy*. If they differ in their composition and/or lattice constant, the term *heteroepitaxy* is used. When the bulk-lattice constant of the substrate differs from that of the epi-material, strain builds up in the growing epilayer. This is because, the epilayer distorts tetragonally during the initial stage of growth, to adopt the lattice constant of the substrate. The nature of the strain is determined by the lattice misfit (alternatively called lattice mismatch), m, given by

$$m = \frac{a_B - a_C}{a_C} \quad (2.1),$$

where a_B and a_C denote the bulk lattice constants of the epilayer and the substrate, respectively. A positive (negative) value of m signifies compressive (tensile) strain within the growing epilayer. It is the relief of this misfit induced strain, or in other words, the stored elastic energy, which drives the self-assembly of different nanostructures.

As mentioned in Chapter 1, fabrication of QDs requires the self-assembled structures to resemble tiny “islands”, having all three dimensions in the nanoscale. The simplest explanation how islands self-assemble in semiconductor heteroepitaxy is provided by the thermodynamics of equilibrium crystal growth. From a thermodynamic point of view, crystallization represents a phase transition, wherein atoms/molecules condense from the vapor/liquid phase (G) to the crystal phase (B). At thermodynamic equilibrium their chemical potentials, μ_G and μ_B, are equal, i.e.

$$\mu_G(P,T) = \mu_B(P,T) \quad (2.2),$$

where P and T are the pressure and temperature of the two-phase system. If P or T is changed in a way that the system deviates from equilibrium, the chemical potential of one of the two phases is lowered and this phase becomes relatively stable. Thus, if the condition

$$\Delta\mu = \mu_B - \mu_G < 0 \quad (2.3),$$

is satisfied, crystallization takes place. $\Delta\mu$ is the driving force for such a phase transition. In heteroepitaxy, the foreign substrate represents an additional phase C. In presence of lattice misfit m, the chemical potential of the n-th monolayer (ML) of the epilayer reads

$$\mu_B(n) = \mu_B^{\infty} + \Omega^2(\gamma_B + \gamma_I(n) - \gamma_C) \quad (2.4),$$

where γ_B and γ_C, denote the *specific surface energy* of the epilayer and the substrate, respectively and γ_I, the *specific interface energy* of the B-C interface (see BOX 2.1)

[Markov95]. μ_B^∞ denotes the chemical potential of the bulk of *B*, and Ω^2 the area per unit atom. $\gamma_I(n)$ is given by

$$\gamma_I(n) = \gamma_C + \gamma_B - \gamma_{CB} + \tau_e(m^2, n) \qquad (2.5).$$

Here, γ_{CB} denotes the s*pecific adhesive energy* (refer to BOX 2.1) and τ_e is the stored elastic energy per unit area, which is a parabolic function of *m* and a linear function of *n*. The balance between the three terms γ_C, γ_B, and $\gamma_I(n)$ determines the different possible growth modes in heteroepitaxy.

BOX 2.1 *Surface and interface energies*

The energy spent to create reversibly and isothermally a unit area of new surface is called *specific surface energy*. To create a new surface, chemical bonds between the atoms of a crystal need to be broken. Thus, the specific surface energy, as a first approximation, is equal to the sum of the energies of the broken bonds per unit area.

If two crystals B (deposit) and C (substrate) of equal dimensions and lattice-parameters are cleaved reversibly and isothermally, two new surfaces of each of A and B (of size Σ) are produced. The work done to create the four new surfaces is the sum of the energies required to break all B-B and all C-C bonds within the area Σ, U_{BB} and U_{CC}, respectively. When now each half of B is placed in contact with a half of C, energy equivalent to $2U_{BC}$ is gained by creating two new B-C interfaces. Therefore, the net energy spent in creating the two new interfaces[Dupré69]

$$2U_I = U_{BB} + U_{CC} - 2U_{BC}$$

Dividing the above Eqn. by 2Σ gives the expression for *specific interfacial energy* in terms of specific surface energies ($U_{BB}/2\Sigma$ and $U_{CC}/2\Sigma$) of the two crystals. U_{BC}/Σ denotes the *specific adhesive energy.* In Equation 2.5, the additional term τ_e is included to account for the elastic energy accumulated due to the lattice-misfit induced strain between the substrate and the epilayer.

The condition

$$\gamma_B + \gamma_I(n) - \gamma_C > 0 \qquad (2.6)$$

requires minimizing the substrate area covered by the deposit material and growth proceeds by the nucleation of 3D islands on the substrate. This mode of growth is known as the *Volmer-Weber* (VW) growth-mode, depicted pictorially in Fig. 2.1 (a). Substituting the value of $\gamma_I(n)$ from Eqn. 2.5 in Eqn. 2.6, the inequality reads

$$2\gamma_B - \gamma_{CB} + \tau_e(m^2, n) > 0 \qquad (2.7)$$

From Eqn. 2.7, it is evident that even if γ_{CB} exceeds $2\gamma_B$, Eqn. 2.6 might be valid for a large value of τ_e. Since τ_e is proportional to m^2, high lattice misfits favor VW growth [Daruka97]. On the other hand, if *m* is such that $\gamma_{CB} > 2\gamma_B + \tau_e$, the condition

$$\gamma_B + \gamma_I(n) - \gamma_C < 0 \qquad (2.8)$$

is satisfied. The energy balance requires maximizing the area covered by the deposit and growth initiates by formation of at least one complete monolayer. For the successive layers of the deposit, the chemical influence of the substrate (*C*) is largely screened. Therefore, for the growth of the (*n*+1)th layer (of *B*) atop the *n*-th layer ($n > 1$), $\gamma_{CB} \approx 0$. However, due to the linear dependence on *n*, τ_e accrues progressively within the growing epilayer, thereby increasing $\gamma_I(n)$. Eventually, beyond a certain critical thickness t_c (or a critical number of atomic layers, n_c) the condition of Eqn. 2.8 reverts back to that of Eqn. 2.6. This results in the nucleation of 3D islands atop a layer of thickness t_c. It is these 3D islands which form the basis of what is known as epitaxially self-organized QDs. The morphology resulting by this growth-mode, known as the *Stranski Krastanow (SK)* growth-mode, is shown in Fig. 2.1 (b). The layer of thickness t_c, beneath the ensemble of islands is known as the *wetting layer.*

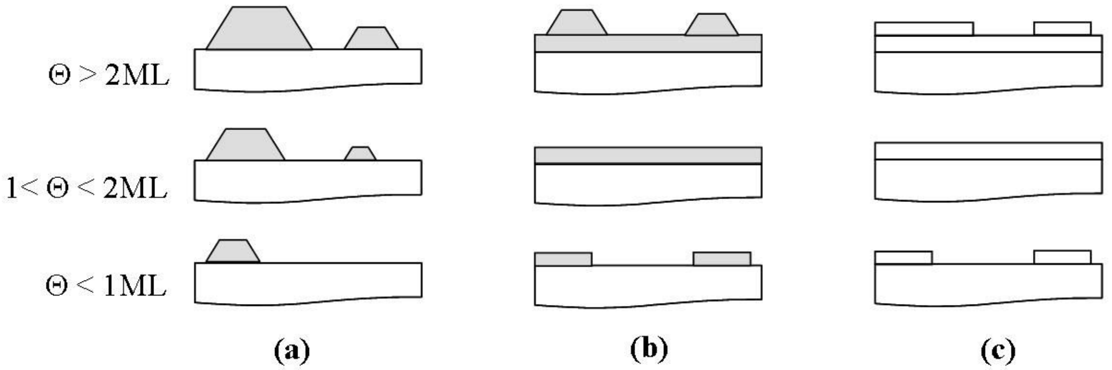

FIG. 2.1: Equilibrium (a) Volmer Weber, (b) Stranski Krastanow, and (c) Frank van der Merwe growth modes. In case of (b) it has been implicitly assumed that $t_c < 2$ ML. The same color of the substrate and the deposit in (c) indicates homoepitaxy.

The limiting condition

$$\gamma_C = \gamma_B + \gamma_I(n) \tag{2.9}$$

can only be fulfilled for *homoepitaxial* systems, for which $\gamma_{CB} = \gamma_C = \gamma_B$ and $\tau_e = 0$. The resulting growth-mode is characterized by unlimited layer-by-layer growth and is known as the *Frank van der Merwe* (*FM*) growth. This is illustrated in Fig. 2.1 (c).

By undergoing the SK transition, the epi-system releases the elastic energy accumulated due to the misfit strain. On the other hand, formation of a large ensemble of nano-size islands results in creation of new surfaces. This signifies an accretion of surface energy. Thus, SK transition is essentially a trade-off between relief of elastic energy and gain of surface energy. The change in total energy of an epi-system in forming a pyramidal 3D island from a 2D layer of equal volume has been derived by Tersoff and LeGoues, in a simple approach combining the elastic and the surface energy terms [Tersoff94]. For the pyramidal island illustrated in Fig. 2.2 (a), it is given by

$$\Delta E = 4\Lambda V^{2/3} \tan^{1/3}\theta_i - 6\kappa V \tan\theta_i \qquad (2.10),$$

where

$$\Lambda = \gamma_n \csc\theta_i - \gamma_b \cot\theta_i \qquad (2.11),$$

and γ_n and γ_b are the specific surface energies for the normal surface and the beveled edges, respectively. V is the volume of the island and $\kappa = \sigma^2(1-\nu)/2\pi\eta$, where ν and η are the Poisson ratio and the shear modulus of the island-forming material, respectively. σ is the bulk stress in the uniform epilayer (before island formation), which is proportional to m. ΔE is plotted versus V in Fig. 2.2(b) (Both parameters are normalized to the corresponding critical values, as explained below).

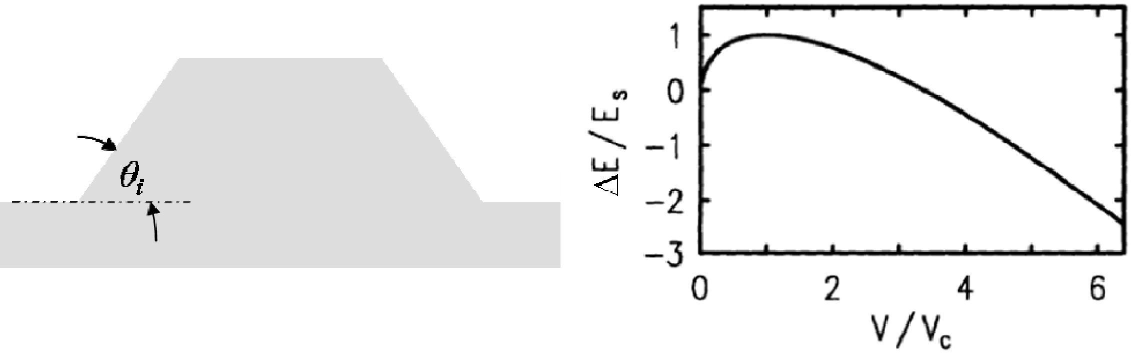

FIG. 2.2: (a) Sketch of a pyramidal SK island. (b) Energy of the island ΔE as a function of its volume V. ΔE and V are normalized to their critical values (see text). Adopted from [Tersoff94]

Clearly, formation of a 3D island lowers the energy of the system once the "volume" of the 2D deposit is sufficiently large. However, there is a barrier E_s which must first be overcome. Maximizing Eqn. 2.10, E_S and V_c, the critical volume for the 2D-3D transition, are derived to be

$$E_S = \frac{64\Lambda^3 \cot\theta_i}{243\kappa^2} \qquad (2.12),$$

and

$$V_c = (4\Lambda / 9\kappa)^3 \cot^2\theta_i \qquad (2.13).$$

E_s and V_c are inversely proportional to the fourth and sixth power of m, respectively.

The SK transition provides a growing hetero-epilayer with an *elastic* pathway for relaxation of the strain energy. However, it should be noted that misfit induced strain can also be released *plastically*, by formation of an array of *misfit dislocations* at the substrate-epilayer interface. Such a case can also be treated within the framework of the equilibrium crystal growth theory, just by replacing τ_e in Eqn. 2.5, by the energy of the misfit dislocations. For a particular heterosystem, whether elastic or plastic relaxation of misfit strain occurs, depends on the relative energy cost of forming islands and misfit dislocations. Also, when the elastic pathway does not lead to sufficient strain relaxation, island formation is succeeded by generation of misfit dislocations.

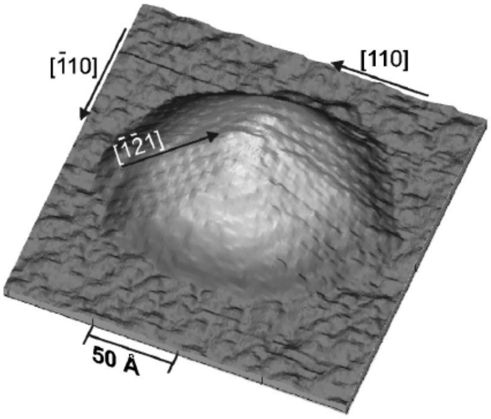

FIG. 2.3: Scanning tunneling microscopy image of a single self-assembled InAs/GaAs(001) island. Adopted from [Márquez01]

Self-organized growth of islands in the SK growth mode has been successfully achieved for a number of heteroepitaxial combinations [Mo90, Guha90, Leon95, Ponchet95, Sopanen95, Carlsson94, Nötzel94]. The two most extensively studied island-forming heterosystems are $In_{1-x}Ga_xAs/GaAs(001)$ and $Ge_{1-x}Si_x/Si$ (001). A single self-assembled InAs/GaAs(001) island is shown in Fig. 2.3 [Márquez01]. In both systems, m can be varied continuously over a wide range of values by varying the composition (x) of the epi-layer. For heteroepitaxial growth of $B_{1-x}C_x$ on C, the lattice misfit is given by

$$m_{BC-C} = m(1-x) \tag{2.14}.$$

where m is given by Eqn. 2.1. Equation 2.14 assumes linear variation of lattice constants, following Vegard's law [Vegard21].

2.2 *Self-assembly of islands and related nanostructures: Beyond SK mechanism*

The SK transition is evidently an activated process, confronted by a barrier given by Eqn. 2.12. E_S depends inversely on m^4. Thus, for very low misfits, island formation by the SK mechanism would be delayed or completely suppressed [Daruka97], due to energetic precedence of plastic relaxation. However, in the SiGe/Se(001) heterosystem, islands assemble even for very low values of m (≤ 0.01) [Sutter00, Tromp00]. To comprehend island formation in low-misfit heterosystems, one needs to turn to the fundamental phenomenon of morphological instability of stressed (epitaxial) surfaces, known as the Asaro-Tiller-Grinfeld (ATG) instability [Asaro72, Grinfeld86, Stangl04]. According to the ATG model, a surface under (compressive) stress and in contact with its liquid or vapor phase develops undulations of a definite periodicity, resulting in a morphology of crests and troughs. The undulations allow the compressed lattice planes of the bulk to relax towards the peaks of the crests [Jesson98]. The minimum wavelength λ_{ATG} of the undulations is determined by the balance between the elastic energy released and the associated cost in surface energy. It is given by

$$\lambda_{ATG} = \frac{2\eta\pi\gamma}{(1-\upsilon)m^2} \tag{2.15}.$$

where, γ is a general expression for the specific surface energy corresponding to the new surfaces formed, and the rest of the terms are as defined in the context of Eqn. 2.10 and 2.11. Phenomenologically, the energetics of the ATG instability are similar to that of the SK transition but the difference is in the fact that in the ATG model *there is no energy barrier involved*, except for kinetic barrier to mass transport (see (next) section 2.3). Undulations are formed for *all* misfits with λ_{ATG} proportional to m^{-2}.

To explain island formation in the low misfit (m = 0.1) $Ge_{0.25}Si_{0.75}$/Si(001) heterosystem, Sutter et al. resorted to the ATG model. The authors argued that island formation in their case did not occur by an activated nucleation process, which is characteristic of the SK growth mode, but by a continuous development of *bi-directional* surface undulations. The atomistic origin of the undulations was assigned to *step-bunching* on strained *vicinal* crystal surfaces (For description of vicinal surfaces, refer to BOX 2.2).

BOX 2.2 *Singular and vicinal crystal surfaces*

When the surface of a substrate is bounded by a low-Miller-index plane, i.e. (100), the surface is known to be *singular* [Fig. 2.4 (a)]. However, due to (un)intentional miscut during processing, the surface plane of a real crystal is always inclined by a small angle α (typically a few tenths of a degree) to a low-index plane, in one or more directions. For geometrical reasons such a surface consists of terraces and steps [Fig. 2.4 (b)]. Crystal surfaces with such morphology of flat terraces, separated by steps, are known to be *vicinal*.

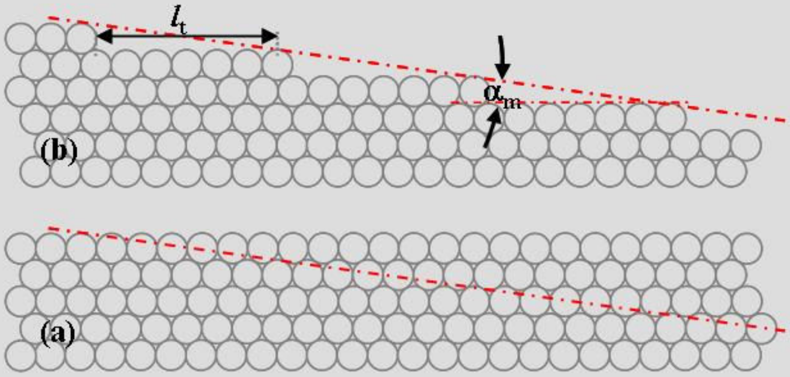

Fig. 2.4: A (a) Singular and (b) vicinal crystal surface. The miscut direction is shown by the red dotted line. The miscut angle and terrace width are denoted by α_m and l_t.

When strained, the equi-spaced steps of a vicinal surface interact via a long-range attractive potential [Tersoff95]. This results in bunching of the steps, as illustrated in Fig. 2.5 (a) [Phang94], and formation of an undulated surface. A step-bunched surface, consisting of ripples (unidirectional undulation), is shown in Fig. 2.5 (b) for a 2.5 nm thick $Ge_{0.45}$ $Si_{0.55}$ epilayer grown on a vicinal Si(100) surface, with a miscut angle α_m = 0.25° in the [110] direction [Teichert02]. The wavelength of the ripple pattern is ~ 650 nm. Sutter et al considered step-bunching in two perpendicular directions such that a quasiperiodic array of well-defined square cells (prepyramids), bounded by bunched-steps, formed at the beginning of island formation (Fig. 2.5 (c)). With continuing deposition, these prepyramids grew in height but not in their lateral size, which was limited by the presence of the neighboring features. The inclination of the beveled surface increased continuously until it approached a value of $\theta_i = 11°$ (refer to Fig. 2.2). At this stage a first order transition from a morphology of step-bunched prepyramids to that of facetted pyramids (bounded by (105) facets, corresponding to $\theta_i = 11°$) took place (Fig. 2.5 (d)).

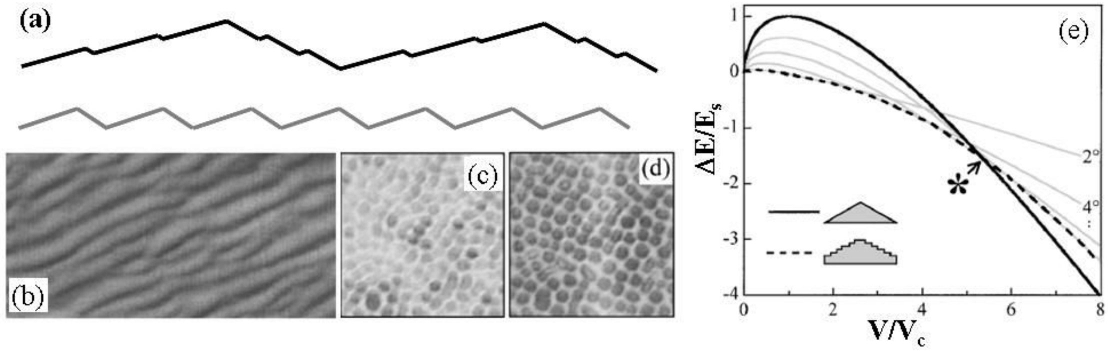

FIG. 2.5: (a) Schematic illustration of step bunching. The grey profile corresponds to the equi-spaced steps of a vicinal substrate. The black profile illustrates the step-bunched surface of the strained epilayer grown atop the vicinal substrate.(b) AFM-image of a typical ripple-pattern on the surface of a 3 nm thick $Ge_{0.45}Si_{0.55}$ layer grown on vicinal (001) Si substrate, with a miscut $\alpha_m = 0.25°$ along the [110] direction. (c) Low-energy-electron-microscopy (LEEM)-image of step-bunched prepyramids on the surface of a 60 ML-thick $Ge_{0.25}Si_{0.75}$ epilayer. (d) (105)-facetted pyramidal islands formed from stepped prepyramids after deposition of an additional 18 ML of the alloy. (e) Energy of a pyramidal island ΔE as a function of its volume V. The solid dark line is the plot for islands bounded by (105) facets, having $\theta_i = 11°$. The grey lines correspond to prepyramids with different θ_i. The dotted line is an envelope of the grey lines for all θ_i values between 0-11°. Fig. (b) adopted from [Teichert02], Fig. (c), (d) and (e) from [Sutter00].

The argument of *barrierless* formation of islands (without activated nucleation) does not contest the model of Tersoff presented before (section 2.2, Figs. 2.2 (a) and 2.2 (b)). To understand this, it is imperative to note that for the plot of Fig. 2.2 (b), θ_i is fixed. When during the course of island formation θ_i is allowed to vary, it is revealed that the island formation process is not confronted by any energy barrier. Fig. 2.5 (e) shows ΔE-versus-V plots, similar to that of Fig. 2.2, but for different θ_i [Sutter00]. The black (solid) curve corresponds to pyramidal islands with $\theta_i = 11°$ (bounded by (105) facets), whereas the grey ones to some prepyramids with $\theta_i < 11°$. The dashed curve is an envelope of several grey curves, for prepyramids with θ_i varying between 0-11°. Evidently, the formation of prepyramids with $\theta_i \leq 11°$ is not confronted by any energy barrier, so that they evolve continuously in height and θ_i. However, at a certain value of V (the crossover point in Fig. 2.5 (e)) it becomes favorable to form pyramids with (105) facets, rather than prepyramids, bounded by step-bunches (see the inset).

2.3 *Kinetics of island-self-assembly*

So far, in discussing the formation of islands, aspects of heteroepitaxy have been delineated based on thermodynamics and without reference to any particular epitaxial growth technique. However, molecular beam epitaxy (MBE), the technique routinely used for the fabrication of QD-ensembles, represents a process *far from thermodynamic equilibrium*. While in equilibrium crystal growth, $\Delta\mu$ (in Eqn. 2.3) is ~ 10 meV/atom, in MBE, $\Delta\mu$ can be as large as ~5 eV/atom. Such high $\Delta\mu$ is an enormous driving force, similar to binding energies of atoms in crystals. The large difference in $\Delta\mu$ between MBE and equilibrium crystal growth implies a conceptual difference in the description of these two situations. For atoms passing the phase boundary from the vapor to the solid phase under crystal growth conditions, only the stable binding sites of the crystal are available for condensation. Metastable binding sites with higher chemical potential can be accessed only temporarily, as otherwise the energy balance between the phases would be invalid. Atoms in the metastable binding sites either re-cross the phase boundary or rapidly switch to stable binding sites. In such a situation, thermodynamics is sufficient to give an adequate description of the process.

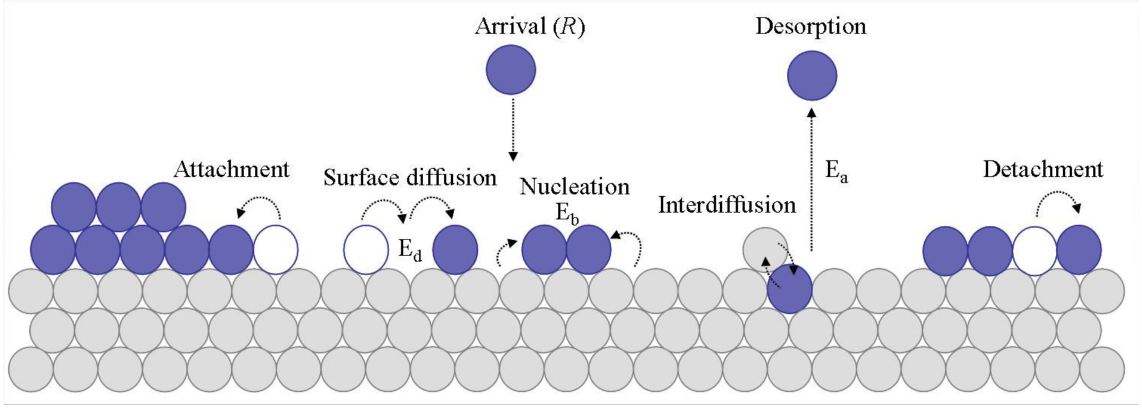

FIG. 2.6: Atomistic processes in MBE growth (heteroepitaxy)

To the contrary, a manifold of metastable sites on the substrate are populated during MBE growth. Chemical potentials of such sites are higher than that of an atom in the bulk but still significantly lower than the gas phase chemical potential. Thermodynamics in this case might set the boundary conditions but would be insufficient for a complete description of the process. Therefore, for practical epitaxial growth scenario, kinetics of the atomistic processes needs to be considered. In heteroepitaxy, energetic (e.g. due to lattice misfit and differences in surface energy) and kinetic effects due to far from equilibrium growth conditions are usually intertwined. Thus, classification of epitaxial growth in terms of Volmer-Weber, Stranski-Krastanow, and Frank van der Merwe equilibrium-models is an oversimplification and sometimes even misleading. Indeed, the discussion of section 2.2 indicated also to other mechanisms of island-formation. Nonetheless, both thermodynamic and kinetic models have been extensively used in describing the formation of islands by the SK phenomenon. While thermodynamics assumes all kinetic processes to be adequately fast for the epitaxial system to reach its equilibrium configuration, kinetic approaches consider that the equilibrium state is never reached and the attributes of the epitaxial system is determined by particular kinetic pathways.

The atomistic processes responsible for the nucleation and growth of epitaxial layers (thin films in general) are indicated in Fig. 2.6. Atoms arrive from the vapor phase at a rate R, or at an equivalent gas pressure p, such that

$$R = p/(2\pi m_A k_B T_{source})^{1/2} \tag{2.16}$$,

where m_A is the atomic mass of the evaporated species and T_{source}, the absolute temperature of the source. This creates single adatoms (or admolecules) on the surface of the substrate, whose areal density $n_1(T_G)$ increases initially as $n_1 = Rt$. Here, T_G is the temperature of the substrate or the growth temperature. At high T_G, these adatoms reside on the substrate surface for a short duration–the adsorption residence time τ_a. During this time they migrate over the surface with diffusion coefficient D. τ_a is given by

$$\tau_a^{-1} = \nu_a \exp(-E_a / k_B T_G) \tag{2.17}$$,

where ν_a is the atomic vibration frequency, of the order of 1-10 THz and E_a, the activation barrier to desorption. In terms of the diffusion barrier E_d and frequency ν_d (typically somewhat less than ν_a), D is given by

$$D = (\nu_d a_j^2 / 4) \exp(-E_d / k_B T_G) \tag{2.18}$$,

where a_j is the jump distance, of the order of 0.2-0.5 nm. The number of substrate sites visited by an adatom in time τ_a is $D\tau_a/N_0$, where N_0 is the areal density of such sites. The rms displacement of the adatom from the arrival site before evaporation is

$$x_{rms} = (D\tau_a)^{1/2} \cong a_j (\nu_d / \nu_a)^{1/2} \exp\left[(E_a - E_d)/2k_B T_G\right] \tag{2.19}$$,

Since typically E_a is several times E_d, (x_{rms}/a_j) can be large at suitably high temperatures. Adatoms in this case encounter, during their migration, other adatoms and form small clusters. While many clusters disintegrate once again, those larger than a critical size, i^* (in terms of number of atoms), become stable. The temporal variation of the concentration of adatoms, n_1, and stable 2D clusters, N_x, on the surface of a growing epilayer is solved based on a set of coupled differential equations, established by Venables *et al* [Venables84]. In homoepitaxy, N_x depends on the deposition rate R, diffusion rate D (in terms of number of diffusion jumps per unit time), the amount of material deposited, or in other words, the coverage Θ, T_G, the energy of the critical cluster $E(i^*)$, and i^* as

$$N_x \propto \Theta^{1/(i^*+2)} \left(\frac{D}{R}\right)^{-i^*/(i^*+2)} \exp\left[\frac{E(i^*)}{(i^*+2)k_B T_G}\right] \tag{2.20}$$,

With subsequent deposition, stable clusters grow in size, due to attachment of mobile adatoms to their edges. A competing adatom-detachment process might also occur at this stage. Both attachment and detachment of adatoms are thermally activated processes.

Finally, when the separation between the clusters becomes comparable to their size, coalescence sets in. Ideally, complete monolayers are formed at the end of coalescence.

In heteroepitaxy, the lattice-misfit-induced strain acts to modify the chemical potential of adatoms at the growth-front and also the activation barriers of the different atomistic processes mentioned above. *D, i*,* and activation barriers to adatom-attachment and -detachment are influenced by the misfit-induced strain. Furthermore, 2D islands "roll up" to form 3D islands, beyond a critical cluster-size, by "up-climb" of adatoms from the edges to the top of the islands.

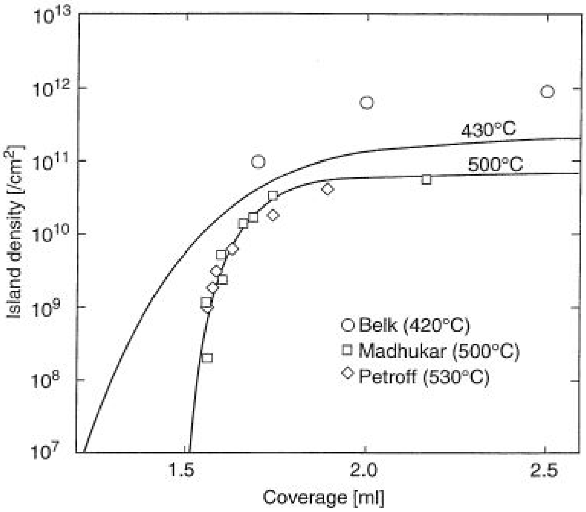

FIG. 2.7: Areal density of InAs/GaAs (100) islands, obtained from rate equations (solid lines), as a function of InAs coverage (ML). The experimental data shown are from Leonard et al. [Leonard93], Kobayashi et al. [Kobayashi96], and Belk [Belk96]. The solid lines are theoretical fits for growth temperatures of 500 °C and 430 °C. Adopted from [Joyce97]

The relative role of kinetics and thermodynamics in the context of QD-growth is highlighted in the fact that self-assembly of InAs/GaAs islands takes place only on the (001) surface, but not on the (110) and (111) A surfaces of GaAs. This would be unexpected if strain-relaxation would be the only driving force for the SK transition. Furthermore, the 2D-3D transition is sensitive to the ratio of In and As fluxes and the *reconstruction* (see Box 3.1) of the (001) GaAs surface. For the InAs/GaAs heterosystem, Joyce et al. studied the kinetics of 2D and 3D island nucleation in presence of misfit strain, following the rate equation model of Venables *et al* [Joyce97]. The density of 3D islands, calculated considering increased (infinite) barrier to adatom-detachment from *strained* 2D (3D) clusters, reduced attachment-barrier to 3D clusters, and a critical cluster size for 2D clusters to roll-up to 3D islands (driven by the possibility of strain relaxation), is shown by the solid curves in Fig. 2.7. The calculated plots show good agreement to experimentally determined values, shown in the figure by the scatter data [Leonard93, Kobayashi96, Belk96].

3D nanostructures are also formed by a purely kinetic phenomenon known as *mounding.* While a thermodynamic argument predicts perfect layer-by-layer FM growth for homoepitaxy, kinetic limitations might lead to deviations from the ideal scenario and result in what is known as "multilayer growth". When 2D clusters of a particular layer are sufficiently large, atoms from the vapor phase might directly land on top of them. For smooth layers to grow, it is important at this stage that these adatoms diffuse down from the top to the edges of the 2D clusters. Thus along with *intralayer* diffusion, *interlayer* diffusion assumes a governing role. When downward interlayer diffusion ("down-climb") is fast, coalescence is efficient and layer-by-layer growth proceeds. When it is slow, the growth-front is characterized by multiple levels of incomplete layers.

BOX 2.3 *Elrich-Schwoebel (Step edge) barriers*

The energy-barrier to adatom hopping is higher at the edge of surface steps or at the peripheries of 2D clusters, compared to that on a flat surface. This is because the co-ordination number of an adatom is reduced at the edge positions.

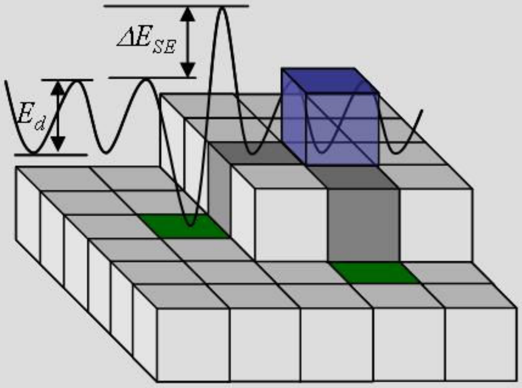

Fig. 2.8: Schematic illustration of adatom hopping (diffusion) across a step-edge. The energy-barrier to adatom hopping shows an increase by ΔE_{ES} at the step-edge.

Fig. 2.8 schematically shows an adatom (blue block) atop a 2D cluster. It has one (four) nearest-neighbor (next-nearest neighbors), with which it shares one face (four edges). The number of nearest-neighbors increases when the adatom climbs down to the positions marked in green (edge sites). However, in the intermediate dark-grey positions, the number of nearest-neighbors remains constant, but that of next-nearest neighbors reduces by one. Occupying these positions is therefore unfavorable for the adatoms. This gives rise to the additional diffusion-barrier at the step-edges, ΔE_{ES}, which is known as the *Elrich-Schwoebel* barrier, or the step-edge barrier.

What hinders efficient down-climb of adatoms is the so called *Ehrlich-Schwoebel* (ES) barrier [Ehrlich66, Schwoebel66], or the step-edge barrier (see BOX 2.3). Mounding might be considered as a special case of multilayer growth, where (*intralayer) surface diffusion is operative but adatom down-climb is hindered or inhibited*, due to the presence of ES barriers [Orme98]. An example of a surface morphology consisting of uniform mounds is shown in Figs. 2.9 (a)-(c) [Michely04]. Clusters of the first layer provide the template on which subsequent clusters of progressively decreasing size, but similar shape, nucleate. The similarity of cluster shapes at different levels substantiates the fact that surface diffusion is existent.

It is interesting to note that, with continuing growth, the slope of the mounds remains constant. This implies that the uncovered terraces at each level have similar widths. Regularization of terrace widths during growth has its origin also in the ES barrier. Due to the ES barrier, adatoms impinging on a particular terrace are reflected from the descending step (impeded down-climb) and are incorporated preferably at the ascending step bounding the terrace.

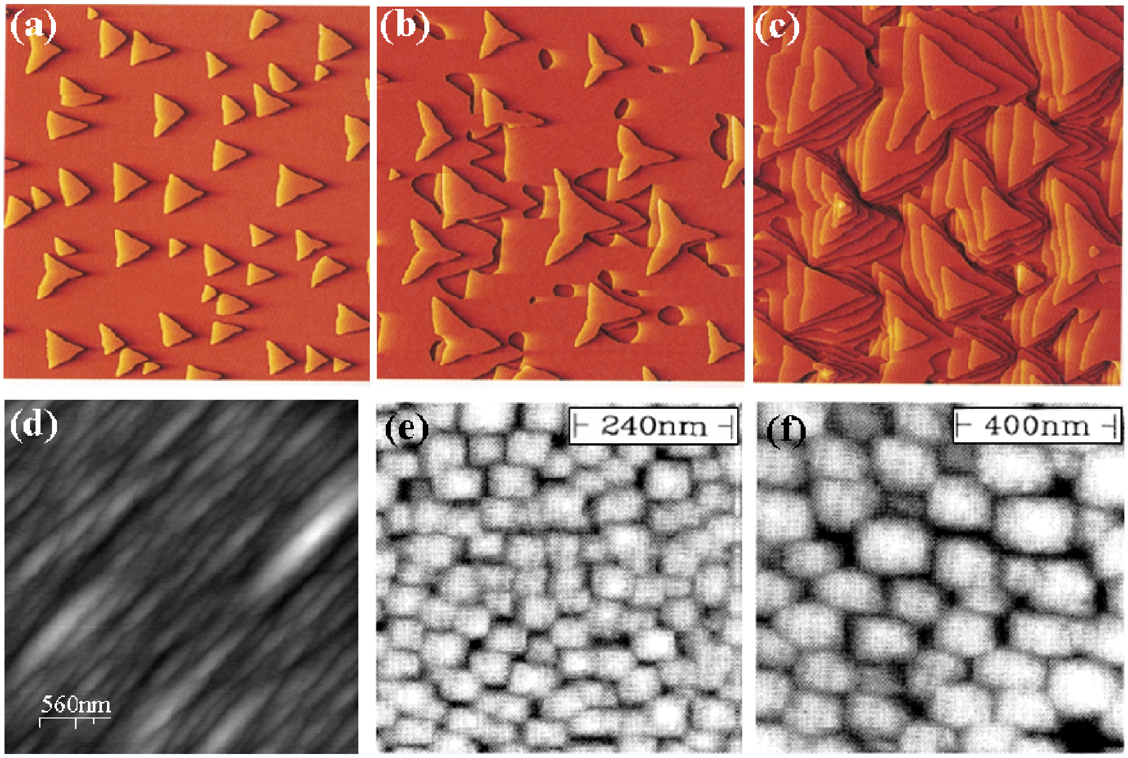

FIG. 2.9: Scanning-tunneling-microscopy-images, recorded after deposition of (a) 0.15 ML, (b) 1 ML, and (c) 5 ML Pt on Pt (111). Adopted from [Michely04]. (d) Atomic-force-microscopy (AFM) image of a 200 nm thick GaAs(001) homoepitaxial layer, grown at T_G = 600 °C. AFM image of a Ge(001) homoepitaxial layer (e) 100 nm thick, grown at T_G = 155 °C and (f) 1000 nm, grown at T_G = 230 °C. Adopted from [Van Nostrand95]

The number of adatoms on a wide step is larger than that on a narrow one, merely due to the larger surface area offered by the former. Hence, preferential attachment of adatoms to ascending steps necessarily causes the wider steps to grow slower than the narrower ones. This phenomenon, after an initial transient period of growth, regularizes the step widths at each level and thereby, conserves the slope of the mounds. Interestingly, even after long duration of growth, the hollow spaces between the mounds are not filled up. This is because the impinging adatoms find it increasingly difficult to climb down the multitude of steps in presence of the ES barrier [Elkinani94].

Mounding occurs also in homoepitaxial growth of semiconductors. In Fig. 2.9 (d), mounds on the surface of a GaAs homoepitaxial layer, grown on nominally singular (001) substrates ($\alpha < 0.1°$) at T_G between 550-620°C are shown [Orme94]. The mounds in this case are elongated along the [1-10] direction. At very low values of T_G, the mounding instability has been also observed in Ge(001) homoepitaxy. Fig. 2.9 (e) and (f) shows mounds formed in MBE growth of Ge(001) at T_G =155 and 230 °C, respectively. The similarity of the regular mound shapes in both images suggests that surface diffusion is existent at both growth temperatures. The smaller size of the mounds of Fig. 2.9 (e), compared to those of Fig. 2.9 (f), might then be assigned to suppressed surface diffusion at a lower T_G. The fact that surface diffusion, though suppressed, is not completely inhibited, and that the mounds have similar shapes, irrespective of the growth temperature and epilayer-thickness, underscores the role of ES barrier in mounding phenomenon.

The mounding instability is an inherently non-equilibrium process. It occurs only when the evolution of the surface is dominated by kinetics rather than by the energetics. When growth is terminated and the surface is allowed to relax to its equilibrium state by annealing, the mounds dissolve.

2.4 *Interdiffusion and segregation during heteroepitaxial self-assembly*

During heteroepitaxial growth, *interdiffusion* processes might also occur, as illustrated in Fig. 2.6. Being a thermally activated process, interdiffusion increases with increasing T_G. For both GeSi/Si and InAs/GaAs heterosystems, interdiffusion occurs for typically chosen values of T_G. Interdiffusion, and concomitant alloying of the epilayer, delays the 2D-3D transition and therefore, results in self-assembly of larger islands. This is comprehensible following Eqn. 2.14, which, for x > 0, implies $m_{BC\text{-}C} < m$. Consequently, V_c in Eqn. 2.13 increases and the onset of the 2D-3D transition is delayed.

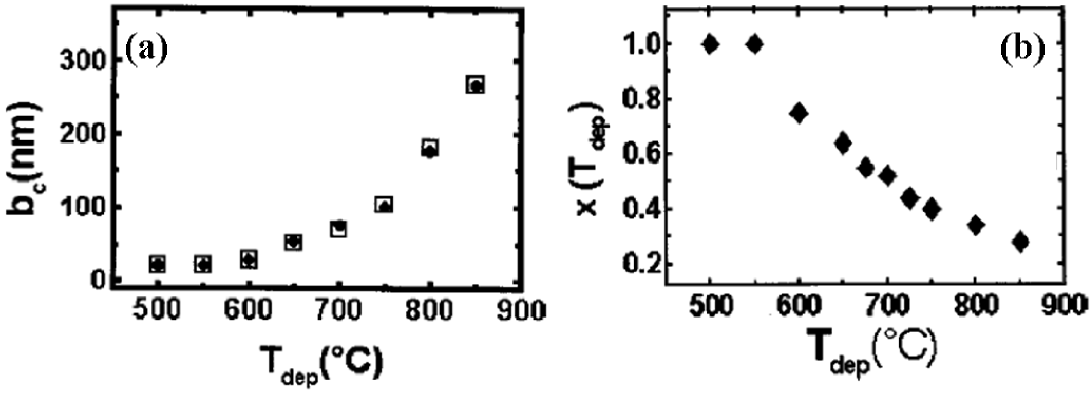

FIG. 2.10: (a) The critical 2D cluster size for the SK transition, b_c, as a function of growth temperature for Ge/Si(001) heteroepitaxy. (b) The average Ge-content of the corresponding self-assembled islands, as a function of the growth temperature. Adopted from [Capellini01]

For Ge/Si heteroepitaxy, Capellini et al. investigated the T_G-dependence of the critical island-base-size, b_c (equivalent to V_c), beyond which 2D islands assume a 3D character

[Capellini01]. The plot is shown in Fig. 2.10 (a), for T_G (T_{dep} in figure) = 500-850 °C. While for $T_G < 600$ °C, b_c remains constant and equal to 25 nm, for growth at 850 °C, it increases to 270 nm. The concomitant decrease in Ge content of the islands is shown in Fig. 2.10 (b).

Alloying and concomitant enlargement of InAs/GaAs(001) islands has been observed by Joyce et al., for $T_G \geq 420$ °C. At a low T_G of 350 °C, interdiffusion is completely suppressed [Joyce97, Belk97]. Interestingly, the amount of material consumed by the 3D islands for growth at $T_G = 350$ °C corroborates well to that deposited *after the occurrence of the 2D-3D transition*. For $T_G \geq 420$ °C, on the other hand, the islands accumulate material from the underlying alloyed wetting layer, substantiated both by measurement of their volume and composition. Based on this observation, Joyce et al. [Joyce04] consider island formation in the InAs/GaAs heterosystem at typical values of T_G to follow a mechanism different from classical SK growth-mode.

While interdiffusion leads to alloying, a reverse process, *segregation*, results in "dealloying". Segregation has been studied intensively in the context of InGaAs growth on GaAs. During InGaAs/GaAs heteroepitaxy, a certain fraction, Z, of In atoms migrate from the penultimate layer to the surface layer, possibly by site-exchange with Ga atoms. This results in a non-uniform In-distribution within the growing epilayer. In presence of segregation, the In-concentration of the n-th monolayer is given by [Muraki92]

$$x_n = x_0(1-Z^n) \qquad (2.21),$$

where x_0 is the nominal In-concentration of the deposit. Within the purview of this model, the amount of In which is not incorporated in the deposit, i.e. which forms a floating InAs-layer at the surface is given by [Toyoshima93]

$$\Theta_{float} = \left(nx_0 - \sum_{i=1}^{n} x_i \right) = \frac{Z}{1-Z} x_0 (1-Z^n) \qquad (2.22),$$

For a particular value of x_0, Θ_{float} saturates to a value given by $\Theta_{float}^{sat} = Zx_0/(1-Z)$. In case of In-segregation, Z has been determined to be ≈ 0.85. This implies that when $x_0 \geq 0.31$, Θ_{float}^{sat} exceeds 1.8 ML InAs. This value corresponds to t_c for pure InAs/GaAs SK transition. Some reports in literature claim that the critical coverage for 2D-3D transition in ternary InGaAs/GaAs(001) heteroepitaxy essentially represents the thickness of the InGaAs deposit for which Θ_{float}^{sat} reaches 1.8 ML, i.e. the t_c for pure InAs/GaAs(001) [Toyoshima93, Gerard92]. This idea is in variance with the argument that the SK transition is delayed in case of ternary InGaAs/GaAs heteroepitaxy due to a reduced lattice-misfit. Experimentally, the minimum In-content for which 3D islands have been observed to self-assemble is $x_0 \approx 0.25$ [Cullis96].

Walther et al. studied the 2D-3D transition in $In_{0.25}Ga_{0.75}As$/GaAs heteroepitaxy and analyzed the composition of the resultant islands [Walther01]. According to the authors, In-concentration increased from the base to the apex of the islands and reached a peak value of 0.62. The authors assigned this to In-segregation to the surface prior to islanding. Tersoff investigated the thermodynamics of island-nucleation for alloyed epi-systems, wherein, in addition to the surface and elastic energy terms, a term due to the enthalpy of mixing was taken into account [Tersoff98]. The calculations revealed that dealloying by segregation of the larger misfit component reduced the barrier to island nucleation and resulted in In-enrichment of islands, as observed by Walther et al.

From a thermodynamic standpoint, it is intriguing to consider both segregation and interdiffusion processes in the island growth of a particular heterosystem. During InAs/GaAs growth, interdiffusion sets in from the very beginning of the growth. This would not be expected if In atoms tend to segregate to the growth front. In other words, if in InGaAs/GaAs heteroepitaxy In atoms segregate to the surface, no intermixing would be expected for growth of pure InAs on GaAs, since both processes involve a site-exchange mechanism. Tentatively, the discrepancy is explained by the fact that initially, interdiffusion provides an effective channel for partial strain relaxation. However, with increasing coverage the epi-system *anticipates* more efficient strain relaxation by islanding and segregation (or, more appropriately, dealloying phase separation) is switched on.

In conclusion, albeit heteroepitaxial self-assembly of 3D nanostructures is often assigned to the Stranski-Krastanow equilibrium growth mode, the details of the phenomenon reveals several peculiarities, which are yet to be fully understood.

2.5 *Capping of self-assembled islands and formation of QDs*

For QDs to form, self-assembled islands must be capped by the substrate (or some other higher-bandgap barrier) material. Capping is far from a simple encapsulation process and modifies the islands significantly [Garcia97, Joyce01, Sonmuang03] . The main effect is vertical truncation and lateral expansion of the islands. In the extreme case, the islands “collapse” completely in an inhomogeneous QW-like structure [Joyce01].

Figure 2.11 illustrates the morphological evolution of InAs/GaAs(001) islands, during capping with GaAs [Joyce01]. Typically, the sidewalls of self-assembled InAs islands are bounded by well-defined facets. This leads to the characteristic RHEED pattern, wherein the spots appear with chevron-shaped wings [left image of the inset of Fig. 2.11(a)]. The chevron-angle is related to a particular aspect ratio of the islands, and therefore, to a particular inclination of the sidewalls. During the initial stages of capping, the chevron-angle reduces rapidly, which signifies truncation of islands. Vertical truncation and concomitant lateral expansion of islands have also been directly observed by STM and AFM [Joyce01, Sonmuang03]. The evolution of the island-height with increasing nominal coverage of GaAs is depicted by the plot of Fig. 2.11(a) (From in-situ STM measurements) . The straight solid line in the plot indicates the height of the islands, (h_0-h_{cap}), as would be expected if the deposited GaAs simply filled up the regions between the islands. The measured values decrease significantly faster. Furthermore, it is evident that the islands collapse rapidly during the initial stages of capping. Fig. 2.11 (b) shows the evolution of the length (measured along [1-10] direction) and width (measured along [110] direction) of the islands with capping. A rapid increase in size, along both directions, is observed. The size enlargement is however anisotropic and is faster along the [110] direction.

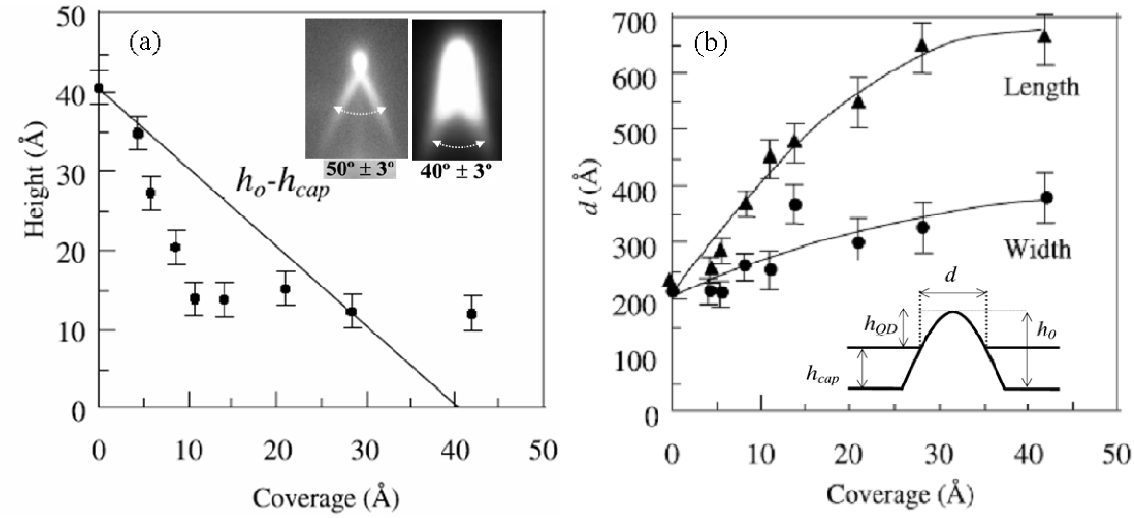

FIG. 2.11: (a) Variation of InAs island height with GaAs coverage, during capping. Inset: Spots of the RHEED pattern corresponding to GaAs-cap-layer thickness of 1 ML (left image) and 5 ML (right image) (b) The variation of the length (along [-110]) and width (along [110]) of the islands with capping. Inset: Schematic illustration of a partially capped island, explaining how the different parameters are defined. Adopted from [Joyce01]

Capping-induced truncation/collapse of self-assembled InAs islands is explained as follows [Srolovitz89, Xie94, Barabási97]: During capping, GaAs growth initiates preferentially in regions between the InAs islands. This is because GaAs growth is unfavorable atop or in the vicinity of the strain-relaxed InAs islands, due to the large lattice misfit. Therefore, adatoms landing close to the islands migrate quickly to regions in-between (Fig. 2.12 (a)). With progressive capping, regions around the InAs islands are eventually filled up, due to which, compressive strain accumulates at the island-edges. This compressive strain at the island-edges forces lateral segregation of In from the uncapped regions of the islands (Fig. 2.12 (b)). The segregated In atoms then migrate long distances on the GaAs cap-surface and form a continuous layer. This leads to the observed truncation/collapse of the islands.

Theoretical calculations further reveal that due to segregation of In atoms from the islands, and subsequent formation of a 2D InAs layer, the total energy of the epi-system is lowered [Songmuang03]. Before capping, it is energetically favorable for In-atoms to reside within the islands, rather than being incorporated in the wetting layer.

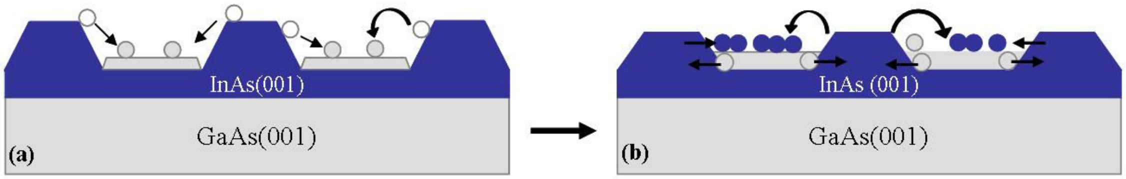

FIG. 2.12: Schematic illustration showing (a) growth of GaAs between the islands during initial stages of capping and (b) In-segregation and Ga-intermixing of islands at a later stage.

After capping partially with GaAs, the energy of the epi-system is lowered when In atoms detach from the islands and form a complete layer (a second wetting layer) on the GaAs surface. This is because InAs has a natural tendency to cover GaAs(001) surfaces (due to a lower energy of the InAs(001) surface compared to that of a GaAs(001) surface [Wang00]). This energy benefit, which is not available to the island-system before initiation of capping, drives the segregation of In. Additionally, the possibility of strain relaxation by alloying results in Ga-admixture of the islands.

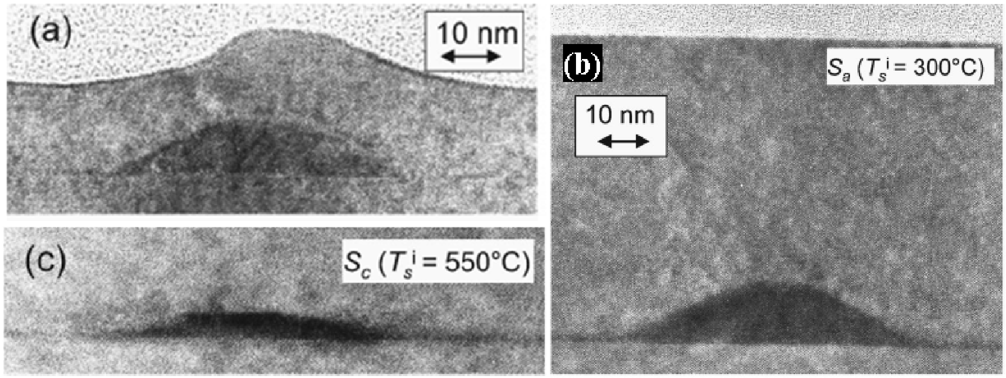

Fig 2.13: HRTEM image of a Ge island (a) capped (by 15 nm of Si) at 300 °C, (b) capped in a two-step process, wherein the first 30 nm of the cap layer was grown at 300 °C and the next 30 nm at 550 °C, and (c) capped (by 60 nm Si) at 550 °C. Adopted from [Rastelli02]

Rastelli et al. demonstrated for Ge/Si(001) heteroepitaxy that while capping at temperatures above 450 °C led to truncation of Ge islands, the morphology of the islands was completely preserved, when capped at 300 °C [Rastelli02]. Due to the reduced temperature of capping, Ge-segregation and Si-alloying of the islands could be arrested. However, for low temperature capping, the Si-cap was observed to follow the profile of the QD-layer, as shown in Fig. 2.13 (a). This is possibly due to reduced surface diffusion of Si adatoms at 300 °C. Based on the explanation given before (for capping of InAs islands with GaAs), it is comprehensible also for Ge/Si(001) heteroepitaxy, that the Si cap layer grow preferentially between the islands. However, this happens only when the adatoms arriving in the vicinity of the islands are able to migrate to regions between them (see Fig. 2.12 (a)). In case surface diffusion is suppressed, this process is hindered, and the profile of the islands is retained in the cap layer.

To obtain a flat cap layer, and at the same time preserve the morphology of the islands, Rastelli et al. followed a different approach. The authors capped the Ge islands first at 300 °C by 30 nm Si, and then ramped up the temperature to 550 °C, where the rest of the capping was performed. Fig. 2.13 (b) shows the TEM image of a Ge island, capped by this approach. For comparison, Fig. 2.13 (c) shows another image where the whole capping was carried out at 550 °C. It is clearly seen that by adopting the two-step capping approach, the authors could preserve the island morphology, and also obtain a flat cap layer.

2.6 *Vertical and lateral ordering of self-assembled islands*

An important factor affecting the optical performance of self-assembled QDs is the uniformity of their size, shape, and composition. The size of a developing 3D island is affected by the area from which the island "collects" adatoms. Therefore, island-size-homogeneity is enhanced when the islands are periodically arranged on the growth surface. An ordered array of islands is desirable not only to achieve size-uniformity but also to realize novel device applications.

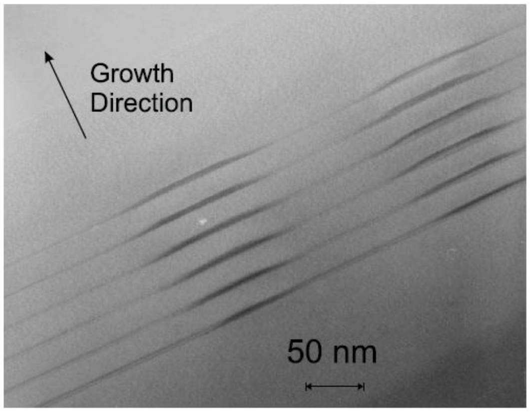

Fig. 2.14: Cross-sectional transmission electron microscopy image of self-ordered stacks of Ge islands in a 6 × (8 ML Ge/30 nm Si) multilayer deposited on (001) Si at T_G = 700 °C. Adopted from [Brunner02].

Typically, the *intraplanar* spatial distribution of heteroepitaxially self-assembled islands, in a single island-layer, is random and devoid of any long-range order. However, when multiple layers of such islands are grown, i.e. in so-called QD-superlattices, the island-positions in successive layers tend to exhibit certain correlation. In both InAs/GaAs(001) and Ge/Si(001) QD-superlattices, islands of a particular layer nucleate directly atop the islands of the previous layer, as shown in Fig. 2.14 [Brunner02]. For certain other heterosystems, the direction of positional correlation is inclined at a particular angle to the surface-normal of the QD-superlattice (growth-direction). Interestingly, both vertical and oblique *interplanar* correlation of islands has been observed to induce a uniformity of size and lateral separation of islands. Unlike the islands of the first layer of a QD-superlattice, which are randomly positioned, those evolving after several repetitions, tend to exhibit a long-range intraplanar ordering.

Vertical correlation occurs also as a result of elastic strain relaxation in islands. In a Ge/Si(001) QD-superlattice for example, consecutive Ge-island-layers are separated by Si “spacer layers” (see Fig. 2.14). In the immediate vicinity of the strain-relaxed Ge islands, the Si spacer layer is strained (tensile). On the other hand, in regions far away from the islands, the cap layer is unstrained or even weakly compressively strained.

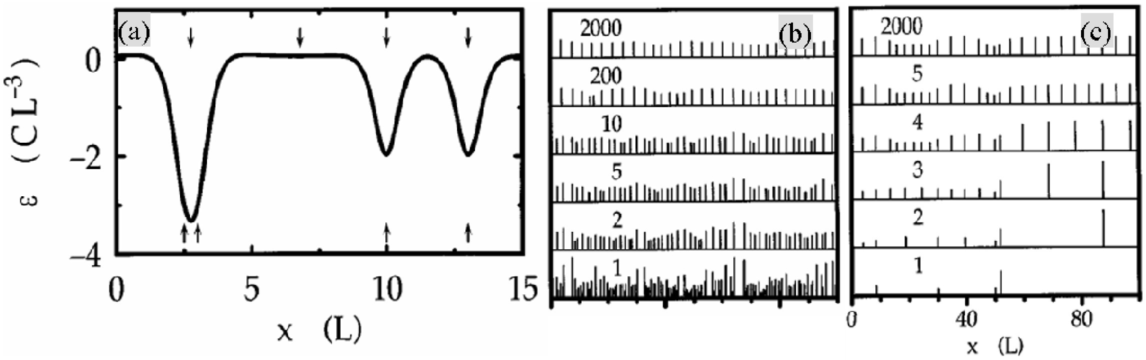

FIG. 2.15: (a) Strain variation at the surface due to point islands buried at a depth *L*. (b) Evolution of vertical and lateral ordering in a QD-superlattice wherein the island-spacing of the first layer is (b) much smaller and (c) larger than *L*. Adopted from [Tersoff96]

Consequently, the strain within the subsequently evolving Ge-island-layer is not uniformly compressive but modulated by local minima at positions directly above the buried islands of the previous layer. Tersoff et al. studied the evolution of a 1+1 dimensional QD-superlattice in the framework of continuum elasticity theory [Tersoff96]. According to their theory, an island buried at a depth *L* leads to a surface strain $\varepsilon(x)$ at lateral position *x* (relative to itself), where

$$\varepsilon(x) = C(x^2 + L^2)^{-3/2}\left[1 - 3L^2(x^2 + L^2)\right] \qquad (2.23).$$

The coefficient *C* is proportional to the volume of the buried island and involves the lattice misfit *m* and the elastic constants [Maradudin80]. The strain distribution is shown in Fig. 2.15 (a), for an arbitrary assembly of buried islands (denoted by the arrows at the bottom of the panel). The evolution of vertical ordering has been studied by the authors assuming growth to be a completely deterministic process wherein, all adatoms diffuse to the nearest island. With this assumption the island volume is proportional to the area of its Voronoi polygon (the region closer to the island in consideration than to any other).

Considering a random distribution of islands in the first layer, with an average intralayer island-spacing much smaller (larger) than the spacer layer thickness *L*, the evolution of the superlattice is shown in Fig. 2.15 (b) (Fig. 2.15 (c)). Vertical correlation is observed in all cases whenever the inter-island spacing is large enough for their strain fields not to overlap.

What is more striking is the fact that, for successive layers, the island size and spacing become progressively more uniform. Regardless of the initial distribution of islands, the lateral island spacing saturates to a value of $3.5L$. This evolution is explained as follows: For initial island-spacing much greater than $3.5L$, new islands nucleate not only vertically atop the buried ones, but also in spaces between them. Conversely, for islands which are closely spaced, no distinct minimum in $\varepsilon(x)$ exists above each island, due to an overlap of the corresponding strain fields. These two opposite effects "select" out an optimum value for the intralayer island spacing. The spacer layer thus acts like a band pass filter for the spatial frequency, in a way that its successive application leads to regularization of the island-spacing.

Within the purview of 1+1 dimensional Tersoff model, vertical correlation and an induced lateral ordering of islands is well-elucidated. However, the model does not address to the case of non-vertical or oblique correlation. Oblique correlation has been studied extensively by Springholz et al. [Springholz98, Holý99, Springholz01]. According to their model, *all* forms of inter- and intraplanar ordering of self-assembled islands can be explained considering the *elastic anisotropy* of the host-lattice, in which the islands are embedded. Considering an island to be a point stress source, the authors determined the relative change in the strain energy density, $\rho(\vec{r})$ (a parameter equivalent to $\varepsilon(x)$), at the surface of a buried island. $\rho(\vec{r})$ is determined by two parameters namely, (a) the elastic anisotropy of the host lattice and (b) the crystallographic orientation of the surface. The elastic anisotropy is characterized by the anisotropy ratio

$$A = 2c_{44}^{c} / (c_{11}^{c} - c_{12}^{c}) \qquad (2.24),$$

where c_{44}^{c}, c_{11}^{c}, and c_{12}^{c} are the elements of the elastic-compliance-matrix. It is roughly equal to the ratio of the Young's modulus along the <111> and <001> directions. Fig. 2.16 (a) shows the variation of $\rho(\vec{r})$ with $\vec{r}$ (measured relative to the position of the buried island), along the [110] direction of a (001) surface. The numbers in the parentheses are the values of A of the corresponding semiconductor materials. Representative contour plots of $\rho(\vec{r})$ are shown in the insets of the figures. While for II-VI, III-V, and group-IV semiconductors (diamond or zinc blende crystal structure) $A > 1$, for rock-salt IV-VI semiconductors, $A < 1$. The hypothetical case $A = 1$ represents an isotropic host crystal. It is observed that for $A \leq 1$, $\rho(\vec{r})$ exhibits a minimum directly above the buried island. On the other hand, for $A > 1$, $\rho(\vec{r})$ is characterized by four minima along the <110> directions. The depth of the minima increases with increasing A. The inclination of the correlation-direction to the QD-superlattice normal, α, is determined by the position of the side minima of $\rho(\vec{r})$ (in turn, dependent on A), relative to that of the buried point island. Figure 2.16 (b) shows, for growth on (001) surfaces, the A-dependence of α. α increases linearly with increasing A. If *several* minima are formed on the surface, they naturally define a correlation of the intralayer island-positions. Together with the vertical correlation, this results in 3D self-ordering of QDs in QD-superlattices. For (001) growth and $A \gg 1$, the four side minima define a preferred square lateral arrangement and a body centered tetragonal 3D lattice, with ABAB vertical stacking sequence, as shown in the upper inset of Fig. 2.16 (b).

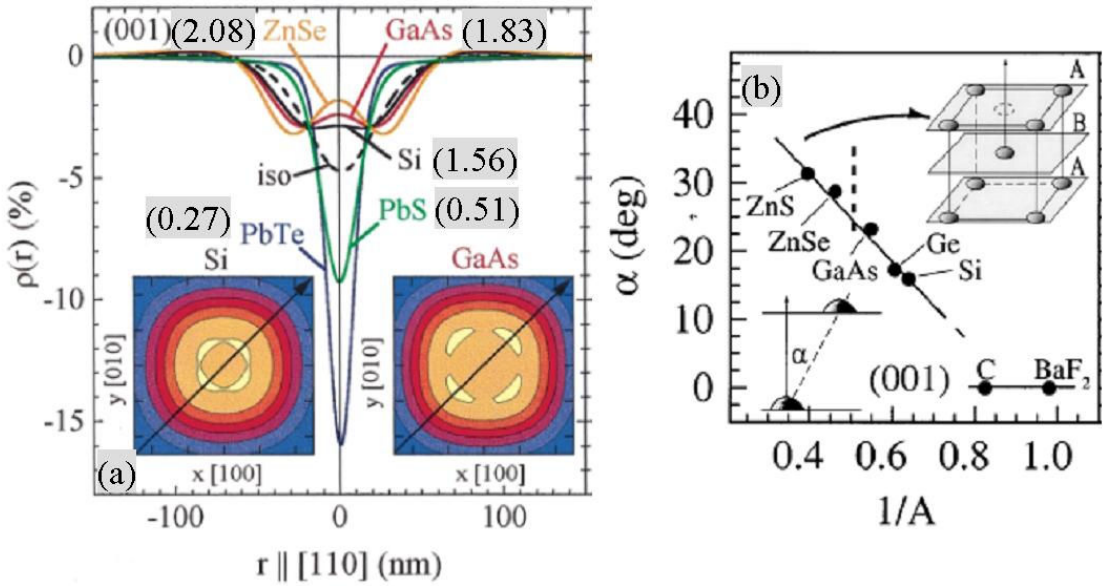

FIG. 2.16: Variation of $\rho(\vec{r})$ with $\vec{r}$ (a) along [110] direction on a (001) surface. The insets show complete contour maps of $\rho(\vec{r})$ versus $\vec{r}$, for a Si and GaAs (b) Dependence of α on 1/A for growth on (001) surface and $A >> 1$. The lower inset shows a schematic, which defines the angleα. The upper inset shows the 3D ordering of QDs. ((Adopted from [Holý99]).

The above model assumes the buried island to be a point stress source. However, real islands have a finite volume, and this fact results in significant modifications to the predictions of the model. The nature of interplanar correlation in case of real islands depends on the ratio of the island in-plane-diameter (d_{QD}) to the spacer layer thickness, L [Springholz00, Springholz01]. For $d_{QD}/L < 1$, the above model holds and oblique correlation is observed. However, for $d_{QD}/L > 1$, the interplanar correlation switches back to a vertical one.

2.7 *Self-assembly of CdSe/ZnSe QDs: Previous work and current understanding*

The success in fabricating and optimizing the morphological, compositional, and optical properties of QDs of several semiconductor combinations, belonging primarily to the III-V and group-IV families, encouraged attempts to realize similar QD-ensembles of the wide bandgap II-VI heterosystems, like CdSe/ZnSe(001) and CdTe/ZnTe(001). QDs of both heterosystems are characterized by luminescence in the blue-green region of the electromagnetic spectrum (see Fig. 1.2) . Therefore, initial attempts to fabricate II-VI QDs were aimed at realization of improved photonic devices, like low-threshold blue-green lasers and light emitting diodes. However, several characteristic features, i.e. large exciton binding energies, strong electron-hole exchange interaction, and strong oscillator strengths impart other interesting and useful properties to II-VI QDs. Recently, II-VI QDs have gained renewed interest in the context of developing visible single photon emitters. The first self-assembled epitaxial CdSe/ZnSe(001) QDs were grown by MBE, way back in 1996, by Flack et al [Flack96]. Since then, considerable progress has been made in fabricating and understanding the attributes of II-VI wide-gap QDs [Xin96, Zhu97, Hommel97, Merz98, Ivanov98, Passow00, Kim00, Kurtz00, Ohishi00, Maehashi00, Schikora00]. However, before delving into the details of the previous work carried out in this field, it is worth considering some material-properties of the CdSe/ZnSe heterosystem. ZnSe crystallizes in the Zinc-blende crystal structure (a_{ZnSe} = 5.6684Å), similar to the III-V semiconductors. When grown on ZnSe, CdSe also assumes the same structure (a_{CdSe} = 6.05Å), although the equilibrium structure of bulk CdSe crystals is Wurtzite-like (a_{CdSe} = 4.298Å, c_{CdSe} = 7.01Å). Thus, the lattice-misfit between ZnSe and CdSe is $m = 0.067$, i.e. very similar to that between InAs and GaAs. Apart from this similarity, the two systems differ significantly in their other attributes. Firstly, the II-VI bonds are more ionic than the III-V bonds. The Philips' ionicity of GaAs is 0.3, while that of II-VI compounds is between 0.6-0.7. Therefore, the II-VI compounds are more prone to plastic deformation by formation of dislocations. Secondly, both group-II and group-VI elements are characterized by high vapor pressures. The vapor pressure of Zn at 344 °C is $\sim 10^{-2}$ Torr while that of Ga at 619 °C is $\sim 10^{-8}$ Torr. Due to this limitation, MBE growth of II-VI compounds is performed at temperatures between 250-350 °C, which is 70-250 °C below the growth temperature of InAs on GaAs. At such low temperatures, surface diffusion of adatoms is suppressed and growth of smooth layers often becomes a formidable challenge. In the MBE of II-VI compounds and in determining the morphology of the resultant surfaces, growth kinetics therefore plays an important role.

In the first report of self-assembly of CdSe/ZnSe(001) QDs, Flack et al. demonstrated QD formation by MBE at a growth temperature of T_G = 425 °C [Flack96]. The authors claimed QD formation beyond a CdSe coverage of Θ = 3 ML. Subsequently however, Ivanov et al. reported QD-like 3D exciton confinement in CdSe layers of all coverages beyond Θ = 0.5 ML [Ivanov98]. Samples were grown in this case at T_G = 280 °C. Formation of 2D QDs was directly observed by transmission electron microscopy (TEM)[†], for Θ = 0.7 ML [Toropov99]. With increasing CdSe coverage, the morphology of these QDs did not change appreciably but their areal density increased rapidly. Ivanov et al. claimed that such QDs formed in CdSe/ZnSe(001) MBE due to composition inhomogeneity and thickness fluctuations of a ternary CdZnSe QW-like structure [Ivanov98]. This claim was later substantiated by cross sectional TEM and composition evaluation by lattice fringe analysis (CELFA) of the same samples [Peranio00, Litvinov00]. The details of the CELFA technique are beyond the scope of this thesis. However, for the purpose of this discussion it is enough to note that the technique provides cross sectional composition-maps based on the analysis of lattice fringes of high

---

[†] The details of the experimental techniques are presented in Chapter 3

resolution TEM images. Color-coded composition maps of the samples fabricated by Ivanov et al. are shown in Fig. 2.17, for different Θ. Based on these images, Peranio et al. demonstrated in [Peranio00] that the CdSe deposit formed a compositionally inhomogeneous CdZnSe layer, approximately 3 nm thick and consisting of flat Cd-rich inclusions. The effect of increasing Θ was to enhance the Cd-content and number of such inclusions, while the QW thickness remained practically constant.

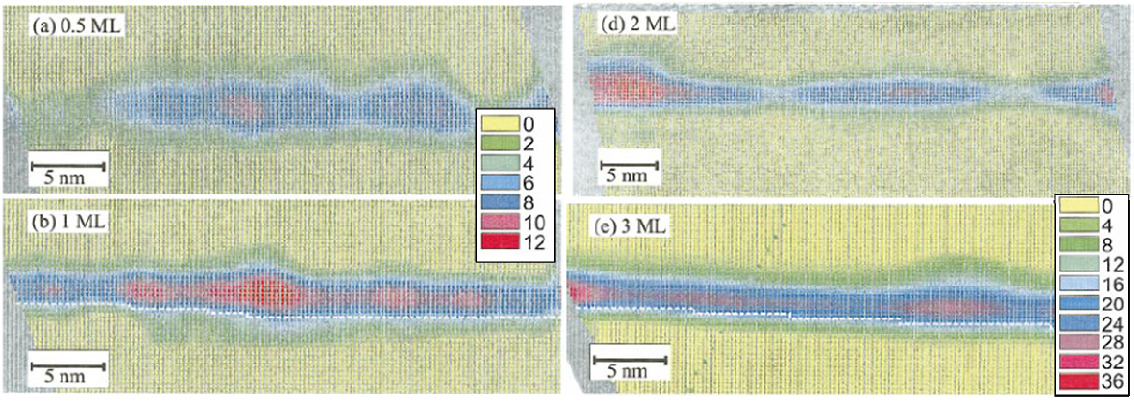

Fig. 2.17: CELFA-generated color-coded composition-maps corresponding to embedded CdSe/ZnSe(001) QD layers, of different CdSe coverages. The numbers in the color scale represent the % of Cd. Adopted from [Peranio00]

In the same report, it was also demonstrated that two different types of QDs co-existed in the QD-layers, i.e. small 2D QDs < 10 nm in diameter and those which extended laterally between 30 to 130 nm. Islands of both size groups were reported to be 2D in character. Such bimodal distribution of QD sizes was subsequently reported by Strassburg et al. [Strassburg00] and Kurtz et al. [Kurtz02]. The former authors claimed that the large islands had a 3D morphology and formed in the SK growth mode, in contrast to [Toropov99].

Merz et al. reported in 1998 the formation of a dilute ensemble of large CdSe/ZnSe(001) islands, based on atomic force microscopy (AFM) imaging [Merz98]. The islands were grown by MBE at $T_G = 375$ °C and were observed to be ~ 20 nm in height and 35 ± 5 nm in diameter. The areal density of the QDs was determined to be as low as $2x10^9$ cm^{-2}. Interestingly, the authors observed a rapid decrease in the areal density and increase in the height of islands on a time-scale of days. This was explained in terms of Ostwald ripening, wherein large islands grew in size at the expense of the smaller ones [Lee98]. Later however, it was disputed whether the observed features corresponded to CdSe QDs or certain SeO_2-related nanostructures, since similar features and a similar phenomenon of ripening were also observed on bare ZnSe surfaces [Smathers98, Zhang98]. Also, the QD-areal-density measured in these samples by micro-photoluminescence spectroscopy was found to be two-orders of magnitude higher than the areal density of islands measured in AFM [Jones03]. Thus, it might be inferred that the QDs of the capped samples did not correspond (only) to the islands of the uncapped samples, observed by Merz et al. Nonetheless, several authors thereafter have assigned similar features observed in AFM to CdSe QDs [Graham04, Perez-Paz05, Lai06].

By MBE and related techniques (e.g. atomic layer epitaxy (ALE), refer to section 3.1, Fig. 3.3), several other groups have grown CdSe/ZnSe QDs (Flack96, Hommel97, Arai00, Maehashi00, Preis01) at different growth temperatures, ranging from T_G = 250-425 °C. The morphological and optical characteristics of QDs obtained in these works are by and large similar. However, from the above discussion it is clear that the origin and attributes of the II-VI QDs appear to be significantly different from those of their III-V and group-IV counterparts. Several features accepted as typical indicators of QD-formation by SK growth are not very clearly established for the II-VI heterosystems. For example, a change from a streaky to a spotty pattern in reflection high energy electron diffraction (RHEED), the first-hand signature of island-formation, is inconspicuous for MBE growth of CdSe on ZnSe [Tinjod04]. Secondly, distinct islands, which might be correlated to the QDs of a capped sample, have not been observed by AFM. Cross-sectional TEM images of capped CdSe deposits reveal that QDs are defined by Cd-rich inclusions of a ternary CdZnSe QW, which form almost from the beginning of CdSe deposition [Peranio00]. Finally, in PL-spectroscopy, the red shift of the QD-emission with increasing CdSe coverage is monotonic [Maehashi00, Rabe98]. This is in contrast to what is known for InAs/GaAs(001) QDs, where the SK transition is manifested in a drastic red-shift of exciton ground state energies at the critical coverage (see section 3.5, Fig. 3.14).

Non-occurrence of distinct, 3D islands in CdSe/ZnSe heteroepitaxy has been attributed to several inhibiting factors. Alternative routes of strain relaxation, i.e. through cation interdiffusion [Kurtz01], low activation barrier to formation of dislocations [Tinjod03], high surface energy cost of forming 3D nanostructures [Tinjod03], and low surface diffusion of adatoms at typical growth temperatures [Schallenberg04], are some of them. Indication of strong intermixing is evident from the CELFA images of Fig. 2.17. The authors of [Peranio00] studied in detail Zn-Cd interdiffusion in CdSe/ZnSe(001) heteroepitaxy and also segregation of Cd during capping. Both effects were found to be particularly strong in the samples studied by them, i.e. CdSe/ZnSe(001) QD-layers grown by ALE at T_G = 280 °C. Based on the Muraki model (Eqn. 2.21), the Cd-segregation coefficient was deduced to be 0.6. A similar value was deduced by Passow et al., based on high resolution x-ray diffraction (HRXRD) studies [Passow2001]. The authors demonstrated that Cd not only segregated but also tended to desorb, when Zn was offered to the surface of a CdSe deposit, and growth was interrupted thereafter. Similar segregation-induced etching of Cd due to exposure of the CdSe surface to Zn flux has been reported very recently also by Kruse et al [Kruse07].

To enhance formation of CdSe/ZnSe QDs, and also in part, to explore the nature of the islanding process, several alternative approaches have been adopted over the last decade.

Passow et al. argued that formation of CdSe QDs took place during capping with ZnSe rather than during deposition of CdSe itself [Passow02]. QD-formation was assigned phenomenologically to segregation of Cd during capping and concomitant Zn-Cd interdiffusion, although no atomistic mechanism was discussed. The authors claimed enhanced segregation of Cd and concomitant QD-formation when the first few monolayers of the ZnSe cap layer were deposited by ALE instead of MBE. However, in TEM images the islands appeared to be Cd-rich inclusions in a QW-like structure, much similar to previous works.

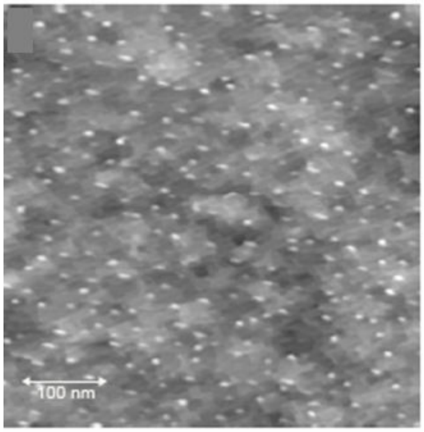

Fig. 2.18: AFM image (recorded in-situ) of CdSe islands formed by low temperature MBE growth of CdSe and subsequent in-situ annealing at a higher temperature. Adopted from [Kratzert01]

Kurtz et al. reported formation of SK CdSe/ZnSe(001) QDs by using CdS as the source of Cd [Kurtz02]. The advantage of using a CdS source was reported to be the high sublimation temperature of CdS (650 °C) in comparison to a standard elemental Cd source (250 °C). This was argued to result in enhanced adatom mobility, due to the larger kinetic energy of the CdS molecules, subliming at 650 °C. However, no distinct transition in RHEED or formation of 3D nanostructures was demonstrated. Keim et al.[Keim00], Toropov et al.[Toropov06], and Möck et al.[Möck01], used fractional-ML (FM) clusters of BeSe, CdTe, and MnSe, respectively, as nuclei to enhance formation of CdSe QDs. FM clusters of both BeSe and MnSe led to a red-shift of the PL emission of the QD-layers, signifying, possibly, suppression of Cd-Zn interdiffusion.

In 1998, Rabe et al. demonstrated the formation of distinct 3D QDs by a technique which combined MBE growth of CdSe at T_G = 230 °C and subsequent in-situ annealing at T_A = 310 °C [Rabe98]. Self-assembly of tiny, but distinct islands was clearly observed in AFM and substantiated by sharp single emission lines in micro-PL measurements. The density of QDs determined by both methods agreed very well. By CELFA, these islands, as well as the CdSe layers grown at T_G = 230 °C, were found to contain up to 100% Cd [Litvinov02]. Kratzert et al. extensively studied the morphology of these QDs by AFM [Kratzert00] and also determined optimal conditions for their self-assembly [Kratzert01]. Fig. 2.18 shows AFM images of such islands, recorded in UHV, before exposure of the island-layer to ambient atmosphere. Kurtz et al. also obtained similar results,

independently [Kurtz00]. Both Rabe et al. and Kurtz et al. observed a weak streaky-to spotty transition in RHEED during the annealing step [Rabe98, Kurtz00].
Another unique approach was developed by Tinjod et al. in 2003 [Tinjod03], initially for self-assembly of CdTe/ZnTe(001) QDs. The authors demonstrated the formation of large CdTe islands on ZnTe by a method of capping a 2D CdTe layer at room temperature with amorphous Te (*a*-Te), and subsequently decapping it at 220 °C. A bright and spotty RHEED pattern was observed after desorption of the *a*-Te layer and well-defined islands were observed in in-situ AFM.

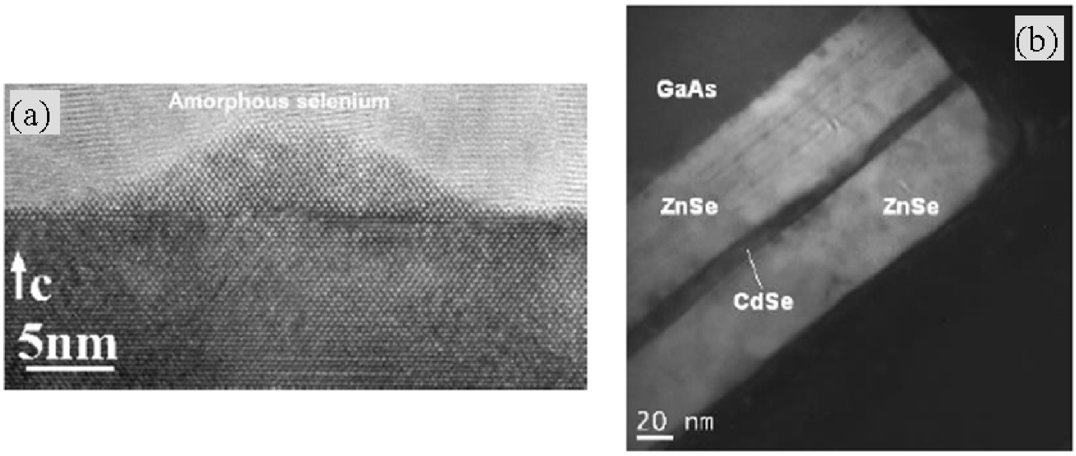

Fig. 2.19: (a) Cross sectional HRTEM image of a CdSe island, formed after deposition of amorphous-Se onto a 3-ML-thick CdSe layer and subsequent desorption. To protect the island from oxidation, amorphous-Se was re-deposited on the island layer before removing from MBE chamber. (b) Cross sectional HRTEM image of a similarly-grown CdSe island-layer, after capping with ZnSe (Note that the GaAs substrate is seen at the top left corner of the Figure). Fig. (a) adopted from [Robin2006] and Fig. (b), from [Bougerol2006]

Subsequently, the technique was applied to the CdSe/ZnSe heterosystem by the authors [Robin05] (and independently in the framework of this work [Mahapatra06]), wherein amorphous Se (*a*-Se) was deposited onto a 2D CdSe layer and subsequently re-desorbed to induce formation of CdSe/ZnSe(001) islands [Robin06]. However, after capping with ZnSe, these islands were also found to collapse into an inhomogeneous ternary ZnCdSe QW-like structure [Bougerol06, Robin07]. Fig. 2.19 (a) and 2.19 (b) show cross-sectional TEM images of a CdSe island before capping and the corresponding QD-layer after capping with ZnSe, respectively. While a well-defined island is seen in the former [Robin06], the later reveals a 2D layer-like structure [Bougerol07, Robin07]. Nonetheless, over the last couple of years, CdSe QDs grown by the last two alternative techniques have shown several interesting properties.

2.8 *Energy levels of confined excitons in QDs*

This section describes in brief the energy levels and spin properties of carriers confined in epitaxial QDs. Determination of the energy states of a real self-assembled QD is far from straightforward. Many attempts have been made to deduce the energy eigenvalues through sophisticated numerical models, which include realistic shapes of the QDs and the influence of strain [Pryor98, Stier99, Wang99]. The outcome of such models depends critically on the chosen parameters of the QDs. However, for the purpose of this thesis, as well as for a general qualitative understanding, adequate insight may be gained by adopting the effective mass approximation. For the periodic potential of a semiconductor crystal, Bloch's theorem gives plane-wave-like solutions for the wavefunction of an electron in the conduction-band, i.e.

$$\psi_e(\vec{r}) = e^{i\vec{k}.\vec{r}} u_{e,\vec{k}}(\vec{r}) \qquad (2.25),$$

where, $u_{e,\vec{k}}(\vec{r}) = u_{e,\vec{k}}(\vec{r}+\vec{R})$, $\vec{R}$ being an arbitrary lattice vector. In the effective mass approximation, the wave function of an electron close to the centre of the Brillouin zone (experiencing a slowly varying potential), is represented by

$$\psi_e(\vec{r}) = f(\vec{r}) u_{e,0}(\vec{r}) \qquad (2.26),$$

where $f(\vec{r})$ is the envelope function, which satisfies the Schrödinger equation

$$\mathrm{H}_e f_e(\vec{r}) = \left[-\frac{\hbar^2 \nabla^2}{2m_e^*} + V_e(\vec{r}_e) \right] f_e(\vec{r}) = E_e f_e(\vec{r}) \qquad (2.27),$$

where $\vec{r}_e$, $V_e(\vec{r}_e)$, m_e^*, and E_e denote the position, effective potential, effective mass, and eigenenergy of the electron, respectively, and $\hbar = h/2\pi$.

Self-assembled QDs in most cases are highly flattened in the growth direction (z-direction) and the corresponding confining potential $V_e(z)$ is often assumed to be infinite square well like. The QD-confining potential, within the plane of the QW (in x- and y-direction) is chosen to be simple harmonic-like [Biolatti02], i.e.

$$V_e(x,y) = \frac{1}{2} m_e^* \omega_0^2 (x^2 + y^2); \qquad |z| \le h_{QD} \qquad (2.28),$$

where h_{QD} defines the height of the QD. The energy eigenstates of an electron, confined within a QD with effective confining potential $V_e(\vec{r}) = V_e(z) + V_e(x,y)$, is then given by

$$E_e(n_x, n_y, n_z) = (n_x + n_y + 1)\hbar\omega_0 + \left(\frac{\pi^2 \hbar^2}{2m_e^* {h_{QD}}^2} \right) n_z^2 \qquad (2.29),$$

where n_x and n_y are integers ≥ 0 and n_z is an integer ≥ 1. Usually h_{QD} is assumed to be so small that only the $n_z = 1$ states are considered. In epitaxially self-assembled QDs, both electrons and holes might be confined. Each particle must then separately satisfy the Schrödinger equation, consisting of the respective confining potential $V_{e,h}(z) + V_{e,h}(x,y)$. The total Hamiltonian is given by

$$\mathrm{H}_{e-h} = \mathrm{H}_e + \mathrm{H}_h \qquad (2.30),$$

Fig. 2.20 shows schematically, an electron and a hole, occupying the respective ground states, within a QD. The Figure depicts the band diagram along the growth direction (*z*), for a typical QD formed in CdSe/ZnSe(001) heteroepitaxy. At the top of the Figure, a section through a particular Cd-rich inclusion of Fig. 2.17 is also shown (rotated by 90°).

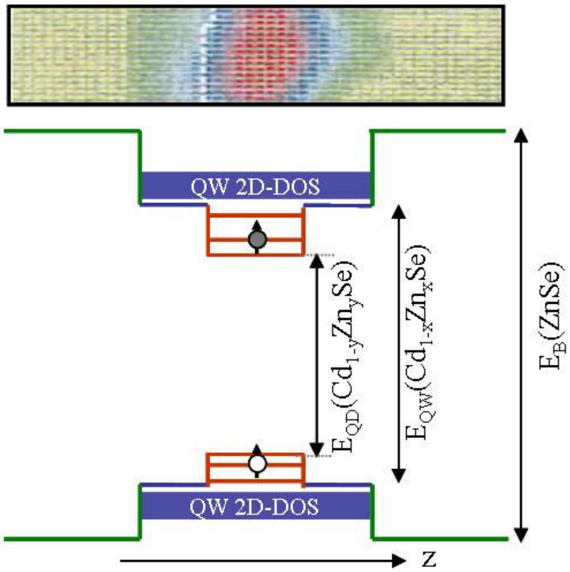

Fig. 2.20: Schematic energy band diagram, across a CdSe/ZnSe QD, typically formed in MBE growth. The QD is formed by a Cd-rich inclusion (shown in the top panel) within a CdZnSe QW.

As mentioned before, the CdSe deposit represents a ternary $Cd_{1-x}Zn_xSe$ QW-like structure with local Cd-rich inclusions ($Cd_{1-y}Zn_ySe$), such that y < x. The band gap of the ternary ZnCdSe alloy decreases almost linearly with increasing Cd-content (refer to Fig. 1.2). Thus, the difference in the bandgaps of $Cd_{1-x}Zn_xSe$ and $Cd_{1-y}Zn_ySe$ defines $V_{e,h}(z)$. QD-states are formed, in the regions of the inclusions, due to the additional in-plane potential, $V_{e,h}(x,y)$. Above the QD-states lies the 2D continuous density of states of the QW. It should be noted that the band-diagram of Fig. 2.20 is a simplified schematic which assumes sharp band discontinuities by neglecting a gradual variation of Cd-content across the ternary QW.

For electrons in the conduction band, the atomic orbital functions contained in $u_{e,0}(\vec{r})$ have *s*-like symmetry and thus, there is only one spin-degenerate conduction band in bulk semiconductor crystals. Consequently, the "ground-electron-states" of the QD are represented as $\left|m_j^e = 1/2\right\rangle = \left|m_l^e = 0, m_s^e = 1/2\right\rangle$ and $\left|m_j^e = -1/2\right\rangle = \left|m_l^e = 0, m_s^e = -1/2\right\rangle$, where, m_j^e, m_l^e, m_s^e are the *z*-projections of the total-, orbital-, and spin-angular-momentum, respectively. Due to *p*-like symmetry of the atomic orbital functions, for the valence band holes, the situation is more complicated. There are three bands, namely, heavy-hole-, light-hole-, and the split-off-band, which can "mix". At the centre of the Brillouin zone (Γ point, *k* = 0) in bulk semiconductors, the light- and the heavy-hole bands are degenerate. This degeneracy is lifted in QDs, due to the confinement potential and strain. For compressively strained QDs (the case of all heterosystems), the highest valence band states, or the hole-ground-states, are assumed to be heavy-hole-like, when the quantization axis is taken to be *z* (the axis of symmetry). These states are in turn two-fold degenerate, and represented as $\left|m_j^h = 3/2\right\rangle = \left|m_l^h = 1, m_s^h = 1/2\right\rangle$ and $\left|m_j^h = -3/2\right\rangle = \left|m_l^h = -1, m_s^h = -1/2\right\rangle$. The first light-hole states are similarly represented by $\left|m_j^h = 1/2\right\rangle = \left|m_l^h = 0, m_s^h = 1/2\right\rangle$ and $\left|m_j^h = -1/2\right\rangle = \left|m_l^h = 0, m_s^h = -1/2\right\rangle$.

When confined within a QD, the electron and the heavy-hole inevitably bind together via the Coulomb interaction and form an exciton. The Hamiltonian of a confined exciton therefore reads

$$\mathrm{H}_{exciton} = \mathrm{H}_e + \mathrm{H}_h + \mathrm{H}_{Coulomb} \tag{2.31}$$

$\mathrm{H}_{Coulomb}$, in turn, has two components, the "direct" and the "exchange" parts. The direct part of the Coulomb interaction is given by [Takagahara00]

$$\mathrm{H}_{Coulomb}^{Direct} = \delta_{m_j^e, m_j^{e'}} \delta_{m_j^h, m_j^{h'}} \int d^3 r_e \int d^3 r_h \left|\psi_e(\vec{r}_e)\right|^2 \frac{-e^2}{\varepsilon_0 \varepsilon_r \left|\vec{r}_e - \vec{r}_h\right|} \left|\psi_h(\vec{r}_h)\right|^2 \tag{2.32}$$

where, ε_0 and ε_r are the permittivity of vacuum and the relative permittivity of the QD-forming semiconductor, respectively. This term gives rise to the exciton "binding energy". An exciton might be formed even in macroscopic semiconductor crystals due to Coulomb binding of an electron and a hole. Such an exciton occupies Hydrogen-like quantized states, characterized by a (excitonic) Bohr radius a_{ex}, given by

$$a_{ex} = \frac{\hbar^2 \varepsilon_0 \varepsilon_r}{m_r^* e^2} = 0.529 \frac{\varepsilon_r}{m_r^* / m_0} \text{ Å} \tag{2.33}$$

where $m_r^* = m_e^* m_h^* / (m_e^* + m_h^*)$ and m_0, the free electron mass. When the size of the QD is smaller than a_{ex}, the quantized states are determined by H_e and H_h, with $\mathrm{H}_{Coulomb}$ acting as a small correction to the energy eigenvalues. This is known as the strong confinement regime. In the opposite case, the Coulomb interaction determines the quantization energy. This is known as the weak confinement regime. In CdSe, a_{ex} is ~ 5.3 nm [Nirmal94].

The *z*-projection of the total angular momentum of an exciton is given by $\left|m_j^X = m_j^e + m_j^h\right\rangle$. Therefore the exciton states are represented by the basis set $\left|m_j^X = 1\right\rangle, \left|m_j^X = -1\right\rangle, \left|m_j^X = 2\right\rangle, \left|m_j^X = -2\right\rangle$. In optical spectroscopy, the exciton states $\left|m_j^X = \pm 1\right\rangle$ couple to the light field, while those with $\left|m_j^X = \pm 2\right\rangle$ do not. Thus, the former are known as bright-, while the later as dark-exciton states.

The exchange part of the Coulomb interaction, which stems from the antisymmetry of fermionic wave functions under exchange of particle label, is given by [Takagahara00]

$$\mathrm{H}_{Coulomb}^{Exchange}=\delta_{m_j^e,m_j^{h'}}\delta_{m_j^{e'},m_j^h}\int d^3r_e\int d^3r_h\psi_e^*(\vec{r}_e)\psi_h(\vec{r}_e)\frac{-e^2}{\varepsilon\left|\vec{r}_e-\vec{r}_h\right|}\psi_h^*(\vec{r}_h)\psi_e(\vec{r}_h) \quad (2.34).$$

Substituting $\psi_e(\vec{r}_e)$ from Eqn. 2.26, and an equivalent expression for $\psi_h(\vec{r}_h)$, in Eqn. 2.34, the exchange term reads,

$$\mathrm{H}_{Coulomb}^{Exchange}=\delta_{m_j^e,m_j^{h'}/3}\delta_{m_j^{e'},m_j^h/3}\int d^3r_e\int d^3r_h f_e^*(\vec{r}_e)f_h(\vec{r}_e)f_e(\vec{r}_h)f_h^*(\vec{r}_h)$$
$$\frac{1}{\Xi^2}\int_\Xi d^3r_e^{'}\int_\Xi d^3r_h^{'}\frac{u_e^*(\vec{r}_e+\vec{r}_e^{\,'})u_h(\vec{r}_e+\vec{r}_e^{\,'})e^2u_e(\vec{r}_h+\vec{r}_h^{\,'})u_h^*(\vec{r}_h+\vec{r}_h^{\,'})}{\varepsilon_0\varepsilon_r\left|\vec{r}_e+\vec{r}_e^{\,'}-\vec{r}_h-\vec{r}_h^{\,'}\right|} \quad (2.35).$$

The integral in the second line can be decomposed into two parts, i.e. a short range exchange interaction ($\vec{r}_e=\vec{r}_h$) and a long range exchange interaction ($\vec{r}_e\neq\vec{r}_h$). In the basis set of exciton states $\{|+1\rangle,|-1\rangle,|2\rangle,|-2\rangle,\}$[‡], $\mathrm{H}_{Coulomb}^{Exchange}$ can be expressed in the matrix form as [Bayer00, Bayer02]

$$\mathrm{H}_{Coulomb}^{Exchange}=\frac{1}{2}\begin{pmatrix}+\Delta_0 & +\Delta_1 & 0 & 0\\ +\Delta_1 & +\Delta_0 & 0 & 0\\ 0 & 0 & -\Delta_0 & +\Delta_2\\ 0 & 0 & +\Delta_2 & -\Delta_0\end{pmatrix} \quad (2.36).$$

The non-zero terms in the matrix lifts the degeneracy of the four basis states, depending on the symmetry of the QD. For a QD with rotational symmetry about the *z*-axis (symmetry group *D2d*), $\Delta_0=\Delta_2\neq 0$ and $\Delta_1=0$. Δ_0 lifts the degeneracy between the $|\pm 1\rangle$ and $|\pm 2\rangle$ states, i.e. the bright and the dark states, while, Δ_2 mixes the two dark states. For a QD which is not symmetric about the *z*-axis, all three terms are non zero. Therefore, in addition to the two effects mentioned above, the bright states are also mixed. The scenario is presented in a tabular form in Table 2.1 [Flissikowski04].

Finally, in presence of a magnetic field *B*, two new terms due to the Zeeman interaction and the diamagnetic effect should be included in the Hamiltonian, which then reads

$$\mathrm{H}_{exciton}=\mathrm{H}_e+\mathrm{H}_h+\mathrm{H}_{Coulomb}^{Direct}+\mathrm{H}_{Coulomb}^{Exchange}+\mathrm{H}_{Zeeman}+\mathrm{H}_{Diamag} \quad (2.37).$$

However, the details of these two terms are beyond the scope of this thesis and are not discussed here.

[‡] For convenience, "$m_j^X=$" has been removed.

D_{2d}		$< D_{2d}$	
Eigenenergy	Eigenfunction	Eigenenergy	Eigenfunction
$+\frac{1}{2}\Delta_0$	$\lvert +1\rangle$	$+\frac{1}{2}\Delta_0+\frac{1}{2}\Delta_1$	$\frac{1}{\sqrt{2}}\left(\lvert +1\rangle+\lvert -1\rangle\right)$
$+\frac{1}{2}\Delta_0$	$\lvert -1\rangle$	$+\frac{1}{2}\Delta_0-\frac{1}{2}\Delta_1$	$\frac{1}{\sqrt{2}}\left(\lvert +1\rangle-\lvert -1\rangle\right)$
$-\frac{1}{2}\Delta_0+\frac{1}{2}\Delta_2$	$\frac{1}{\sqrt{2}}\left(\lvert +2\rangle+\lvert -2\rangle\right)$	$-\frac{1}{2}\Delta_0+\frac{1}{2}\Delta_2$	$\frac{1}{\sqrt{2}}\left(\lvert +2\rangle+\lvert -2\rangle\right)$
$-\frac{1}{2}\Delta_0-\frac{1}{2}\Delta_2$	$\frac{1}{\sqrt{2}}\left(\lvert +2\rangle-\lvert -2\rangle\right)$	$-\frac{1}{2}\Delta_0-\frac{1}{2}\Delta_2$	$\frac{1}{\sqrt{2}}\left(\lvert +2\rangle-\lvert -2\rangle\right)$

Table 2.1: Eigenfunctions and eigenenergies of the exchange-Coulomb Hamiltonian for a symmetric (D_{2d}) and an asymmetric ($< D_{2d}$) QD.

In the discussion so far, only single-exciton states have been considered. However, several other charged and multi-excitonic complexes might be confined within QDs. Two of them, studied extensively in the past, are the “trions” and the “biexcitons”. The complexes are shown schematically in Fig. 2.21, along with an exciton.

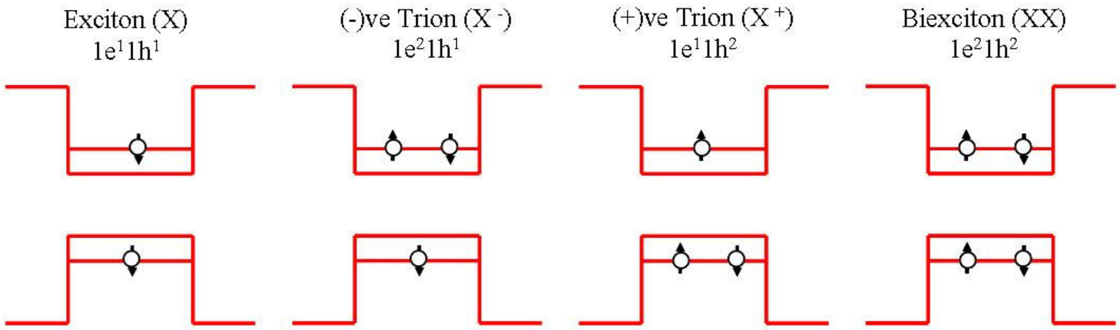

Fig. 2.21: Schematic representation of an exciton (X), a negative trion (X^-), a positive trion (X^+), and a biexciton (XX)

A trion is a charged complex composed of either two electrons and a hole or two holes and an electron. The former is known as a negative trion and is labeled as X^-, while the latter is known as a positive trion and labeled as X^+. A trion may be considered as an exciton bound through Coulomb interaction to an additional electron (X^-) or an additional hole (X^+). The (trion) binding energies can be determined in PL-spectroscopy (see section 3.5). Patton et al. have reported trion binding energies for epitaxially self-assembled CdSe/ZnSe(001) QDs in the order of 15-22 meV [Patton03].

A biexciton is a complex formed due to Coulomb binding of two excitons. Since it involves two electrons and two holes, the biexciton is a neutral complex. It is labeled as XX. Due to the Coulomb interaction, the ground state energy of a biexciton is smaller than twice the ground-state-energy of an exciton. The difference is denoted as the biexciton binding energy (BBE). In self-assembled epitaxial CdSe/ZnSe(001) QDs, BBE values ranging between 19-26 meV [Patton03, Lowisch99] have been measured. In QDs, other multi-excitonic species, such as negatively-charged biexciton ($1e^2 1h^2 2e^1$ (XX^-)) etc. have also been detected.

Summary

In summary, this chapter addressed primarily to the different mechanisms by which self assembled nanostructures might be obtained in epitaxial growth, or more specifically in molecular beam epitaxy. Examples were taken from different well-studied homo- and heteroepitaxial systems to elucidate several instabilities in MBE growth and to present a few of the self-assembled morphologies which result thereof. The field of QD-self assembly in the wide-bandgap CdSe/ZnSe heterosystem was also reviewed. Finally, the energy states of self-assembled epitaxial QDs and the properties of confined excitons and multi(charge)-excitonic complexes were presented in brief.

Tools and techniques for sample preparation and characterization

3

This chapter presents the MBE system used for growth and the different tools used for characterization of the samples. The fundamental principles underlying a few of the characterization techniques are explained in considerable detail.

3.1 *The MBE apparatus*

In MBE, epitaxial growth of materials occurs due to chemical interaction of one or more molecular (or atomic) beams of different compositions and fluxes, at the surface of a single-crystalline substrate maintained at a definite temperature. The schematic diagram of a typical MBE apparatus is shown in Fig. 3.1. The atomic/molecular beams are generated by sublimation of ultra-pure, solid sources in ultra-high vacuum (UHV) (~ 10^{-11} Torr). To reach the required UHV conditions, the MBE chamber is provided with UHV pumps, i.e. cryo-, titanium-sublimation-, and ion-getter pumps. The pumping efficiency is further enhanced by creating liquid-Nitrogen (LN_2) cryogenic traps around the inner wall of the chamber (bottom part). The solid sources are heated within resistively heated Knudsen effusion cells. The cells are surrounded by a LN_2 cooled shroud to avoid radiation cross-heating of neighboring cells. Each cell is provided with a shutter, the position of which prevents or allows impingement of a particular beam to the substrate surface. Individual cells are heated to the required sublimation temperature by DC power supplies, controlled by PID feedback loops.

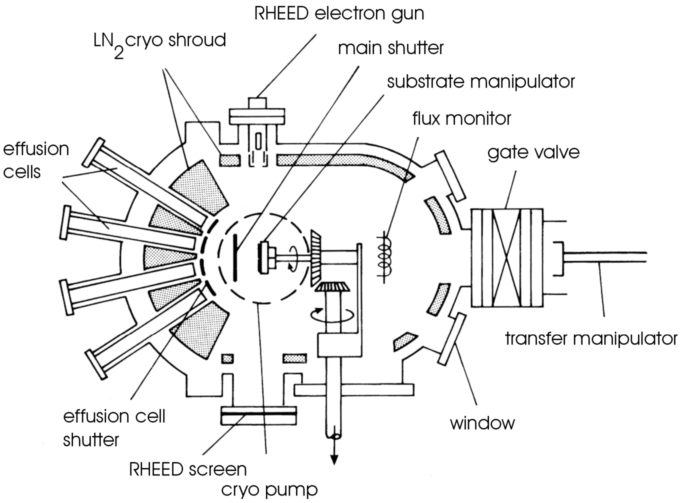

FIG. 3.1: Plan view of a MBE chamber (RIBER 32 design).

The substrate, glued or clamped to a molybdenum block, is transferred to the chamber by the transfer manipulator and mounted on a heater, held by the substrate manipulator. The substrate manipulator is capable of rotating the substrate into or out of the beam fluxes (see the direction of rotation indicated for the substrate manipulator). The beam fluxes are measured by the flux monitor, attached to the substrate manipulator on the side opposite to the substrate heater. The temperatures of both the substrate and the effusion cells are measured by suitably placed thermocouples. The chamber is provided with several ports, used either as windows to monitor different processes or to mount instruments for *real-time* measurements, like RHEED.

The MBE cluster of EP3, Universität Würzburg, is shown in Fig. 3.2. Six MBE chambers (denoted by CMT, CT, GaAs, ZnSe, MnGaAs, and NiMnSb) are interconnected through an ultra-high-vacuum (UHV) transfer module (base pressure: 1-2x10^{-10} Torr).[†] For the purpose of this work, III-V layers (mostly GaAs) were grown in the RIBER 2300 (RIBER 32 design), horizontal MBE chamber labeled as “GaAs”. The GaAs chamber is equipped with sources of elemental Ga, Al, Sb, In, Be (for p-doping), Si (for n-doping), and As. For As, a special valved cracking effusion cell (VEECO EPI 500 V-S) is used. All II-VI layers, except those described in Chapter 7, were grown in the chamber denoted by “ZnSe”. The ZnSe chamber is equipped with effusion cells of Zn, Cd, Mg, Te, Se, ZnS, Mn and Al. For the samples of Chapter 7, the II-VI layers were grown in the other II-VI chamber labeled as “CT”. This chamber is equipped with a valved cracker cell for Se. The heating and cooling of the effusion cells, as well as the movement of the shutters, can be regulated manually or in remote mode, via a computer.

All samples investigated in this thesis were grown on epi-ready GaAs:Si(001) substrates (Wafer Technology Ltd., UK), with miscut-angles, $\alpha = \pm 0.1°$ (direction not specified).

[†] Currently, the MBE cluster is being modified.

Typically, a quarter of a two-inch wafer was used for most samples. The substrate-piece was glued with molten Indium on a Molybdenum block and inserted into the load-lock of the UHV system (denoted by Schleuse on the right hand side of Fig. 3.2). After pumping down the load-lock to a pressure below 1x10^{-7} Torr, the sample was transferred to a heater, where it was degassed for 20 minutes at 300 °C. The degassed substrate was subsequently transferred to the GaAs MBE chamber for initiation of epitaxial growth.

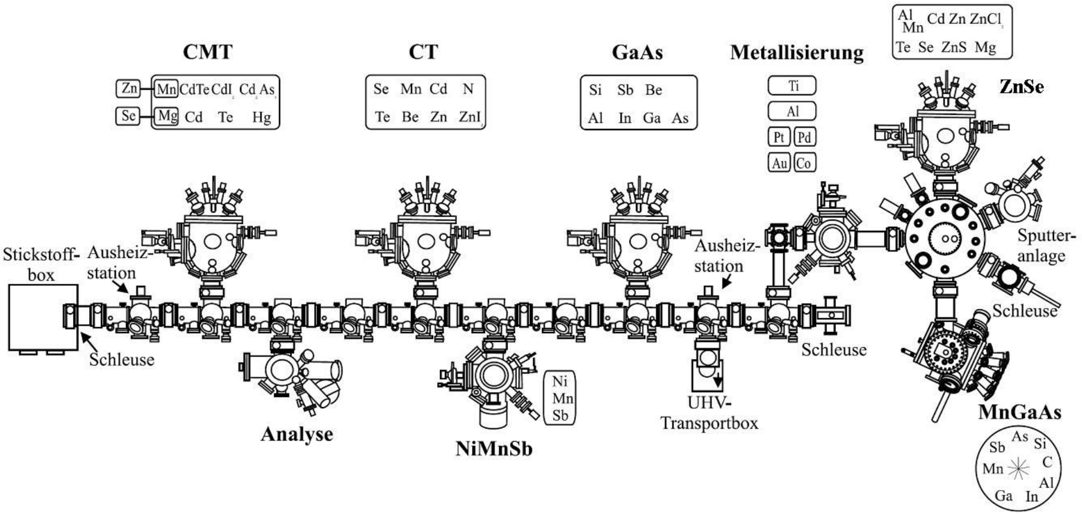

FIG. 3.2: Plan view of the MBE cluster of EP3 at the University of Würzburg.

Epitaxial growth might be performed either by conventional MBE or by some simple variants such as atomic layer epitaxy (ALE) and migration enhanced epitaxy (MEE). The three approaches essentially differ in the mode in which different fluxes are offered to the growing epi-surface.

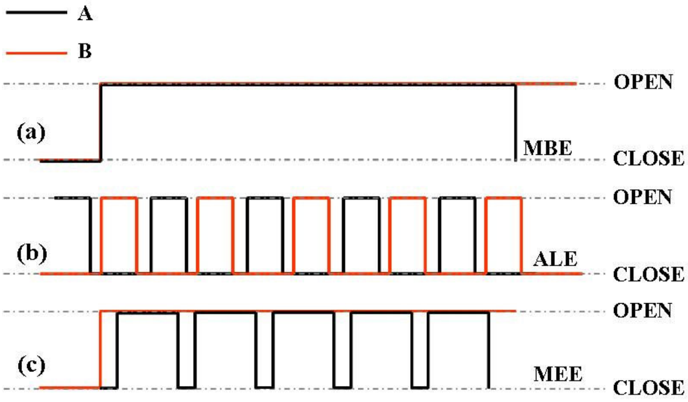

FIG. 3.3: Delivery (shutter movement) sequence during (a) MBE, (b) ALE, and (c) MEE growth

In conventional MBE of a binary compound AB, A and B are co-deposited. Both shutters are kept open during the entire interval of growth, as shown in Fig. 3.3 (a). In ALE, A and B fluxes are offered sequentially to the growth front, with intervals of "interrupted-growth" in between (Fig. 3.3(b)). Ideally, each cycle of ALE leads to the growth of a single ML of AB (An A-atomic-layer plus a B-atomic-layer). When deposited sequentially, A-adatoms equivalent to only a single atomic layer are strongly chemisorbed to the underlying B-atomic-layer, and vice versa. Excess A-adatoms are only weakly physisorbed to the freshly-deposited A-layer and desorb back to the vapor phase, during the subsequent interval of growth interruption. Thus, when the substrate temperature and the durations of delivery of the different fluxes are appropriately chosen, ALE results in growth of a single ML per cycle.

In MEE, one of the species is delivered continuously while the other in short pulses (Fig. 3.3(c)). Here, the rationale is to provide enough time for the migration of the pulsed species to energetically favorable sites before incorporation to the growing crystal. Thus MEE enables growth of layers smoother than those grown by conventional MBE.

Details specific to the epitaxial growth of different layers of the samples are presented in the corresponding chapters.

3.2 *Reflection high energy electron diffraction (RHEED)*

RHEED is a tool to probe the structure and chemistry of an epi-surface, *during epitaxial growth* (real-time). Further, it provides information on the nature of epitaxy and allows determination of the growth rate. As the name suggests, RHEED is a diffraction technique, wherein a beam of high energy electrons are diffracted by the *surface lattice* of an epilayer. The necessary elements, i.e. an electron gun to generate a beam of electrons (with accessories for focusing) and a fluorescent screen to record the diffraction pattern, are integrated to the MBE chamber in suitable ports (see Fig. 3.1). Typically, a beam of electrons, with energy ~ 20 keV, is directed to the epi-surface at a glancing angle (1°-3°). Due to the glancing incidence of the primary electron beam, RHEED is sensitive only to a few atomic layers at the surface.

The diffraction condition, according to the kinematical scattering theory, is given by

$$\vec{k}_i - \vec{k}_e = \vec{G} \qquad (3.1),$$

where $\vec{k}_i$ and $\vec{k}_e$ are the wave-vectors of the incident and the diffracted electron beams and $\vec{G}$, a reciprocal lattice vector of the diffracting crystal. For elastic scattering, $|\vec{k}_i| = |\vec{k}_e|$ and the diffraction condition can be cast into the geometrical construction of the Ewald sphere in reciprocal space. For a beam energy of 20 keV, $|\vec{k}_i| = 785\,\mathrm{nm}^{-1}$. This value is about 70 times larger than the reciprocal lattice unit of most semiconductor materials. Consequently, the Ewald sphere in RHEED produces a planar cut through several points of the reciprocal lattice. All these points satisfy Eqn. 3.1 and produce a diffraction pattern on the fluorescent screen. The situation is depicted schematically in Fig. 3.4 (a) (Top view). Due to the small penetration depth of the electron beam, RHEED is insensitive to the periodicity of the epilayer in the direction normal to the surface (*z*-direction)

Consequently, the reciprocal lattice points (RLP) of the plan view translate to 1D rods in side-view (Fig. 3.4 (b)). The Ewald sphere cuts through every rod and the resultant pattern consists of equi-spaced streaks, as shown for a Se-terminated ZnSe surface in Fig. 3.4 (c). The streaks exhibit a finite thickness due to lattice imperfections and thermal vibrations, and also due to the fact that the Ewald-sphere-periphery is broadened by electron energy spread and beam divergence. The streaks, or equivalently the reciprocal rods, are labeled with the surface Miller indices (hk), where h and k are integers. However, additional streaks, between the labeled ones, are seen in the image. The origin of these streaks is in surface reconstruction (see BOX 3.1).

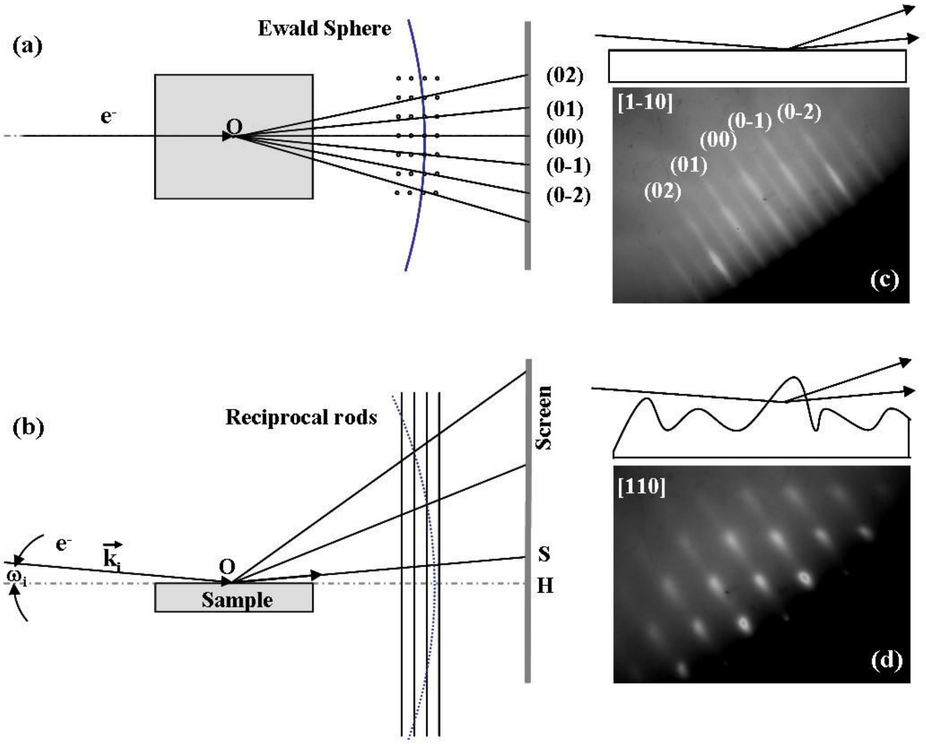

FIG. 3.4: Schematic illustration of the RHEED geometry in (a) top and (b) side-view, along with a section of the surface reciprocal space. (c) Streaky RHEED image, recorded along the [110] direction, from a Se-terminated CdSe surface. The streaky pattern is a signature of a smooth layer which results in quasi-true-reflection diffraction (d) Spotty RHEED image from a surface consisting of three-dimensional CdSe islands. The islands act like surface asperities and result in transmission-reflection diffraction (see text). (a) and (b) adopted from [Hernández-Calderon83]

The diffraction process in RHEED is not a true reflection, as has been implicitly assumed in the previous discussion. Most epitaxial surfaces are rough to certain extent and the diffraction pattern is produced in transmission through the surface asperities. This transmission-reflection condition results in formation of spotty features superposed on the streaks. In the extreme case, where the surface consists of a high density of 3D nanostructures, the streaks disappear completely and a spotty pattern emerges, as shown in Fig. 3.4 (d). The transition from a streaky to a spotty RHEED pattern serves as a signature of island formation during lattice mismatched heteroepitaxy and allows determination of the critical thickness, t_c.

BOX 3.1 Surface reconstruction

The energy of a crystal surface depends on the density of unsaturated “dangling” bonds of the surface atoms. Thus, surface energy is reduced when surface atoms bind together and reduce the density of such dangling bonds. Bonding of surface atoms results in what is known as *reconstruction* of the surface. An example is shown in Fig. 3.5.

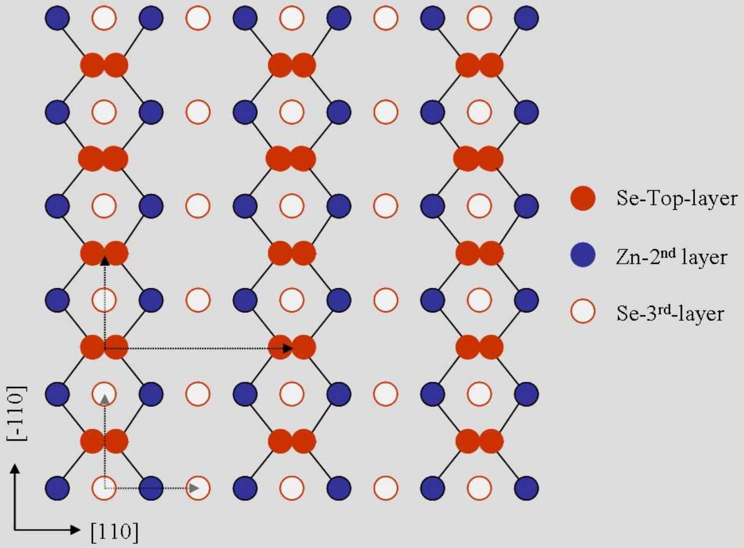

Fig. 3.5: Schematic top view of Se-terminated ZnSe surface. The surface-Se atoms dimerize along the [110] direction, leading to doubling of the lattice-constant. Consequently, additional streaks are observed in RHEED along the [110] azimuth.

On the Se-terminated ZnSe (100) surface, Se atoms dimerize along the [110] direction. The resultant reconstructed surface lattice is characterized by a lattice parameter, along the [110] direction, twice as large as that of the unreconstructed surface, causing additional rods to appear in the reciprocal space. Along the perpendicular [-110] direction, the lattice parameter remains unchanged and the corresponding reconstruction is labeled (2x1). More complicated reconstructions are known for other (hetero)epitaxial surfaces, which occur due to periodically missing dimer rows.

RHEED also provides information on the nature of epitaxial growth. When epitaxy proceeds in the layer-by-layer mode, by nucleation, growth, and coalescence of 2D clusters, the intensity of the specular reflection (the point S in Fig. 3.4 (a)), exhibits an oscillatory behaviour, with the period of oscillation corresponding to the growth of a single ML. The evolution of the specular spot intensity (SSI) for growth of 1.5 ML of an arbitrary epilayer, in the layer-by-layer mode, is illustrated in Fig. 3.6 [Joyce86]. At the beginning and end of the deposition of a particular monolayer, i.e. for coverages $\Theta = 0$, 1 ML … etc., the SSI is at its maximum. For intermediate Θ, the reflectivity falls, and passes through a minimum for $\Theta = 0.5$ ML, 1.5 ML…etc. In real growth scenario, ideal layer-by-layer growth never takes place and the growth-front always consists of some 2D clusters. This results in damping of the oscillations. If multilayer growth takes place, i.e. by formation of multiple incomplete atomic layers (see section 2.3, Fig. 2.9), the surface consists of a high density of asperities. In this case, the oscillations are completely damped and the SSI profile exhibits an exponential decay. Typically, this occurs for low growth temperatures, where surface diffusion is strongly suppressed, or in presence of strong ES barriers.

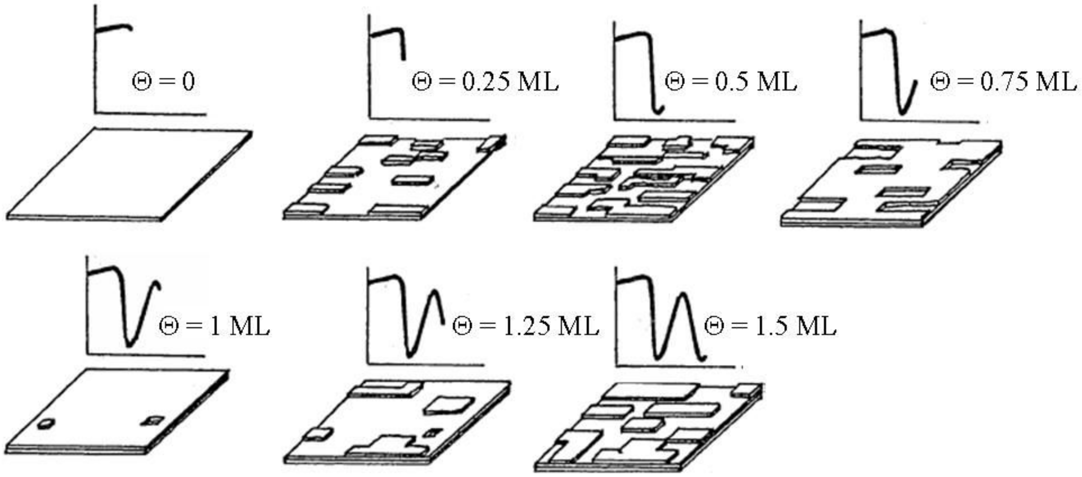

Fig.3.6: Evolution of the surface during layer-by-layer epitaxy (horizontal panels) and the corresponding changes in the RHEED SSI profile (vertical panels). Adopted from [Joyce86]

Interestingly, SSI oscillations die out also for very high growth temperatures. This occurs when the adatom diffusion lengths become comparable to or larger than the separation of the surface steps (see Box 2.2, Fig. 2.4). Growth in this case does not occur by nucleation and coalescence of 2D islands but by incorporation of adatoms at the surface steps. This growth mode, known as *step flow* growth, has proven to be beneficial for fabrication of ultra-smooth surfaces and interfaces.

3.3 *X-ray techniques*

(a) High resolution x-ray diffraction (HRXRD)

Like RHEED, HRXRD is also a diffraction technique and therefore, the fundamental working principle is governed by Eqn. 3.1. However, instead of generating a diffraction pattern, HRXRD records the diffraction intensity at a particular RLP. The information obtained from HRXRD concerns the composition and uniformity of epitaxial layers, their thicknesses, the built-in strain and strain relaxation, and the crystalline quality related to their dislocation density and mosaic spread. Furthermore, interfacial phenomena, like interdiffusion and segregation, can also be probed in certain circumstances.

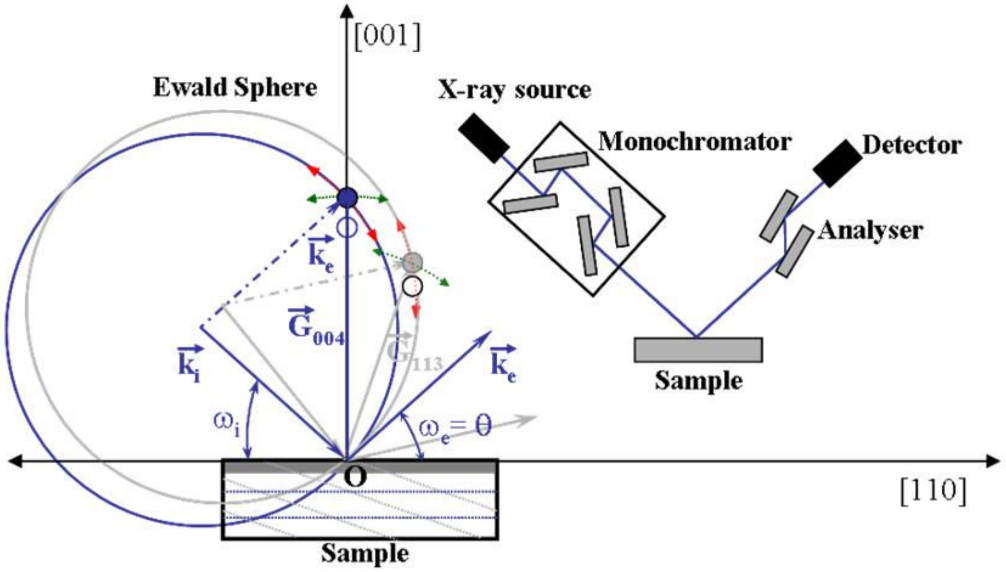

FIG. 3.7: Schematic illustration of the geometry of HRXRD in reciprocal space (main Fig.) and real space (inset) The configuration of the incident and diffracted beams, along with the respective Ewald "circles", is shown (in blue) for the symmetric 004-RLP and (in grey) for the asymmetric 113-RLP.

The diffraction geometry of a conventional diffractometer is shown in Fig. 3.7. The shown sample is assumed to be a fully strained (pseudomorphic), 100 nm thick, ZnSe epilayer on the (001) surface of GaAs. Short wavelength x-rays (typically Cu $K_{\alpha 1}$ with wavelength $\lambda_X = 1.54$ Å) are diffracted by the lattice planes of the sample crystal. Albeit the figure depicts diffraction from two sets of lattice planes, namely those with Miller indices (004) (shown in blue) and (113) (shown in grey), the following discussion is restricted to the former case only. For the (004) planes, the reciprocal lattice vector, $\vec{G}_{004}$, points outwards parallel to the surface normal and the corresponding RLP lies on the [001] axis. This geometry is known to be symmetric.[‡] In Fig. 3.7, the RLPs are denoted by filled and open circles, for the GaAs substrate and the ZnSe epilayer, respectively. Being compressively strained, the ZnSe epilayer is tetragonally distorted. Its lateral lattice constant, $a_{ZnSe}^{\parallel}$, is similar to the bulk lattice constant of GaAs, a_{GaAs}. Therefore the lateral coordinates of the ZnSe and GaAs RLPs coincide. On the other hand, the vertical lattice constant of the strained ZnSe epilayer is given by

$$a_{ZnSe}^{\perp} = a_{GaAs}\left[1 + \frac{1+\nu}{1-\nu} m_{ZnSe-GaAs}\right] \tag{3.2}$$

where, $m_{ZnSe\text{-}GaAs}$ is the lattice-misfit between GaAs and ZnSe (0.0027) and ν the Poisson ratio of ZnSe (0.376). Since $a_{ZnSe}^{\perp} > a_{GaAs}$, the vertical coordinates of the ZnSe RLPs are

---

[‡] When the chosen RLP does not lie on the [001] axis, as in the case of the 113-RLP, the geometry is known to be asymmetric.

smaller that those of GaAs. When the angle of incidence, ω_i, of the primary beam ($\vec{k}_i$) and the exit angle, ω_e, of the diffracted beam ($\vec{k}_e$) are so adjusted that Eqn. 3.1 is satisfied for a particular reciprocal vector $\vec{G}_{hkl}$, the diffraction intensity exhibits a peak. Another angle of importance is the so-called angle of diffraction, θ. By definition, θ is the angle subtended by the diffracted beam on the corresponding lattice planes, and is related to ω_i and ω_e as

$$\omega_i + \omega_e = 2\theta \tag{3.3}$$

For the symmetric geometry, $\omega_i = \omega_e = \theta$. θ appears in the well-known Bragg's law of diffraction, which is essentially Eqn. 3.1 cast in terms of real-space parameters and is given by

$$\lambda_X = \frac{2a\sin\theta}{\sqrt{h^2+k^2+l^2}} \tag{3.4}$$

where, λ_X is the x-ray wavelength and (*hkl*) represent the Miller indices of the diffracting planes, or in other words, the co-ordinates of the RLP, and a the lattice parameter of the crystal under investigation. To record a (004) diffraction pattern, the diffraction geometry is first adjusted around the (004) RLP of the GaAs substrate (using Eqn. 3.3 and with a_{GaAs} known *a priori*) and then angular scans are performed to trace the diffraction peaks. Angular scans across a RLP can be performed in three different directions as follows: (a) tangential to the reciprocal lattice vector (along the green dotted arc), by changing ω_i in small steps, while keeping ω_e fixed, (b) along the circumference of the Ewald "circle" (along the red dotted arc), by keeping ω_i fixed and changing ω_e stepwise, and (c) along the reciprocal lattice vector, by changing both ω_i and ω_e in steps of equal size. The three scans are traditionally known as ω-, 2θ-, and θ-2θ scans. It is easy to imagine that for the (004) RLP, a θ-2θ scan would reveal diffraction peaks for both GaAs substrate and the ZnSe epilayer[§], when performed over an adequate range. An ideal (004) θ-2θ diffractogram for the sample considered here is shown in Fig. 3.8 (a). The intensity (in counts/sec) is plotted versus ω/θ. From the angular separation, $\Delta\theta$, between the ZnSe and GaAs peaks, $a^{\perp}_{ZnSe}$ can be determined using Bragg's law (Eqn. 3.4).

The diffraction peaks of ZnSe and GaAs in Fig. 3.8 (a) are superposed on a background of oscillating intensity. These are known as the thickness fringes, since they allow determination of the epilayer thickness, based on the Eqn. [Bowen98]

$$\Delta\theta_p = \frac{\lambda_X \sin\omega_e}{t_{ZnSe}\sin 2\theta} \tag{3.5}$$

where $\Delta\theta_p$ is the angular separation of two consecutive extrema.

[§] For typical thicknesses of epitaxial structures (≤ a few μm) X-rays penetrate the substrate without significant absorption or extinction, provided ω_i is sufficiently large.

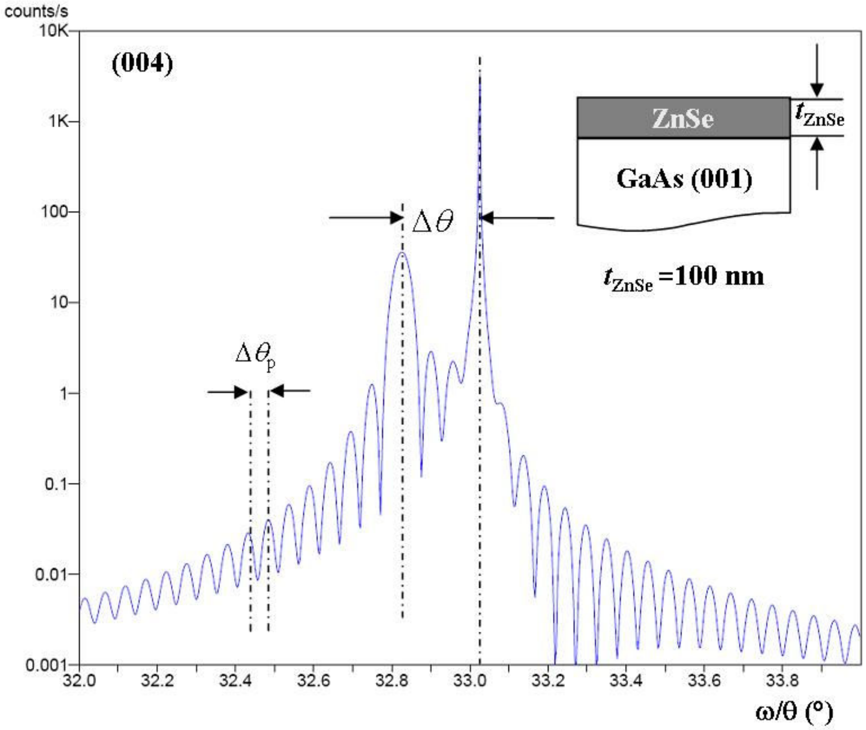

FIG. 3.8: An ideal (004) θ-2θ diffractogram of a 100-nm-thick, pseudomorphic ZnSe layer on GaAs(001) substrate. The inset shows the sample structure. The diffraction peaks due to ZnSe and GaAs are separated by $\Delta\theta$ and the thickness fringes by $\Delta\theta_p$.

(b) X-ray interferometry (XRI)

When the epilayer relaxes plastically by formation of dislocations, the thickness fringes disappear and the diffraction peak of the layer is broadened (both in ω- and θ-2θ scans). On the other hand, thickness fringes are not clearly discernible below an epilayer-thickness of ~ 60 nm. Thus, a simple HRXRD pattern does not help to determine the thickness of a highly strained epilayer, where only a few MLs can be grown, before plastic relaxation sets in. In this case, an alternative technique, known as X-ray interferometry (XRI), serves as a powerful tool. An epitaxial structure, wherein a thin layer of composition A (for example, CdSe) is sandwiched between two thick cladding layers of composition B (for example, ZnSe), serves as a Bragg-case interferometer for short wavelength x-rays. A typical sample is schematically depicted in the inset of Fig. 3.9. Due to the different lattice constants of CdSe and ZnSe, a phase shift is introduced between the x-rays diffracted from the bottom- and the top-ZnSe layers. The phase shift results in a modulation of the thickness fringes of the recorded diffractogram, the pattern of which depends on the thickness of the CdSe layer. Ideal (004) diffractograms of two structures, with 6 and 12.032Å of CdSe, sandwiched between two 50-nm-thick ZnSe layers, are shown in the main panel of Fig. 3.9 (in green and red, respectively). For comparison, the (004) diffraction pattern of a 100-nm-thick ZnSe layer is also shown (in blue). To explain different aspects of the diffractogram (of the sandwich structure) it is helpful to consider the intensity of the scattered waves, which, according to the kinematic theory, is given by [Holloway90]

$$I = [\sin^2 N_B\phi + \sin^2 N_T\phi + 2\sin N_B\phi \sin N_T\phi \cos(N_B + N_T + 2\zeta)\phi] / \sin^2 \phi \qquad (3.6),$$

for the general case where N_B and N_T planes of A are separated by a B-layer of thickness $na_A+\Delta d$, where a_A is the lattice constant of A and n, an integer. $\phi = (2\pi/\lambda_X)\, a_A \sin\theta$ and $\zeta = \Delta d/a_A$. When $\Delta d = 0$, i.e. when the B-layer-thickness is an integral multiple of the lattice-constant of A, Eqn. 4.4 changes to

$$I = [\sin^2 N_B\phi + \sin^2(N_B + N_T)\phi / \sin^2 \phi \qquad (3.7).$$

This is equivalent to the scattered intensity collected from a standard layer of A with (N_B+N_T) planes, i.e. in absence of the separator B-layer, and is known as the in-phase condition. $\Delta d \neq 0$ represents the out-of-phase condition. In the extreme case, when $\Delta d = (1/n_d)a_A$ ($n_d = \sqrt{(h^2+k^2+l^2)}$ being the order of diffraction),

$$I = [2\sin^2 N_B\Phi + 2\sin^2 N_T\Phi - \sin^2(N_B + N_T)\Phi] / \sin^2 \Phi \qquad (3.8),$$

with $\Phi = \phi - n_d\pi$, expressed relative to the Bragg condition, where $\Phi = 0$. When $N_B = N_T = N$, Eqn. 3.8 simplifies to

$$I = \sin^4 N\Phi / \sin^2 \Phi \qquad (3.9).$$

The corresponding diffractogram is characterized by a double peak structure. The position of the notch corresponds to that of the diffraction peak corresponding to $2N$ layers of A, without the separator-B-layer. The second noteworthy feature is that the pattern repeats, irrespective of the thickness of the A layers, when the B-layer thickness increases by multiples of a_A/n_d. In the above ideal case, misfit induced strain has not been considered. For the (004) diffraction of the interferometer considered here, i.e. thick ZnSe layers separated by a thin CdSe layer, the vertical lattice constants should account for the misfit-induced strain. In this case the diffraction patterns would coincide for thickness-change of the CdSe layer, given by

$$\Delta d = \frac{a^{\perp}_{ZnSe}(1 + m^{\perp}_{ZnSe-CdSe})}{n_d m^{\perp}_{ZnSe-CdSe}} \qquad (3.10).$$

where $m^{\perp}_{ZnSe-CdSe} = (a^{\perp}_{ZnSe} - a^{\perp}_{CdSe}) / a^{\perp}_{ZnSe}$. For CdSe/ZnSe heteroepitaxy, Δd = 12.032Å (n_d = 4). Therefore, this thickness results in the first in-phase diffractogram, which coincides with that of a pseudomorphic layer of pure ZnSe.

Typically, the recorded diffractograms are fitted with simulated profiles, generated for different thicknesses of the CdSe layer. The relative intensity of the two subsidiary maxima depends strongly on the CdSe-layer-thickness. The precision of the technique is illustrated in the inset of Fig. 3.9, where the patterns corresponding to Δd = 5, 6, and 7 Å are shown (Enlarged sections around the subsidiary maxima). Clearly, sub-ML variations of the amount of deposited CdSe can be detected by this method. Another advantage of the method is in its insensitivity to the morphology of the separator layer, i.e., whether it is a smooth 2D layer or an ensemble of 3D QDs. However, if the density of QDs is very low, such that the 3D features do not contribute to coherent diffraction, then the determined thickness would correspond only to the wetting layer beneath the islands.

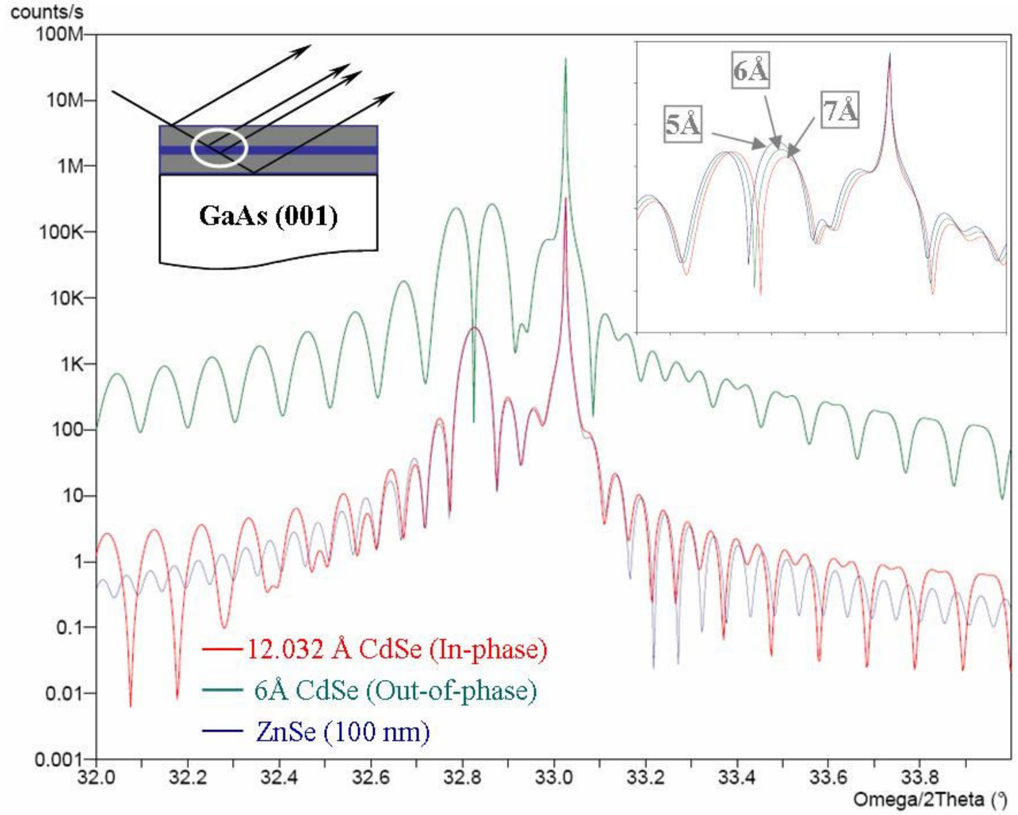

FIG. 3.9: Ideal (004) diffractograms of a "Bragg-case-interferometer" (schematically shown in the left inset) consisting of 6 and 12.032 Å thick CdSe layers, sandwiched between two 50-nm-thick, pseudomorphic ZnSe layers. The whole heterostructure is pseudomorphic to the underlying GaAs(001) substrate. The (004) diffractogram of a 100 nm thick ZnSe/GaAs(001) layer is also shown. The right inset shows an enlarged view of the subsidiary maxima, simulated using different thicknesses for the CdSe layer.

(c) Glancing incidence x-ray diffraction (GIXRD)

Finally, another x-ray technique which has emerged in the recent years as an excellent tool for evaluating the strain, shape, and composition of self-assembled islands is glancing incidence x-ray diffraction (GIXRD). In GIXRD, the primary x-ray beam is directed to the sample-surface at a glancing angle α_i, smaller than the angle of total external reflection for the substrate, α_c (0.31° for GaAs) (Fig. 3.10 (a)). This makes the technique sensitive to a region within 5 nm from the surface (in contrast to conventional

HRXRD). The diffracted beam is collected by a position sensitive detector (PSD), for a large range of detector angles, α_e (see the detector geometry).

In GIXRD, the diffraction from planes perpendicular to the substrate surface, i.e. those with Miller indices (hk0) are recorded. Therefore, the in-plane components of the incident and the diffracted k-vectors, i.e. $\vec{k}_{i,\parallel}$ and $\vec{k}_{e,\parallel}$, must satisfy the diffraction condition (Eqn. 3.1). Often intensity maps around a particular RLP, the so-called reciprocal space maps (RSM), are recorded.[**] This is done by rotating the sample around its surface normal (the angle φ in Fig. 3.10) in small steps $\Delta\varphi$, and recording θ-2θ scans at every step.

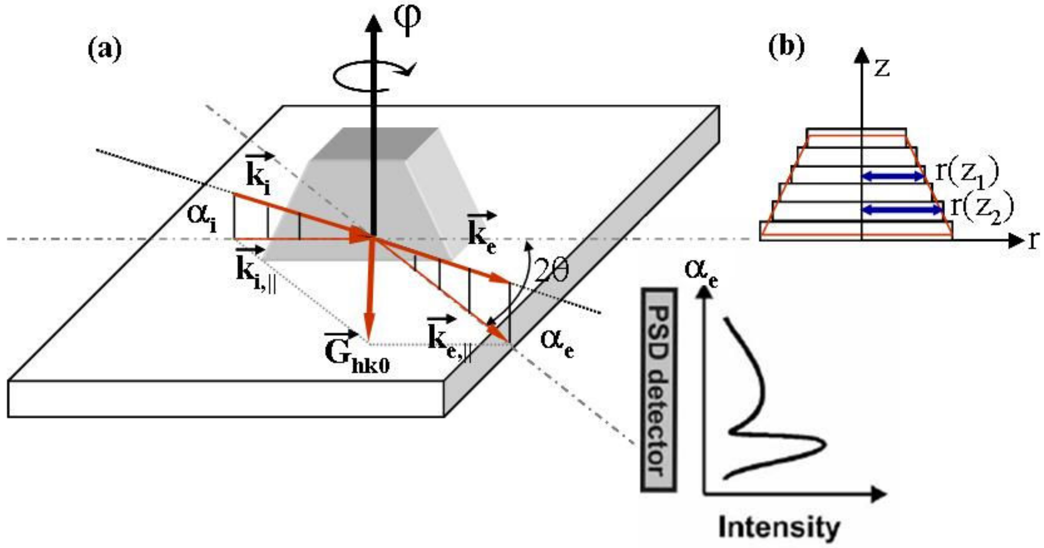

FIG. 3.10: (a) Schematic illustration of GIXRD. (b) The QD modelled as iso-strain disks of different radii r(z) at different heights z.

The co-ordinates of the RSM are defined by the vectors $\vec{Q}_r = \vec{k}_{e,\parallel} - \vec{k}_{i,\parallel}$ and $\vec{Q}_a$, which is perpendicular to $\vec{Q}_r$. Their magnitudes are given by

$$\left|\vec{Q}_r\right| = \frac{4\pi}{\lambda_X}\sin\theta, \text{ and } \left|\vec{Q}_a\right| = \left|\vec{Q}_r\right|\sin\left(\Delta\varphi\right) \tag{3.11}$$

To evaluate information about the shape and strain of the islands from the recorded RSMs, the iso-strain model, developed by Kegel et al. [Kegel01], is used. Moving from the base to the apex of a self-assembled island, for example InAs/GaAs(001), the lattice spacing of a chosen set of vertical planes ((2-20) in Fig. 3.11) varies continuously, due to elastic strain relaxation [Krause05]. This leads to a continuous intensity distribution in the

---

[**] RSMs can also be recorded in conventional HRXRD geometry. For a RSM around the 004-RLP, ω is varied in small steps and at each position a θ-2θ scan is recorded.

RSM, between the radial positions $\left|\vec{Q}_r\right| = \left|\vec{G}^{GaAs}_{2-20}\right|$ and $\left|\vec{Q}_r\right| = \left|\vec{G}^{InAs}_{2-20}\right|$ (Fig. 3.11(a)). Fig. 3.11 (b) shows a line-scan along $\vec{Q}_r$ at $\left|\vec{Q}_a\right| = 0$ and along $\vec{Q}_a$ for two different values of $\left|\vec{Q}_r\right|$.

The iso-strain model divides an island into slices of equal strain (iso-strain slices) at different heights z, across which $\left|\vec{Q}_r\right|$ is constant (Fig. 3.10(b)) [Kegel01]. The radius, *r*(z), of a particular slice is obtained from the intensity profile along the $\vec{Q}_a$ direction at the corresponding value of $\left|\vec{Q}_r\right|$. It is given by $I(\left|\vec{Q}_r\right|, r) = \left|F(\left|\vec{Q}_r\right|, r)\right|^2$, where

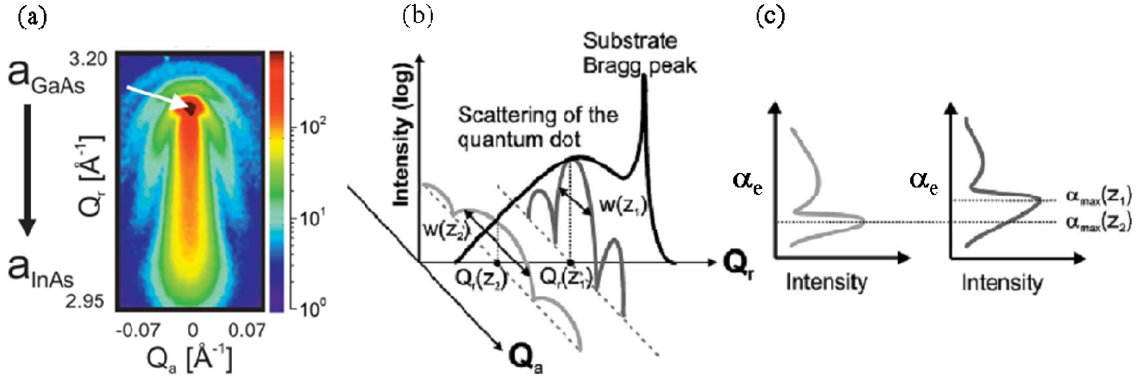

FIG. 3.11: (a) RSM recorded from an InAs/GaAs(001) QD layer around the (2-20) RLP. (b) A $\vec{Q}_r$-line-scan across the RSM at $\left|\vec{Q}_a\right| = 0$ and two $\vec{Q}_a$-line-scans for two different values of $\left|\vec{Q}_r\right|$. (c) α_e-dependence of the diffracted intensity. Adopted from [Krause05].

$$F(\left|\vec{Q}_a\right|, r) = \frac{2\pi r}{\left|\vec{Q}_a\right|} J_1(r\left|\vec{Q}_a\right|) \tag{3.12}$$,

and $J_1(x)$, the Bessel function.

Finally, the height z of a particular slice is calculated from the α_e-dependence of the intensity, shown in Fig. 3.11(c). z is related to the maximum of the plot, $\alpha_{\max}$, by the relation

$$z = \frac{1}{\left|\vec{k}_i\right| \alpha_{\max}} \cos^{-1} \frac{\alpha_{\max}}{\alpha_c} \tag{3.13}$$,

Based on the three independently-determined parameters, $\left|\vec{Q}_r\right|$, *r*(z), and z, the shape, and the strain-status of an island are determined.

For the purpose of this work, GIXRD measurements were performed at the synchrotron beamline BW2 of HASYLAB, Hamburg. Data presented in this work have been recorded and analyzed in detail by Kumpf et al. [Kumpf07]

3.4 *Atomic force microscopy*

Atomic force microscopy (AFM) belongs to the family of scanning probe microscopic techniques, developed in 1981 by Binnig, Rohrer, Gerber, and Weibel [Binnig82, Binnig87]. AFM allows mapping of the surface topography of all kinds of materials, i.e., metals, semiconductors, and insulators. A schematic of an AFM is shown in Fig. 3.12 (a). It essentially consists of a micro-cantilever with a sharp tip (probe) at its end, which is used to scan the specimen surface. Tips used in this work measured, typically, 4-5 μm in height and ~ 12-15 nm in radius of curvature.

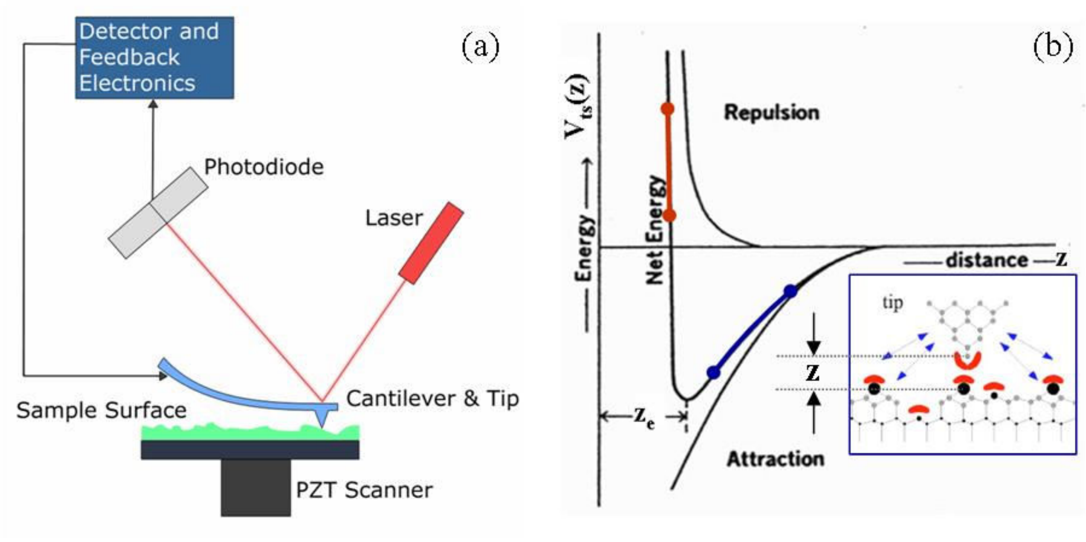

Fig. 3.12: Schematic illustration of an AFM (b) A typical profile of the interaction potential between the AFM tip and the sample surface, plotted as a function of the tip-sample separation. Inset: Schematic of an AFM-tip close to the sample-surface. The red crescents denote the short range chemical forces and the blue arrows, the long-range forces. Adopted from [Giessibl03]

When the tip is brought into proximity of a sample surface, forces between the tip and the sample, f_{st}, lead to a deflection of the cantilever according to Hooke's law. Typically, the deflection is measured using a laser spot reflected from the top of the cantilever into an array of photodiodes.

If the tip were scanned at a constant height, there would be a risk that the tip would collide with the surface, causing damage. Hence, in most cases a feedback mechanism is employed to adjust the tip-to-sample distance in a way such that a constant force between the tip and the sample is maintained. Traditionally, the sample is mounted on a piezoelectric tube that can move the sample in the z direction for maintaining a constant force, and in the x and y directions for scanning the sample. The resulting map of f_{st} represents the topography of the sample.

The inset of Fig. 3.12 (b) shows a sharp tip at a distance z from a particular feature on the sample surface [Giessibl03]. A typical profile of the interaction potential, V_{st}, between the atoms of the tip and those at the surface of the specimen is shown in the main panel of the Figure. The total energy of interaction is the sum of an attractive and a repulsive component. The short range chemical forces, measured by the AFM tip, f_{st}, is essentially the derivative of the interaction potential V_{st}, i.e.

$$f_{st} = -\frac{\partial V_{st}}{\partial z} \qquad (3.14).$$

This is denoted by the red crescents in the inset. Certain long range forces may also originate, which are indicated by the blue arrows. The AFM can be operated in a number of modes, depending on the application. The primary modes of operation are static (contact) mode and dynamic (non-contact) mode. In the static mode operation, which is discussed here, the static tip deflection is used as a feedback signal. Because the measurement of a static signal is prone to noise and drift, low stiffness cantilevers (with force constants varying between 0.02-0.5 Nm^{-1}) are used to boost the deflection signal. However, close to the surface of the sample, attractive forces can be quite strong, causing the tip to "snap-in" to the surface. Thus static mode AFM is almost always done in contact where the overall force is repulsive (the region marked in red in the potential profile of Fig. 3.12 (b)). Consequently, this technique is typically called "contact mode". In contact mode, the force between the tip and the surface is kept constant during scanning by maintaining a constant deflection. In non-contact mode, the tip-sample separation is such that the measurement is carried out in attractive region (marked in blue in Fig. 3.12 (b)) of the interaction potential.

AFM allows quantitative analysis of the morphology of self-assembled islands with high accuracy, provided the size and separation of the islands are larger than the tip-diameter. While the lateral resolution in AFM is limited by the tip-diameter, the vertical resolution can be in atomic dimensions. Typically, AFM is carried out in atmospheric ambient. However, surfaces which tend to easily oxidize, and thereby change their topography, may exhibit additional unwarranted features, in atmospheric-ambient-AFM. Nowadays, it is possible to integrate the AFM apparatus to the UHV system of MBE.

3.5 *Photoluminescence*

Photoluminescence (PL) spectroscopy is a very useful tool to probe the discrete energy levels of QDs. The basic idea of a PL experiment is shown in Fig. 3.13 (also refer to Fig. 2.20). A laser beam of appropriate wavelength excites the electrons of the valence band to the conduction band and creates electron-hole pairs. These pairs might be directly excited into the discrete levels of the QDs (resonant-excitation), or above them (non-resonant excitation), i.e., within the 2D density of states (DOS) of the QW or the ZnSe barrier. For the purpose of this work, in all cases, non-resonant excitation has been used. Excitation above the barrier bandgap is convenient since a large area of the ZnSe layer acts as an absorber. Once excited, the charge carriers diffuse to the discrete levels of the QDs. Electrons and holes might be "captured" by the QDs separately or together as excitons. Within the QDs, the electrons and holes relax to the ground state non-radiatively. Relaxation to the ground states is a fast process and is attributed to longitudinal optical (LO) phonon scattering. The confined electron-hole pair (or more appropriately, the exciton) resides in the ground QD-state for a definite period of time (the exciton lifetime or radiative decay time) before recombining radiatively (luminescence). The energy, intensity, and polarization of the emitted photons are then analyzed. The evolution of PL with time (time-resolved PL), external (magnetic and electric) fields, temperature, and the energy, power, and polarization of the exciting photons, provides a host of information regarding the electronic and confinement properties of the QDs and the energies and momenta of different confined (quasi)-particles.

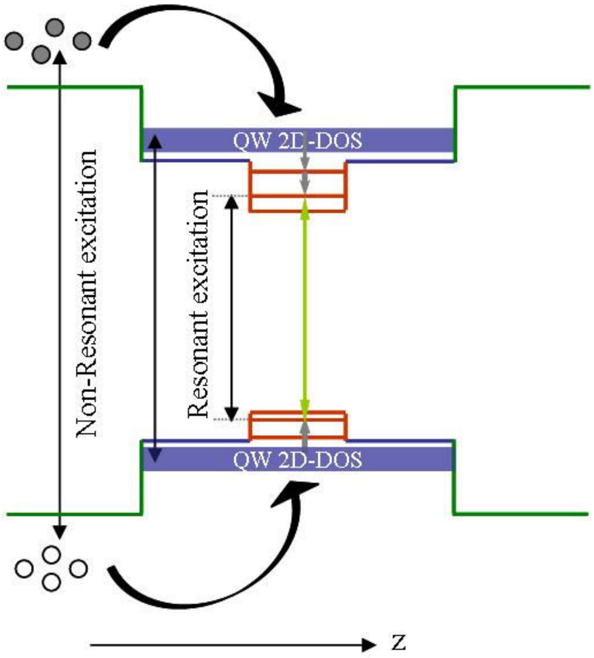

Fig. 3.13: Schematic illustration showing the excitation and emission of photoluminescence in a CdSe/ZnSe(001) QD.

In the simplest approach, PL emission is recorded in a macro-optic set up, i.e. where the exciting laser is focused to a spot size of 50-100 μm (macro-PL). In this case (for the CdSe/ZnSe(001) heterosystem), an ensemble of as much as ~10^5 QDs is probed simultaneously. The ground state energies of different QDs within the ensemble differ due to their different size and composition. Thus, the PL spectrum of a QD-ensemble is inhomogeneously broadened and has a Gaussian shape. The full width at half maximum (FWHM) of such a spectrum (typically a few tens to few hundreds of meV) is a qualitative measure of the size and composition homogeneity of the QD-ensemble. The energy-position of the spectrum yields information on the strength of quantum confinement.

Macro-PL measurement also allows determination of the critical thickness for 2D-3D transition, t_c, in SK growth. As the coverage of the island-forming epi-material is increased to t_c or beyond, the PL emission undergoes a drastic red-shift and a broadening of the spectrum. This is illustrated for the InAs/GaAs heterosystem in Fig. 3.14, for which the spectral position and FWHM of the PL spectra are plotted versus the InAs coverage [Seifert96]. Both parameters show a discontinuous jump at $t_c = 1.7$ ML.

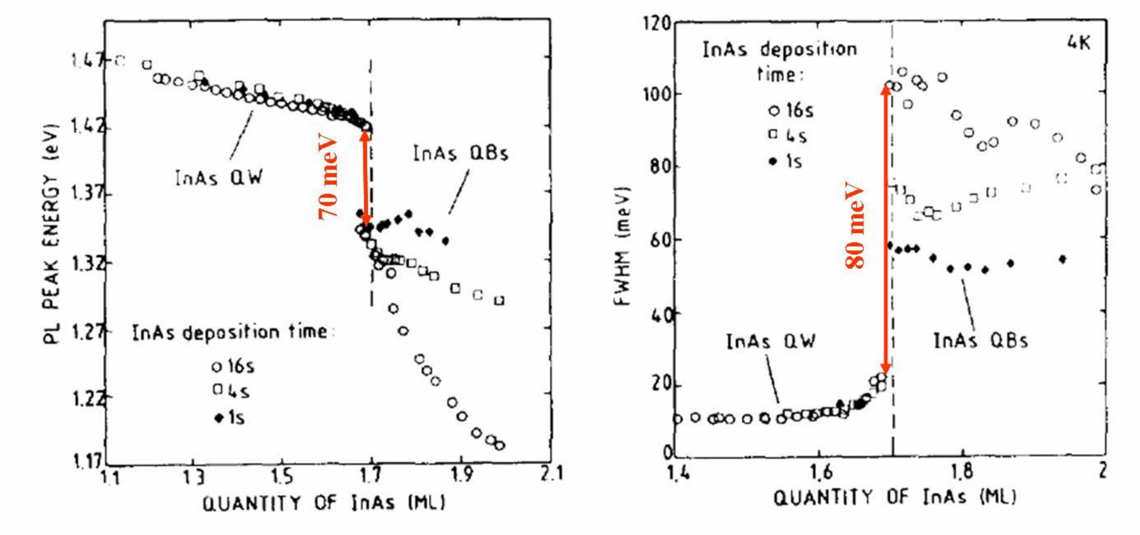

Fig. 3.14: Variation of the PL-intensity-maximum (left panel) and the FWHM of the spectra (right panel) with increasing InAs coverage, during InAs/GaAs(001). Adopted from [Seifert96]

The condition for obtaining clear emission peaks in PL spectroscopy of QDs, which is characteristic of systems with strong spatial confinement, is the lack of thermal broadening. Therefore, PL spectra are often recorded at temperatures in the order of few K, so that the thermal energy (k_BT) is less than the energy-spacing between the quantized QD-levels. At low temperatures, the intensity of the PL-emission is generally the highest and governed primarily by the radiative lifetime of the excitons. With increasing temperature the intensity falls off exponentially. This is because, with the additional thermal energy, the excitons overcome the localization barrier of the QDs and are emitted into the 2D continuum of the QW or even into the barrier layer. Subsequently, they find their way in non-radiative recombination channels, like defect- or surface-states. The temperature dependence of the integrated PL-intensity is given by

$$I_{PL}(T) = \frac{I_0 \tau_R}{\tau_{eff}(T)} \qquad (3.15),$$

where, τ_R and $\tau_{eff}(T)$ are the radiative- and temperature-dependent effective-PL-decay times, respectively. I_0 is the normalization factor that depends on the number of photo-excited carriers (equivalently, the excitation density). $\tau_{eff}(T)$ includes the effect of thermally activated non-radiative loss of excitons and is given in terms of τ_R and a non-radiative decay time τ_{NR} as [Bacher91]

$$\tau_{eff} = \frac{\tau_R}{1+(\tau_R/\tau_{NR})e^{-\Delta E_A/k_B T}} \tag{3.16),}$$

where ΔE_A is the localization energy. At higher temperatures, $\tau_{eff}(T)$ might be approximated as $\tau_{eff} = \tau_{NR}e^{\Delta E_A/k_B T}$ and the value of ΔE_A might be obtained from Eqn. 3.15. At low temperatures, $(\tau_R/\tau_{NR})e^{-\Delta E_A/k_B T} \approx 0$ and the PL intensity is governed by τ_R.

ΔE_A might also be determined from temperature-dependent, time-resolved PL spectroscopy. In time-resolved PL, short (picosecond) laser pulses are used to produce photo-excited carriers and the temporal evolution of the PL emission is studied. The temporal decay of the PL intensity, at a particular temperature T, is given by

$$I_{PL}(t,T) = I_{PL}(0,T)e^{-t/\tau_{eff}(T)} \tag{3.17).}$$

From Eqn. 3.17, $\tau_{eff}(T)$ is determined directly. Since at low temperatures, $\tau_{eff}(T) \approx \tau_R$, time-resolved PL allows determination of the radiative PL decay time. By measuring $\tau_{eff}(T)$ at different temperatures, ΔE_A is obtained from Eqn. 3.16.

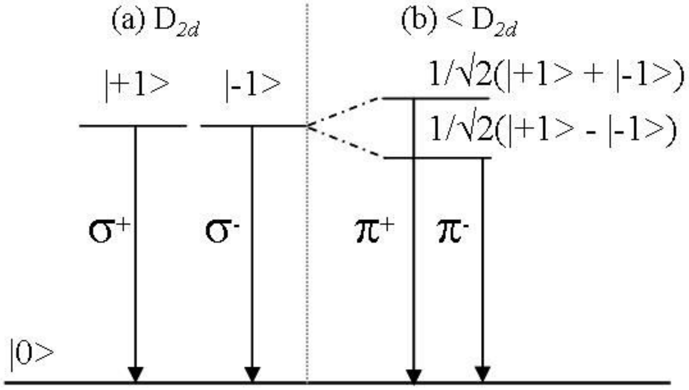

Fig. 3.15: Schematic representation of the PL-polarization corresponding to (a) a symmetric and (b) an asymmetric QD. Adopted from [Kulakovskii99]

While the PL spectrum of an ensemble of self-assembled QD, characterized by size- and composition-spread, is inhomogeneously broadened, that of a single QD is narrow and Lorentzian in shape. Ideally, the emission of a single QD, at low temperature, is broadened only due to the radiative lifetime, τ_R. Several studies of interesting quantum phenomena and device proposals call for access to emission from individual QDs. For this purpose, mesas, with diameter as small as 50 nm, are fabricated by e-beam lithography and etching. The QD-layer is etched away from everywhere other than the mesas. Additionally, the exciting laser is focused to a spot size of a few μm, by using a microscope objective lens (μ-PL). When the size of the mesa is adequately small, emission lines due to individual QDs are detected. The areal density of the QDs can be estimated from the number of such lines and with a prior knowledge of the mesa size.

The shape anisotropy of self-assembled QDs is known from the energy splitting and polarization of the single-QD-exciton emission. As discussed before in section 2.8, when the QD symmetry is D_{2d}, the bright exciton states, $|\pm 1\rangle$ are degenerate. The optical transitions $|+1\rangle \rightarrow |0\rangle$ and $|-1\rangle \rightarrow |0\rangle$ are right (σ^+) and left (σ^-) circularly polarized, respectively, where $|0\rangle$ represents the state after the electron-hole recombination. When the QD symmetry is $< D_{2d}$, the exchange part of the Coulomb interaction results in mixing of the two bright states, thereby, lifting the degeneracy (see section 2.8, Eqn. 2.34). The corresponding transitions $\left(|+1\rangle + |-1\rangle\right)/\sqrt{2} \rightarrow |0\rangle$ and $\left(|+1\rangle - |-1\rangle\right)/\sqrt{2} \rightarrow |0\rangle$ are spectrally separated (by 0-0.8 meV, for CdSe/ZnSe QDs) and linearly polarized in directions parallel and perpendicular to the QD-long-axis (π^+ and π^-, respectively) [Kulakovskii99]. The transitions are depicted schematically in Fig. 3.15.

Emission from charged and multi-exciton complexes, such as negative (X^-) and positive (X^+) trions and biexcitons (XX), is also often observed, both in macro-PL and μ-PL spectra [Herz97, Bayer98, Gindele99, Kulakovskii99, Besombes00]. Biexciton emission appears on the low-energy side of the exciton-PL, red-shifted by the biexciton binding energy (BBE). Trion emission might occur both on the red- and blue- side of the exciton line [Hartmann00] While exciton luminescence shows a linear dependence on the excitation density, both trion and biexciton emission show a superlinear dependence. Ideally, the exponent of the superlinear dependence is 2 for a biexciton [Lowisch99].

For the purpose of this work, macro-PL spectra were recorded at several temperatures, between 2 and 300 K, using excitation energies above the band gap of ZnSe. In most cases, an Ar^+ (multiple UV lines) and a solid-state diode laser (λ = 405 nm) were used for excitation. The PL emission was analyzed with a 1 m spectrometer with 1200 mm^{-1} grating, and detected either with a LN_2 cooled CCD camera or a Si-photodiode. Time-resolved measurements were carried out using a tunable, frequency-doubled, Ti-sapphire laser, generating 1.5 ps pulses, with a repetition rate of 82 MHz. The transient PL signal was spectrally resolved by a 0.46 m monochromator and detected with a Streak camera, followed by a Peltier-cooled charge coupled device (CCD) camera. The overall temporal resolution of the setup is about 20 ps. For μ-PL measurements, mesas were fabricated and the laser beam was focused by a microscope objective of 19 mm focal length to a laser spot of 5 μm in diameter.

3.6 *Other techniques*

(a) Transmission electron microscopy

Transmission electron microscopy (TEM) is an imaging technique wherein a beam of electrons is transmitted through the specimen. The formed image is magnified and directed to appear either on a fluorescent screen, a photographic film, or a CCD camera. In electron microscopy the transmitted intensity is attenuated due to diffraction by the crystalline material and not due to absorption, as is common for light microscopes. Optical contrast in a TEM image results due to several factors, i.e., the volume and density of a particular material and strain. TEM allows direct imaging of nanostructures, as well as extended defects in epitaxial samples. In high resolution TEM (HRTEM), individual lattice planes can be identified. By analyzing the variation of the lattice parameter, along a particular direction, it is possible to derive information on the strain-status and the composition of QDs. For the purpose of this work, TEM images were recorded with a JEOL 4000EX microscope. For HRTEM images, the electron beam was operated at 400keV. Lattice-parameter variation was analyzed by the geometrical phase method [Hÿtch02].

(b) Raman Spectroscopy

Raman spectroscopy relies on inelastic scattering, or Raman scattering, of monochromatic light, due to its interaction with phonons or other excitations in a system. The energy of the monochromatic photons is shifted either up (Anti-Stokes scatter) or down (Stokes-scatter), due to phonon-scattering. The energy shift is known as the Raman shift. In Raman scattering, both frequency and wave vector are conserved. Therefore, from the Raman shift, a particular phonon mode of the system can be identified [Yu96].

For typically used laser sources (with wavelengths in near-UV, visible, or near infrared), (one-phonon) Raman scattering probes only the phonons at, and close to, the centre of the Brillouin zone. In this work, Stokes-shifted Raman spectra were recorded in a backscattering geometry at 77 K, using various emission lines of an Ar^+ laser. Due to the Raman selection rules, in the back scattering geometry, only the longitudinal optical (LO) phonons of polar, zinc-blende semiconductors are Raman-active. The LO phonon frequency depends strongly on the composition of the investigated system and hence, by Raman spectroscopy, the composition of a layer of self-assembled QDs can be determined. However, in epitaxially strained layers the contribution of strain to Raman shift also needs to be taken into account.

Apparently, Raman spectroscopy involves a direct interaction between photons and phonons. However, unless the photon and the phonon frequencies are comparable, the strength of such a direct interaction (spontaneous inelastic scattering) is very weak, and has not been observed so far [Yu96]. When visible photons are used to excite Raman scattering in semiconductors, the scattering process rather proceeds through different intermediate states. For example, one possible pathway could be as follows: The incident photon excites the semiconductor to an intermediate state $\left|a\right\rangle$ by creating an electron-hole pair (or an exciton). The electron-hole pair is then scattered to another intermediate state $\left|b\right\rangle$, by emission of a phonon. Finally, the electron-hole pair in $\left|b\right\rangle$ recombines radiatively with emission of the scattered photon. The Raman scattering probability (and therefore the scattered intensity) depends on the strengths of all the involved intermediate interactions. Therefore, the scattered intensity is enormously enhanced when the exciting radiation field is tuned into resonance with one of these intermediate interactions- for example, the electron-excitation-field interaction, in the pathway considered above. This is the principle of resonant Raman spectroscopy (RRS). The confined exciton of a QD, due to its large oscillator strength, is also a good candidate as an intermediary in the Raman scattering process. Therefore, in this work, the incident laser wavelength was tuned to resonance with the luminescence of the QD-layer. In resonance with the QD exciton-transitions, a distinct phonon line could be observed from the CdSe-rich QD-layer, while out of resonance, the signal of the ZnSe matrix dominated.

(c) Photoelectron spectroscopy

In x-ray photoelectron spectroscopy (XPS), the kinetic energy of electrons, ejected when a solid is irradiated with monochromatic x-ray photons, is measured. The binding energy of the ejected electron can then be calculated by taking the difference between the energy of the incident x-ray photons and the measured kinetic energy. From the calculated binding energy of the ejected "photoelectron", elements of the specimen can be identified. A typical XPS set-up consists of a monochromatic x-ray source, an electron-energy analyzer and an electron detector. XPS is a surface sensitive technique, since the depth of the specimen from which the photoelectrons are collected, i.e. the escape depth, is only 10-20 Å. In this work, XPS spectra were recorded using a monochromatized Al K_α source ($h\nu = 1486.6$ eV), and without any surface preparation.

Summary

This chapter discussed the fundamental aspects of MBE and the details of RHEED, HRXRD, XRI, AFM and PL characterization techniques. TEM, RRS, and XPS were also described briefly.

GaAs(001) buffer- and ZnSe/GaAs(001) barrier-layers: Growth and topography

4

This chapter deals in brief with the growth and topographies of GaAs(001) homoepitaxial buffers and ZnSe barrier layers, grown atop them.

4.1 *Growth of GaAs(001) buffers and ZnSe barrier layers*

All commercially-available epi-ready GaAs substrates are covered with a thin oxide layer. Prior to growing epitaxial layers on such substrates, it is first essential to remove the "native" oxide. From the GaAs(001) surface, the native oxide desorbs at a sharply-defined temperature of 582 °C. The oxide-removal process leaves behind an extremely rough surface, dotted with pits. Such a surface is not ideal for growth of high quality epilayers. To overcome this shortcoming, ~ 200-nm-thick, nominally undoped GaAs buffer layers were grown on the oxide-desorbed epi-ready substrates, prior to growth of the II-VI heterostructures. For this purpose, degassed substrates were inserted in the "GaAs chamber" (see Fig. 3.2) and heated up to the oxide removal temperature under As beam equivalent pressure (BEP)[†] of 3x10^{-6} Torr. Subsequently, the oxide-desorbed GaAs surface was annealed (also under As-flux) for 5 mins at 620 °C. Then the temperature was lowered to 600 °C, and GaAs was grown by MBE. A Ga BEP of 2x10^{-7} resulted in a growth rate of ~ 1 Å s^{-1}. The growth was terminated by closing the Ga-shutter and the sample was gradually cooled down to ~ 220 °C. The As flux was maintained till 550 °C, which ensured a β(2x4) As-terminated GaAs surface for the subsequent growth of the ZnSe layer.

The interface between ZnSe and GaAs(001) can be formed either by Zn-As or Ga-Se bonds. While the Zn-As configuration leads to a smooth interface and low density of defects, formation of Ga-Se bonds, to the contrary, is known to be detrimental for the crystalline quality of ZnSe epilayers [Kuo97, Ohtake98]. To promote formation of the desirable Zn-As bonds, it was ascertained that the surface of the GaAs buffer was β(2x4) As-terminated. However, this precaution does not completely preclude the formation of the Ga-Se bonds, when Zn and Se are co-deposited (i.e. in MBE mode) directly atop the GaAs buffer. Se adatoms are known to replace As atoms of the surface-layer and bind with the Ga-atoms of the penultimate layer [Ahsan97]. Therefore, certain other precautions and a specific method were adopted for ZnSe growth. Before insertion of the GaAs buffer into the “ZnSe chamber”, the Zn shutter was opened for ~ 1 min. This was performed to passivate any background Se vapor within the II-VI chamber. The freshly grown buffer was then transferred from the GaAs to the ZnSe chamber, within ~ 2 mins. This ensured that the substrate temperature did not drop down excessively, so that ZnSe growth could be initiated immediately after insertion of the buffer. Once the buffer was inserted, the Zn shutter was re-opened and the substrate was ramped up to 210 °C. During this interval, the substrate manipulator was fixed in a position where the buffer did not face the effusion cells. Subsequently, ZnSe growth was initiated with 10 ALE cycles at 210 °C, wherein Zn and Se shutters were opened for 9 s and 1 s respectively, interspersed by growth interruptions of 2 s. Following this, the substrate temperature was ramped up to 280-300 °C within 3 mins. During these 3 mins, growth was performed by MEE. The Se flux was offered in pulses of 10 s, while the Zn shutter was kept continuously open. Finally, on reaching the required T_G = 300°C, MBE growth was carried out at a Se:Zn BEP ratio of F_{Se}:F_{Zn} = 2 (Zn BEP: 1x10^{-6}) and a growth rate of 1.7 Å s^{-1}. The crystalline quality of ZnSe epilayers is known to be optimum when grown in a Se-rich condition (characterized by F_{Se}:F_{Zn} = 2-4) [Riley96].

The specific method described above was adopted for growth of all ZnSe barrier layers, except those related to the work discussed in Chapter 7. As mentioned before in section 3.1, the samples of Chapter 7 were grown in the “CT chamber”, equipped with a valved Se-cracker cell. Due to the use of the valved cell, the background partial pressure of Se in the CT chamber could be maintained to negligibly low values. Thus the low temperature ALE and MEE steps were considered redundant, for ZnSe growth in this chamber.

[†] The BEP is related to the flux by Eqn. (2.16)

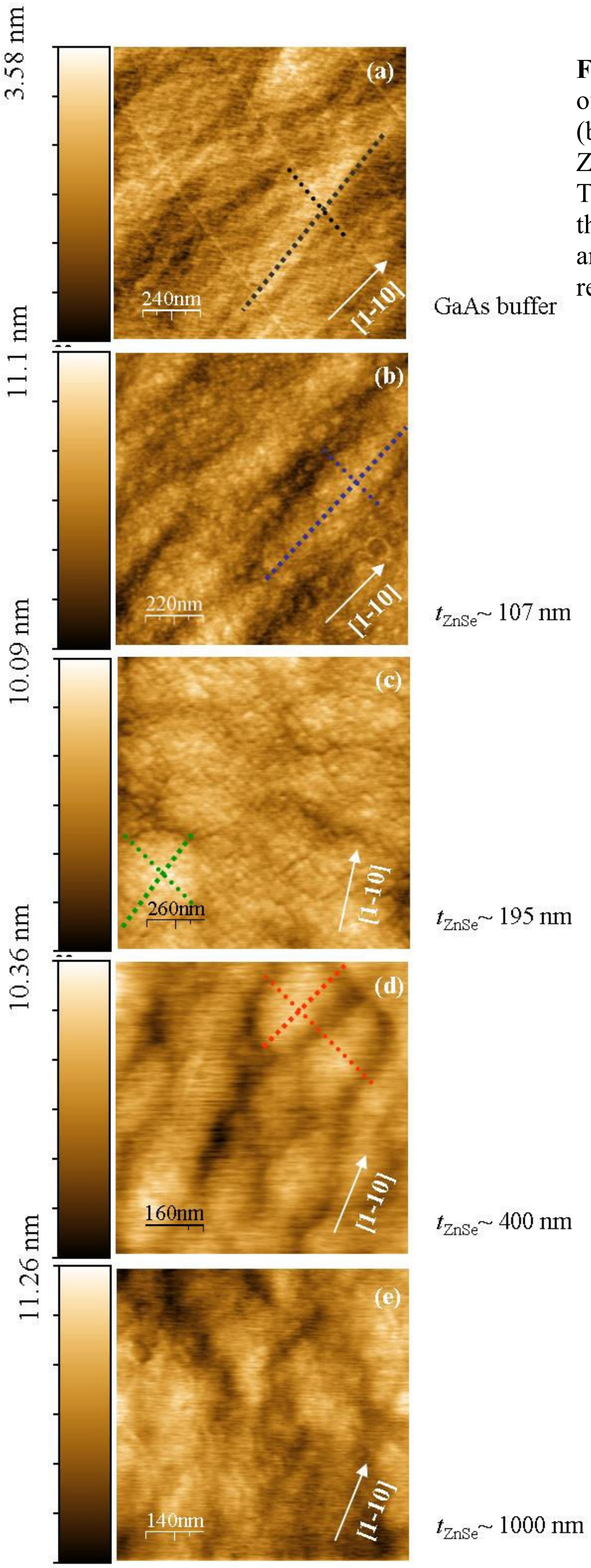

Fig. 4.1: (a) AFM image of the surface of a (200-nm-thick) GaAs(001) buffer. (b)-(e) AFM images of the surfaces of ZnSe layers of different thicknesses. The ZnSe layers of different thicknesses were grown by A. Benkert and co-workers, following the same recipe mentioned in Section 4.1

4.2 *Topography of the GaAs buffer- and the ZnSe barrier-layers*

An AFM image of the surface of a typical GaAs(001) buffer is shown in Fig. 4.1 (a). The surface is very smooth, with a root-mean-square (rms) roughness of 0.5 nm. However, very shallow mounds, similar to those mentioned in [Orme94], are also seen here. The mounds are 1-1.5 nm high and 600-800 nm long. The slope of the mounds is ~ 1°. The length (measured along [1-10]) and width (measured along [110]) of a particular mound, indicated in Fig. 4.1 (a) by dotted lines, is shown in the top panels of Fig. 4.2 (a) and (b), respectively. From the geometry of the sample probed by AFM, it could only be ascertained that the long axes of the mounds are parallel to one of the <110> directions. More specifically, based on the work of [Orme94] (Fig. 2.9 (d) of section 2.3), it is assumed that the mounds are aligned along the [1-10] direction.

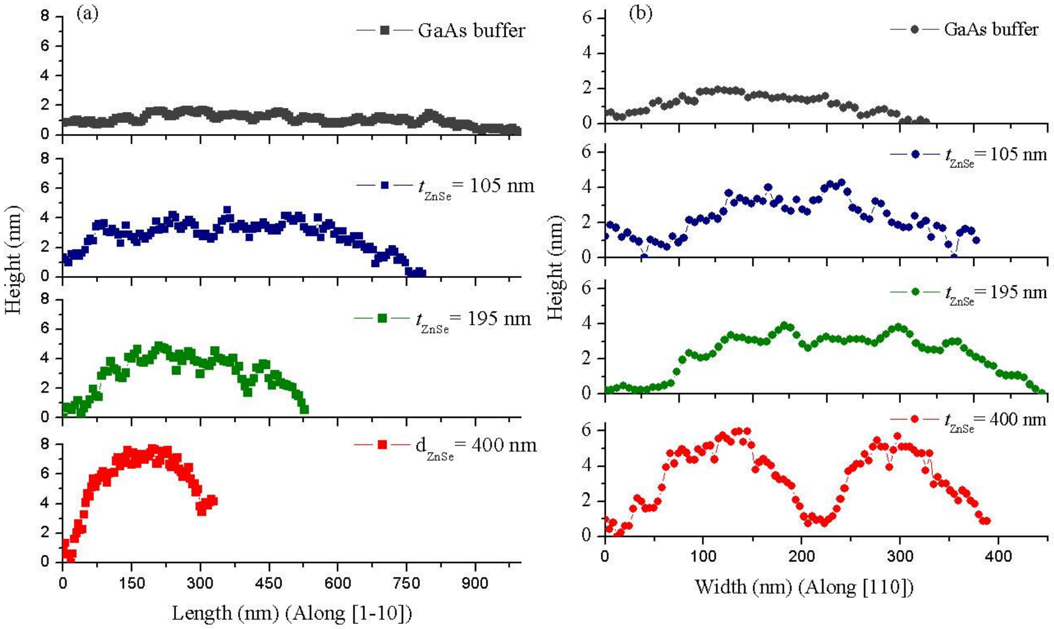

Fig. 4.2: (a) Length (measured along [1-10]) and (b) width (measured along [110]) of mounds, formed on the surface of the GaAs(001) buffer and ZnSe layers of different thicknesses, t_{ZnSe}.

The surface of a fully strained (pseudomorphic) ZnSe layer (t_{ZnSe} = 107 nm) grown atop the GaAs buffer, at T_G = 280 °C, is shown in Fig. 4.1 (b). The morphology resembles closely that of the underlying GaAs buffer but the rms roughness is 1.5 nm. Similar mounds are observed in this image as well. However, in this case, they are ~ 4 nm high, but of comparable lateral dimensions (Second panels of Fig. 4.2 (a) and (b)).

Fig 4.1 (c) shows the surface of a similarly-grown, 195-nm-thick, ZnSe layer. By *in-situ* HRXRD measurements[‡], it was ascertained that at a thickness of 195 nm, the layer was still pseudomorphically strained to GaAs, but was on the verge of plastic relaxation. The mounds in this case appear to be circular and devoid of any preferred direction of elongation. The lateral extent of a typical mound is ~ 400 nm and its height, ~ 4 nm [Third panels in Fig. 4.2 (a) and (b)].

In Fig. 4.1 (d), the surface of a 400-nm-thick ZnSe layer is shown. At this thickness, the ZnSe layer is partially relaxed by formation of misfit dislocations (plastic relaxation). A very different morphology of the surface is clearly evident. Well-defined mounds are seen in the AFM image. The mounds are ~ 300 nm long and only 200 nm wide, while their heights reach up to 8 nm (Fourth panels in Fig. 4.2 (a) and (b)).

Finally, when the ZnSe layer is almost completely relaxed, at a thickness of t_{ZnSe} ~ 1000 nm, the surface is devoid of any pattern (Fig. 4.1(e)).

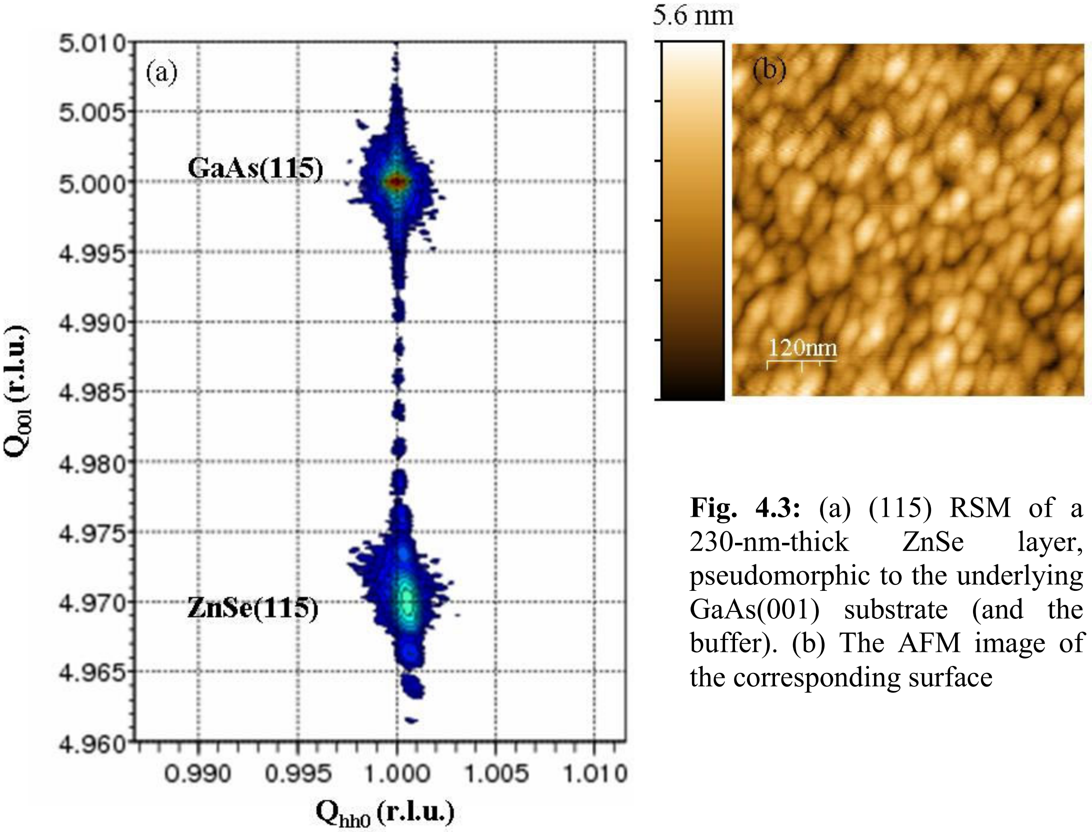

Fig. 4.3: (a) (115) RSM of a 230-nm-thick ZnSe layer, pseudomorphic to the underlying GaAs(001) substrate (and the buffer). (b) The AFM image of the corresponding surface

Fig. 4.3 (a) and (b) show the (115) reciprocal space map (RSM) of another 230- nm-thick ZnSe layer and the AFM image of the corresponding surface, respectively. Unlike the ZnSe layers shown in Fig. 4.1(b)-4.1 (e), for this sample the growth of ZnSe was not initiated by the special recipe mentioned in section 4.1, but by conventional MBE, directly at the growth temperature of T_G = 280 °C. The abscissa and the ordinate of the

---

[‡] In situ HRXRD has been extensively investigated by Benkert et al.[Benkert07]

RSM are shown in reciprocal lattice units (r.l.u), so that the scattered intensity at $Q_{hk0} = 1$ and $Q_{00l} = 5$ represent the 115-RLP of GaAs (refer to Fig. 3.7). The RSM clearly shows that the sample is pseudomorphically strained (The scattered intensity corresponding to the ZnSe lies also at $Q_{hk0} = 1$). Despite being pseudomorphically strained, the surface of this layer consists of a dense ensemble of distinct 3D nanostructures. The nanostructures are ~ 2.5-3 nm high and asymmetric in their in-plane dimensions. Their length varies between 70-90 nm and width, between ~ 30-50 nm. The areal density of the nanostructures is ~ 6×10^{10} cm^{-2}.

4.3 *Morphological evolution of the ZnSe/GaAs(001) surface: An interplay between plastic and elastic relaxation?*

For the purpose of this work, CdSe QD-layers have been fabricated on pseudomorphic, 45-60 nm thick, ZnSe layers. Therefore only the ZnSe surface corresponding to Fig. 4.1 (a) is of direct relevance. However, it is interesting to analyze the morphological evolution of the ZnSe surface, with increasing layer thickness. Epitaxial growth of ZnSe/GaAs(001) has been widely studied in the past [Petruzello88, Gonsalves90, Guha93, Kuo97, Nurmikko97, Ohtake98]. Especially, strain relaxation of ZnSe layers has been the subject of many investigations, due to its importance in fabrication of blue-green lasers [Tomiya95, Chu96, Heun97, Wang00A]. The lifetime of such devices was found to be severely limited due to the presence of misfit dislocations and stacking faults, which formed as a result of plastic strain relaxation [Grillo95, Nurmikko97, Gunshor96].

Presence of dislocations can also lead to morphological modification of a growing surface. Earlier works have suggested that due to plastic strain relaxation, the epitaxial growth rate is locally enhanced in regions directly above the dislocations. This has been argued to cause surface undulations [Jonsdottir95]. However, the morphological evolution described here is presumably not mediated (only) by dislocations/stacking faults of the ZnSe layer. This is because the surface reorganization sets in even when the ZnSe layer is observed (by HRXRD) to be pseudomorphically strained (Fig. 4.1 (c) and 4.3 (b)). Albeit pseudomorphic ZnSe layers are not “dislocation-free”, the density of such defects is expected to be low. An estimate of the dislocation density can be made from the width of the HRXRD peak (of the layer), in a ω-line-scan [Ayers94]. From the RSM of Fig. 4.3 (a), the ω-width was measured to be 0.00694°. For such a low ω-width, Constantino et al. have shown using Ayers model that the density of dislocations is < 10^5 cm^{-2} [Constantino98]. The value is five orders of magnitude lower than the density of nanostructures seen in Fig. 4.3(b). Thus, the formation of these nanostructures might not be directly correlated to an enhanced growth rate in strain-relaxed regions above dislocations.

A comparison of Fig. 4.1 (a) and 4.1 (b) shows that the mound-morphology of the ZnSe surface is remarkably similar to that of the underlying GaAs buffer layer. As argued to be the case for GaAs(001) homoepitaxy [Orme94, Orme98] (refer to section 2.3, Fig. 2.9), also on the ZnSe surface, the mounding phenomenon is possibly related to presence of ES barriers (see BOX 2.3, Fig. 2.8). The fact that the form of the mounds is preserved, even after deposition of 107 nm of ZnSe, would then mean that intraplanar surface diffusion of adatoms is not strongly suppressed-at least on length-scales defined by the lateral dimensions of the mounds.

Another possibility might be that an ATG-like instability (see section 2.2) is triggered in the ZnSe barrier layer by the mound-template of the GaAs homoepitaxial buffer. The mounds of the ZnSe surface might then be assumed to elastically release a small fraction of the misfit strain. This argument is supported by the surface-evolution closer to the onset of plastic strain relaxation (t_{ZnSe} = 195 nm). The AFM image of Fig. 4.1 (c) is suggestive of a bi-directional periodic modulation of the surface. Such a phenomenon has been discussed by Jesson [Jesson98], in the context of low-misfit GeSi/Si(001) heteroepitaxy, and termed as "ripple-fission". Ripple fission is driven by the possibility of enhanced (elastic) strain relaxation, by forming a bi-directionally undulated surface.

Fig. 4.1 (d) represents a partially (plastically) relaxed ZnSe layer. Here the mounds are clearly-defined. According to the ATG model, stress builds up in the trough regions defined by a bi-directionally undulated surface, which eventually leads to nucleation of dislocations. Such a phenomenon has been observed by AFM in case of Ge$_{0.03}$Si$_{0.97}$/Si(001) (liquid phase) heteroepitaxy (m = 0.0013) [Albrecht95]. The authors observed that initially a bi-directionally undulated surface developed (for thickness < 300 nm), as shown in Fig. 4.4 (a). For larger thicknesses, dislocations were nucleated (Fig. 4.4 (b)). In case of ZnSe/GaAs(001) heteroepitaxy (m = 0.0027), a similar phenomenon might be expected.

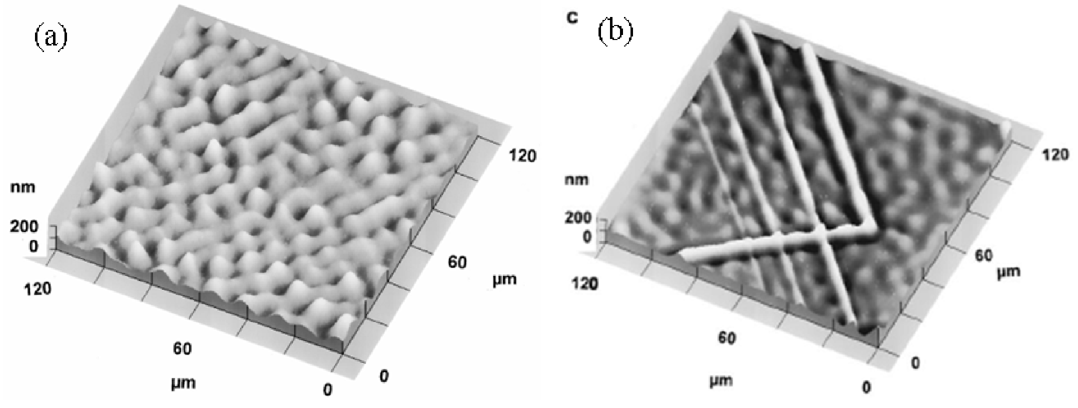

Fig. 4.4: (a) Bi-directional undulations on the surface of a 200-nm-thick Ge$_{0.3}$Si$_{0.97}$/Si(001) layer, grown by liquid phase epitaxy. (b) A "cross-hatch" pattern, related to misfit dislocations, superposed on the undulated morphology, for a layer thickness < 300 nm. Adopted from [Albrecht95]

The surface of the ZnSe layer shown in Fig. 4.3 (b) is difficult to comprehend. It shows a dense array of nanostructures, typically formed due to elastic strain relaxation in highly lattice-mismatched heterosystems. The corresponding RSM of Fig. 4.3 (a) suggests that the layer is pseudomorphically strained. As mentioned before, enhanced growth rate directly atop dislocations would not account for the areal density of the nanostructures. On the other hand, the high density of small nanostructures contests also the tenets of ATG theory. For the surface shown in Fig. 4.4 (a), Albrecht et al. determined the undulation periodicity to be 11.5 ± 0.7 μm [Albrecht95]. The undulation-periodicity for a ZnSe/GaAs(001) surface can then be approximated to be ~ 2.5 μm, assuming all parameters in Eqn. 2.15 (see section 2.2), other than the misfit m, to be similar for the two heterosystems. This is ~ 40 times the lateral dimensions of the observed nanostructures. This discrepancy suggests that a complex interplay between elastic and plastic strain relaxation governs the thickness-dependence of the surface morphology in ZnSe/GaAs(001) heteroepitaxy. Further insight calls for more rigorous investigations.

Summary

In summary, this brief chapter dealt with the growth of GaAs homoepitaxial buffers and ZnSe barrier layers, along with an analysis of the morphological evolution of ZnSe/GaAs(001) surfaces with increasing layer-thickness. Though somewhat speculative, the evolution indicates to an interplay between elastic and plastic strain relaxation.

CdSe/ZnSe(001) MBE: Growth and QD-formation

5

This chapter deals with the formation and properties of QDs, in conventional MBE growth of CdSe on pseudomorphic ZnSe(001) barrier layers. In the first and the second sections, the details of sample growth and evaluation of CdSe growth rate, respectively, are briefly discussed. The third section presents in details the morphology, composition, and luminescence properties of the QDs. The last section is devoted to the understanding of the fundamental mechanism underlying QD formation, which also reveals interesting peculiarities of CdSe/ZnSe(001) epitaxy.

5.1 *Sample fabrication*

For all samples discussed in this chapter, CdSe growth was carried out by conventional MBE, typically, on 40-60-nm-thick ZnSe barrier layers. QD-formation has been studied systematically for CdSe growth at T_G = 300 °C. Both uncapped samples for AFM and capped samples for XRI, PL, TEM, and Raman spectroscopy were prepared. Capping was done by MBE-growth of 35-50 nm of ZnSe atop the CdSe layer, also at 300 °C. No growth interruption was introduced before capping. To investigate fundamental aspects of CdSe/ZnSe(001) epitaxy, CdSe growth was also performed at T_G = 170-235 °C. The BEP of Se and Cd, used for the growth of all samples (at both T_G), were $2x10^{-6}$ Torr and $1x10^{-7}$ Torr, respectively.

5.2 *Determination of CdSe growth rate*

To determine the growth rate of CdSe, XRI (section 3.3 (b), Fig. 3.9) was employed. Fig. 5.1 shows the (004) diffractogram (blue) recorded from a sample consisting of $\Theta = 2.38$ ML CdSe (grown by MBE at $T_G = 300$ °C), sandwiched between two 42-nm-thick ZnSe layers. The Figure also shows the simulated profile (red), from which Θ was determined. While for $T_G = 300$ °C, the growth rate was deduced to be 0.06 ML s^{-1}, for $T_G = 230$ °C, it was 0.071 ML s^{-1}. The slightly lower growth rate at higher T_G is possibly due to lowering of the Cd sticking coefficient with increasing growth temperature, similar to the behavior of Zn in ZnSe epitaxy [Wolfframm00].

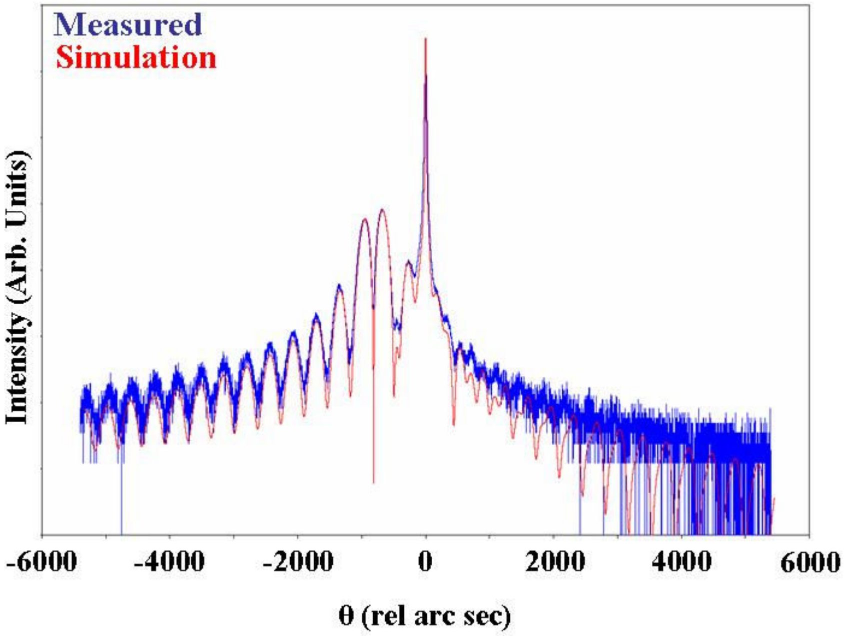

Fig. 5.1: (004) x-ray diffractogram (blue) of a sample consisting of $\Theta = 2.38$ ML CdSe, sandwiched between two 42-nm-thick ZnSe layers. The simulation-profile is also shown (in red).

For growth at $T_G = 230$ °C, the growth rate was also verified by RHEED. RHEED specular spot intensity (SSI) profiles were recorded during CdSe growth at different values of T_G. The angle of incidence of the electron beam with respect to the substrate surface was fixed at ~3°. Fig. 5.2 shows the recorded profiles. SSI oscillations are observed for CdSe growth at $T_G \leq 235$ °C, but not for growth at $T_G = 307$ °C. The growth rate of CdSe at $T_G = 215$-235 °C was found to be 0.078 ML s^{-1}. The value is in good agreement with that determined by XRI.

5.3 *CdSe/ZnSe(001) MBE at $T_G = 300$ °C: Formation and properties of QDs*

To study the formation of QDs by conventional MBE growth of CdSe at $T_G = 300$ °C, a series of samples, with CdSe coverage varying between $\Theta = 1$-4 ML, were prepared. For the whole range of Θ, no transition from a streaky to spotty RHEED was observed during deposition of CdSe. A streaky (2x1) pattern, characteristic of a Se-terminated quasi-2D CdSe surface, persisted during the entire duration of growth. However, the individual streaks were observed to be considerably broadened, compared to those seen during growth of the underlying ZnSe barrier layer.

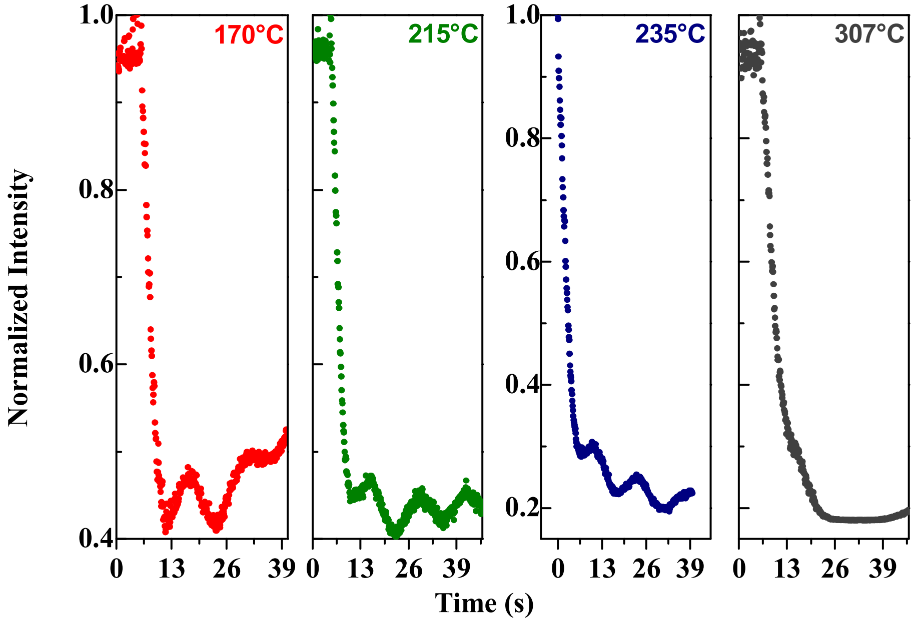

Fig. 5.2 RHEED SSI profiles recorded during MBE of CdSe on ZnSe at different growth temperatures, T_G.

The topology of a few uncapped samples was studied by AFM. In Fig. 5.3 (a), (b), and (c), AFM images of an uncapped sample, with $\Theta = 3$ ML are shown, corresponding to surface-areas of 1200 x 1200 nm^2, 500 x 500 nm^2 and 217 x 250 nm^2, respectively.

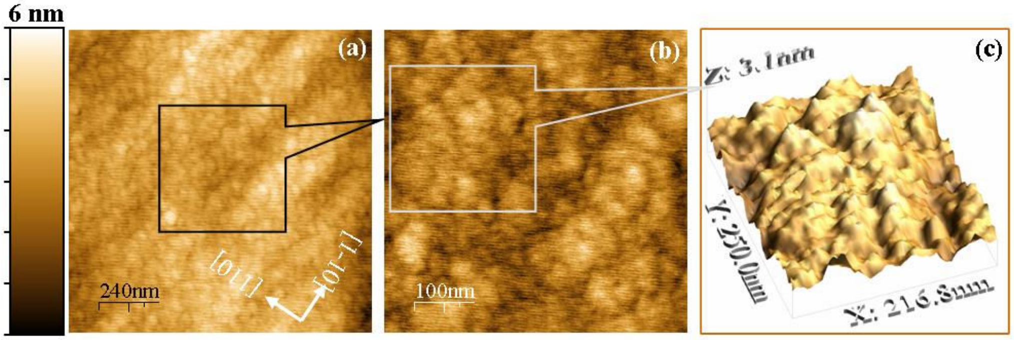

Fig. 5.3: AFM images, of an uncapped CdSe layer, with $\Theta = 3$ ML, corresponding to surface-areas of (a) 1200 x 1200 nm^2, (b) 500 x 500 nm^2, and (c) 217 x 250 nm^2 (3D view), respectively.

The long “ridges” of Fig. 5.3 (a) resemble closely the mounds of the pseudomorphic ZnSe/GaAs(001) layer, shown previously in Fig. 4.1 (b). It is therefore assumed that these features (henceforth called ridges) of the CdSe surface are also defined by the morphology of the underlying ZnSe barrier layer. However, in contrast to the image of Fig. 4.1 (b), the entire scanned area of this image is uniformly dotted with very tiny "mounds", seen more prominently in the image of Fig. 5.3 (b). The heights of most of these mounds were found to be below 1 nm (3 ML CdSe). Albeit their contours are not well defined, their weak tendency to elongate and align in a direction perpendicular to the long ridges, i.e. along the [110] direction, is observed. The actual areal density of the mounds could be higher than that observed in the image, since features smaller than the diameter of the AFM tip (12-15 nm), would not be resolved separately. However, distinct, well-separated, 3D islands, as obtained in SK growth, are not observed in the images of Fig. 5.3. The morphology better represents a rough 2D surface, consistent with the absence of a distinct streaky-to-spotty transition in RHEED.

The morphology of the CdSe deposit, after capping with ZnSe was probed by HRTEM. Fig. 5.4 shows a bright field image corresponding to the sample with $\Theta = 2$ ML. The CdSe deposit is seen as a QW-like layer of darker contrast, compared to the surrounding ZnSe barrier and cap layers. Within the QW, small zones of still darker contrast are seen. These represent regions, wherein the local Cd-concentration is higher than the average Cd-content of the QW. The observations are in accord with several previous reports which have convincingly demonstrated the formation of compositionally inhomogeneous CdZnSe QWs in CdSe/ZnSe(001) epitaxy, for a wide range of Θ values [Peranio00, Litvinov00, Litvinov01].

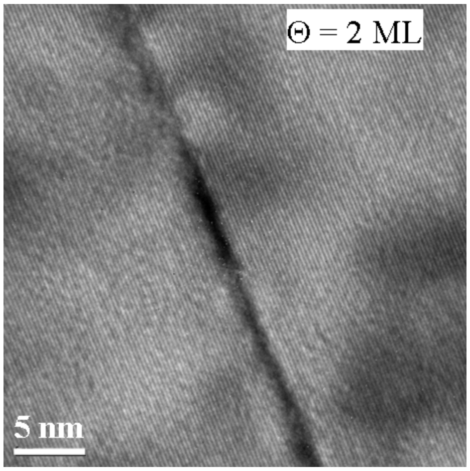

Fig. 5.4: Cross sectional HRTEM image (bright field) of the sample with $\Theta = 2$ ML

From the whole series of capped samples with varying Θ, PL spectra were recorded both at 2 and 300 K. The spectra at 2 K are shown in Fig. 5.5. All samples showed bright luminescence at low temperature. At 300 K, the emission weakened considerably. The spectra shown in Fig. 5.5 are inhomogeneously broadened and for $\Theta \leq 2.8$ ML, weak low energy tails are clearly visible. Ouadjaout and Marfaing have demonstrated for several ternary II-VI QWs that such low energy tails arise due to the presence of local compositional inhomogeneities in QWs [Ouadjaout90]. This substantiates the fact that the structures formed in CdSe/ZnSe(001) MBE at $T_G = 300$ °C are alloyed CdZnSe QWs, with local Cd-rich inclusions, possibly of different sizes and composition. Such inclusions would confine single particles (either electrons or holes) or whole excitons, depending on their size and composition, especially since the exciton Bohr radius of CdSe is only ~ 5 nm. With increasing Θ, it is observed that the PL spectra broaden and the tail weakens. This is attributed to an increase in the size, Cd-content, and areal density of the local inclusions, wherein most excitons are confined three-dimensionally, like in QDs.

Fig. 5.6 (a) and (b) respectively, show the peak-positions (of the spectra recorded both at 2 and 300 K) and the full widths at half maxima (FWHM) (of the spectra, recorded only at 2 K), as functions of Θ. Exciton transition energies derived by variation calculation, assuming uniform, 1-4 ML thick, pure CdSe QWs, are also plotted in Fig. 5.6 (a) [Puls96].

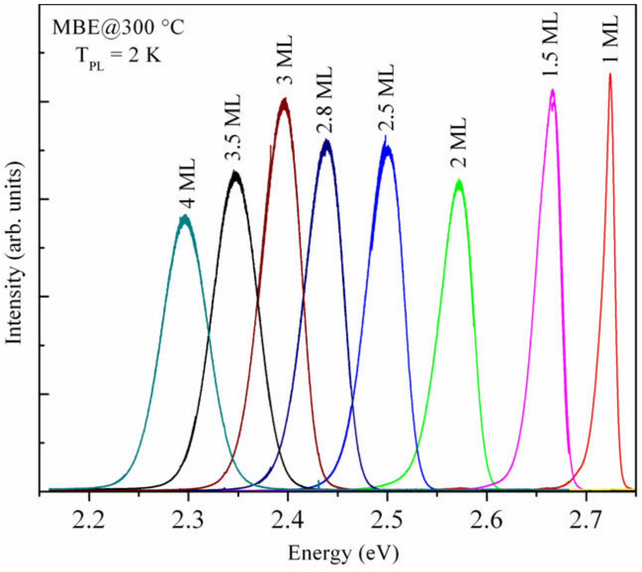

Fig. 5.5: PL spectra recorded at 2 K from the series of MBE-grown CdSe layers, with Θ varying from 1-4 ML.

Unlike the QDs formed in SK mode (Fig. 3.14), in this case, both PL-peak-positions and FWHM-values change monotonically. Further, the Θ-dependence of PL-peak-positions, corresponding to the QD-layers, follows the same trend as that of the exciton transition energies, derived for the QWs. It is also observed that the PL-peak-positions of the QD-layers are blueshifted compared to the calculated exciton transition energies of *pure* CdSe QWs. The PL-blueshift is necessarily due to Zn-admixture of the CdSe QD-layer and concomitant widening of the exciton bandgap (see Figs. 1.2, 2.20, and 3.13).

Three-dimensional confinement of excitons (and hence, formation of QDs) is substantiated by the results of μ-PL spectroscopy. Corresponding to Θ = 3 ML (refer to Fig. 5.5), the μ-PL spectra recorded at 2 K, for mesas of different diameters, Φ_{mesa}, are shown in Fig. 5.7 (a). With decreasing Φ_{mesa}, the broad inhomogeneously-broadened spectrum de-convolutes into narrow emission lines, characteristic of individual QDs. By counting the emission lines corresponding to the smallest mesa in

Fig. 5.7 (a), the areal density of QDs was determined to be ~ 10^{12} cm^{-2}. Such a high areal-density requires the QDs to be necessarily ≤ 10 nm in diameter. This inference is also in agreement with previous reports which demonstrated the formation of sub-10-nm QDs (see section 2.7), characterized by a "speckle" contrast in plan-view TEM images, when recorded in weak-beam condition [Litvinov00, Strassburg00, Litvinov01] (section 2.7, Fig. 2.16). However, it should be borne in mind that the values derived from μ-PL spectra provide only an upper limit of the QD-areal-density, since in counting the emission lines, it is implicitly assumed that multi- and charged-excitonic complexes are not formed.

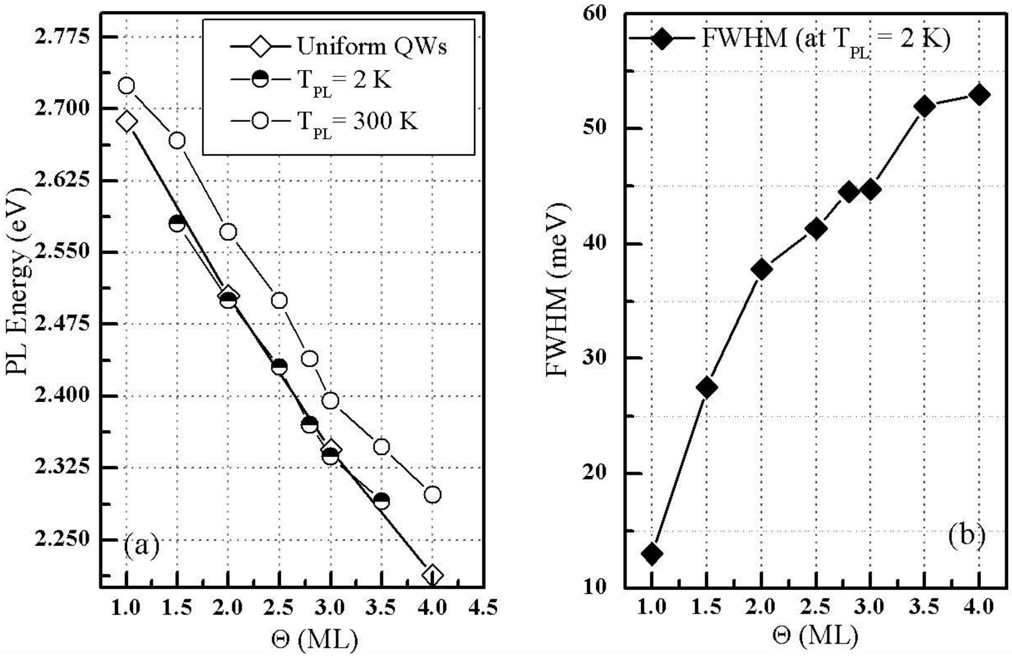

Fig. 5.6: (a) Θ-dependence of the spectral position of PL-peaks, recorded both at 2 and 300 K. (b) The evolution of full widths at half maxima of the spectra with Θ (recorded at 2 K).

The temperature dependence of the integrated-PL-intensity, corresponding to a sample with Θ = 3.5 ML, is shown in Fig. 5.7 (b). From the slope of the linear fit to the fast-decaying high temperature region of the plot (following Eqn. 3.15 and 3.16), the activation energy for non-radiative decay was determined to be ΔE_A = 55 meV. The same value of ΔE_A was derived also by Robin et al. for 3-ML-thick CdSe/ZnSe(001) QD-layers (grown by ALE at T_G = 280 °C) from the temperature-dependence of the PL-decay-times, in time-resolved PL-measurements [Robin04]. The observed low value of ΔE_A is attributed to the high areal density of QDs. While the vertical confinement within the QD-layer is strong, the energy barrier to lateral tunneling of excitons, between the QDs of a dense ensemble, is expected to be small. Therefore, the low ΔE_A reflects the average lateral confinement barrier within the QD-layer ($V_{e,h}(x,y)$ in the context of Eqn. 2.28).

By a novel, angle-resolved polarised-PL spectroscopic technique [Kiessling06], the shape of the QDs was investigated. As mentioned before in section 3.5 (Fig. 3.15), the shape-anisotropy of the QD-lateral dimensions manifests itself in a linear polarization of the PL emission along the direction of the QD-long-axis [Kulakovskii99].

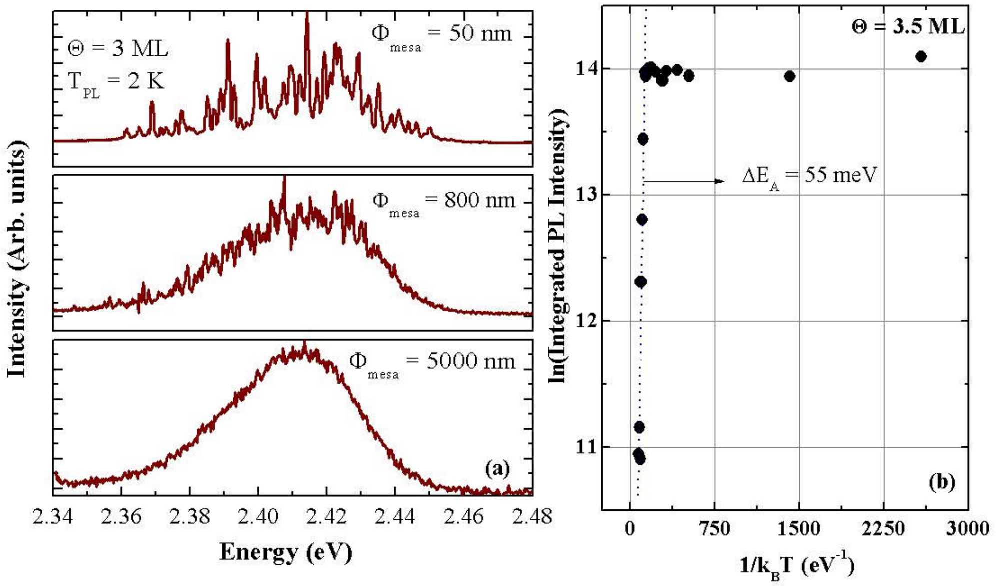

Fig. 5.7: (a) μ-PL spectra recorded at 2 K from mesas of different size, Φ_{mesa}, for a sample with Θ = 3.0 ML (b) Temperature-dependence of the integrated-PL-intensity of a sample with Θ = 3.5 ML. The dotted line is a linear fit to the exponentially-decaying part of the plot.

In angle resolved polarized-PL-spectroscopy [Kiessling2006], π^+ and π^- -polarized PL emission are recorded, while rotating the sample about an axis parallel to the k-vector of the exciting laser beam (the growth axis, for this work). The degree of linear polarization (DLP) is then plotted as a function of the rotation angle.

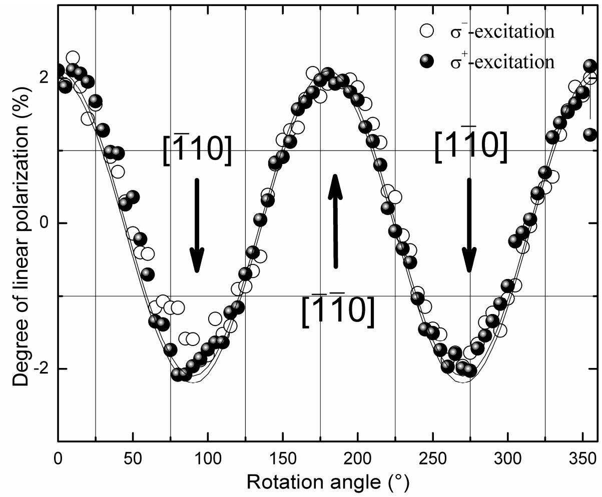

Fig. 5.8 Crystallographic-direction dependence of the PL-degree-of-linear-polarization, corresponding to a QD-sample with Θ = 2 ML (for both right and left circularly polarized excitation), revealing the anisotropic shape of the QDs.

Orienting the sample initially along a known crystallographic direction, the rotation angle can be related to the different in-plane crystallographic axes. Fig. 5.8 shows a typical plot for both σ^+ and σ^- excitation, corresponding to Θ = 2.5 ML. It is observed that the DLP attains a maximum value of 2% along the [110] directions. This implies that the long axes of a majority of the QDs are oriented along one of the <110> axes. However, whether it is parallel or perpendicular to the [110] axis, is not directly evident from this measurement.

The composition of several CdSe QD-layers of the series with varying Θ was investigated by resonant Raman spectroscopy (RRS) (see section 3.6(b)). In Fig. 5.9, the observed ZnCdSe LO phonon frequencies are plotted versus Θ. An increasing Cd content of the QD-layer manifests in a red-shift of the LO phonon frequency, from the value corresponding to pure ZnSe to that of pure CdSe. In contrast to bulk crystals however, a competing blueshift due to lattice-misfit-induced compressive strain has to be taken into account, in case of the QD-layers studied here. For this purpose, the LO phonon frequencies corresponding to a pseudomorphic ZnSe layer and a reference, biaxially strained, ZnCdSe QW sample, containing 33% Cd (determined by XRI), are also shown in Fig. 5.9. By comparison with the aforesaid reference values, the Cd concentration was deduced to reach up to 70% for Θ = 4 ML.

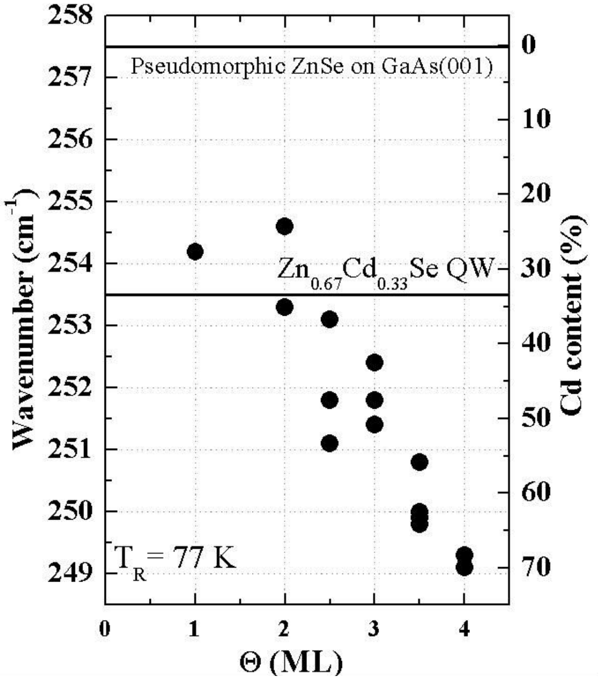

Fig. 5.9: LO phonon frequencies and calculated Cd % of the QD-layers, as functions of the CdSe coverage, Θ

For Θ = 2 ML, the composition of the QD-layer was also estimated by mapping the c-parameter-variation in the corresponding HRTEM image (Fig. 5.4). The color-coded map is shown in Fig. 5.10 (a). Formation of a CdZnSe QW, with local Cd-rich inclusions is explicitly demonstrated by this map. The Cd distribution, measured through the middle of the 7-nm-wide inclusion, shown in Fig. 5.10 (a), is presented in Fig. 5.10 (b). The abscissa of the plot is given by the position along the growth direction (z-axis). The Cd concentration peaks at 70 % and falls to below 10 % within a span of 1.2 nm. This outcome is in variance to that indicated by RRS, according to which, for Θ = 2 ML, the Cd-content of the QD layer is ~ 35 % (Fig. 5.9). The discrepancy might be due to the fact that both RRS and c-parameter analysis have their own limitations in determining the composition of QDs. The value deduced by the former technique represents only an average Cd-content of the QD-layer. Depending on the actual size and composition of the QDs, the wave function of the confined exciton spreads out to different extents within the surrounding ZnSe barrier. Therefore, in resonance with the excitonic transition, RRS would average the measured Cd-content of the QDs.

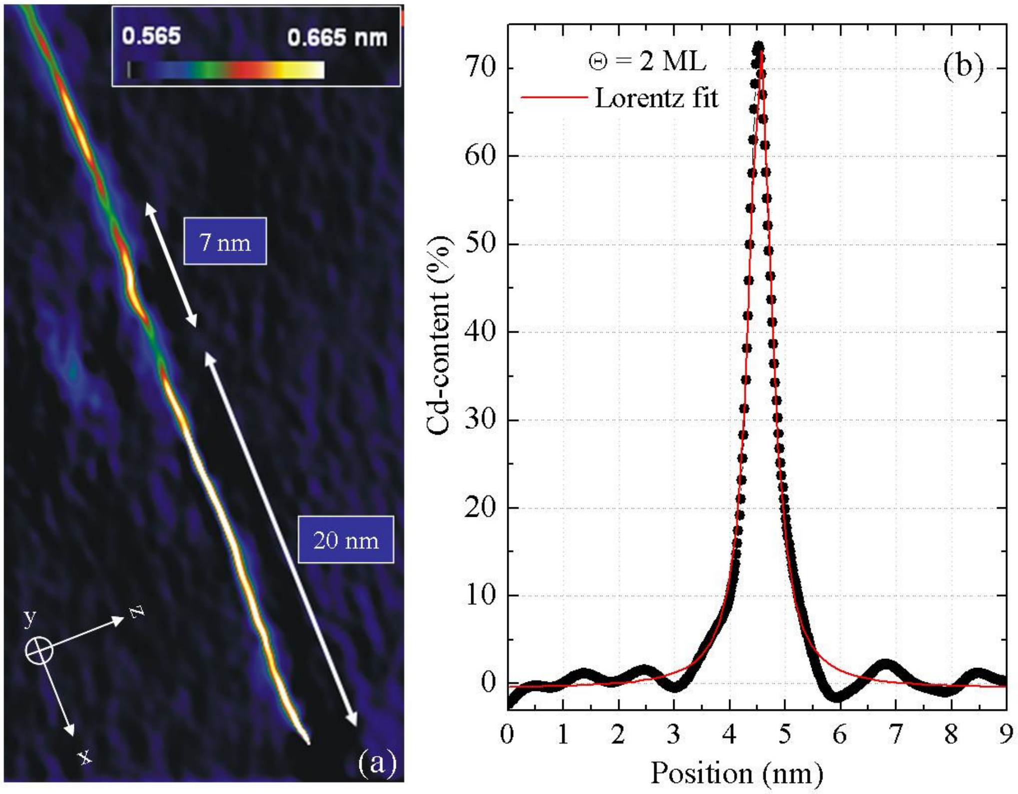

Fig. 5.10: (a) Color-coded map of c-parameter variation, corresponding to the HRTEM image of the sample with Θ = 2 ML (Fig. 5.4). (b) Variation of Cd-content through the middle of the 7-nm-wide QD.

Composition analysis based on the variation of the c-parameter in HRTEM on the other hand, is limited by the fact that sample preparation affects the measured lattice-parameter in complicated ways. The volume over which the c-parameter is averaged is assumed to contain only one QD (Cd-rich inclusion). However, depending on the thinning of the sample (in the y-direction) this volume might contain more or less than one QD and thereby over- or underestimate the Cd-content. Secondly, the ambiguity in the actual strain status of the QD, i.e. whether it is hydrostatically (in case of no strain-relaxation due to island formation), biaxially (in case of strain relaxation due to island formation), or uniaxially (due to strain relaxation by island formation and additional thinning of the sample in the y-direction) strained, would also result in discrepancies.

5.4 *Mechanism of QD-formation and the nature of CdSe/ZnSe(001) epitaxy*

Despite a lattice misfit comparable to the prototypical InAs/GaAs(001) system, the CdSe/ZnSe(001) system evidently does not undergo island formation in the classical

Stranski-Krastanow growth mode, at least when conventional MBE growth is performed. Instead, certain features, which might be assigned to roughness of a 2D layer, act as QDs, after overgrowth with ZnSe. The purpose of this section is to analyze the formation of these features, and discuss certain aspects of CdSe/ZnSe(001) heteroepitaxy, based on the characterizations performed in this work and some previous literature reports.

Fig. 5.2 demonstrates that RHEED SSI oscillations, characteristic of layer-by-layer growth (also refer to Fig. 3.6), are not seen for CdSe deposition at T_G = 300 °C. On the other hand, damped but clear oscillations are evident for $T_G \leq 235$ °C. Similar results have been observed before by Rabe [Rabe98A] and Kratzert [Kratzert02]. In the conventional understanding of epitaxial growth, disappearance of RHEED SSI oscillations with increase in T_G would be interpreted as a transition from the layer-by-layer- to the step-flow growth mode (refer to section 3.2). However, in case of CdSe/ZnSe(001) MBE, the disappearance of RHEED oscillations might rather be assigned to *a transition from layer-by-layer to multilayer growth mode.* This is justified based on the following arguments and observations:

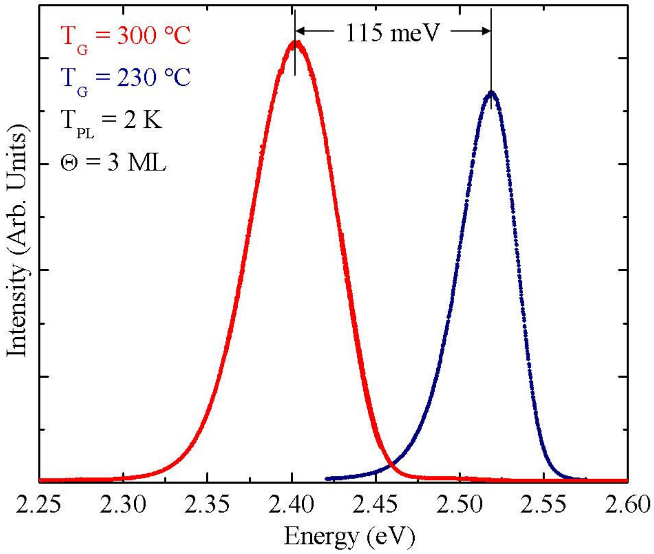

Fig. 5.11: PL spectra recorded at 2 K from 3-ML-CdSe embedded layers grown at T_G = 300 °C (in red) and 230 °C (in blue).

For commercially-available, nominally-singular, GaAs (001) substrates (used in this work), the misorientation angle is < 0.1°. This implies that typical terrace widths are ~ 150 nm. For step-flow growth to take place adatoms would then be required to migrate on length scales of at least 75 nm (from the middle of a step to its edges, assuming absence of ES barrier). In GaAs(001) homoepitaxy, a transition from layer-by-layer- to step-flow growth mode occurs at $T_G \approx 600$ °C [Shitara92]. On a GaAs(001) surface, the diffusion length (refer to Eqn. 2.19) of Ga adatoms at T_G = 580 °C, has been estimated to be $x_{rms} \approx 1$ μm [Koshiba94]. At T_G = 300 °C, it is easy to estimate that x_{rms} drops to a value ~10 nm. In the absence of required surface diffusion data for CdSe/ZnSe(001) epitaxy, if it is even assumed that the x_{rms} values of

Cd adatoms are comparable to those of Ga adatoms (an overestimation, since the adsorption residence time τ_a for group-II adatoms at 300 °C is less than that of Ga adatoms at 580 °C), CdSe heteroepitaxy is not expected to proceed in the step-flow mode for T_G = 300 °C.

In addition to the above argument, Fig. 5.11 reveals that CdSe/ZnSe(001) MBE at T_G = 300 °C leads to formation of rougher QWs, compared to those grown at T_G = 230 °C (where RHEED SSI oscillations could be recorded). In the Figure, PL spectra recorded from two 3-ML-thick CdSe layers, grown and capped at T_G = 300 and 230 °C, are compared. The spectrum corresponding to T_G = 300°C is redshifted by 115 meV, compared to that for T_G = 230 °C. This might not be attributed to enhanced intermixing or desorption, with increasing T_G, since both phenomena are expected to blueshift the PL-spectrum. Therefore, the PL-redshift unambiguously demonstrates formation of roughness-induced QDs, for higher T_G values. This strongly indicates to a transition from layer-by-layer- to multilayer growth, with increasing T_G. In other words, the appearance of RHEED SSI oscillations for $T_G \leq 235$ °C is related to the (partial) recovery of the layer-by-layer growth mode.

In absence of additional stabilizing effects, it is not surprising that for low growth temperatures (T_G = 300 °C), epitaxy proceeds in the multilayer growth mode and corrugated 2D surfaces are formed (see the examples in section 2.3, in the context of kinetic mounding (Fig. 2.9)). Interestingly however, the surface roughness in not completely random, as would be expected in absence of intralayer adatom surface-diffusion. Instead, tiny and significantly regular mounds, weakly oriented along the [110] direction, are observed (Fig. 5.3). In analogy to the cases of Pt/Pt (111), GaAs(001) and Ge(001) homoepitaxy (section 2.3, Fig. 2.9), and also Fe/MgO(001) heteroepitaxy [Thürmer95], the formation of fairly regular features, instead of completely random roughness, might be attributed to the presence of step-edge barriers (ES barriers) (refer to Fig.2.8). Provided the ES barrier hinders down-climb of adatoms, the 2D clusters formed in the sub-ML deposition regime would grow vertically by subsequent accumulation of adatoms impinging directly onto them. The fact that the mounds are omnipresent on the CdSe(001) surface (Fig. 5.3) and that the measured QD-density is ~ 10^{12} cm^{-2} (which requires the QDs to abut each other even when they are 10-nm in lateral dimensions) strongly suggests that the mounds of the uncapped surface correspond to the QDs of the capped samples. The inference is substantiated by the fact that the mounds are observed to be elongated in the [110] direction, which is possibly correlated to the shape anisotropy of the QDs, detected by angle-resolved polarized-PL spectroscopy (Fig. 5.8). However, certain material-redistribution during capping with ZnSe does possibly also take place.

Finally, it is imperative to explore how layer by layer growth of CdSe on ZnSe(001) is recovered by *lowering* T_G to values (230-170 °C) below those at which multilayer growth occurs (300 °C). With decreasing T_G, intralayer surface diffusion of adatoms becomes increasingly sluggish. Concomitantly, during the early (sub-ML) stages of deposition, 2D clusters nucleate in larger areal densities and tend to be smaller in size, and more irregular in shape. While at sufficiently high values of T_G, fast surface diffusion of adatoms enables 2D clusters to assume their equilibrium shapes, at low growth temperatures, the edges of the 2D clusters consist of several kink sites, as shown in Fig. 5.12 (compare with fig 2.8). At these kink sites, the ES barrier is broken-down/weakened, whereby down-climb of adatoms is re-established. This leads to the recovery of layer-by-layer growth at very low growth temperatures, despite suppressed intralayer surface diffusion. The phenomenon, known as the *re-entrant layer-by-layer growth*, has been observed previously in a homoepitaxial growth of Pt (111) [Kunkel90], Ag(111) [Stoldt00], GaAs (111)A [Steans99], and GaAs (001) [Shen98].

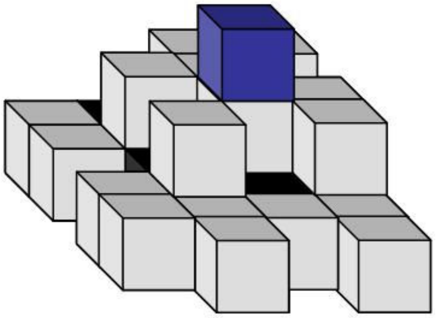

Fig. 5.12: Kink sites at the periphery of an irregularly shaped 2D clusters (shown in black).

It is worth noting here that presence of "dendritic" 2D clusters, with a high density of kinks along their peripheries, as known to nucleate in low temperature epitaxy of metals [Hwang91, Hwang96], is not absolutely necessary for the re-establishment of down-climb of adatoms. Merely due to the reduced size of the 2D clusters, the probability that adatoms impinge directly on the edges of the islands would increase and thereby, down-climb would be enhanced.

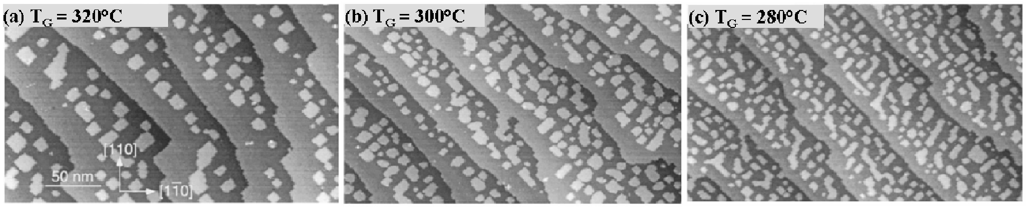

Fig. 5.13: STM images of 2D clusters, nucleated after deposition of 0.5 ML CdTe on a 50 nm-thick CdTe/$Cd_{0.96}Zn_{0.04}Se(001)$ layer , at T_G = (a) 320 °C, (b) 300 °C, (c) 280 °C. Adopted from [Martrou00]

Unfortunately, the nucleation and growth phenomena in CdSe/ZnSe(001) have not been studied adequately, which makes the argument presented above partly speculative. However, the morphology and areal density of 2D clusters, formed during the initial growth-stages of a similar heterosystem, CdTe/$Cd_{0.96}Zn_{0.04}Te(001)$, have been studied by Martrou et al. [Martrou00, Martrou99]. Fig. 5.13 (a), (b), and (c) show the 2D islands nucleated on the surface of a 50-nm-thick CdTe layer, when additional 0.5 ML CdTe is grown at different T_G. It is evident that indeed with reducing T_G, the size (areal density) of the 2D clusters shrinks (grows) and 2D clusters of more irregular shapes are formed. A similar behavior might be expected for CdSe epitaxy, performed at comparable values of T_G.

Summary

In summary, the results presented above clearly demonstrated that QDs formed in CdSe/ZnSe(001) MBE at T_G = 300 °C are essentially Cd-rich inclusions within a ternary CdZnSe QW. Such inclusions are formed even for very low values of Θ. Their areal density, Cd-content, and possibly also the lateral dimensions increase with increasing CdSe coverage, which leads to a monotonic redshift of PL-peak positions. The areal density of such QDs increases to up to 10^{12} cm^{-2} for $\Theta = 3$ ML. The topography of the uncapped CdSe-surface reveals a rough surface, consisting of nearly merged tiny mounds, elongated along the [110] direction. The QDs, formed after capping with ZnSe, are most likely related to these mounds.

As also demonstrated, in CdSe/ZnSe(001) heteroepitaxy, the layer-by-layer growth mode is recovered at temperatures below the T_G-window for multilayer growth. This re-entrant behavior is possibly related to the breakdown/suppression of ES barrier.

Formation of CdSe/ZnSe(001) QDs by low temperature epitaxy and in-situ annealing

6

In this chapter, the formation and properties of CdSe/ZnSe(001) QDs by a technique combining MBE growth of a CdSe layer at a low growth temperature of T_G = 230 °C and subsequent in-situ annealing at T_A = 280-340 °C, is presented. The approach adopted here is similar to that developed by Rabe et al. [Rabe98]. The main motivation of this work was to investigate the fundamental mechanism underlying the formation of QDs by this technique and thereby obtain control over the QD-properties. In this chapter, first, the properties of the QDs are detailed and compared to those grown by conventional MBE at T_G = 300 °C. This is followed by an analysis of the QD-formation mechanism and a discussion on how the QD-areal density might be controlled by this technique.

6.1 *The "low temperature epitaxy and in-situ annealing" technique and sample fabrication*

In this technique, after growth of the ZnSe buffer layer (~ 50 nm), the sample was cooled down under Se flux to T_G = 230 °C. Subsequently, a CdSe *layer* was grown at T_G, with a Se:Cd flux ratio of 20:1 and at a rate of 0.071 ML s^{-1}, as mentioned before in sections 5.1 and 5.2. Immediately after CdSe deposition, the sample was heated up to T_A = 280-310

°C and annealed for t_A = 15-20 mins. Both temperature-ramp-up and annealing were performed under Se-flux. During this annealing step (within the first 2-3 mins) the growth-front evolved from a flat surface to an ensemble of 3D islands. All samples, except those intended for AFM imaging, were capped with 35-50 nm of ZnSe.

6.2 *Formation and properties of QDs*

Figure 6.1 (a) and (b) show the RHEED images corresponding to the surface of a CdSe layer after growth at T_G and after subsequent annealing at T_A = 310 °C, respectively. The CdSe coverage of the sample is Θ = 3.3 ML. The streaky RHEED of Fig. 6.1 (a) demonstrates that the CdSe deposit forms a quasi-2D layer. On the other hand, after temperature ramp up to T_A and annealing (for t_A = 20 mins), a weakly spotty pattern develops, as illustrated by the image of Fig. 6.1 (b). This suggests formation of 3D features on the surface (refer to Fig. 3.4 (d)). The spotty pattern appears within 2-3 mins of annealing, and persists thereafter. A completely streaky pattern is recovered during subsequent capping, after deposition of ~ 5 nm of ZnSe.

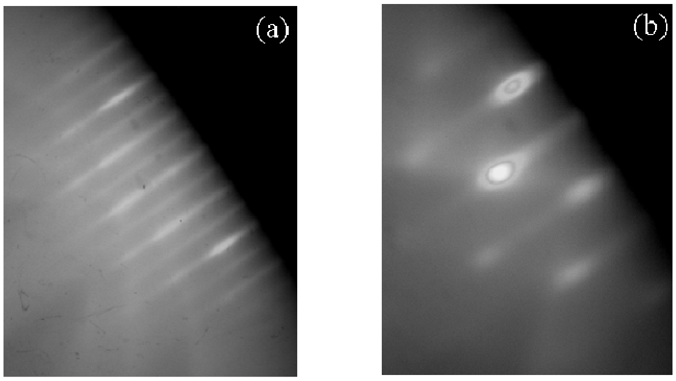

Fig. 6.1: RHEED images corresponding to the surface of a 3.3-ML-thick CdSe layer (a) after growth at T_G = 230 °C and (b) after subsequent in-situ annealing (under Se flux) at T_A = 310 °C, for t_A = 20 mins.

Island-formation by this technique is demonstrated in the AFM images shown in Fig 6.2. Before annealing, the as-grown CdSe surface (Θ =3 ML) shows the typical ridges, discussed in detail before in sections 4.2 and 5.2 (see Figs. 4.1, 4.2 and 5.3(a)). On the other hand, the surface morphology of the annealed (T_A = 310 °C) sample with similar CdSe coverage, shows distinct 3D islands on top of the mounds (Fig. 6.2 (b) and (c)). The islands are ~ 2 nm high, ~ 20 nm in diameter, and with an areal density of 2-5x10^{10} cm^{-2}. From the dimensions and the areal density of the islands, it is estimated that material equivalent to ~ 0.3 ML CdSe is consumed in the islands.

Fig. 6.3 shows the PL spectra recorded from a series of samples, wherein the annealing temperature was varied between T_A = 280- 340 °C, for a particular value of Θ (= 3.3 ML). In the same Figure, the spectrum corresponding to a 3.3-ML-CdSe layer, grown and immediately capped at T_G = 230 °C, is also shown. It is evident that in-situ annealing at all values within the investigated range of T_A leads to a redshift of the PL emission, compared to that of the unannealed sample (grown and capped at T_G). The PL-redshift can be explained only by a reduction of the quantum confinement energy, due to formation of QDs. Since both formation of 3D islands and PL-red-shift are consequences of the in-situ annealing step, it might be inferred that the QDs of the capped samples are correlated to the islands of the uncapped samples. Furthermore, similar PL-redshifts for all values of T_A indicate that, once formed, the islands are stable against Cd-desorption, Cd-Zn intermixing, or Ostwald ripening.

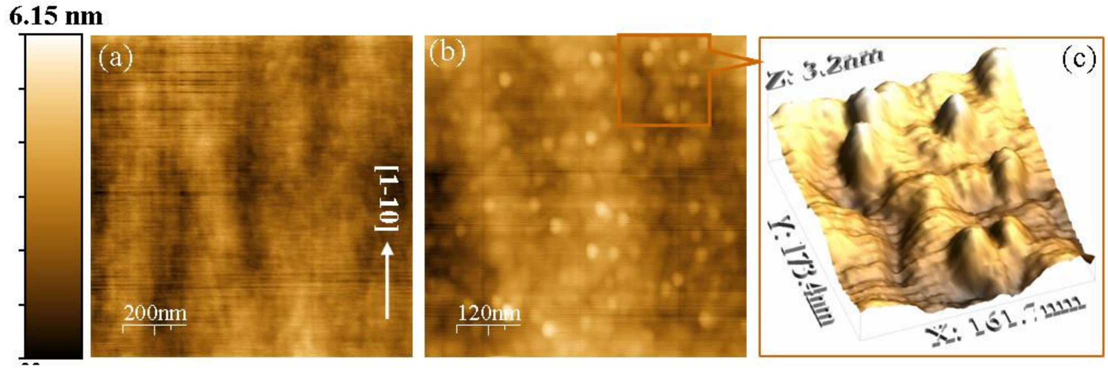

Fig. 6.2: AFM image of an uncapped 3 ML-CdSe surface (a) after growth at T_G = 230 °C and after subsequent in-situ annealing at T_A = 310 °C. (c) An enlarged section of the image in 3D view.

To investigate systematically the properties of the QDs, a series of capped samples, with CdSe coverage varying between Θ = 2-4.5 ML, were prepared. For the whole series, T_A was chosen to be 310 °C.

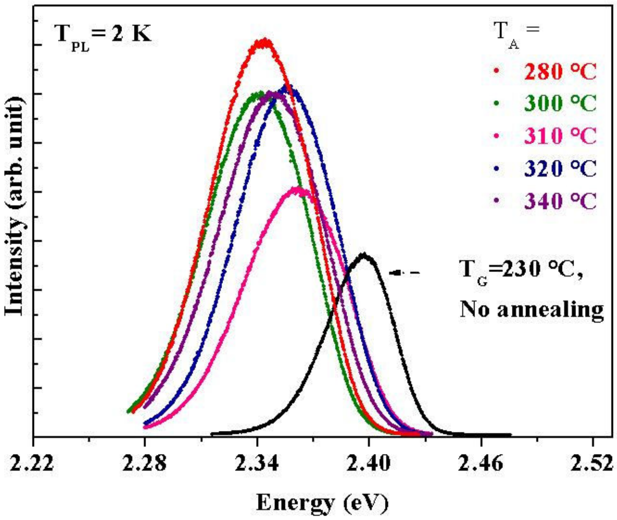

Fig. 6.3: PL spectra of a set of samples (Θ = 3.3 ML) annealed at different T_A, along with that of a sample grown and immediately capped at T_G = 230 °C.

In Fig. 6.4, (004) x-ray diffractograms of a few samples are shown. Despite island formation, a good agreement is evident between the measured and the simulated profiles, up to Θ = 3.5 ML. The calculated values of Θ also agree well to those targeted. This substantiates the fact that no significant Cd-desorption takes place during annealing, even at T_A = 340 °C. Beyond Θ = 3.5 ML, the recorded pattern begins to deviate from the simulated one, and the fringes tend to smear out increasingly. This evolution is attributed to the generation of stacking faults [Passow00].

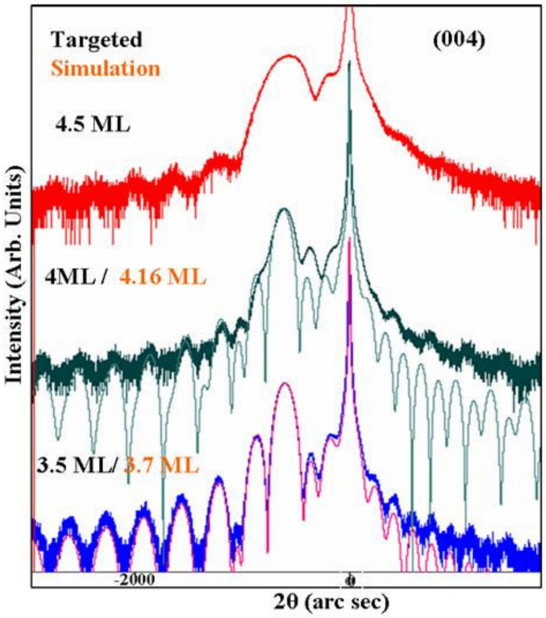

Fig. 6.4: (004) X-ray diffractograms of a set of samples with different CdSe coverages, along with the simulated profiles. Values targeted and used for simulation are shown in black and orange, respectively.

Fig. 6.5 shows the PL spectra recorded at 2 K, for the whole series of samples with varying Θ. Despite the long growth interruptions during annealing, the PL at 2 K is bright. For Θ = 4 ML, the PL-intensity drops significantly. This is attributed to plastic relaxation of the QD-layer by formation of stacking faults, as indicated previously by the x-ray diffractograms (Fig. 6.4).

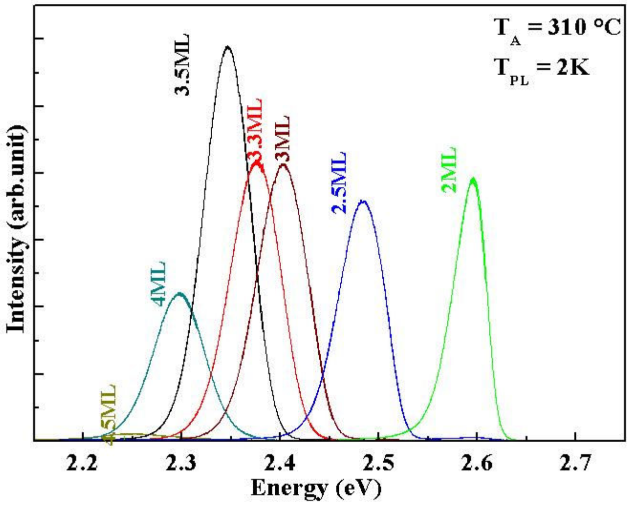

Fig. 6.5: PL spectra, at 2 K, of a series of samples, with different Θ

While for $\Theta \leq$ 2.5 ML, the PL spectra consist of low energy tails, for $\Theta \geq$ 3 ML, the spectra are more symmetric in shape. This suggests that the QD-density increases with increasing Θ, similar to that observed for MBE-grown samples (Fig. 5.5). At 300 K, the PL was observed to weaken by an order of magnitude.

Fig. 6.6 shows the energy positions of the PL spectra recorded at 2 K, as a function of Θ. For comparison, the data for the MBE-grown samples, and the calculated exciton transition energies for *pure* CdSe QWs are also plotted (from Fig. 5.6(a)).

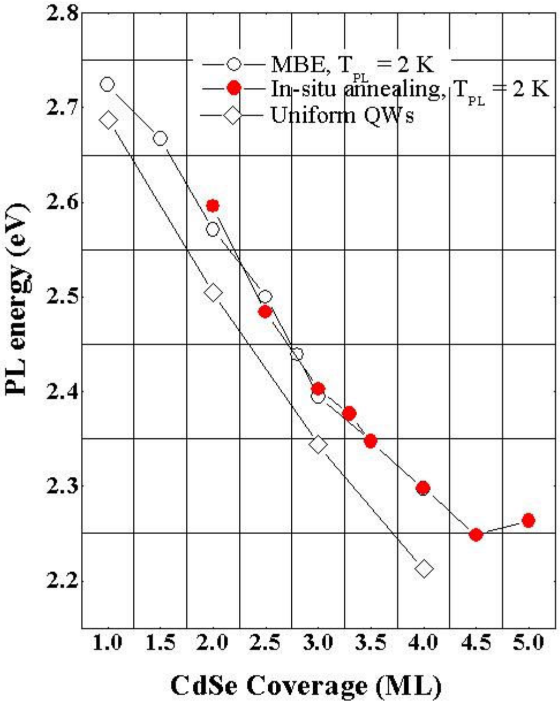

Fig. 6.6: Θ-dependence of the energy-positions of PL spectra, recorded at 2 K. For comparison the data of the MBE-grown samples and the calculated exciton transition energies for *pure* CdSe QWs are also plotted.

Evidently, the PL-redshift with increasing Θ is monotonic, similar to the case of conventional MBE growth. Thus, it might be inferred that also in this case QD formation in not associated with any distinct transition in exciton ground state energies, and therefore, also not with any critical coverage for elastic relaxation of misfit strain. The blue-shift of the experimental data points relative to the calculated exciton transition energies for *pure* CdSe QWs indicate that Zn-Cd intermixing of the QD-layer is prevalent.

What is more striking in Fig. 6.6 is the fact that not only the monotonic redshift trend, but also the values of the PL-energies, obtained by “low temperature epitaxy and in-situ annealing”, are the same as those of samples grown by conventional MBE, for almost all values of Θ. This suggests that by both techniques, the composition and the dimension of the QDs, in the confining direction (i.e., their heights), are identical. Since distinct 3D islands are formed by “low temperature epitaxy and in-situ annealing”, this similarity necessarily implies that the 3D islands, formed after in-situ annealing, are modified during subsequent capping with ZnSe. The modification of the islands is possibly driven by segregation of Cd and Zn-alloying of islands during capping, as observed also in previous investigations [Peranio00, Passow01, Kruse07]. The effects might either truncate or compositionally compensate for the larger size of the islands. Explained in other words, the latter consequence implies that a reduction in the quantization energy due to larger size of the QDs is exactly compensated by an enhanced Cd-Zn alloying process, as known for other heterosystems [Larsson06].

RRS was also used in this case to probe the composition of a few QD-layers. The Θ-dependence of the Cd-content of the QD-layers is shown in Fig. 6.7, along with the corresponding plot for MBE grown samples (from Fig.5.9).

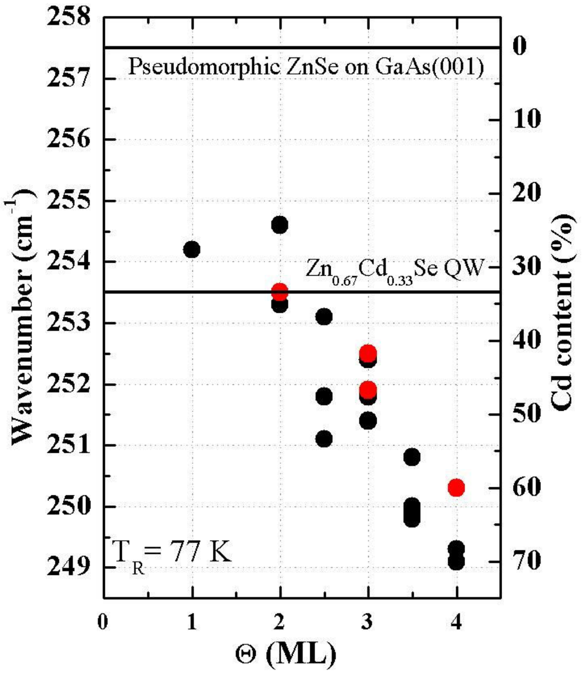

Fig. 6.7: LO phonon frequencies and calculated Cd-content-values of the QD-layers, as functions of the CdSe coverage, Θ for a few samples grown by low temperature annealing and in-situ annealing (red) and conventional MBE (black)

It is seen that the average Cd content of the investigated QD-layers agrees well to that of the corresponding samples grown by conventional MBE. This fact strengthens the requirement that the dimension of the QDs in the growth direction (the confining direction) formed by both techniques are comparable. Otherwise, the Θ-dependence of the PL-redshifts would not show the observed parallelism.

Fig. 6.8 (a) shows the cross-sectional TEM image of a QD-layer with Θ = 3.8 ML. The QD-layer, similar to the case of conventional MBE growth, appears to be a ternary QW, with Cd-rich inclusions. The observation qualitatively substantiates collapse of islands, due to segregation of Cd and concomitant Zn-alloying during capping. A color-coded map of the c-parameter variation, calculated for the region marked by the box in Fig. 6.8 (a), is shown in Fig. 6.8 (b). The core of the measured region appears to consist of pure CdSe, which is ~ 1.6 times the amount of Cd deduced by RRS, for a QD-layer of comparable CdSe coverage (60 % Cd, for Θ = 4 ML). The possible reasons for this discrepancy have already been discussed in section 5.3 (refer to Fig. 5.9 and 5.10).

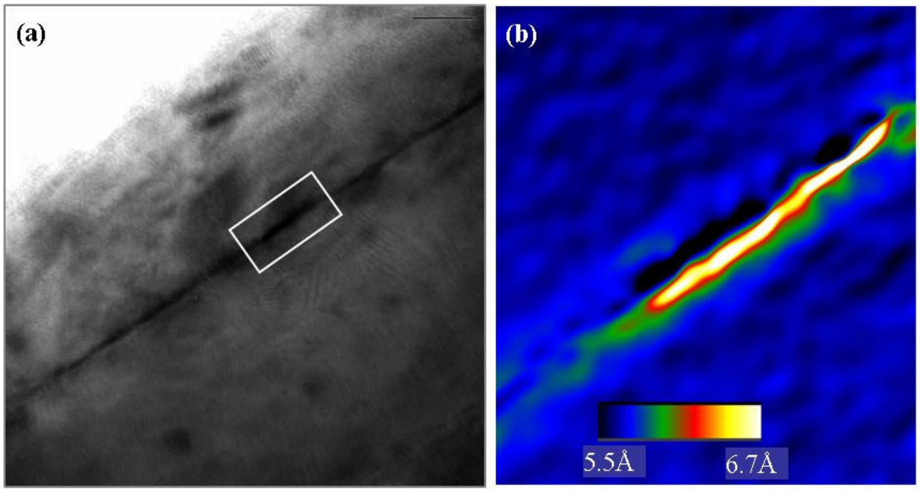

Fig. 6.8: (a) Cross sectional HRTEM image (bright field) of a capped sample with Θ = 3.8 ML. (b) Color-coded map depicting the c-parameter variation across the QD-layer, in the region marked by the white box in (a).

The areal density of QDs was probed by μ-PL measurement. Fig. 6.9 shows the μ-PL spectra of a sample with Θ = 3.5 ML (refer to Fig. 6.5), recorded at 2 K, from mesas of different sizes, Φ_{mesa}. Emission lines due to individual QDs are evident, even for Φ_{mesa} = 350 nm.

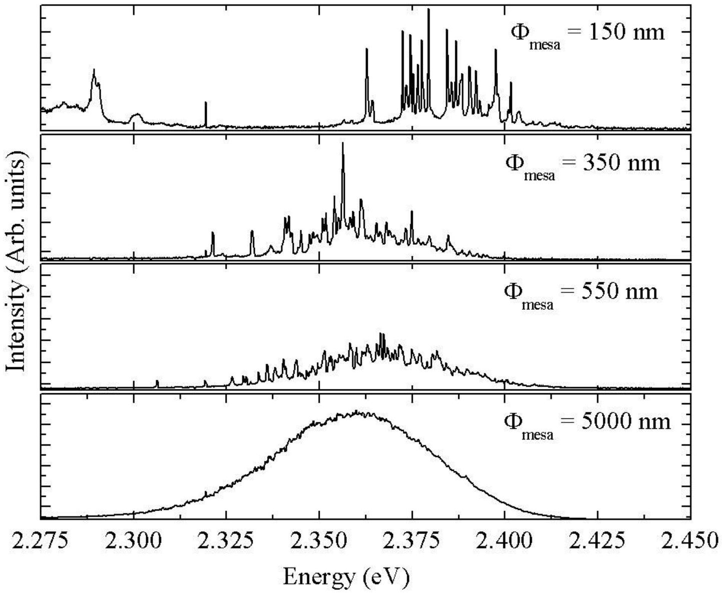

Fig. 6.9: μ-PL spectra (at 2) K from mesas of different size, Φ_{mesa}, for a sample with Θ = 3.5 ML

The areal density of QDs, estimated by counting the emission lines of several Φ_{mesa} = 150 nm-mesas, is ~ 2-5 $\times 10^{10}$ cm^{-2}. The value is in good agreement with the areal density of islands, observed in AFM imaging. This corroborates to the previous inference that the islands formed after annealing (observed in AFM (Fig. 6.2 (b)) represent the QDs formed after subsequent capping (which localize excitons three-dimensionally). The μ-PL result further establishes that albeit the size and composition of the QDs formed in "low temperature epitaxy and in-situ annealing" are similar to those resulting from conventional MBE, the former technique allows reduction of the QD-areal-density by more than an order of magnitude.

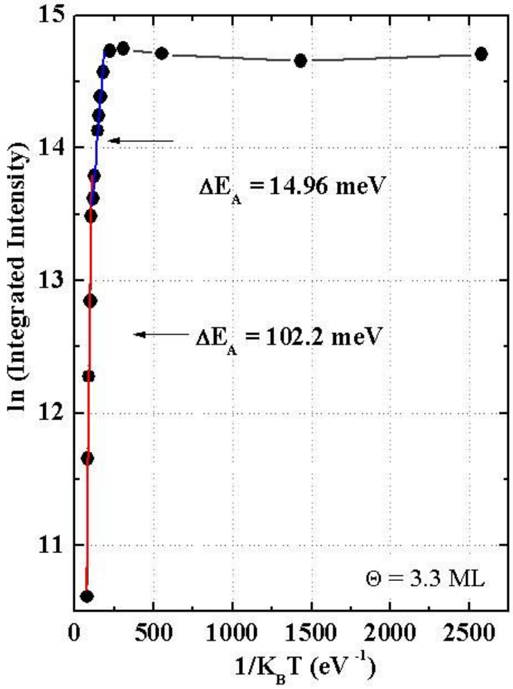

Fig. 6.10: ln (integrated PL intensity) versus ($1/k_BT$) plot for a sample, with Θ = 3.5 ML CdSe. The solid lines (blue and red) correspond to the linear fits of the high temperature region of the plot.

The integrated PL intensity of the sample was also measured at different temperatures. The logarithmic plot of intensity versus $(k_BT)^{-1}$ is shown in Fig. 6.10. Two different activation energy values, i.e. ΔE_A = 14.96 and 102.2 meV, were deduced from the plot. While E_A = 14.96 meV may be attributed to redistribution of carriers within the QD-ensemble, ΔE_A = 102.2 meV is assigned to thermal emission of excitons out of the QDs and non-radiative recombination at surface or defect states. The value is almost twice as large as that measured for a Θ = 3.5 ML CdSe layer grown by conventional MBE at T_G = 300 °C. The higher value of ΔE_A measured here is attributed to a stronger lateral confinement within the QDs formed by "low temperature epitaxy and in-situ annealing". A stronger lateral confinement results possibly due to the reduced areal density of QDs, whereby carrier escape by tunneling is suppressed.

The QDs fabricated by low temperature epitaxy and in-situ annealing were also found to be anisotropic in shape, similar to those formed in conventional MBE growth. The long axes of the QDs in this case are similarly oriented along one of the <110> directions. The degree of linear polarization was also found to be of comparable value.

6.3 *QD-bilayers realized by "low temperature epitaxy and in-situ annealing"*

In addition to the series of samples, investigated in the previous section, a QD-bilayer sample was prepared. Both QD-layers were fabricated by "low-temperature epitaxy and in-situ annealing”. This implies that the bottom QD-layer went twice through the in-situ annealing step, first without and next with the ZnSe spacer layer atop. In both QD layers, the CdSe coverage was $\Theta = 2$ ML CdSe. The thickness of the ZnSe spacer layer between the CdSe QD-layers was chosen to be $L = 3$ nm.

Fig 6.10 (a) shows the TEM image of the QD-bilayer. A color-coded c-parameter map recorded around the bottom-most arrow of Fig. 6.11 (a) is shown in Fig. 6.11 (b). In both images, the QDs clearly show a positional correlation. The correlation appears to be (nearly) vertical.

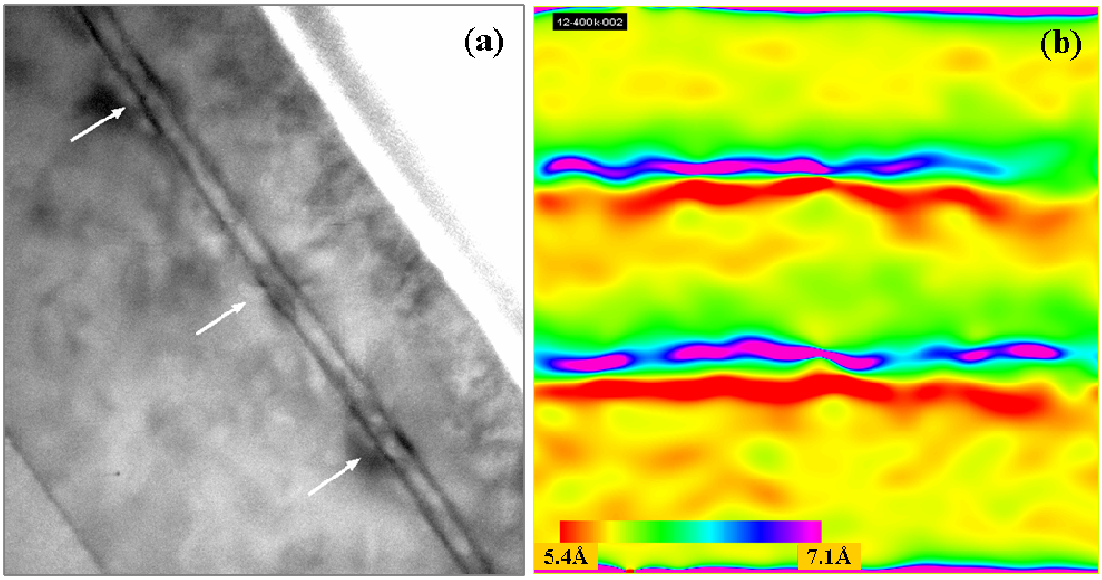

Fig. 6.11: Cross-sectional HRTEM image (bright field) of the QD-bilayer. (b) A color-coded map of c-parameter variation, taken around the rightmost arrow in the HRTEM image.

As discussed in section 2.6, positional correlation is driven by the strain fields around buried QDs. This requires the self-assembled islands to be (partially) strain-relaxed (refer to discussion in the context of Fig. 2.15 in section 2.6). Therefore, the positional correlation of QDs observed in Fig. 6.11 strongly suggests that elastic relaxation of misfit strain occurs by formation of islands, even for CdSe coverages as low as $\Theta = 2$ ML. The observed vertical correlation of QD-positions is explained by the fact that the thickness of the spacer layer (L) is smaller than the QD-in-plane-diameter (d_{QD}), so that $d_{QD}/L > 1$ (see section 2.6).

6.4 *Mechanism of QD formation and control of QD areal density*

The focus of this section is on the mechanism of QD-formation by “low temperature epitaxy and in-situ annealing”. At the outset it is helpful to recall that at the chosen temperature of growth, $T_G = 230$ °C, CdSe/ZnSe(001) heteroepitaxy occurs in (re-entrant) layer-by-layer mode (section 5.4 and Fig. 5.2). As discussed in section 5.4, due to the suppression/breakdown of step edge barriers, adatom down-climb is reestablished for T_G

< ~ 240 °C. However, the recovery of the layer-by-layer growth is only partial. This is indicated by the strong damping of the RHEED SSI oscillations in Fig 5.2 (a)-(c).

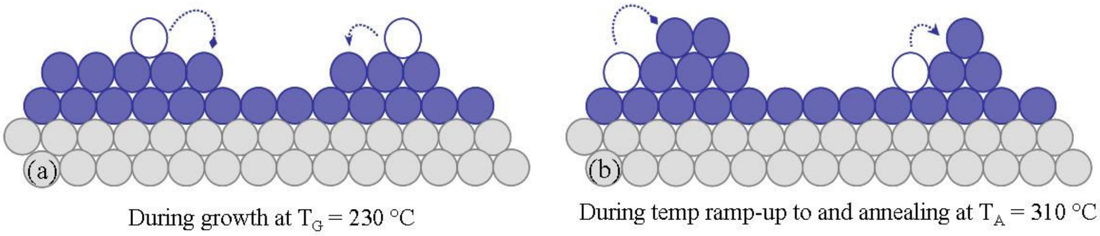

Fig. 6.12: Schematic diagram depicting (a) the down-climb of adatoms during growth at T_G = 230 °C and (b) the reverse up-climb during ramp up and annealing at T_A = 310 °C

In turn, it implies that the surface of the as-grown CdSe layer is not perfectly two-dimensional but consists of a certain concentration of 2D clusters and unincorporated adatoms. At T_G, such unincorporated adatoms atop the 2D clusters predominantly tend to climb down to the penultimate layer, as shown in Fig. 6.12 (a). This fact is substantiated by the existence of the RHEED SSI oscillations.

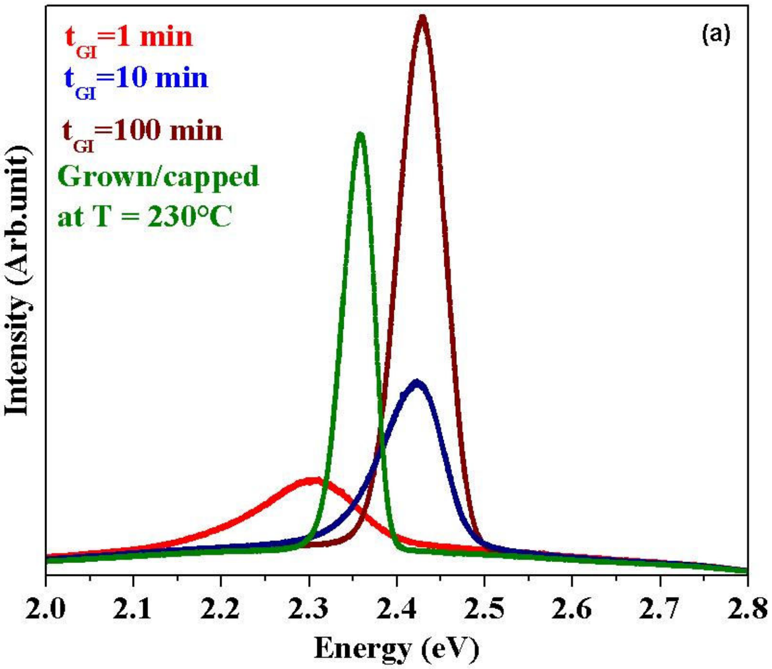

Fig. 6.13: PL spectra for a series of samples with 3.8 ML CdSe, for which GI were introduced at T_G under Se flux for t_G = 1, 10, and 100 min, before ramp-up to and annealing at T_A. Spectrum of a sample with 3.8 ML CdSe, grown and capped at T_G, is also shown.

When immediately after CdSe growth, the temperature of the surface is rapidly ramped up to the annealing temperature T_A, a reverse upward interlayer diffusion ("up-climb") of adatoms is activated. In absence of required diffusion data, assuming the diffusion barrier ($E_d + \Delta E_{ES}$) to be ~ 1.5 eV (comparable to GaAs(001) homoepitaxy), ramp-up to T_A = 310 °C from T_G = 230 °C, implies an enhancement of the up-climb rate by two orders of magnitude. The adatom up-climb might also (in part) be driven/enhanced by a possibility of strain relaxation by formation of islands, as known for SK growth. This leads to a fraction of the adatoms climbing onto the 2D clusters and subsequently, nucleating new 3D islands (Fig. 6.12 (b)). The areal density of QDs is reduced by this technique, compared to conventional MBE, due to the fact that only a fraction of the 2D clusters are sufficiently large to support nucleation of 3D islands by up-climbing adatoms.

Within the purview of the model, it would be expected that, after growth of the CdSe layer, when instead of immediately raising the temperature of the surface to T_A = 310 °C, growth interruptions (GI) are introduced at T_G = 230 °C, the as-grown layer smoothens. The fact that this indeed happens is revealed by the PL spectra shown in Fig. 6.13.

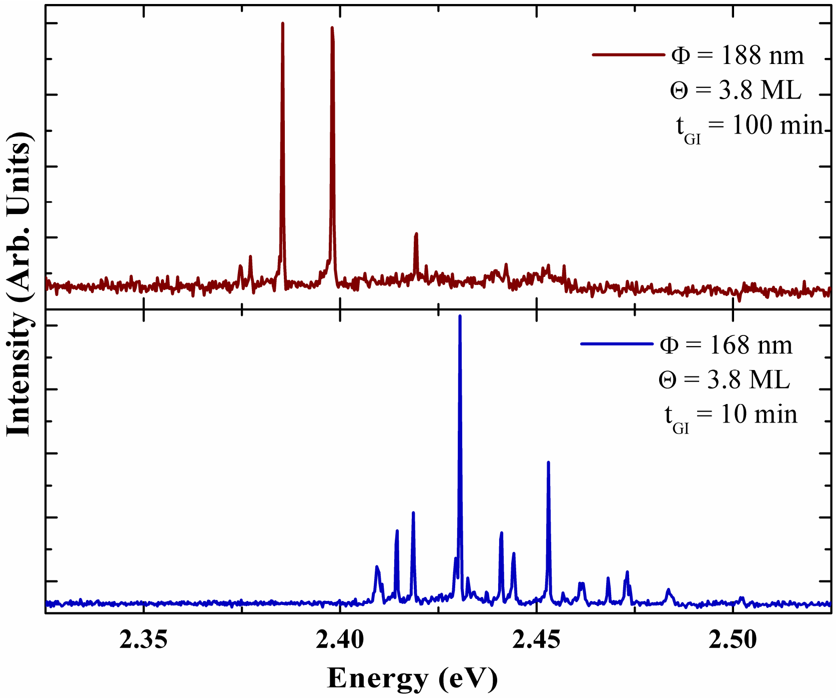

Fig. 6.14: μ-PL spectra, corresponding to the two samples of the series, for which GI were introduced at T_G, before ramp-up to and annealing at T_A.

The spectra belong to a series of samples with 3.8 ML CdSe, for which GI for t_{GI} = 1, 10, and 100 min were introduced at T_G (under Se flux) before temperature ramp-up to T_A = 310 °C. Also shown in the Figure is the PL spectrum of a reference 3.8 ML CdSe layer, grown and immediately capped at T_G. For t_{GI} = 1 min, the PL emission shows a red-shift of about 50meV, and a strong spectral broadening with respect to the reference sample. This behavior is very similar to that observed before for samples without any GI (Fig. 6.3), and therefore suggests a similar formation of 3D islands. For t_{GI} ≥ 10 mins on the other hand, the PL exhibits a blue-shift with respect to the reference sample, with a concomitant narrowing of the spectrum. This blueshift and narrowing of the PL spectra with increasing t_{GI} strongly suggests suppression of islanding, evidently due to loss of mobile adatoms, which would otherwise be available for 3D islanding. Additionally, the fact that for $t_{GI} \geq 10$ mins, the PL shifts to energies beyond the spectrum of the reference sample, indicates that the post-growth mobile adatoms are lost due to their down-climb and subsequent incorporation at the edges of the 2D precursor islands, leading to further smoothening of the as-grown layer.

An even more convincing evidence of suppression of island formation by introduction of GI at T_G is provided by the μ-PL spectra, corresponding to $t_{GI} = 10$ and 100 mins, shown in Fig. 6.14. Clearly, the density of single emission lines (or equivalently that of QDs) is much lower than that seen in Fig. 6.9, corresponding to no GI. The QD areal density for $t_{GI} = 100$ min is as low as 8×10^9 cm^{-2}. This demonstrates that a judicious choice of t_{GI} would allow tuning of the areal density of such QDs.

Summary

From the results presented above it is established that distinct 3D CdSe islands are formed by the technique of "low temperature epitaxy and in-situ annealing". The island-formation is triggered by the enhancement of (thermally activated) adatom up-climb, during the in-situ annealing step, and is characterized by a weak streaky-to-spotty transition in RHEED. The resultant islands are distinctly discernible in AFM images. They are stable against desorption, intermixing or Ostwald ripening, but not against Cd-segregation during capping with ZnSe. While the dimension and composition of the QDs are comparable to their MBE-grown (at $T_G = 300$ °C) counterparts, their areal density is reduced by more than an order of magnitude. This leads to stronger lateral confinement of excitons within the QDs. The QD-areal density can be further tuned by appropriately delaying the in-situ annealing step.

Amorphous selenium mediated self-assembly of CdSe/ZnSe(001) QDs: Single QD-layers and QD-superlattices

7

This chapter deals with another variant of conventional-MBE to induce self-assembly of CdSe/ZnSe(001) QDs. In 2003, Tinjod et al. demonstrated formation of large CdTe/ZnTe(001) QDs by deposition of amorphous tellurium onto an epitaxially strained CdTe layer and its subsequent desorption [Tinjod03]. In this work, the approach has been adopted for the CdSe/ZnSe(001) heterosystem, in parallel to the efforts of the same authors. Similar to the case of the CdTe/ZnTe(001) heterosystem, QD-self-assembly takes place also when an epitaxially strained CdSe layer is capped with amorphous selenium (*a*-Se) and subsequently decapped. In the first part of this chapter, the fabrication technique and the properties of the resultant QDs are discussed. The rest of the chapter deals with fabrication of QD-superlattices, for which the first (seed) QD-layer was grown by this technique and the subsequent ones by MEE.

7.1 *The "a-Se mediated self-assembly" technique and sample fabrication*

Similar to the samples of the previous chapter, here also, the CdSe layer was grown by conventional MBE at T_G = 230 °C, on 45-50 nm thick ZnSe barrier layers. A Se:Cd flux ratio of 20 resulted in a growth rate of 0.05 ML s^{-1}. Following CdSe growth, the sample was cooled down to ~ 45 °C, in approximately 60 mins. Subsequently, Se-flux was offered to the CdSe surface. At 45 °C, the deposited Se formed an amorphous layer (*a*-Se), at a rate of ~ 2 Å s^{-1}. The thickness of the *a*-Se-cap layer was chosen to be d_{cap} = ~ 60 nm. After capping the CdSe surface, the temperature of the sample was ramped-up for desorption of *a*-Se to T_D = 230 °C, within a fixed interval of 15 mins. Desorption of *a*-Se took place much earlier, at a temperature as low as ~ 145 °C. After *a*-Se desorption, CdSe/ZnSe(001) islands were formed. In the temperature interval of 200-230 °C, Se flux was offered once again to the re-exposed CdSe surface (with QDs). This was performed to hinder desorption of Cd. The value of T_D = 230 °C and the ramp-time of 15 mins were chosen based on some preliminary optimization steps, performed to obtain the best morphological attributes of the self-assembled islands [Eschenbach07]. All samples, except those intended for AFM imaging, were subsequently capped with ZnSe layers of thickness 45-50 nm, grown also at 230 °C, by conventional MBE.

7.2 *Formation and properties of QDs*

RHEED images, corresponding to different steps of the process, are shown in Fig. 7.1. The streaky pattern of Fig. 7.1 (a) represents the flat CdSe layer, after growth at T_G = 230 °C, as shown before in Fig. 6.1 (a).

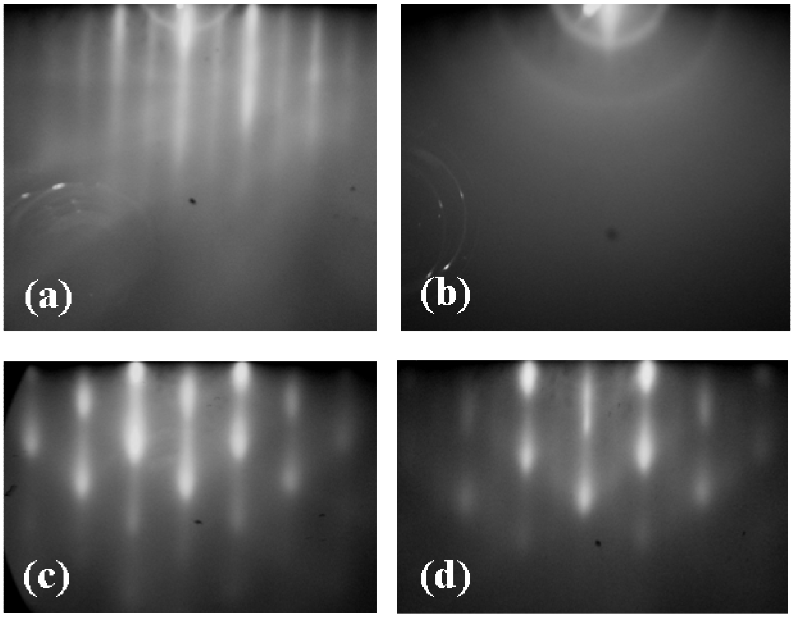

Fig. 7.1:RHEED images recorded (a) after growth of 3 ML CdSe at T_G =230 °C, (b) after subsequent capping with *a*-Se at 45 °C, (c) at an intermediate stage (~ 170 °C) during temperature-ramp up to T_D and (d) at T_D = 230 °C, under Se flux. See text for details.

After the CdSe surface was capped with *a*-Se, the streaky pattern disappeared and a diffuse image, as shown in Fig. 7.1(b), emerged. On ramping up the temperature for *a*-Se desorption, at ~ 145 °C, the distinctly spotty pattern of Fig. 7.1 (c) appeared, revealing the formation of 3D nanostructures. This spotty pattern existed thereafter. When Se-flux was offered to the re-exposed CdSe surface above 200 °C, a weak (2x1) reconstruction could also be seen, as shown in Fig. 7.1 (d). Surprisingly, the spotty patterns of Fig. 7.1 (c) and (d) were observed also for CdSe coverages down to $\Theta = 1$ ML.

Fig. 7.2 shows an AFM image of an island-layer, corresponding to CdSe coverage of $\Theta = 3$ ML. Well defined 3D islands are clearly seen in the Figure. The islands are between 2-4 nm high and 35-50 nm in base diameter. The length (measured along [110]) and width (measured along [1-10]) of a particular island are also shown. The QD-areal density is in the range of $2\text{-}5\times10^{10}$ cm^{-2}.

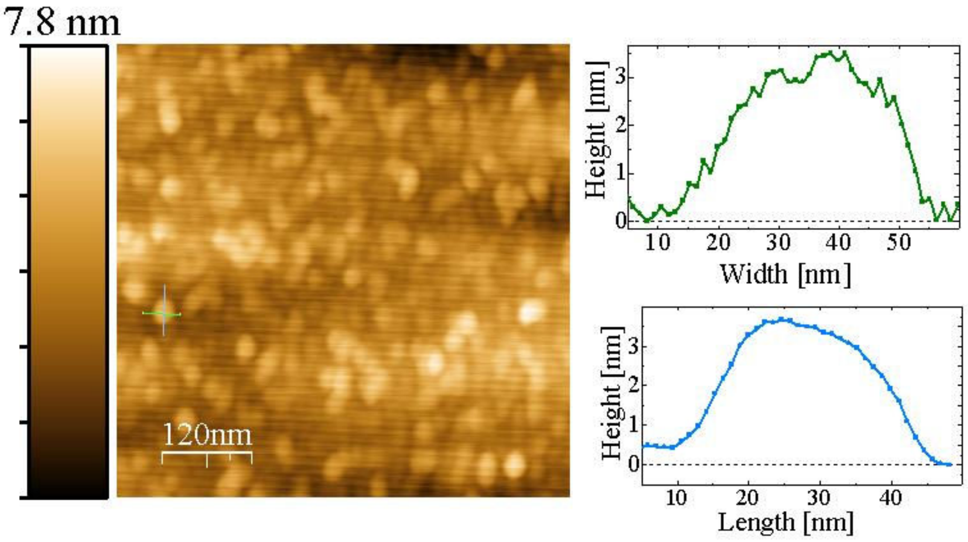

Fig. 7.2: (left) AFM image of an island layer, corresponding to $\Theta = 3$ ML CdSe, $d_{cap} = \sim 60$ nm, T_G and $T_D = 230$ °C. (right) Width (along [1-10] and length (along [110]) of a particular island, marked in the AFM image.

A series of capped samples, with Θ varying from 1-3 ML, were prepared for XRI, PL, and RRS investigations. For the entire series of samples, (004) x-ray diffractograms were recorded, similar to those of "low temperature epitaxy and in-situ annealing" (Fig. 6.4). However, in contrast to the samples grown by the previous techniques, for the series presented here, significantly lower values of CdSe coverage were measured (Θ_{XRI}), in comparison to those targeted ($\Theta_{nominal}$). The $\Theta_{nominal}$ values are based on XRI determination of the CdSe growth rate, as discussed in section 5.2. For the XRI-sample, the thick ZnSe barrier and cap layers, as well as the CdSe separator layer, were grown by MBE at $T_G = 230$ °C. [†] A plot of Θ_{XRI} versus $\Theta_{nominal}$ is shown in Fig. 7.3 (blue data points). The grey dotted line serves as a reference, representing the case of $\Theta_{nominal} = \Theta_{XRI}$. In the inset, $\Delta\Theta = \Theta_{nominal} - \Theta_{XRI}$ is plotted versus $\Theta_{nominal}$. It is seen that $\Delta\Theta$

[†] The calibration sample was grown together with the series of QD-samples

increases linearly with increasing $\Theta_{nominal}$ up to $\Theta_{nominal}$ = 2.6 ML. Beyond 2.6 ML, $\Delta\Theta$ drops quite drastically. The trend is substantiated by the additional data points (in red and green) shown in the plot. The red points correspond to two samples, similar to those of the series, except for the choice of T_D (= 280 °C). The green point belongs to a sample nominally similar to the corresponding sample of the series ($\Theta_{nominal}$ = 3.01 ML). It is worth noting here that a similar mismatch between the nominal and measured CdSe coverages has been observed (independently) by Robin et al. [Robin07]. The authors reported, based on XRI and c-parameter analysis of HRTEM images, $\Delta\Theta = 0.64\pm0.15$ ML (XRI)/0.8±0.2 ML (HRTEM) and 0 (XRI)/0.2±0.2 ML (HRTEM), for $\Theta_{nominal}$ = 2 and 3 ML, respectively. However, the parameters d_{cap}, T_D (= 280 °C), the temperature of *a*-Se deposition (-10 °C), and the ramp-rate (to T_D) are slightly different from those chosen for this work. Furthermore, in [Robin07], the first few monolayers (40-80) of the ZnSe cap layer were grown in ALE mode.

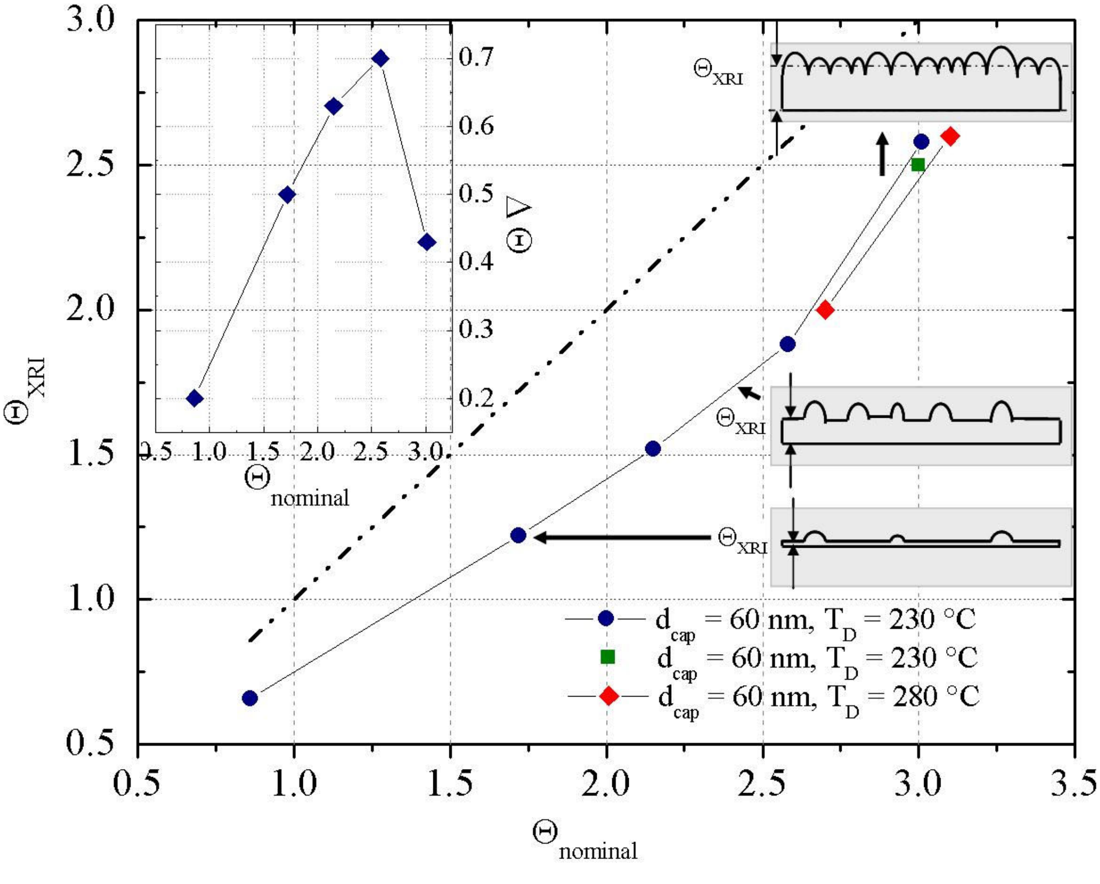

Fig. 7.3: Θ_{XRI} versus $\Theta_{nominal}$ plotted for the series of QD-layers with different CdSe coverages. The inset shows $\Delta\Theta = \Theta_{XRI} - \Theta_{nominal}$ as a function of $\Theta_{nominal}$. The schematic on the right side shows a model to explain the trend of the plot (see text below)

The observed deviation of the measured CdSe coverage from the values targeted might be attributed to two different reasons, or a combination of both. To discuss these reasons, it is helpful to recall at the beginning that a spotty RHEED was observed after *a*-Se desorption, for all values of Θ_{nominal}. Hence, it might be inferred that 3D islands are formed for all CdSe coverages. In the first model, it is postulated that islands formed for coverages up to Θ_{nominal} = 2.6 ML are unstable (similar to kinetic mounds) and Cd segregates away from their apices during capping with ZnSe. The areal density and/or the size of such islands possibly increase(s) with increasing Θ_{nominal} and therefore, Cd-segregation, and in turn, $\Delta\Theta$ increases.

The scenario changes with Θ_{nominal} = 3 ML. Possibly for this coverage (or some intermediate value between 2.6 to 3 ML) a transition from unstable mounds to stable (facetted) islands takes place, as known for self assembly of Ge/Si(001) islands [Vailionis00, Tersoff02] and discussed in section 2.2 (Fig. 2.5 (c) and 2.5 (d)). Due to this transition the islands are stabilized and Cd-segregation is suppressed, resulting in the sudden drop of $\Delta\Theta$.

The second explanation is based on the specifics of the XRI measurement technique. Once again, it is assumed that islands are formed for all CdSe coverages and their areal density and /or size increase(s) with increasing Θ_{nominal}. For $\Theta_{\text{nominal}} \leq 2.6$ ML, the areal density of islands is tentatively low and the amount of CdSe consumed in the islands does not contribute to a coherent phase shift between the x-rays scattered from the cap- and the barrier-ZnSe layers, as mentioned previously in section 3.3 (b) (refer to Fig. 3.9). The coherent contribution to the phase shift comes only from the amount of CdSe distributed as a 2D layer, beneath the 3D islands (Bottom and middle schematic in Fig. 7.3). This explains the non-zero value of $\Delta\Theta$. Although with increasing Θ_{nominal}, both thickness of the 2D CdSe layer and the areal density and/or the size of the islands increase, XRI registers only the former. The increase of $\Delta\Theta$ is then explained by the fact that the rate at which the islands grow in number and/or size is higher than the rate at which the underlying 2D layer grows with increasing Θ_{nominal}. In SK growth of InAs/GaAs(001) islands, it is well known that the wetting layer thickness remains constant at ~ 1.7 ML, irrespective of the InAs coverage. InAs deposited beyond 1.7 ML is consumed completely by the islands, which thereby grow in size. This process is favored due to the fast surface diffusion of In adatoms, which also suppresses nucleation of new islands. Thus, the areal density of islands also remains unchanged with increasing InAs coverage. Here, due to slow diffusion of adatoms and the fact that islands are not nucleated during growth, but rather during a post-growth manipulation of the surface, the thickness of the 2D CdSe layer, as well as, the size and/or areal-density of the islands increases with increasing Θ_{nominal}. However, the fact that $\Delta\Theta$ increases with Θ_{nominal} suggests that once formed, the islands in this case also tend to accumulate more material, similar to SK QDs.

Within the purview of this model, the fall of $\Delta\Theta$ for Θ_{nominal} = 3 ML is also explained by the increase in the areal density of islands. When the ensemble of islands becomes sufficiently dense, it once again contributes to the coherent phase shift of the scattered x-rays. For Θ_{nominal} = 3 ML, Θ_{XRI} therefore corresponds to the thickness of a 2D CdSe layer plus the mean “thickness” of the QD-ensemble (see the top schematic of Fig. 7.3).

Both models explain the observed trend of the plot in Fig. 7.3 sufficiently. However, a combination of both effects might not be ruled out. Results of other characterizations, discussed below, provide more insight into the topic.

Fig. 7.4 shows the PL spectra of the whole series of samples, recorded at 7 K. Despite long growth interruptions, thermal cycling, and complexity of the fabrication process, the PL emission at low temperature is bright. The spectra broaden with increasing CdSe coverage and beyond Θ = 1.7 ML, they are best fitted with two Gaussian profiles, as shown in Fig. 7.5, for Θ = 3 ML.

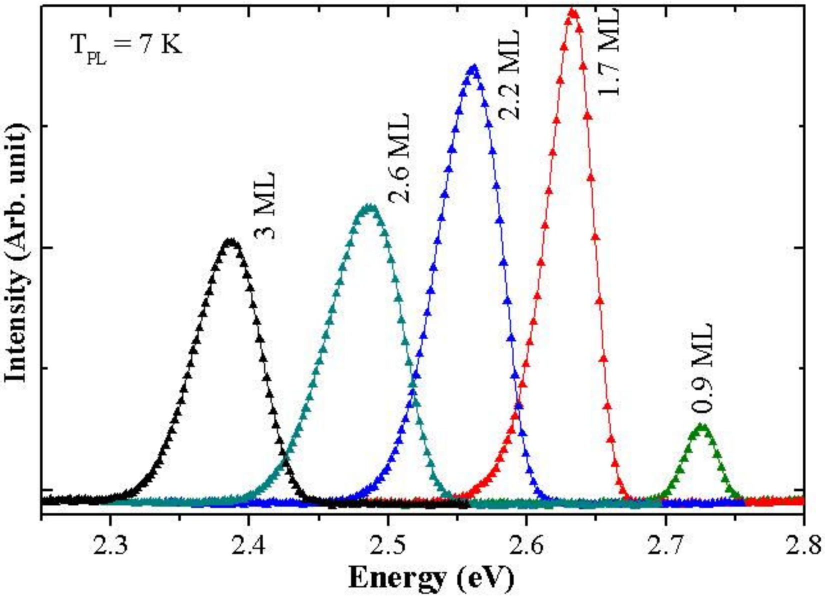

Fig. 7.4: PL spectra recorded at 7 K from the series of samples, with Θ varying from 0.9-3 ML.

The spectral separation between the two Gaussian profiles is 22.9 meV. Comparable values were deduced also for other coverages (26.1 and 22 meV for Θ = 2.6 and 2.2 ML, respectively). The bimodal PL-intensity profile might be assigned either to a bimodal distribution of QD-sizes or combined emission from excitons and multi- or charged-excitonic-complexes. However, it is unlikely to form two subsets of QDs, differing in size and composition in a way that their ground state energies differ by such small values. A difference of 25 meV in the ground state exciton energy, for example, would correspond to a difference of ~ 0.15 ML difference in the height of the QDs (refer to Fig. 7.6), assuming their compositions to be the same. The low energy Gaussian might rather be attributed to biexciton or trion emission (refer to section 3.5). Indeed the measured spectral separation of the two Gaussians in Fig. 7.5 falls well within the values of biexciton- or trion binding energies measured before (see section 2.8, Fig. 2.21) (Gindele99, Lowisch99, Patton03). A more convincing evidence calls for a measurement of the PL-intensity as a function of the excitation density. This has unfortunately not been done.

The variation of PL-spectral position with CdSe coverage Θ[‡] is shown in Fig.7.6 (filled blue circles). For comparison, the plots corresponding to the series of samples grown by both conventional MBE (empty black circles) and "low temperature epitaxy and in-situ annealing" (filled red circles) are also shown in the same Figure. The empty black diamonds in the plot represent the calculated exciton transition energies for pure CdSe QWs. Apparently, the PL peak positions of the QD-ensembles formed in "*a*-Se mediated self-assembly" coincide with those corresponding to the former growth techniques, for almost all Θ. Similar to the arguments made in section 6.2 (in the context of Fig. 6.6), the coincidence of the PL peak positions here as well might be attributed to Cd-segregation and concomitant Zn-alloying of the islands, during capping.

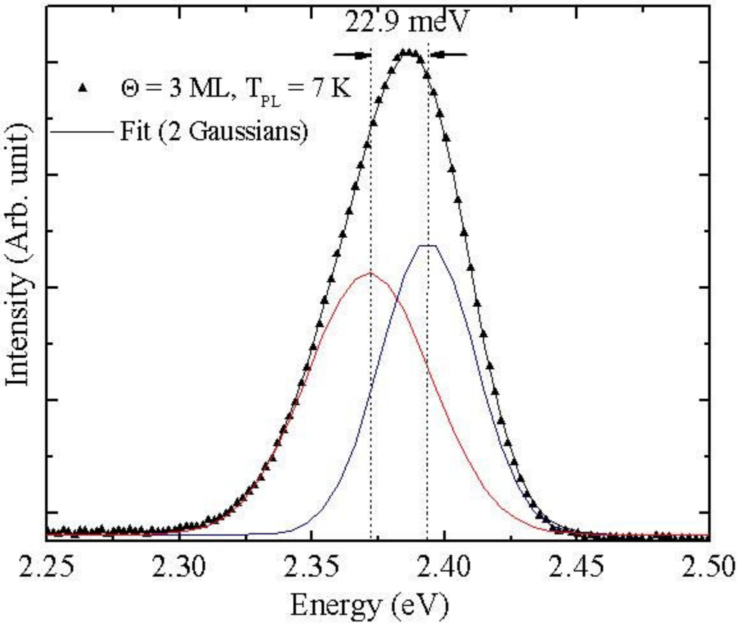

Fig. 7.5: PL spectrum of the sample with Θ = 3 ML, fitted with two Gaussian profiles.

It is then tempting to relate ΔΘ of Fig. 7.3 to the segregation model. However, if the segregation model is considered alone (assuming XRI measures the entire amount of material distributed both in the islands and the 2D layer, for all CdSe coverages), the PL peak positions should be plotted versus Θ_{XRI}, instead of $\Theta_{nominal}$. The corresponding plot is then represented by the filled green circles in Fig. 7.5. It might then be argued that "*a*-Se mediated self-assembly" leads to a clear redshift of the PL peak positions, in comparison to conventional MBE or "low temperature epitaxy and in-situ annealing". The large ΔΘ values suggest that albeit island formation is enhanced by this method, segregation of Cd is also stronger, in comparison to conventional MBE. Thus the QDs formed by "*a*-Se mediated self-assembly" are not expected to be significantly different from their conventional-MBE-counterparts, as has also been observed in HRTEM images

---

[‡] Θ is equivalent to $\Theta_{nominal}$, unless stated otherwise.

[Robin00, Bougerol06]. An explanation which reconciles the XRI and the PL results requires a combination of the two models presented before. It might be inferred that the main contribution to $\Delta\Theta$ is due to the low areal density of QDs. However, Cd-segregation during capping is prevalent which leads to similar (or inter-compensated) size and composition of the QDs, by all fabrication techniques.

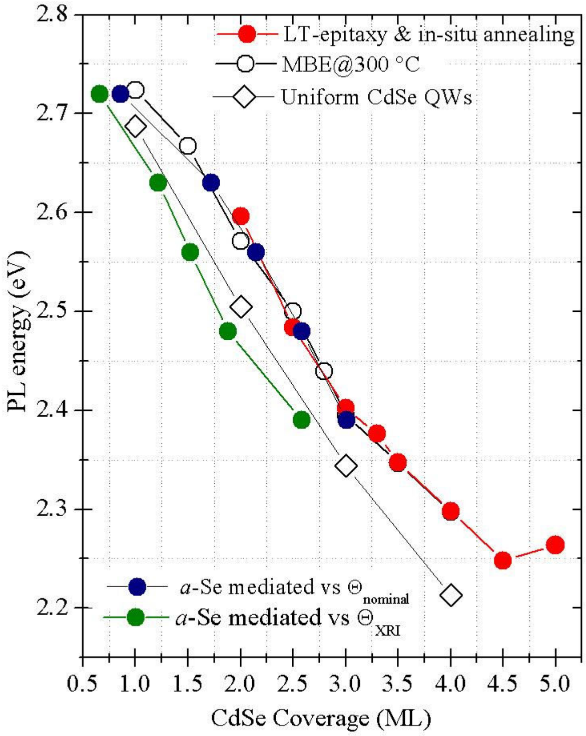

Fig. 7.6: Dependence of the PL-peak positions on Θ_{nominal} (blue circles) and Θ_{XRI} (green circles). For comparison, the data of the samples grown by conventional MBE (open circles) and "low temperature epitaxy and in-situ annealing" (red circles) are plotted together. The calculated exciton transition energies for *pure* CdSe QWs are also shown (open diamonds).

7.3 *Fabrication and properties of CdSe/ZnSe(001) QD-superlattices*

To investigate whether strain-mediated positional correlation of CdSe/ZnSe(001) QDs might be achieved , QD-superlattices were fabricated. The first QD-layer (the seed-layer), in all cases, was prepared by the "*a*-Se-mediated-self-assembly" method, described in the previous sections. Of the three methods of QD formation, studied in this thesis, the QDs formed by "*a*-Se-mediated self-assembly" are morphologically most robust, as observed by AFM. They are distinctly discernible and larger than those formed by the other two techniques. The areal density of such QDs is also sufficiently low. Since elastic strain relaxation within larger islands is expected to be higher and a low areal density is favorable for (strain-mediated) positional correlation of QDs (refer to section 2.6, Fig. 2.15), "*a*-Se-mediated self-assembly" was considered the most suitable method for fabrication of the seed-layer. Therefore, the seed layer was grown following the recipe of section 7.1 and for all structures, the CdSe coverage was chosen to be $\Theta = 3$ ML

The subsequent QD-layers of the superlattices were fabricated by MEE. This choice was guided by several factors. Firstly, taking into account the time (~ 100 min for each layer) and complexity involved in "*a*-Se-mediated QD-self-assembly", it would have been impracticable to grow the entire superlattice by this technique. Moreover, different QD-layers would have undergone different thermal treatments, in terms of the number of cooling (to 45 °C, for *a*-Se capping) and heating (to T_D = 230 °C, for *a*-Se desorption) cycles. Although MEE growth leads to no discernible self-assembly of distinct CdSe/ZnSe(001) islands in single QD-layers, it was assumed that the strain fields of the buried QDs of the seed layer would define preferred sites for QDs of the subsequent layers to nucleate. To favor this process, MEE, instead of conventional MBE, was chosen, since, the former method allows extra time for adatom migration, between two consecutive growth cycles (see section 3.1, Fig. 3.3). For MEE also, a coverage of $\Theta = 3$ ML was chosen, with growth of each monolayer interspersed by growth interruptions under Se-flux. The interval of growth interruption (40 s) was chosen to be double the duration of growth of a ML (20 s). The MEE-QD-layers, for all samples discussed here, were grown at T_G = 230 °C. T_G was chosen based on some preliminary optimization steps, performed to obtain a relatively low density of well defined QDs [Eschenbach07].

A crucial issue in growth of QD-superlattices is the morphological quality of the spacer layers between the individual QD-layers. For III-V or group-IV QD-superlattices, flat spacer-surfaces are recovered, well below the maximum thicknesses permissible for strain-mediated positional correlation of QDs to occur. Nucleation of islands on correlated sites is then assigned solely to local strain fields of buried QDs. During growth of a particular QD-layer, these strain fields define local chemical potential minima for the diffusing adatoms, where QD-nucleation is favored (section 2.16, Fig. 2.15). In case a flat surface is not recovered after growth of the spacer layer, the chemical potential of the adatoms would additionally be influenced by asperities of the spacer-surface.

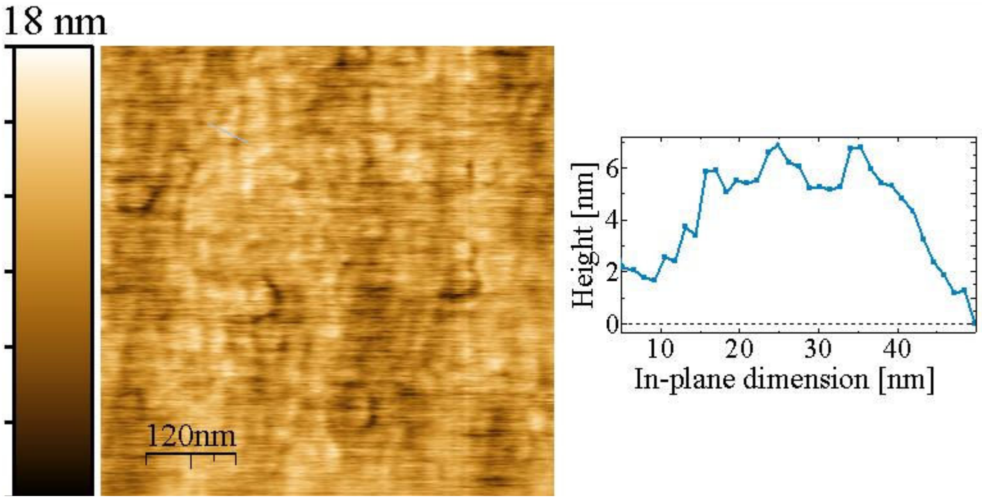

Fig. 7.7: AFM image of a 2 nm thick ZnSe spacer layer, grown atop the seed-QD layer, at T_G = 230 °C (left). The line-profile of a 3D feature of the spacer-surface is also shown (right).

Therefore, before fabrication of multiple QD-layers, the growth and morphology of thin ZnSe spacer layers atop the seed-QD-layer was studied. For the samples studied in this section, spacer layers were grown at $T_G = 230$ °C. The evolution of the spacer layer was monitored real-time by inspection of the RHEED pattern. After formation of the seed-QD-layer, the RHEED pattern was similar to that shown in Fig. 7.1 (d). With subsequent ZnSe deposition, a streaky pattern appeared within a thickness of $L = 2$ nm, albeit the spotty pattern did not disappear completely. Thereafter, the mixed streaky-spotty pattern continued for thicknesses up to even 25 nm. The morphology of a spacer layer, 2 nm thick, is shown in Fig. 7.7. The surface is observed to be significantly rough, with a rms roughness double as much as the underlying seed-QD-layer (measured for the image of Fig. 7.2.).Certain 3D features are also seen in the image.

The observed morphology of the ZnSe cap layer indicates strongly to a situation similar to that observed by Rastelli et al, in capping Ge islands at 300 °C (section 2.5, Fig. 2.13) (Rastelli02). In accordance with the explanation provided in the context of Fig. 2.13 (a), capping of CdSe at 230 °C might also be considered to be shape-preserving. The fact that a smooth ZnSe cap is not recovered, even after a thickness of 25 nm, might then be assigned to suppressed surface diffusion of Zn adatoms at the low capping temperature of 230 °C, whereby, the profile of the CdSe islands is preserved in the ZnSe cap layer. The situation is illustrated schematically in Fig. 7.8 (a).

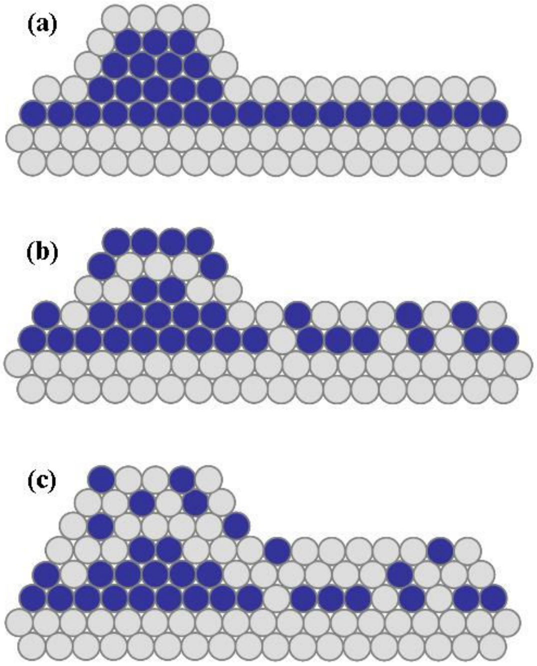

Fig. 7.8: Schematic illustration of "shape preserving" capping of CdSe islands with ZnSe. (a) shows the hypothetical situation just after deposition of the first monolayer of ZnSe. (b) shows an intermediate stage wherein Cd atoms, close to the apex of the island exchange sites with the deposited Zn atoms (segregation) (c) shows the situation after deposition of the second monolayer of ZnSe, where the segregated Cd atoms are seen to wander vertically away from the islands. The profile of the islands is clearly seen to be preserved during capping.

With the assumption of shape-preserving capping, Cd-segregation and Zn-alloying cannot be explained by the model established for the standard capping scenario in InAs/GaAs(001) or Ge/Si(001) heteroepitaxy (see Fig. 2.12). For the InAs/GaAs(001) heterosystem, it has been argued that during capping, GaAs grows preferentially between the islands.

Lateral segregation of In from the islands takes place during capping, due to mounting compressive strain at the island edges. The segregated In atoms migrate large distances to form a 2D layer. As suggested by the morphology of the ZnSe cap layer and the schematic illustration of Fig. 7.8 (a), this is not the case here. For the shape-preserving capping situation, rather, a *vertical* segregation model is more appropriate.

Unlike In-adatoms in InAs/GaAs(001) heteroepitaxy, Cd adatoms are sluggishly mobile at 230 °C (The PL blue-shift after annealing for up to 100 mins in section 6.4, Fig. 6.13, substantiates this fact). Therefore, though segregation takes place, the segregated Cd-atoms do not wander (laterally) far away from the islands (fig. 7.8 (b)). Rather, they migrate vertically upwards in the growing cap layer, as shown in Fig. 7.8 (c). Here segregation takes place, most likely, due to site-exchange between Cd and Zn atoms, which is promoted by the possibility of strain relaxation. As seen in the schematic illustration of Fig. 7.8, vertical Cd-segregation does not interfere with the shape-preserving capping mechanism but may rather stabilize it.

In order to enhance migration of adatoms and thereby achieve smoothening of the ZnSe cap layer, capping at T_D = 280 °C was also attempted. Also, the two step capping approach of Rastelli et al. (Fig. 2.13 (b)) was tried out [Rastelli02]. In the two step approach, the first 2 nm of the cap layer was grown at 230 °C and another 12 nm at 350 °C. Unfortunately however, none of the two approaches led to significant smoothening of the spacer surface. Consequently, for growth of the QD-superlattices, both MEE QD-layers and the spacer layers between them were grown at 230 °C. By adopting the same temperature for growth of both QD- and spacer-layers, unnecessary thermal cycling and complexity could be avoided. Spacer layer thicknesses of L = 6 and 13 nm were chosen for the superlattices.

Several QD-superlattice structures were fabricated, corresponding to both L = 6 and 13 nm. The number of superlattice period in case of L = 6 nm was chosen to be 2, 7, 9, and 12 (i.e. 1, 6, 9, and 11 MEE QD-layers atop the seed layer). For L = 13 nm, 2- and 7-period superlattices were only fabricated. Fig. 7.9 shows surfaces of QD-layers, at different levels, for both L = 6 and 13 nm. Well-defined islands are clearly seen in the image corresponding to the first MEE layer of the superlattice, for both values of L. The islands in both cases are ~ 1.5-2.5 nm high, 40-60 nm in base diameter, and fairly symmetric in shape. The areal density of the islands is ~ $3\text{x}10^{10}$ cm^{-2}.

On the surface of the 6th, as well as the 9th MEE layer, the islands are seen to be preferentially elongated perpendicular to the long-range ridges, i.e. in the [110] direction. At the 11th level, the features are not clearly resolved any more, but their anisotropic shapes are still visible. The preferential elongation of the islands might be attributed to a surface diffusion bias of Cd atoms along the direction of the Se-dimers (see Fig. 3.5). Alternatively, it might be assigned to preferential sticking of Cd along the dimer rows. A similar but weaker tendency of elongation along the [110] direction was also observed for the mounds on the surface of conventional-MBE-grown CdSe layers (Fig. 5.3 (b)).

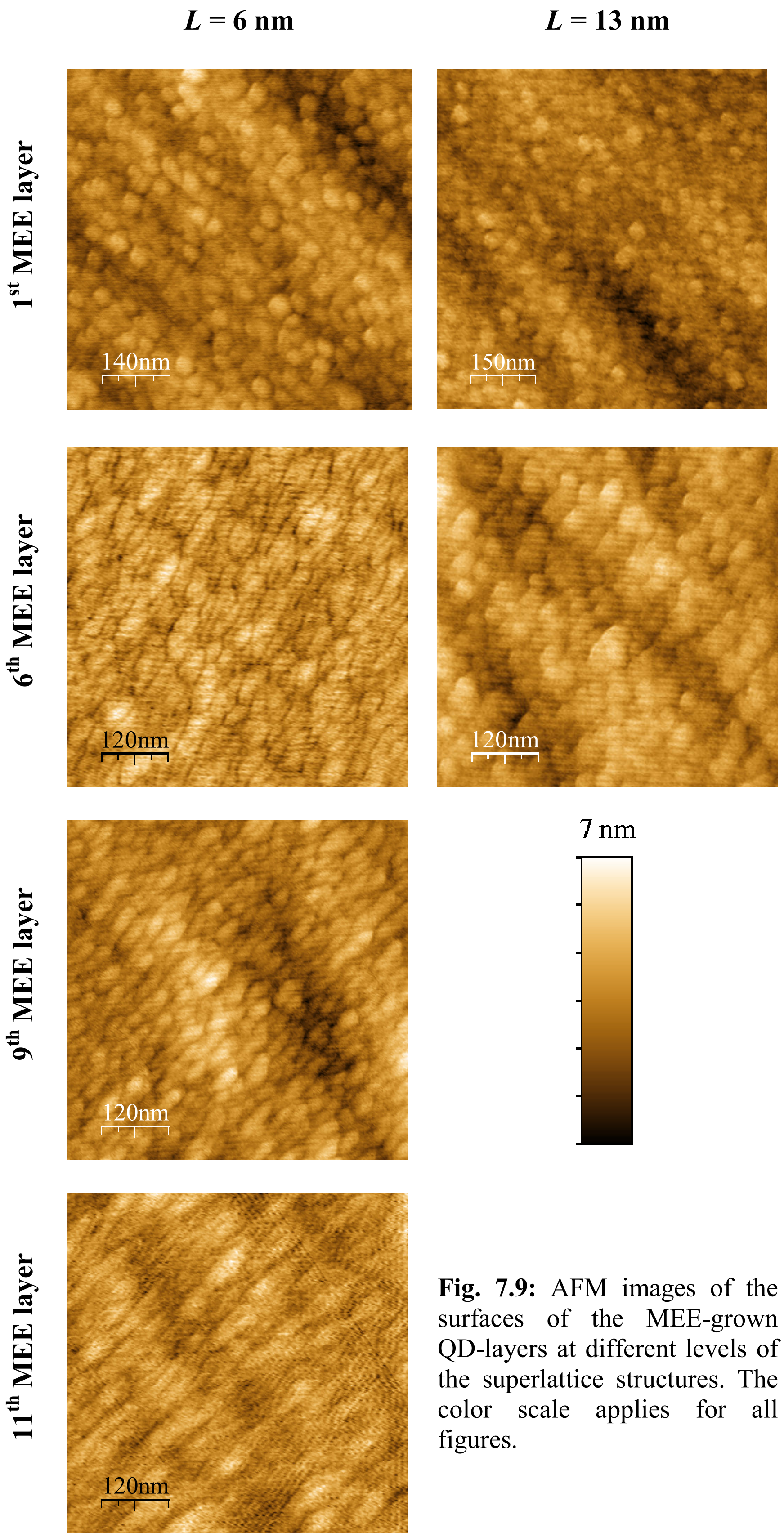

Fig. 7.9: AFM images of the surfaces of the MEE-grown QD-layers at different levels of the superlattice structures. The color scale applies for all figures.

The AFM images do not bear any obvious indication of positional correlation of QDs in the superlattices. To obtain confirmative evidence, cross-sectional HRTEM was performed. Fig. 7.10 (a) and 7.10 (b) show the images, recorded for the 9-period QD-superlattice, with L = 6 nm. The two images correspond to cross-sections along the [110] and [1-10] directions. However, which of the two images is parallel/perpendicular to the [110] axis is not known. A section of Fig. 7.10 (a) is magnified in the inset.

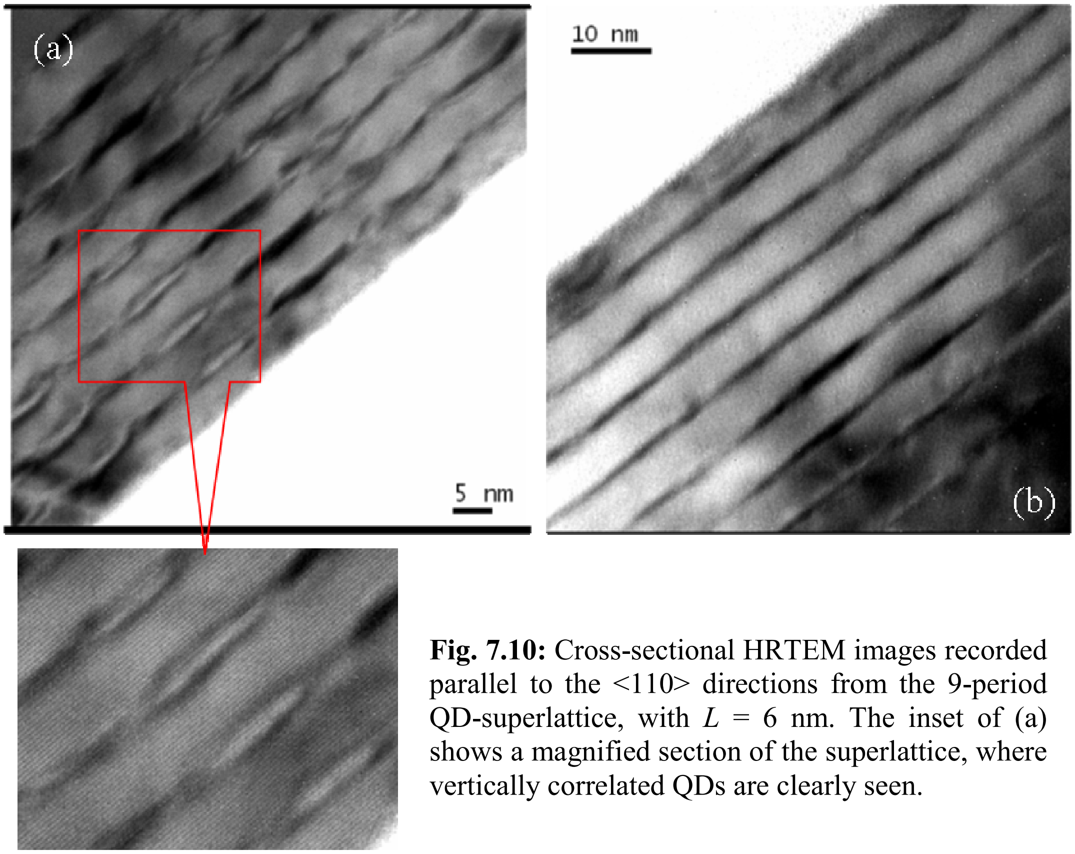

Fig. 7.10: Cross-sectional HRTEM images recorded parallel to the <110> directions from the 9-period QD-superlattice, with L = 6 nm. The inset of (a) shows a magnified section of the superlattice, where vertically correlated QDs are clearly seen.

Vertically-correlated QDs are clearly evident, particularly in Fig. 7.10 (a). The QDs are also better-defined in this image. In the inset, the QDs of the four consecutive layers appear to have, by and large, the same in-plane diameter, d_{QD}. This is in variance to what is known for QD-superlattices of other heterosystems (see Fig. 2.14). At progressively higher levels of a QD-superlattice, the strain minima above the buried QDs deepen and thereby results in enhanced accumulation of adatoms. Concomitantly, the lateral extent of the QDs increases progressively at higher-lying layers of a QD-superlattice. For the QDs seen in the inset, d_{QD} is ~ 10 nm. Thus, $d_{QD}/L > 1$, and the observed vertical correlation is in agreement with the model of Springholz et al. [Springholz00, Springholz01] (see section 2.6, Fig. 2.16).

Comparing the length scales of Figs. 7.10 (a) and (b), it is seen that the QDs are anisotropic in shape. In Fig. 7.10 (a), they appear to be shorter. Therefore, it might be inferred in conjunction with the corresponding AFM image (Fig. 7.9) that Fig. 7.10 (a) represents the [1-10] cross-section of the QD-superlattice. Secondly, it is observed that the QD-layers bear a wavy profile, especially along the [1-10] direction. This strongly supports the claim of shape-preserving ZnSe-capping of the CdSe islands (Fig. 7.8). In turn, it serves as a caveat that apart from strain, possibly also the surface asperities of the ZnSe spacer layers influence the observed vertical correlation of the QDs in the QD-superlattices.

Summary

In this chapter, essentially two different topics were dealt with. In the first part, QD formation by the "*a*-Se mediated self-assembly" technique was described. The morphology of uncapped islands and PL characteristics of the (capped) QDs were presented. Detailed x-ray investigations indicated to v*ertical* segregation of Cd during capping with ZnSe. The second part addressed to positional correlation of CdSe QDs in QD-superlattices. For such superlattices, the first QD-layers were always grown by "*a*-Se mediated self-assembly" and the subsequent ones by migration enhanced epitaxy. It was observed that ZnSe capping at the chosen growth temperature of T_G = 230 °C did not lead to complete collapse of the islands, but preserved their shapes to some extent. The islands at the higher levels of the superlattices were observed to be preferentially elongated in the [110] direction. HRTEM revealed a clear vertical correlation of islands.

Tellurium mediated self-assembly of CdSe(Te)/ZnSe(001) quantum-dot-based structures

---

8

This chapter addresses to the formation and properties of QD ensembles by a technique similar to "*a*-Se mediated self-assembly"- the only difference being in the use of tellurium, instead of selenium, as the amorphous-cap-forming material. Though the approach is technically similar to the previous one, the substitution of Se with Te resulted not only in large alteration of the morphological and optical attributes of the QDs, but also led to formation of unique self-assembled island-patterns. Albeit not expected, the QDs formed in this method were found to be alloyed with Te. This chapter discusses in detail, the self-assembly, morphology, composition, and luminescence properties of these QDs, and investigates the mechanism underlying the formation of self-assembled island-patterns.

8.1 *The "Te-mediated self-assembly" technique*

As mentioned before, the process steps involved in this technique are similar to those of "*a*-Se mediated self-assembly". However, some of the parameters involved in the different steps of the process are slightly different. For capping with Te, the CdSe surface in this case was cooled down to 50 °C. Different thicknesses of the Te-cap layer, d_{cap}, were chosen. The temperature to which the sample was subsequently heated up for Te-desorption, T_D, was also varied.

After some preliminary optimization growth-runs, the first series of uncapped samples were prepared, wherein the CdSe coverage was maintained constant at $\Theta = 3$ ML, but the thickness of the Te cap layer was chosen to be d_{cap} = 1, 5, 15, and 60 nm. This was prompted by a serendipitous observation that the self-assembled patterns of the QD-ensembles were governed by d_{cap}. Subsequently, a similar series of capped samples (except for d_{cap} = 15 nm) were also prepared, for X-ray, HRTEM, and PL characterization. The study was then extended to the case of constant d_{cap} but varying Θ.

8.2 *Formation and properties of QDs*

Fig. 8.1 shows the typical evolution of the RHEED pattern, during different steps of the process. The streaky pattern of Fig. 8.1 (a) corresponds to the flat CdSe layer, as shown previously in Fig. 6.2 (a) and 7.2 (a). After capping the CdSe surface with *a*-Te at 50 °C, the streaky pattern disappeared and a diffuse image, as shown in Fig. 8.1(b), emerged. However, this purely diffuse pattern was observed only for d_{cap} = 1 nm. For higher values, a weak pattern of rings, characteristic of polycrystalline morphology, was observed together with the diffuse RHEED. Later on, it was verified that the appearance of the ring pattern depended strongly on the temperature chosen for Te-capping, d_{cap}, and also Θ.

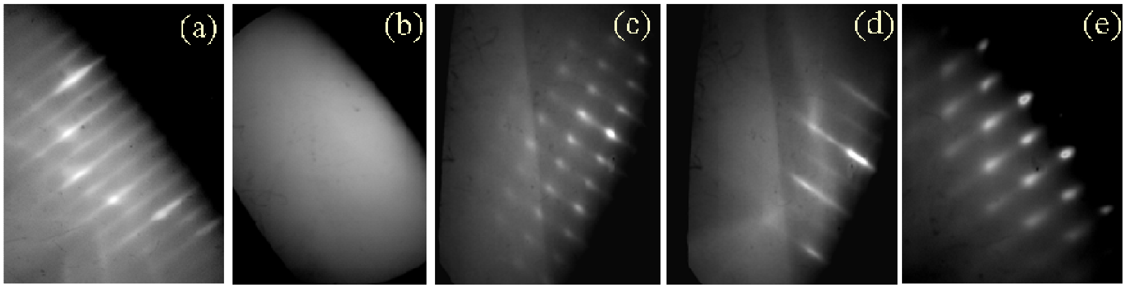

Fig. 8.1: RHEED images recorded at different stages of QD-fabrication by “Te-mediated self-assembly” technique. See text for details.

On raising back the substrate temperature for desorption of Te, a combination of weakly streaky and primarily spotty pattern appeared above ~190 °C, as shown in Fig. 8.1 (c). The symmetry of this pattern suggests that it does not belong to any semiconductor-related feature, which possesses a diamond or zinc blende (face centered cubic) crystal structure. The pattern might rather be assigned to pure Te, which crystallizes in triclinic structure. Since the pattern consists of both streaks and spots (instead of pure streaks or rings), it is assumed to arise from a rough, but epitaxially oriented, polycrystalline Te-layer, directly atop the CdSe surface (The topography of this layer is shown later in Fig. 8.16). This RHEED pattern was observed in all cases, irrespective of d_{cap} and Θ. It might therefore be inferred that while the choice of d_{cap}, Θ, and temperature of Te-capping govern the nature of the as-deposited cap layers (amorphous or a combination of amorphous and randomly polycrystalline), during ramp-up to T_D, an oriented polycrystalline Te-layer is formed in all cases. The pattern of Fig. 8(c) existed up till ~ 290 °C. At this temperature a streaky RHEED, with a mixed c(2x2) and (2x1) reconstruction, appeared momentarily [Fig. 8 (d)]. The appearance of this pattern signified the re-exposure of a flat 2D CdSe(Te) surface. Within the next 2-3 s of this evolution, a spotty pattern, typical for three dimensional (3D) semiconductor nanostructures, appeared (Fig. 8.1(e)). This pattern was found to be stable for long durations (verified for durations up to 10 mins), even at temperatures as high as 320 °C. For the series where d_{cap} was varied, the only exception was the case of d_{cap} = 1 nm, wherein, the mixed streaky reconstruction appeared at ~ 190 °C and did not evolve any further. This was also the case for growth of samples with $\Theta < 2.5$ ML.

AFM images of uncapped island-layers, corresponding to a few combinations of Θ/ d_{cap}/ T_D values are shown in Fig. 8.2. In 8.2 (a), an island layer, characterized by the parameters (2.5 ML/ 10 nm/ 280 °C), is shown. Θ = 2.5 ML represents the minimum CdSe coverage for which the spotty pattern of Fig. 8.1 (e) was observed. A dilute ensemble of well-defined islands are seen in the image. The islands are ~ 3-5 nm high and 50-70 nm in base diameter. Their areal density is ~ 1x 10^{10} cm $^{-2}$. Apart from these islands however, very tiny features, < 3 nm high and with a significantly larger areal density, are also observed in the image, in regions between the large islands. One such region is magnified in 3D view in Fig. 8.2 (g).

For Θ = 3 ML, it is observed that a rich variety of patterned nanostructure-ensembles are formed, depending on d_{cap} (Fig. 8.2 (b)-(e)). For the four samples shown, T_D was chosen to be 310 °C. Dashes, up to 600 nm long, ~ 150 nm wide, 5-8 nm high, and aligned along one of the <110> axes, are seen for d_{cap} = 1 nm (Fig. 8.2 (b)). Corresponding to d_{cap} = 5 nm, Fig. 8.2 (c) shows a dense ensemble of up to 300 nm long and nearly straight chains of islands. Within each chain, the islands appear to be significantly uniform, albeit within the whole ensemble, the island-height varies between 5-7 nm. The island-chains become buckled and their areal density is reduced, when d_{cap} is increased to 15 nm (Fig. 8.2 (d)). In this case, the height of the islands reaches up to ~ 10 nm. For both d_{cap} = 5 and 15 nm, the base-diameter of the islands varies between 45-60 nm. For d_{cap} = 60 nm, a dilute ensemble of island-pairs is formed, with almost all island-pairs aligned along one of the <110> directions. Fig. 8.2(h) shows a selected island-pair in 3D view. While each island-pair consists of two abutting and equi-sized islands, within the whole ensemble, island-heights vary between 6-30 nm. Thus, it is evident that d_{cap} strongly influences the reorganization of the CdSe surface and the resultant self-assembled island-patterns. Specifically, the height of the islands increase and patterns with lower island-areal-densities are formed with increasing d_{cap}.

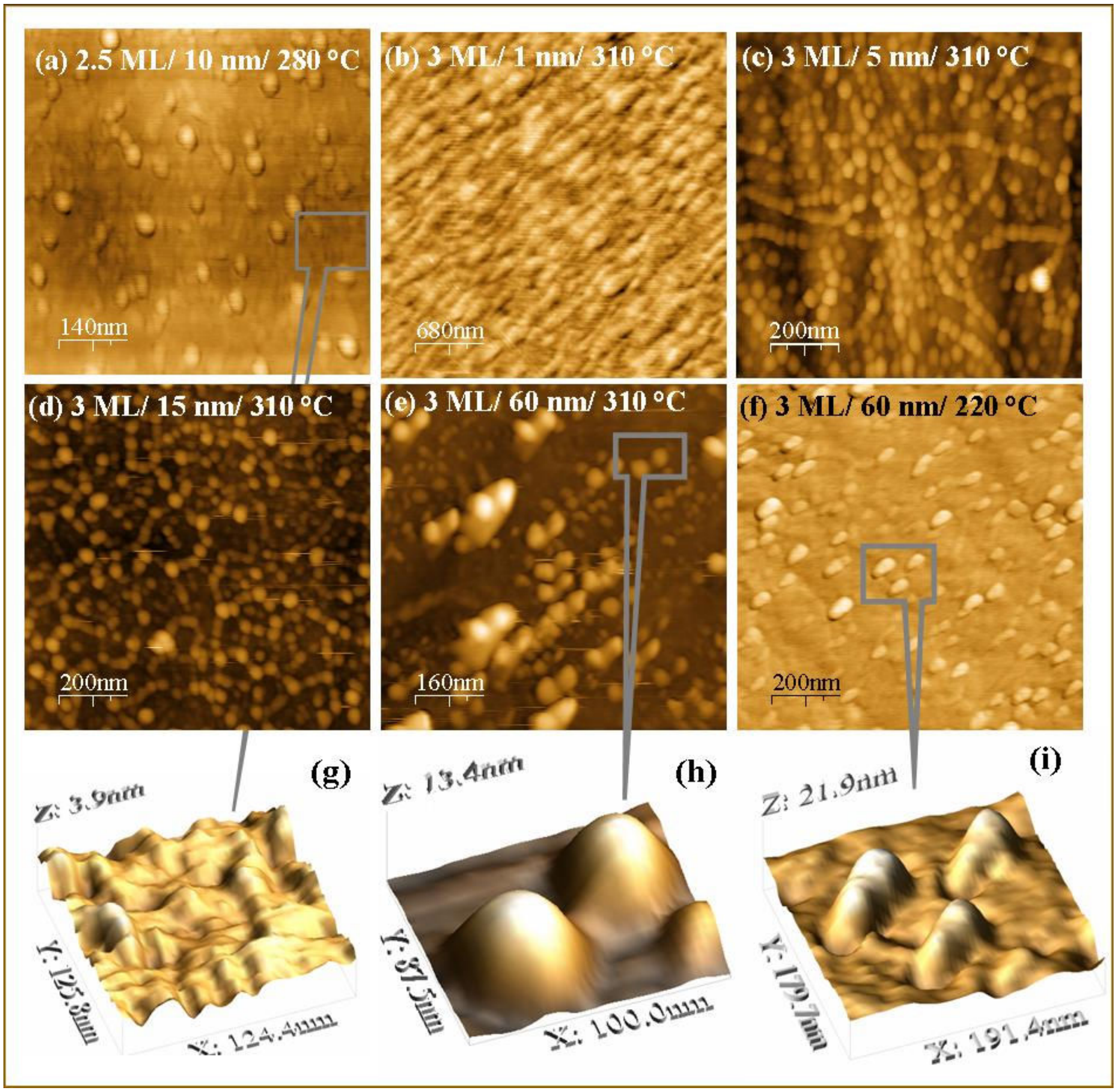

Fig. 8.2:(a)-(f) AFM image of a island layers, corresponding to different combinations of Θ/ d_{cap}/ T_D (g)-(f) Selected parts of images (a), (e), and (f) in 3D view.

On the other hand, the choice of T_D was found to have only a weak influence on the island-sizes and separation. This is illustrated by the AFM image of a sample corresponding to d_{cap} = 60 nm, but T_D = 220 °C, shown in Fig. 8.2 (f) and 8.2 (i). Elongated nanostructures, aligned similar to the island-pairs of Fig. 8.2 (d), are seen in the 2D image (Fig. 8.2 (f)). The 3D view of a selected part (Fig. 8.2 (i)) reveals that similar to the case of T_D = 310 °C, these nanostructures also represent (nearly merged) island-pairs. However, the size and separation of islands, constituting the island-pairs, are smaller than in the case of T_D = 310 °C.

Following the AFM study of the island morphologies, the composition of a few of the island-layers was investigated. The interest was in determining whether the islands were composed of pure CdSe or were alloyed with Te. However, before studying the composition of the island layer, a simple experiment was performed to ascertain that the observed nanostructures represented II-VI based islands, and not mere droplets of incoherent Te. For this purpose, the surface of a pseudomorphic ZnSe/GaAs(001) layer was treated similar to the thin CdSe layers, i.e., a 15-nm-thick Te layer was deposited onto this layer at ~ 50 °C and subsequently desorbed at T_D = 280 °C. A bright streaky RHEED pattern appeared after Te-desorption. Fig. 8.3 (a) shows an AFM image of the ZnSe surface, after desorption of Te. It shows no evidence of 3D nanostructures, like those observed for the island-layers. This confirms that the nanostructures of the island-layers are indeed related to strained II-VI islands.

To investigate whether Te was incorporated in the epitaxial layer during any stage of the process, a 54 nm thick ZnSe/GaAs(001) layer was treated similar to that mentioned above and subsequently capped with another 54 nm of ZnSe. A (004) x-ray diffractogram was then recorded from this sample to detect the presence of any ZnTe. The diffractogram, along with a simulated profile, is shown in fig. 8.3 (b).

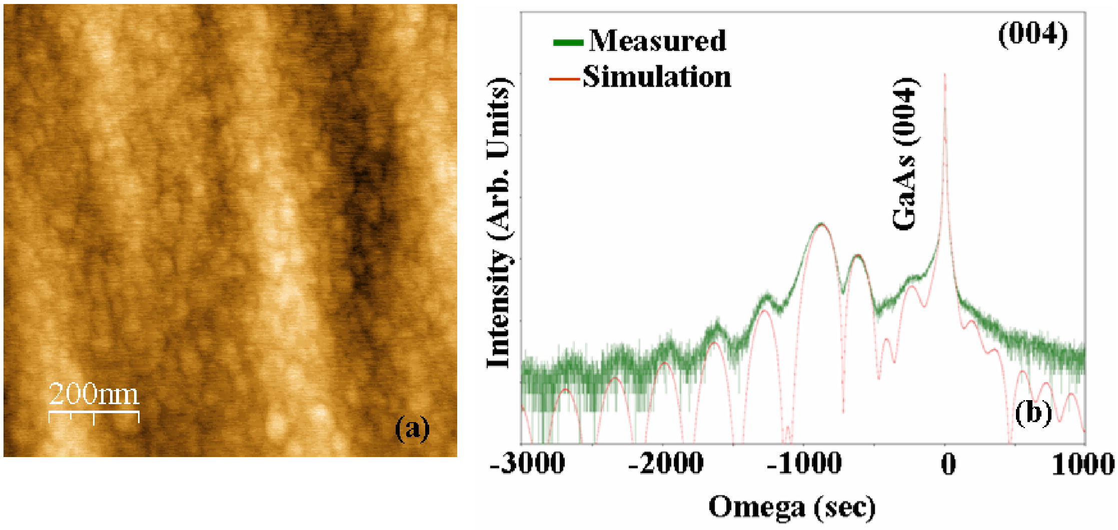

Fig. 8.3:(a)Surface of a 54-nm thick ZnSe layer, which underwent all the steps of the "Te-mediated self assembly" technique (b) (004) HRXRD profile (green) recorded from a sample wherein a 54 nm thick ZnSe layer was grown atop a surface similar to that of (a). Also shown is the simulated profile (red) for a structure consisting of 1 ML ZnTe sandwiched between two 54-nm-thick ZnSe layers.

A good match of the recorded diffractogram could be obtained for a ZnTe thickness of 1 ML. However, as discussed in section 3.3 (Fig. 3.9), similar simulation profiles can also be generated for ZnTe thicknesses of 4.77 ML, 8.55 ML, etc. (i.e., for every increase of 3.77 ML). Though not conclusive, two reasons can be given in favor of the minimum thickness of the ZnTe separator layer. For sandwich structures containing CdSe separator layers between thick ZnSe barrier layers, dislocations are generated at ~ 4 ML and consequently, the XRI fringes tend to overlap (see Fig. 6.3). Since the lattice constant of ZnTe (6.1 Å) is slightly larger than CdSe (6.05 Å), a similar effect would be expected also in this case, for the two other quoted values. Secondly, if at all, Te would be expected to replace only the weakly bound Se atoms of the topmost monolayer. The reason is as follows: In epitaxial growth of ZnSeTe alloy layers, Se is preferentially incorporated in the epilayers [Yao78]. The reason for this occurrence has been attributed to the larger heat of formation of ZnSe (39.0 kcal/mol), compared to ZnTe (28.1 kcal/mol), due to which, chemisorption (and incorporation) of Se is faster [Phillips73]. Here, Te is introduced to the ZnSe surface long after growth of the ZnSe layer. Thus, all but a small fraction of Se adatoms (weakly physisorbed) at the surface layer would be incorporated in the growing crystal and therefore, unavailable for replacement with Te. This would limit the maximum thickness of the formed ZnTe layer to 1 ML.

Unfortunately however, XRI would not be useful for a direct determination of the amount of Te in the island-layers. This is because a similar phase shift would result for different combinations of coverage and composition (ratio of Se to Te) of the island-layer. Based on the arguments presented below, it was expected (at the beginning of this work) that Te-alloying of the CdSe island-layer would not be more than that of the ZnSe layer. (a) The heat of formation of CdSe (32.6 kcal/mol) is larger than that of CdTe (22.1 kcal/mol) [Phillips73]. (b) The energy cost of Te-alloying an already highly strained CdSe layer would be larger than that for a very weakly strained ZnSe layer (The bulk lattice constant of CdTe is 6.48 Å, signifying a lattice misfit of m = 0.146, with GaAs). Even if it is assumed that Te would be incorporated atop fully strain-relaxed islands, after they are formed, the lattice misfit (with CdSe) would still be as high as m = 0.07.

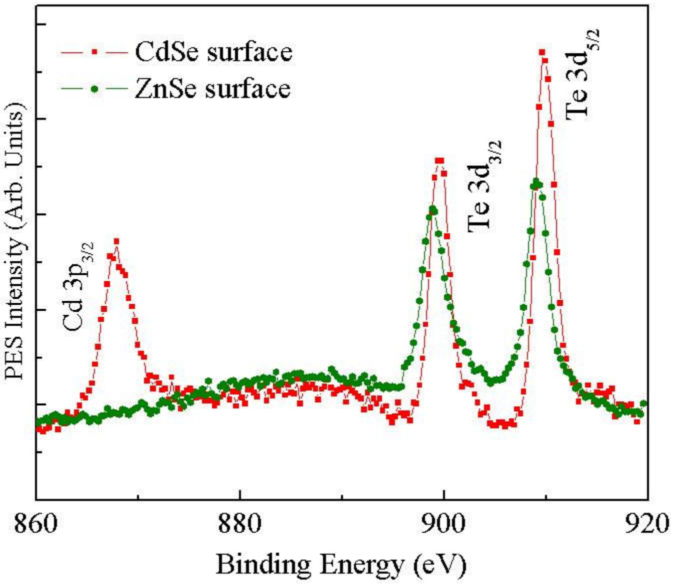

Fig. 8.4: XPS spectra, recorded from the QD-layer shown in Fig. 8.2 (c) (straight chains) (red) and the ZnSe surface shown in Fig. 8.3 (a) (green).

Nonetheless, to verify the assumption, XPS spectra were recorded from the surfaces of the island-layer of Fig. 8.2(c) (straight chains) and the ZnSe layer of Fig. 8.3 (a). Fig. 8.4

shows the spectra. The spectra were recorded at a take-off angle of 0° (normal) for both samples. The information depth for normal take-off is ~ 20 Å. Spectra for both surfaces show the $3d_{3/2}$ and $3d_{5/2}$ binding energy peaks of Te. Both peaks show a slightly stronger intensity for the QD-surface. Though this signifies (~ 1.3 times) higher amount of Te in the island-layers, it must be borne in mind that the difference in the surface topologies of the two samples can obscure the comparison [Oswald06]. Further, a direct comparison of the absolute intensities (without normalizing to a standard which is present in both samples, i.e. Zn) is also not appropriate. Unfortunately, the Zn binding energy peaks were not recorded.

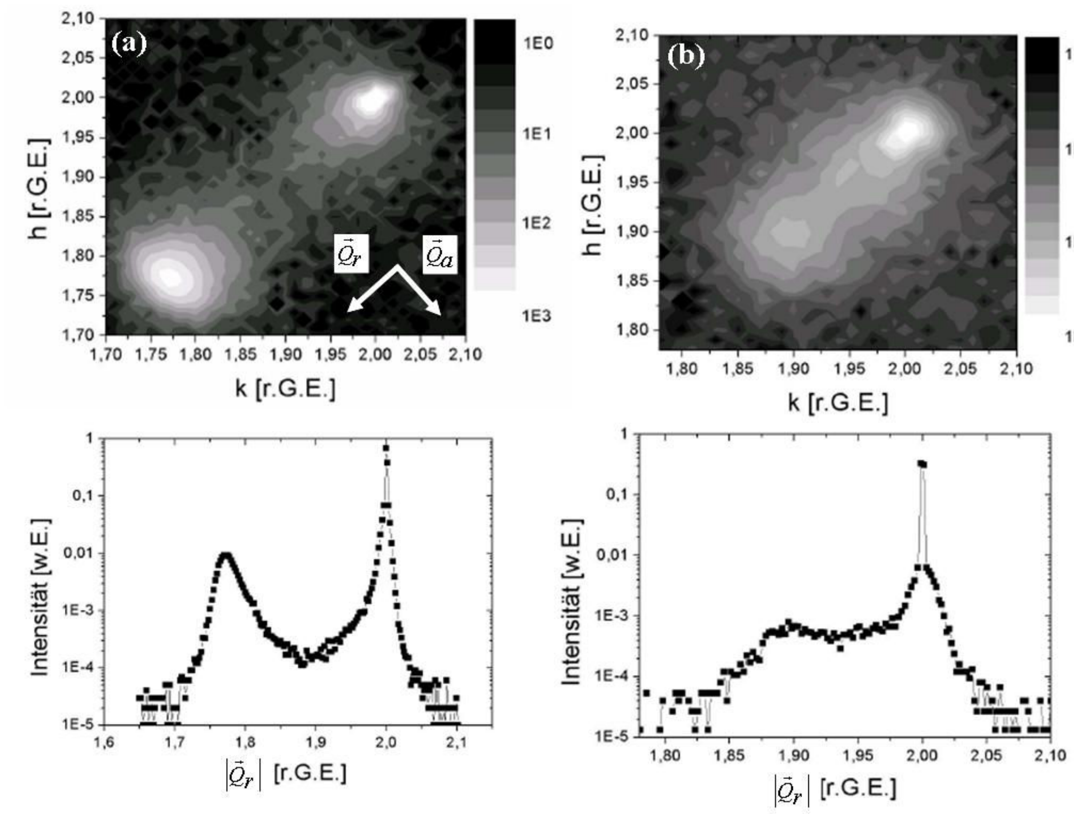

Fig. 8.5: (Top panels) Reciprocal space maps (RSMs) recorded from the (uncapped) island-layer of (a) Fig.8.2 (e) (island-pairs, T_D = 310 °C) and (b) Fig. 8.2 (f) (island-pairs, T_D 0 220 °C). (Bottom panels) Corresponding $\vec{Q}_r$ line-scans at $\vec{Q}_a = 0$.

While the above experiments proved the presence of some amount of Te in the island-layers, no information could be obtained regarding its distribution. Specifically, whether the islands were admixed or capped with Te or whether Te existed only in regions between the islands could not be determined. To delve deeper into the analysis of the island-composition, GIXRD diffractograms were recorded from uncapped island-layers, corresponding to the images of Fig. 8.2 (d) and 8.2 (e) [Kumpf07, Gierz07]. The top panels of Fig. 8.5 (a) and (b) show the corresponding (220) RSMs. The axes of the RSMs are shown in units of the surface Miller indices (reciprocal lattice unit (English) or reziproke Gitter Einheit (German)), so that the intensity distribution at h =2 and k = 2 corresponds to the GaAs substrate. In the bottom panels, line-scans in the $\vec{Q}_r$ direction at $\vec{Q}_a = 0$, are shown.

It is helpful to discuss Fig. 8.5 (b) first. A continuous distribution of scattered intensity is seen in the RSM between $|\vec{Q}_r| = 2$ to $|\vec{Q}_r| \approx 1.85$. The intensity distribution is very similar to that recorded for InAs/GaAs(001) islands, by Krause et al [Krause05] (refer to Fig. 3.11 (a)). The intensity at $|\vec{Q}_r| = 2$ is assumed to arise due to scattering by the pseudomorphically strained ZnSe barrier layer, a 2D CdSe(Te) "wetting layer", and also the lower part of the (coherent) islands. In the $|\vec{Q}_r|$-line scan of the bottom panel, it is seen that the scattered intensity remains fairly constant down to $|\vec{Q}_r| \approx 1.88$, beyond which it falls gradually. As discussed in section 3.3 (refer to Fig. 3.10 and 3.11), every value of $|\vec{Q}_r|$ corresponds to a particular iso-strain slice of the island. Based on Eqn. 3.13, the height at which a particular iso-strain slice is located might also be determined. It is then possible to plot $|\vec{Q}_r|$ as a function of height.

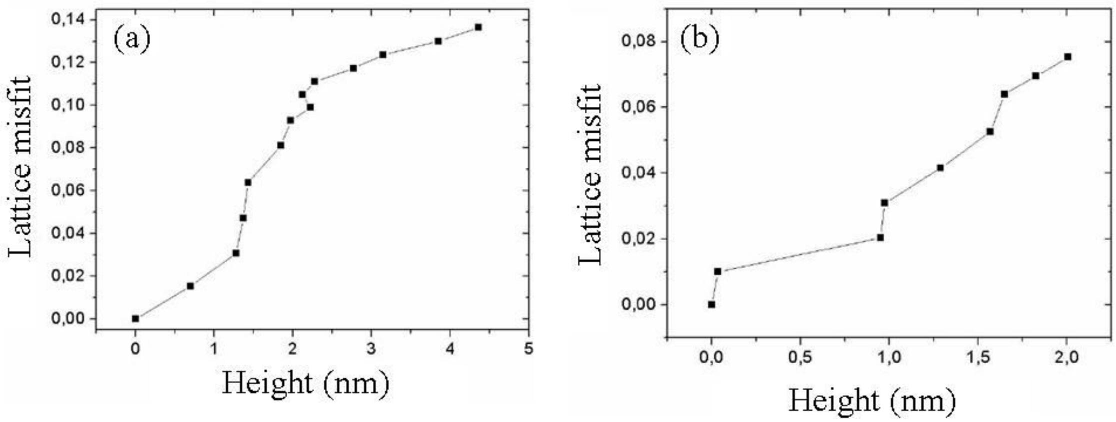

Fig. 8.6: Lattice misfit versus height, extracted from the RSMs of Fig. 8.5, for the island-layers of (a) Fig. 8.2 (e) (island-pairs, T_D = 310 °C) and (b) Fig. 8.2 (f) (island-pairs, T_D = 220 °C).

A more convenient way of representation is to plot the height-dependence of the lattice misfit, with respect to the lattice constant of GaAs. For the RSMs of Fig. 8.5 (a) and 8.5 (b), the plots are shown in Fig. 8.6 (a) and 8.6 (b), respectively. In Fig. 8.6 (b), it is seen that the maximum misfit corresponds to 0.075. The lattice misfit between CdSe and GaAs is 0.071. Thus, it might be inferred that the islands of Fig. 8.2 (e), are admixed with some Te. Once again however, the extent of Te-admixture remains uncertain since the strain-status of the islands is not independently known. Thus, the misfit of 0.075 would mean fully strain-relaxed islands, alloyed with 0-4% Te, or, in the extreme case, 50 % strain relaxed pure CdTe islands.

It is also observed in Fig. 8.6 (b) that the measured island height is ~ 2 nm. This value is only 0.25 times of that measured by AFM. The discrepancy is tentatively explained by oxidation of the island-layer in atmospheric ambient. GIXRD probes only the crystalline core of the islands, while AFM records their external morphology. Nonetheless, a four-fold increase in the island height due to oxidation is rather difficult to comprehend.

The RSM of Fig. 8.5 (a), on the other hand, shows scattered intensity distribution from $\left|\vec{Q}_r\right| = 2$ to $\left|\vec{Q}_r\right| \approx 1.73$. $\left|\vec{Q}_r\right| \approx 1.73$, corresponds to a lattice misfit (with GaAs) of 0.14. This value is only marginally less than the misfit between GaAs and pure CdTe (0.146). The height-dependence of the measured lattice-misfit is shown in Fig. 8.6 (a). It is seen that the maximum misfit reaches a value of 0.14 and the island height measures 5 nm.

From the height dependence of the deduced misfit values, it might be concluded that regions with very high amount of CdTe are present within the islands of Fig. 8.2 (e), at least close to their apices. However, certain peculiarities of the RSM need to be analyzed carefully. The distribution of scattered intensity in this case does not appear to be similar to the previous case (or as predicted by the iso-strain model of Kegel et al [Kegel01]). Below the peak at $\left|\vec{Q}_r\right| = 2$, the scattered intensity is seen to first fall and then again rise in form of a peak around $\left|\vec{Q}_r\right| \approx 1.77$. More appropriately, comparing the absolute values of the scattered intensities in the $\left|\vec{Q}_r\right|$ line scans of the bottom panels of Fig. 8.5 (a) and (b), it might be inferred that in Fig. 8.5 (a), the peak at $\left|\vec{Q}_r\right| \approx 1.77$ is superposed on a intensity profile, similar to that of 8.5 (b). For the typical shapes of self assembled islands, it might be expected that the higher-lying iso-strain slices (with smaller $\left|\vec{Q}_r\right|$ values) are smaller in lateral dimensions. Thus the scattering volume, corresponding to increasing $\left|\vec{Q}_r\right|$ should reduce, leading to a fall in the intensity, as seen in the RSM of Fig. 3.11 (a). Here, to the contrary, a new peak is observed to rise in intensity, below $\left|\vec{Q}_r\right| \approx 1.87$.

The discrepancy is tentatively explained by the large distribution of island sizes observed for this sample in the corresponding AFM image (Fig. 8.2 (e)). It might be assumed that the smaller (coherent) islands of this surface are similar to those of the previous sample and they contribute to the shoulder-like scattered-intensity distribution in Fig. 8.5 (a) (lower panel). The additional peak comes most likely from the very large islands, which are significantly admixed with Te. The fact that these islands do not contribute to enhance the intensity for $\left|\vec{Q}_r\right| \geq 1.87$ suggests that most of them are dislocated.

From the GIXRD measurements it is quite conclusively established that the islands are admixed with Te. The amount of Te incorporated in the islands is possibly correlated to their size, T_D, and possibly, also to the total time over which decapping takes place.

From the series of the capped samples with varying d_{cap}, cross-sectional HRTEM images were recorded for the samples corresponding to $d_{cap} = 1$ and 5 nm. The HRTEM image for $d_{cap} = 5$ nm, and a corresponding color-coded map of the c-parameter variation are shown in Fig. 8.7 (a) and (b), respectively.

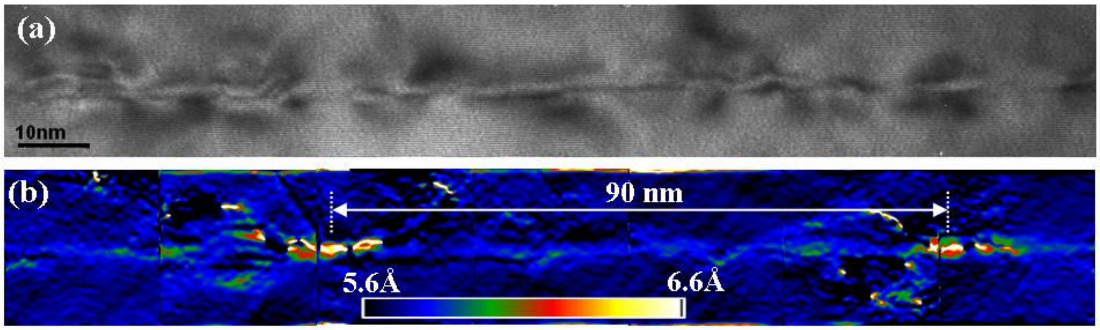

Fig. 8.7:(a) HRTEM image (bright-field) and (b) a color-coded c-parameter map (same region), recorded from a capped sample, corresponding to $d_{cap} = 5$ nm, $\Theta = 3$ ML, and $T_D = 310$ °C.

Instead of distinct islands, as observed in the AFM image (Fig. 8.2 (c)), the HRTEM image reveals an undulated layer-like structure, with thickness fluctuations. A similar structure was also seen in case of $d_{cap} = 1$ nm. The fact that no well-defined island-like structures are seen in the image might be attributed to segregation of Cd during capping, as discussed in the previous chapters in detail. The c-parameter map of Fig. 8.7 (b) reveals that flat but Cd-rich regions, extending laterally up to 8 nm, exist within the compositionally-inhomogeneous layer. However, it would be inappropriate to quote the amount of Cd within these regions since what the map displays is essentially the variation in the c-parameter (or the vertical lattice constant). As the extent of Te-admixture of the structures is not known (at least for this sample), the vertical lattice-constant values cannot be unambiguously correlated to the composition of the QDs. This would further be obscured by the uncertainty in their strain status (see discussion in section 5.2 in the context of Fig. 5.9 and 5.10). What is evident is that local Cd-rich inclusions exist within a QW-like structure, the global Cd-content of which is comparatively low. Two such inclusions are seen in the image, separated by ~ 90 nm. The separation corresponds approximately to the centre-to-centre distance between the 3D features of the uncapped sample (Fig 8.2(c)). It might therefore be inferred that the Cd-rich regions of the c-parameter map define the locations, where the islands existed before capping.

In large-area low resolution TEM images, the cap layer of the sample corresponding to $d_{cap} = 5$ nm showed some stacking faults, while for $d_{cap} = 1$ nm, no such stacking faults could be seen. This is attributed to the presence of certain dislocated islands in case of the former. In AFM, it was observed that the size of the islands increased with increasing d_{cap}. Indeed, well-defined islands are formed for $d_{cap} \geq 5$ nm. Some of these islands are possibly very large and/ or strongly alloyed with Te.

For d_{cap} = 1, 5, and 60 nm, the PL spectra recorded at 7 and 300 K, are shown in Fig. 8.8 (a) and 8.8 (b), respectively. Despite long growth interruptions and thermal cycling during growth, Te-capping, and de-capping, the luminescence intensity at 7 K is considerably high, for all three samples. It is seen that the low-temperature PL for d_{cap} = 1 nm is most intense. For higher values, the intensity is weakened. This might be related to the increasing density of stacking faults, with increasing d_{cap}.

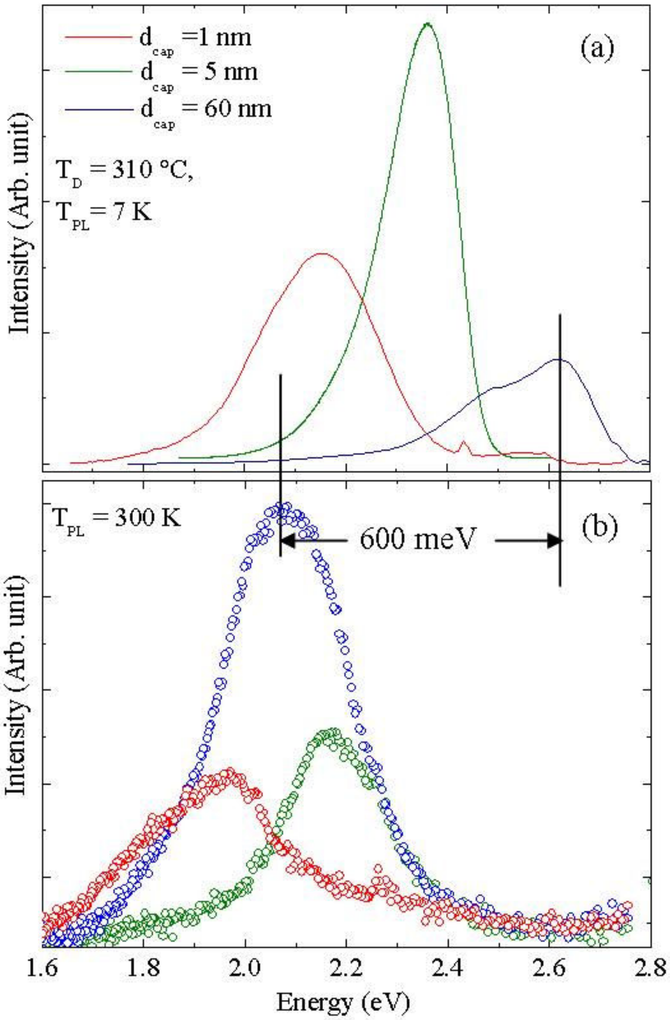

Fig. 8.8: PL spectra of different capped samples from the series where d_{cap} was varied. The spectra were recorded at (a) 7 K and (b) 300 K.

For d_{cap} = 1 nm, the PL maximum lies at 2.35 eV. The spectrum reaches values down to 2.1 eV. On increasing d_{cap} to 5 nm, The PL-maximum shifts to 2.15 eV. Albeit the HRTEM images corresponding to both d_{cap} = 1 and 5 nm revealed a layer-like morphology, the inclusions of the latter are possibly richer in Cd and more pronounced. Consequently, exciton confinement is stronger in case of d_{cap} = 5 nm, thus explaining the 200 meV redshift of this spectrum, compared to that for d_{cap} = 1 nm. Some weak features are also observed at ~2.6 eV. These features might be assigned to some inhomogeneities of the 2D "wetting layer" (between the Cd-rich regions), as observed in Fig. 8.7(b). The exciton Bohr radius of CdSe being small (~ 5 nm), even small compositional inhomogeneities of the wetting layer would confine excitons three-dimensionally. For d_{cap} = 60 nm, the spectrum reveals a maximum at 2.6 eV and is broadened over a large range of 800 meV. The high-energy-edge of the PL spectrum reaches the excitonic ZnSe bandgap. This indicates to the absence of a *continuous* 2D layer between the QDs. In absence of a continuous wetting layer, exciton capture within the large QD-pairs and redistribution within the whole ensemble in general, is rather inefficient at low temperatures. Thus the corresponding PL emission is contributed by QD-pairs of almost all sizes and also the compositional inhomogeneities of the discontinuous wetting layer. This explains the observed broad spectrum.

At 300 K, the PL spectra (Fig. 8.8(b)) of all three layers are significantly narrower. For d_{cap} = 60 nm, the peak-maximum is enormously (600 meV) redshifted. This suggests that at high temperatures, the excitons easily escape the shallow confining potential of the very small QD-pairs and the wetting-layer-inhomogeneities, and relax into the larger QD-pairs. A smaller but similar exciton-redistribution also takes place within the ensemble corresponding to d_{cap} = 5 nm. Therefore, the room-temperature PL for all three samples is attributed solely to the large features observed in the AFM images.

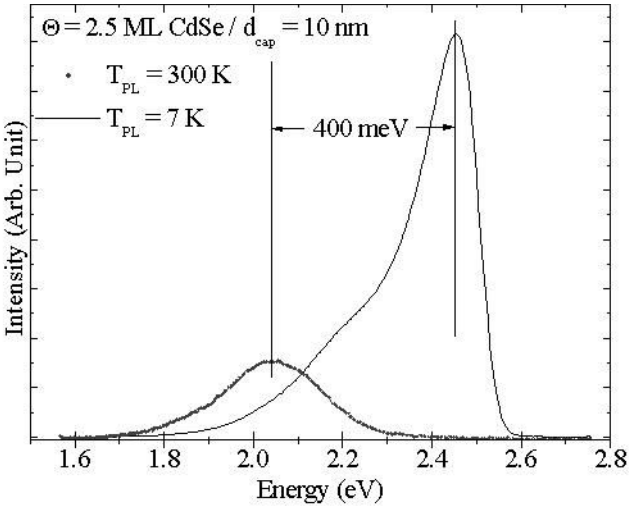

Fig. 8.9: PL spectra of the QD-layer, corresponding to Θ = 2.5 ML, d_{cap} = 10 nm, recorded at 7 and 300 K.

Fig. 8.9 (a) shows the PL spectra recorded at 7 and 300 K for the sample with Θ = 2.5 ML (AFM image of Fig. 8.2 (a)). The broad spectrum at 7 K consists of a peak at 2.45 eV and a shoulder reaching values down to 2.05 eV. It is noteworthy that the areal density of QDs in this case, similar to that of the QD-pairs corresponding to d_{cap} = 60 nm, is low. Thus, the low temperature PL of this sample is also assigned to two different types of QDs, namely, the large islands observed in AFM and those within the inhomogeneous 2D-layer between them. At 300 K, similar to the samples with Θ = 3 ML, the emission arises solely from the large QDs, leading also in this case to a large red-shift of 400 meV.

BOX 8.1 Te-isolelectronic centers in ZnSe$_{1-x}$Te$_x$

Isoelectronic impurities incorporated in binary compounds introduce trapping potentials due to difference in electronegativity. If the impurity atom is less electronegative than the host atom it substitutes (e.g. Te$_{Se}$ in ZnSe), a hole is localized by the strong short-range interaction. An electron is then bound to the localized hole by Coulombic interaction to form a localized exciton at the isoelectronic trap. Since localization of carriers is fast and non-radiative Auger recombination involving a third particle does not occur, radiative recombination of such excitons can be very efficient. ZnSe$_{1-x}$Te$_x$ belongs to an interesting class of semiconductors in which Te acts both as an isoelectronic trap and as a constituent of the alloy [Yao88].

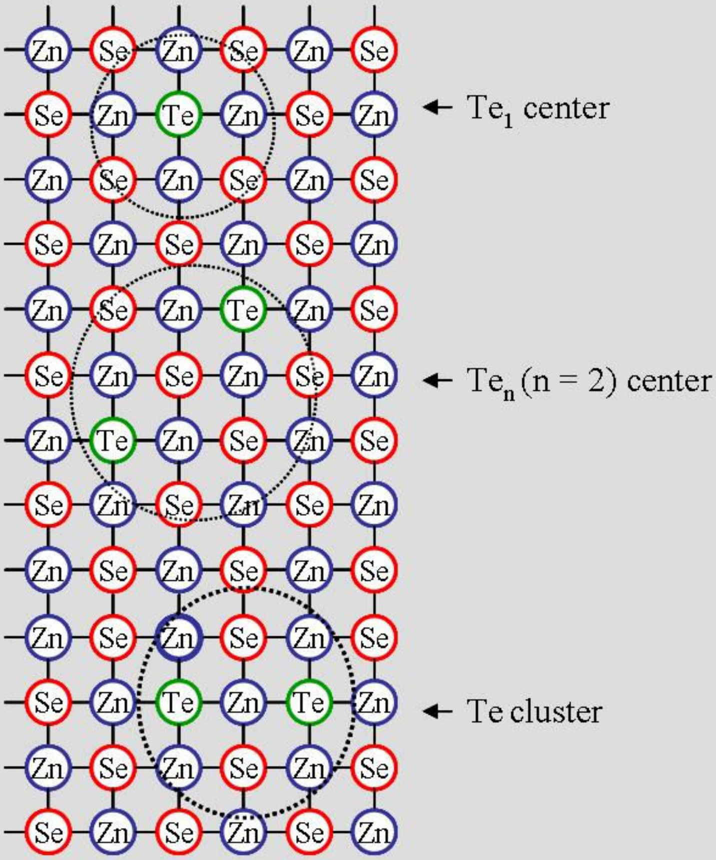

Fig. 8.10: Te isoelectronic centers in ZnSe$_{1-x}$Te$_x$ (adopted from [Yang98])

At very low concentrations of Te, isoelectronic traps are formed by isolated Te$_{Se}$ impurities (see Fig 8.10), which are called Te$_1$ centers. For higher concentrations, more such isolated Te$_{Se}$ impurities form the trap. If two or more Te$_{Se}$ impurities share a common Zn atom, the trap is known to be a Te cluster. If they are attached to different Zn atoms they are termed as Te$_n$ ($n \geq 2$) centers [Yang98]. Te-clusters and Te$_n$ centers have deeper potentials compared to Te$_1$ centers. Te-isoelectronic centers have been observed also in other II-VI alloy systems, e.g. CdS$_{1-x}$Te$_x$ [Goede81, Heimbrodt86] and CdS$_{1-x}$Se [Permogorov82]. Unfortunately, the CdSe$_{1-x}$Te$_x$ system has not been studied so far.

So far, in explaining the PL characteristics, the role of Te in the QD-layer has been implicitly neglected. Albeit the evolution of the spectra with d_{cap} and temperature could be sufficiently explained by considering only the size, size-distribution, and areal density of the QDs, certain peculiar features clearly indicate to the presence of Te. Corresponding to $d_{cap} = 5$ nm, the low-energy edge of the PL-spectrum at 7 K (Fig. 2.8 (a)) reaches values down to 1.8 eV. At 300 K, some PL-intensity is observed even at 1.7 eV, in all spectra. These energy values correspond to the bandgap of CdSe at the respective temperatures. Considering quantum confinement to raise the energy of the ground electron and hole states in a QD, the PL at such low energies might be comprehended as an additional signature of Te-alloying of the QDs. The broad spectrum corresponding to $\Theta = 3$ ML ($d_{cap} = 60$ nm) and $\Theta = 2.5$ ML ($d_{cap} = 10$ nm) might then be attributed not only to a large distribution of QD-sizes, but also to a distribution of QD-composition (i.e. Te-content).

The consequence of Te-admixture of the QD-layer might be more than this humble red-shift of the PL band, compared to conventional-MBE grown QD-layers. In particular, one effect needs special consideration. It is related to the luminescence from excitons bound to Te-"isoelectronic" centers in II-selenides. This subject has been extensively studied for $ZnSe_{1-x}Te_x$ alloy layers, with x varying between 0.005-0.4 [Lee87, Yao88, Dhese92, Lee92, Yang98, Kuskovsky2001, Gu05]. The basic definition of isoelectronic centers, consisting either of a single Te atom (Te_1), more than one Te atoms (Te_n, $n \geq 2$), or Te-clusters is presented in BOX 8.1.

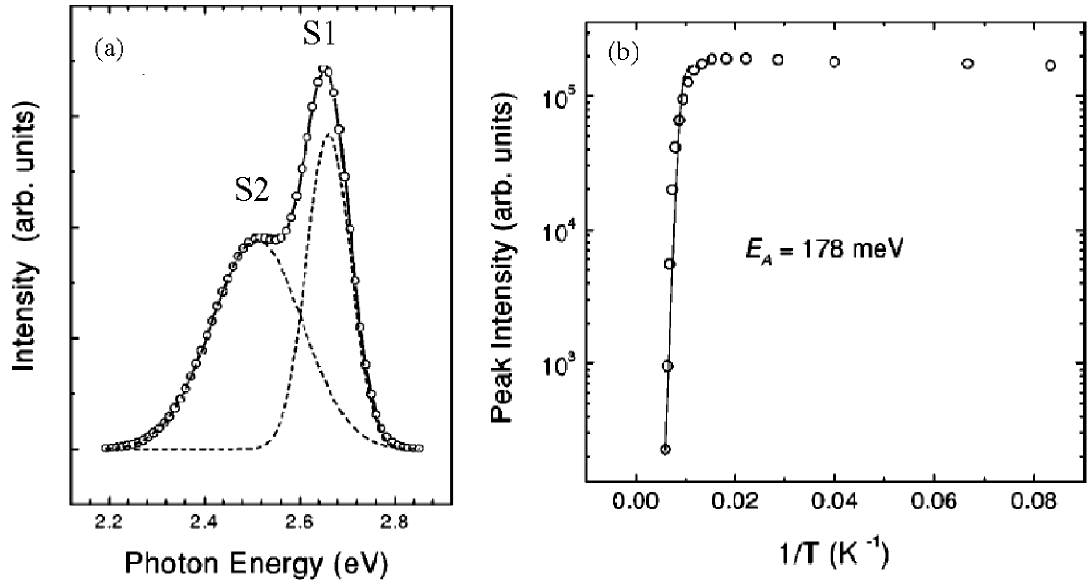

Fig. 8.11: (a) PL due to Te_1 (S1) and Te_n (S2) centers, recorded from a ZnSe layer consisting of several δ-doped Te layers. (b) Luminescence intensity versus inverse temperature plot of the S2 band of (a). Adopted from [Kuskovsky01]

In bulk ZnSeTe crystals, as well as thick epilayers, excitons trapped to Te_1 and Te_n centers result in PL-bands (at $T_{PL} \leq 50$ K) centered at 2.6-2.65 eV ("blue" or S1 band)

and 2.48-2.5 eV ("green" or S2 band), respectively [Dhese92]. The PL spectrum corresponding to a thick ZnSe layer, consisting of multiple δ-doped layers of Te, is shown in Fig. 8.11(a). As clearly seen, the line-shape of this spectrum is similar to that corresponding to $\Theta = 2.5$ ML (Fig. 8.9). The evolution of the S1 and the S2 bands with increasing T_{PL} is also not trivial. The luminescence intensity of both bands decrease rapidly with temperature. The S1 band is quenched above $T_{PL} = 100$ K but the S2 band persists up to $T_{PL} \approx 200$ K [Dhese92]. The temperature dependence of the S2-band intensity is shown in Fig. 8.11 (b). Qualitatively, it is similar to what has been measured for QDs in the previous chapters (refer to Fig. 5.7 (b) and 6.9).

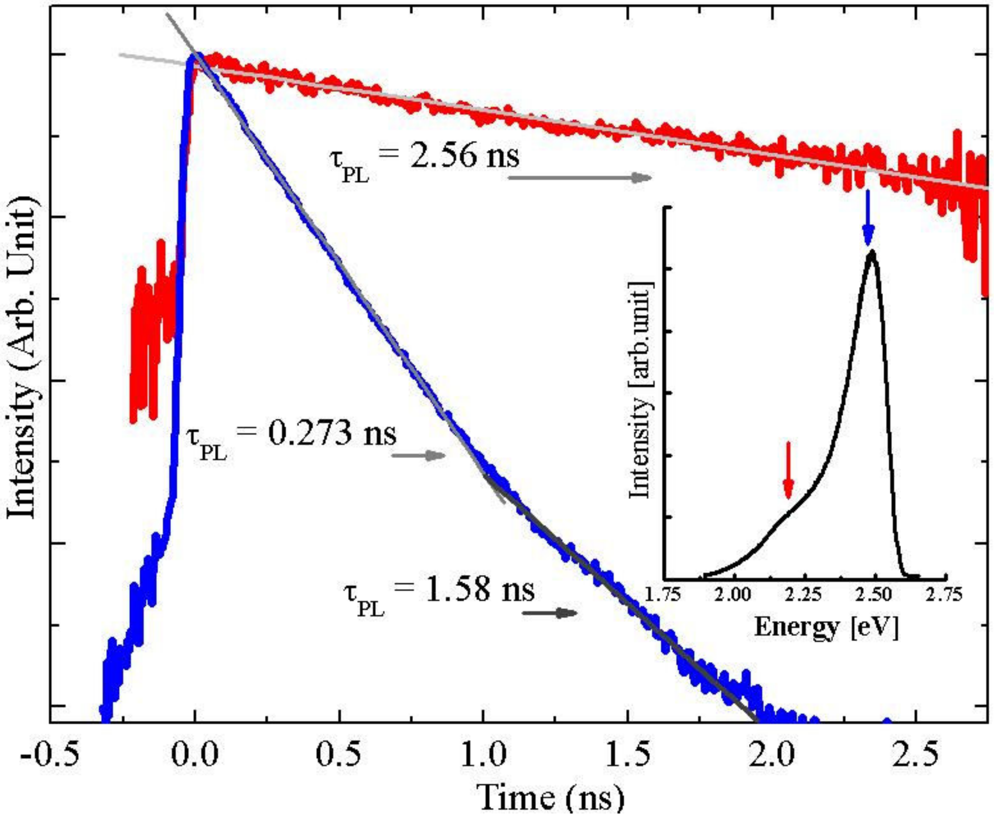

Fig. 8.12: Time-resolved PL spectra recorded for the sample with $\Theta = 2.5$ ML ($d_{cap} = 10$ nm, Fig. 8.2 (b)) at two different detection energies (marked by the arrows in the PL spectrum shown in the inset).

The role of Te in CdSe epilayers has not been studied in the past. However, PL from such Te-isoelectronic traps has been recently observed in CdSe:Te nanocrystals, synthesized pyrochemically [Franzl07]. In the samples discussed here, it is logical to expect that if at all, Te-isoelectronic centers would be present, both within the CdSe QD-layer and the ZnSe cap-layer (due to segregation), together with Te-alloyed/pure CdSe QDs. Albeit it is difficult to distinguish the different contributions to luminescence, some observations are made in the following discussion, based on time-resolved PL and micro-PL studies.

Fig. 8.12 shows the time-resolved PL spectra of the sample with $\Theta = 2.5$ ML ($d_{cap} = 10$ nm), recorded at 2 K. The two spectra correspond to detection energies of 2.16 eV (red) and 2.48 eV (blue), as shown by the respective arrows in the PL spectrum of the inset. The excitation energy was chosen to be 2.71 eV, i.e. below the bandgap of ZnSe. Thus, carriers were excited directly into the 2D continuum of states of the wetting layer. As seen in the Figure, the blue spectrum does not show a mono-exponential behavior, as would be expected following Eqn.3.17. Rather, the plot might be fitted with two exponential functions, yielding two different values of PL-decay-time, i.e. $\tau_{PL} = 0.273$ and 1.58 ns. Such a bi-exponential decay behavior has been observed for the luminescence of a single- (epitaxially self-assembled) CdSe/ZnSe(001)-QD-exciton, by Patton et al. [Patton03]. The values of τ_{PL} measured by the authors are 0.24 and 2.5 ns, i.e. comparable to the values obtained here. The two different decay-times are explained by a three-level model, which includes the bright and the dark exciton ground states. The initial short decay-time accounts for the radiative recombination of the bright exciton, as well as, exciton-transition from bright to dark states [Patton03]. The long-time component is then attributed to exciton-repopulation of the bright- from the dark-states and subsequent recombination.

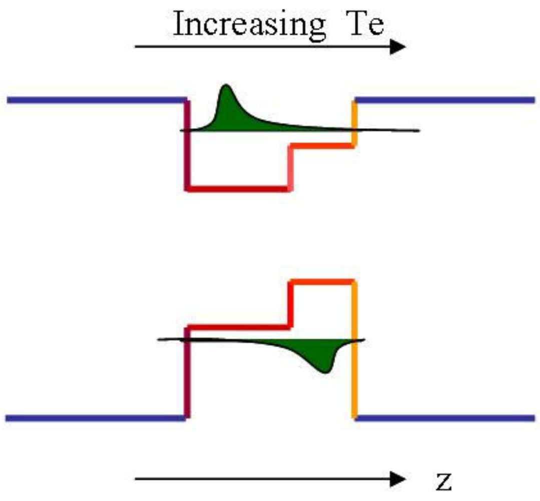

Fig. 8.13: Schematic representation of the QD-potential in the growth direction (z), considering an increasing Te-alloying from the bottom to top of the island

On the other hand, the PL-decay at the low detection energy (the red spectrum) is mono-exponential, characterized by a decay time of 2.56 ns. An increase in τ_{PL} with decreasing detection energy is characteristic of QD-ensembles and has also been observed for conventional-MBE grown samples [Gindele99]. At lower detection energies the QDs probed are larger in size and the increase in τ_{PL} is assigned to smaller confinement energy [Sugawara95]. However, the value of 2.56 ns is much larger than what is known for typical CdSe/ZnSe(001)-QDs [Gindele99]. The reason for this discrepancy might be the large size of the QDs formed in “Te-mediated self-assembly”. The splitting between the light and the dark exciton states decreases with increasing QD-size [Efros96]. Consequently, for larger QDs, it might be assumed that the rate of exciton transition from the bright to the dark states is higher. The temporal decay of the luminescence is then characterized only by the long-time component, due to repopulation of bright states and subsequent recombination. Based on the previous discussion of (time-integrated) PL, at the detection energy of 2.16, it might be assumed that only the large QDs are probed. However, the splitting between the bright and the dark exciton states depends critically on the band structure of the QD-material [Efros96] and should therefore, also be affected by Te-alloying of the QDs.

Considering Te-alloying of the QDs, another reason might be given for the long decay times. The explanation is based on the assumptions that the Te-alloying is stronger in larger QDs and that the alloying occurs predominantly at the apices of the islands. These assumptions are supported by the GIXRD measurements. With a gradient in Te-admixture along the growth direction, the band diagram of such QDs might be represented by the (simplified) schematic of Fig. 8.13. To comprehend the shown band-diagram, it is helpful to note at the outset that at a hetero-interface between pure CdSe and CdTe, the band-alignment is of type-II. In type-II heterostructures electrons and holes are confined in opposite sides of the interface, since the conduction and the valence band offsets are of opposite sign (see Fig. 8.13). Thus, in presence of a gradient in the Te-alloying, the hole-wave-function would be confined more strongly in the Te-rich “top part” of the QD, while the electron wave-function in the Se-rich “bottom part”. This spatial separation of the electron- and hole-wavefunctions would reduce the overlap between them and result in longer decay-times [Hatami98]. The PL-decay characteristics might then be explained simply by considering luminescence contributions from QDs of different size and Te-content and therefore, different extent of overlap between the electron and hole wave-functions. At the lower detection energy, possibly, only the larger QDs, with higher Te-content, are probed, which leads to the mono-exponential temporal decay of PL, characterized by a long decay-time.

Finally, it is imperative to consider a third possibility. The long-decay time might also result due to the presence of some Te-isoelectronic centers within or in the vicinity of the QDs. Since the Te-isoelectronic centers bind holes (see BOX 8.1), their presence would influence the overlap of electron- and hole-wave-functions and thereby, the exciton decay time. For the S_2-band-maximum of Fig. 8.11, Gu et al. recorded a mono-exponential decay with τ_{PL} as large as 86 ns [Gu05]. The value of only 2.56 ns measured here at the detection energy of 2.16 eV would therefore suggest that the excitons are predominantly confined within the QDs, however bearing some influence of the isoelectronic traps.

In Fig. 8.14, a μ-PL spectrum of the sample with $\Theta = 2.5$ ML ($d_{cap} = 10$ nm), recorded at 2 K, is shown. For every investigated mesa of comparable size, a large number of narrow emission lines were recorded between 2.4-2.5 eV, and relatively few of them in the range between 2.15-2.3 eV. Such narrow emission lines might be assigned to excitons confined within QDs. Further, the fact that only a few lines are observed in the low energy range and a significantly larger number of them in the high energy range substantiates the assumption that the PL at low temperature is contributed both by the dilute ensemble of large QDs observed by AFM (Fig. 8.2 (a)) and a high density of composition-inhomogeneities of the 2D wetting layer between them (Fig. 8.2 (g)). The characteristic energy splitting of the excitonic ground state and the corresponding linear polarization trends, due to anisotropic shape of the QDs were also observed [Hanke07]. Additionally, several charged and multi-excitonic complexes (refer to section 2.8, Fig. 2.21), such as negative trions ($1e^21h^1$), biexcitons ($1e^21h^2$), and charged biexcitons ($1e^22e^11h^2$) could also be identified in the spectrum, based on their spectral positions and polarization-attributes [Hanke07, Beha07]. The observation of such multi-excitonic complexes suggests that the PL emission arise from QDs.

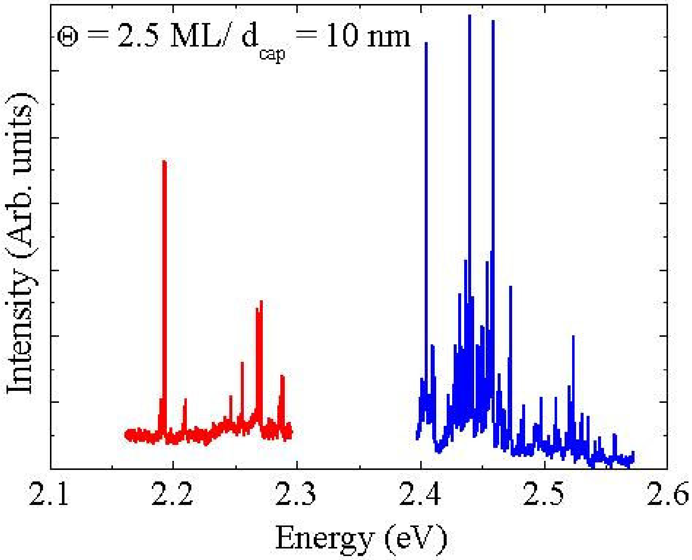

Fig. 8.14: μ-PL spectra recorded at 2 K from the sample with Θ = 2.5 ML (d_{cap} = 10 nm).

As a caveat however, it is worth noting that whether sharp emission lines might also be assigned to excitons or even multi-excitonic complexes bound to Te_n centers with different n-values (including 1), is not known. An argument against the possibility is as follows: Corresponding to each value of n, excitons bound to Te_n centers should have well-defined energy states. Thus in μ-PL measurements, emission lines should be observed at a few definite spectral positions for all mesas. However, a considerable scatter in the spectral positions of the single emission lines was observed for different mesas. Secondly, excitons bound to Te-isoelectronic centers are known to couple strongly to phonon modes, leading to broadening of the luminescence spectra [Dhese92]

The luminescence of the capped sample corresponding to d_{cap} = 60 nm (Θ = 3 ML) showed strong preferential linear polarization along the <110> axes. The plot of DLP versus the rotation angle, measured in angle-resolved-polarized-PL spectroscopy (refer to section 5.2, Fig. 5.8), is shown in Fig. 8.15. Similar to the case of conventional-MBE grown QDs (Fig. 5.8), the DLP peaks along the <110> directions. However, the absolute value of DLP in this case is an order of magnitude higher. To analyze this enhancement it is useful to note that the above measurement is based on the luminescence of a large (~ 10^4-10^5) ensemble of QDs. When only a small fraction of the QDs are preferentially elongated along a particular direction, while the shape-asymmetry and orientation of the others are mostly random, the DLP is low, simply due to statistical averaging. This is typically the situation in MBE-grown samples. Referring back to Fig. 8.2 (e), it is seen that for the sample measured here, almost all QD-pairs are aligned and elongated along one of the <110> directions. This results in the enhancement of the DLP. The enhancement of DLP might be counted as one more evidence in favor of the claim that excitons confined within QDs predominantly contribute to the luminescence of these samples.

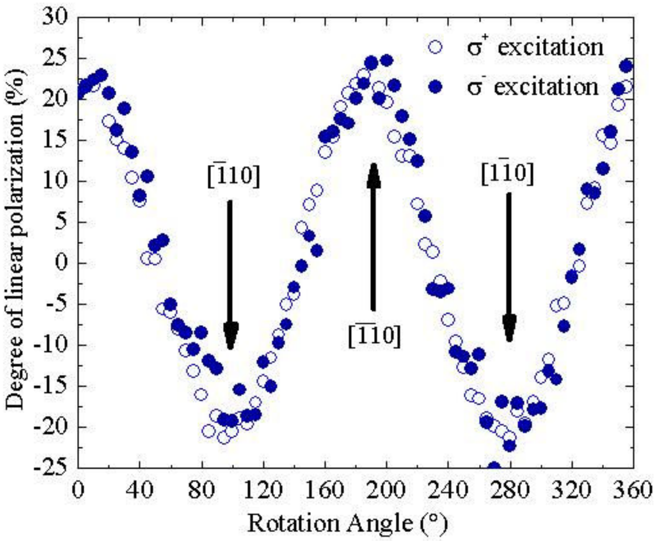

Fig. 8.15: Crystallographic-direction dependence of the PL-degree-of-linear-polarization, corresponding to the sample with d_{cap} = 60 nm and Θ = 3 ML (for both right and left circularly polarized excitation).

8.3 *Formation mechanism of self-assembled island-patterns*

Having analyzed the structure, composition, and luminescence characteristics of the QDs formed in "Te mediated self assembly", in this section, the formation-mechanism of self-assembled island-patterns by this technique is analyzed. At the outset, it is helpful to consider two unique aspects of the technique, on which the premise of the model is based.

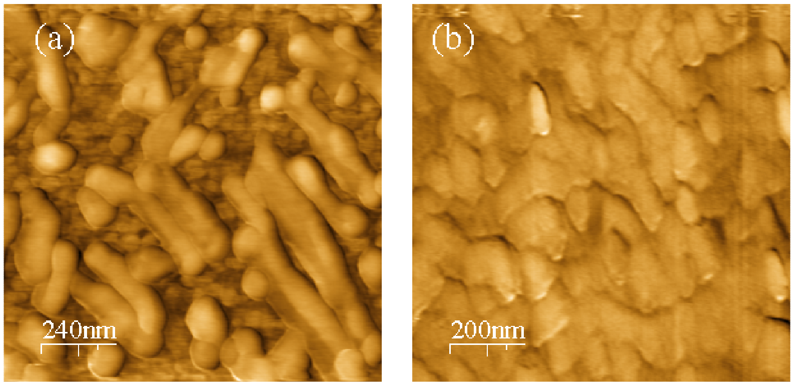

Fig. 8.16: AFM image of the surface of a partially desorbed Te-cap, at a stage corresponding to the RHEED image of Fig. 8.1(c), for d_{cap} = (a) 5 nm and (b) = 15 nm.

Firstly, in epitaxial self-assembly, the areal density of islands depends critically on the temperature of formation (T_D in our case) [Joyce97]. Here, to the contrary, both areal density and the spatial patterns of the islands are strongly governed by d_{cap}, while T_D influences only marginally their size and separation.

Secondly, in "*a*-Se mediated self assembly" (discussed in Chapter 7), *a*-Se does not crystallize during temperature ramp-up to T_D and the resultant island-ensembles are devoid of any pattern. To the contrary, in "Te-mediated self-assembly", distinct RHEED pattern, related to a polycrystalline (but epitaxially oriented) Te layer is observed (Fig. 8.1 (c)), for all $d_{cap} \geq 1$ nm.

Both facts suggest strongly that the self-assembled patterns of the islands are influenced by the morphological evolution of the Te-cap layer, during temperature ramp-up to T_D. Therefore, the topography of the Te-layer, corresponding to the RHEED image of Fig. 8.1(c) was investigated. Two samples, with d_{cap} = 5 and 15 nm, were heated up to 230-240 °C, held for 5 mins, and cooled down for AFM imaging. The corresponding surfaces are shown in Fig. 8.16 (a) and 8.16 (b), respectively. A polycrystalline layer is clearly seen, for d_{cap} = 15 nm (Fig. 8.16 (b)). The network of the grain boundaries of the Te-layer resembles closely the pattern of buckled island-chains, seen in Fig. 8.2 (d). Under similar treatment, the Te-layer corresponding to d_{cap} = 5 nm appears to have already desorbed on certain areas, exposing the underlying CdSe surface. On these exposed regions, 3D features, characteristic of the initial stages of island-formation, are observed. The Te-residues and the "trenches" between them are elongated in a particular direction, similar to the island-chains of Fig. 8.2 (c).

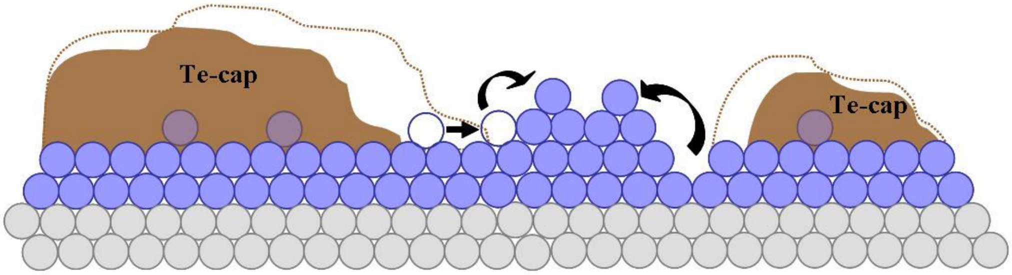

Fig. 8.17: Schematic illustration of the formation-mechanism of island-patterns. The blank and filled contours represent the Te cap at an earlier and later instant, respectively, during desorption. With desorption of the Te layer, adatoms are progressively set free, which are then grabbed by the initially formed nuclei.

Based on these observations, the model for formation of self-assembled island-patterns is postulated as follows: Desorption begins preferentially along the grain boundaries of the polycrystalline Te-layer. This exposes the underlying CdSe surface first in narrow trenches, which follow the pattern of the grain boundaries. Within these trenches islands nucleate by aggregation of surface adatoms, "remobilized" after Te-desorption. This situation is illustrated schematically in Fig. 8.17. Subsequently, the nuclei accumulate more adatoms from the surrounding CdSe surface, exposed progressively with continuing Te-desorption. Material transport occurs also from the "bulk" of the CdSe layer to the nucleated islands (see Fig.8.17). This is substantiated by the absence of a continuous wetting layer in case of d_{cap} = 60 nm and is also known in SK growth of islands (refer to section 2.4).

For d_{cap} = 60 nm (Θ = 3 ML and T_D = 310 °C), the CdSe layer is presumably exposed in isolated, short, and oriented trenches, where the island-pairs nucleate. The separation between the islands of the pairs is tentatively determined by the repulsive elastic interaction of strain-relaxed islands [Shchukin95]. The observed smaller size of the islands, within the pairs formed at the lower T_D = 220 °C (Fig. 8.2(f)), is explained by reduced surface migration of adatoms. The smaller inter-island separation is then assigned to a lower repulsive elastic interaction between the islands, in turn, due to reduced strain-relaxation of smaller islands.

Within the purview of the model, the participation and role of Te atoms in the whole process is not clear. Te might play an active role in promoting island-nucleation at the initial stages. Due to the large lattice misfit between CdTe and GaAs (0.146), sub-ML CdTe clusters would act as “stressor” nuclei, providing sinks for subsequent migration of adatoms. Such stressor-CdTe nuclei have also been used in the past to enhance formation of CdSe/ZnSe(001) islands [Toropov06]. The assumption of a gradient in Te-content of the islands (with higher amounts close to the apices) is then explained by the tendency of Te to segregate, due to the lower heat of formation of CdTe (in comparison to CdSe). The segregation would also be driven by the lower elastic energy cost of integrating Te in strain relaxed CdSe layers, at higher levels of the islands. However, Te might also be simply incorporated to the islands during the interval when desorption is not complete, yet island-nucleation has initiated (The situation of Fig. 8.16 (a)).

8.4 A proposal for controlled positioning of individual QDs

In view of the above model, a simple and “clean” method for controlled positioning of individual QDs or extended QD-based structures is proposed, in this section. Controlled positioning of QDs is in the focus of current research, since applications like single photon sources and solid-state qubits require access to individual QDs. In the above discussion, it was argued that the morphology of the island-ensembles was determined by the configuration of the grain boundaries of the polycrystalline Te cap layer. Instead of depending on such grain boundaries of a polycrystalline layer, sites for island-nucleation can be defined by direct writing of shallow holes in a smooth, *non-crystallizing*, amorphous cap layer (i.e. *a*-Se for CdSe/ZnSe(001) QDs), using techniques like focused-ion-beam (FIB)-, scanning-tunneling (STM)-, or even (in-situ) atomic-force-microscopy (AFM)-patterning. Desorption, as explained before, would initiate preferably in the predefined sites, thus defining the positions for island nucleation. While the pattern of the holes would determine the position and type of nanostructures (single, pair, or chains of QDs), the size of the QDs might be tuned by the choice of T_D and Θ. The approach might be extended to other heterosystems as well, i.e. *a*-Te/CdTe/ZnTe or a-As/InAs/GaAs.

Lithography is the standard tool used to position single QDs and to obtain large-scale lateral-ordering. In most cases, the substrate is pre-patterned to define positions for island-nucleation during subsequent heteroepitaxial self-assembly [Zhong04, Stangl04].

However, standard e-beam or photolithography and etching techniques involve usage of organic photoresists and etchants. This leads to chemical contamination of the surface, which is unwarranted for a UHV growth-system, as well as, for self-assembly of coherent nanostructures.

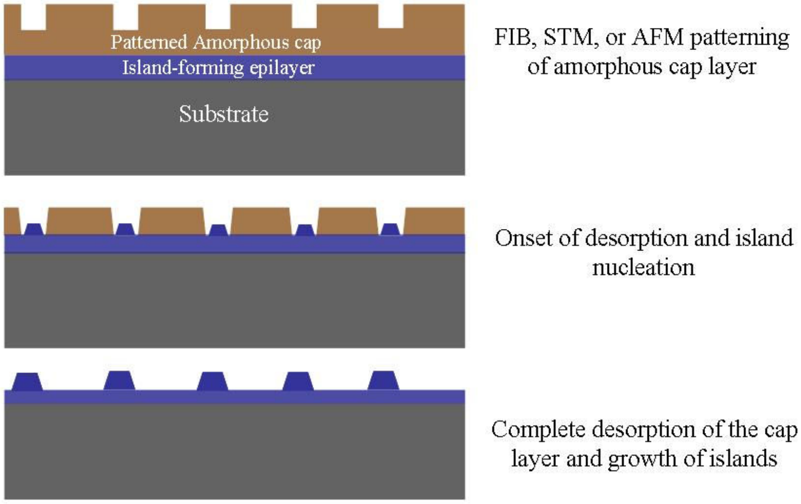

Fig. 8.18: Schematic representation of the proposal for controlled positioning of individual QDs.

By the technique proposed here, since no substrate pre-patterning is necessary, the use of organic chemicals is completely avoided. Additionally, since the involved patterning is performed on the amorphous cap layer, the epitaxial layers underneath are protected from the atmospheric ambient, during the interval out of the UHV system. Furthermore, using an AFM or STM or cross-beam-FIB facility connected to the MBE system (with slightly more favorable patronage of the funding agents) all process steps of the proposed QD-positioning technique might be performed in UHV.

Summary

In summary, this chapter dealt with formation of CdSe(Te) QDs by “Te mediated self-assembly”. The technique is similar to “*a*-Se mediated self assembly”- the only difference being in the use of Te, instead of Se, as the cap-forming material. The simple substitution of Se with Te led to profound changes in the morphological, compositional, and luminescence properties of the resultant QDs, and also to the self-assembly process itself. The islands were found to assemble in different patterns, i.e. straight and buckled chains and oriented island-pairs. Te-admixture of the islands could also be detected. In capped samples, PL emission was recorded at values as low as 1.9 eV. Luminescence at such low energies is typically not obtained from conventional-MBE grown samples. Strong anisotropic optical response was also seen for the ensemble of QD-pairs, in agreement with their preferential alignment and elongation in a particular direction. Finally, the mechanism underlying the formation of different self-assembled morphologies of the island-ensembles was analyzed and correlated to the crystallization of the Te-layer during ramp up to the desorption temperature. Based on the analysis, a method for controlled positioning of individual islands was also proposed, in the last section.

Conclusions and outlook

9

The purpose of this thesis was to explore the properties and formation mechanism of epitaxial CdSe/ZnSe(001) quantum dots (QDs), self-assembled in conventional molecular beam epitaxy (MBE) and a few other related alternative techniques. The main conclusions that might be drawn from the work are as follows:

1. In conventional MBE growth of CdSe on ZnSe(001) surfaces (at $T_G = 300$ °C), a high density of QDs are formed by local Cd-rich regions of an inhomogeneous CdZnSe QW-like structure. The uncapped surface is devoid of any well-defined three-dimensional (3D) islands but is characterized by a dense morphology of shallow mounds, elongated and weakly oriented in the [110] direction. The origin of such mounds is in multilayer growth of CdSe at $T_G = 300$ °C.

   While at $T_G = 300$ °C, CdSe growth occurs in the multilayer mode, at $T_G \leq \sim 240$ °C, the layer-by-layer-growth mode is partially recovered. The recovery is presumably due to suppression/breakdown of ES barrier at the concomitant reestablishment of adatom “down-climb”.

2. Among the alternative techniques, in “low temperature epitaxy and in-situ annealing”, tiny but distinct islands are formed. While growth at low temperature (T_G = 230 °C) leads to the formation of a quasi-two-dimensional (quasi-2D) CdSe layer, subsequent annealing at a higher temperature (310 °C) results in reorganization of the surface and formation of the three dimensional (3D) islands. The surface reorganization is driven by a thermally activated “up-climb” of adatoms onto two-dimensional (2D) clusters (or precursors). These adatoms subsequently aggregate and form the 3D islands. However, in capped samples the QDs appear to be similar to those formed in conventional MBE, i.e. Cd-rich inclusions of a ternary CdZnSe QW. This is presumably related to segregation of Cd during ZnSe-capping. By this technique, the areal density of QDs is reduced by more than an order of magnitude, in comparison to conventional-MBE growth. Further reduction is possible by appropriately delaying the temperature ramp-up to T_A, after CdSe growth at T_G.

3. In the second variant technique, QD-formation is induced by capping of a 2D CdSe layer (grown at T_G = 230 °C) with amorphous Se (*a*-Se) at room temperature and its subsequent decapping at T_D = 230 °C. The resultant islands are larger than those formed by the previous techniques. However, even in this case, the islands are modified to some extent during capping, due to Cd-segregation.

   A distinct vertical correlation of well-defined islands takes place in QD-superlattices, consisting of a “seed” QD-layer grown by the above technique and subsequent QD-layers grown by migration enhanced epitaxy (MEE).

4. The third technique studied in this work is similar to the previous one, the only alteration being the replacement of Se with Te as the cap-forming material. This technique leads to formation of island-ensembles in different self-assembled patterns. Long dashes, chains of islands, and island-pairs are formed, depending on the thickness of the Te-cap layer. Unlike the *a*-Se cap layer in the previous method, the Te cap layer undergoes (poly)crystallization during temperature ramp-up (from room temperature to T_D) for decapping. The self-assembled patterns of the island-ensembles are determined by the pattern of the grain boundaries of the polycrystalline Te layer. The islands are however partially alloyed with Te. Luminescence at very low energies (down to 1.7 eV at room temperature) was recorded from the capped samples.

Quantum dots of the wide band-gap CdSe/ZnSe heterosystem might pave the way for several promising applications in future. However, the formation-mechanism of such

QDs is far from trivial and current fabrication techniques allow minimal optimization in terms of QD-size and areal density. Therefore, research efforts are warranted for a thorough understanding of different aspects of CdSe/ZnSe(001) heteroepitaxy in general and QD-self-assembly in particular. Some studies that might be pursued in future are listed below:

I. In-situ scanning tunneling microscopy (STM) could be employed to investigate the atomistic processes of CdSe/ZnSe(001) heteroepitaxy. Several inferences made in this thesis, partly speculatively, might be verified. For example, the mechanism underlying the recovery of layer-by-layer growth at low temperature and surface reorganization during annealing (by the first alternative technique) might be directly probed. Additionally, STM would also provide valuable information regarding diffusion lengths of adatoms, intermixing and segregation, and might therefore help identify the main limitation of island formation in CdSe/ZnSe(001) heteroepitaxy.

II. To suppress segregation of Cd and concomitant collapse of the tiny islands formed in "low temperature epitaxy and in-situ annealing", low temperature capping might be tried out. If the low temperature capping turns out to be shape-preserving, QD-superlattices might be grown to study coupled QDs.

III. The "*a*-Se mediated self-assembly method" might be tried out for high-index GaAs substrates, especially GaAs(110). This could lead to ordering of the resultant QDs along the step edges.

IV. The method for positioning of single QDs and QD-based extended nanostructures, explained in section 8. 4, might turn out to be technologically beneficial for future applications requiring access to a single or a few QDs. If successful, the method would eliminate pre-patterning of substrates and concomitant unwarranted contamination.

V. A new system which might be studied to obtain luminescence below 2.0 eV is the ternary CdSeTe system. The system would allow variation of lattice misfit and confinement energies over a large range. Besides, the bandgap variation of the alloy is characterized by a strong bowing, which might also be of interesting consequences.

VI. In the past, (including this work), CdSe growth has been always performed under highly Se-rich growth conditions. The resultant QDs are anisotropic in shape and preferentially elongated in the direction of the Se dimer rows [110]. A plausible way to manipulate the shape anisotropy of the QDs would be to switch to Cd-rich growth conditions.

Bibliograpy

[Ahsan97] S. Ahsan, A. Kahn, M. D. Pashley, *Appl. Phys. Lett.* **71**, 2178 (1997).

[Aichele04] T. Aichele, V. Zwiller, O. Benson, *New J. Phys.* **6**, 90 (2004).

[Albrecht95] M. Albrecht, S.Christiansen, J. Michler, W.Dorsch, H. P. Strunk, P. O.Hansson, E. Bauser, *Appl. Phys. Lett.* **67**, 1232 (1995).

[Arai00] K. Arai, T. Hanada, T. Yao, *J. Cryst. Growth* **214/215**, 703 (2000).

[Asaro72] R. J. Asaro, W. A. Tiller, *Metall. Trans.* **3**, 1789 (1972).

[Ayers94] J. E. Ayers, *J. Cryst. Growth* **135**, 71 (1994).

[Bacher91] G. Bacher, H. Schweizer, J. Kovac, A. Forchel, H. Nickel, W. Schlapp, R. Losch, *Phys. Rev. B* **43**, 9312(1991).

[Baklenov98] O. Baklenov, H. Nie, K. A. Anselm, J.C. Campbell, B. G. Streetman, *Electron. Lett.* **34**, 694 (1998).

[Barabási97] A.L. Barabási, *Appl. Phys. Lett.* **70**, 2565 (1997).

[Bayer02] M. Bayer, G. Ortner, O. Stern, A. Kuther, A. A. Gorbunov, A. Forchel, P. Hawrylak, S. Fafard, K. Hinzer, T. L. Reinecke, S. N. Walck, *Phys. Rev. B* **65**, 195315 (2002).

[Bayer00] M. Bayer, O. Stern, A. Kuther, A. Forchel, *Phys. Rev. B* **61**, 7273 (2000).

[Bayer98] M. Bayer, T. Gutbrod, A. Forchel, V. D. Kulakovskii, A. Gorbunov, M. Michel, R. Steffen, K. H. Wang, *Phys. Rev. B* **58**, 4740 (1998).

[Beha07] K. Beha, *Master's Thesis*, Universität Konstanz (2007).

[Belk96] J. G. Belk, *Ph.D. Thesis* (University of London, unpublished, 1996).

[Belk97] J.G. Belk, C.F. McConville, J.L. Sudijono, T.S. Jones, B.A. Joyce, *Surf. Sci* **387**, 213 (1997).

[Benkert07] A Benkert, C Schumacher, K Brunner, RB Neder, *Appl. Phys. Lett.* **90**, 162105 (2007).

[Besombes00] L. Besombes, K. Kheng, D. Martrou, *Phys. Rev. Lett.* **85**, 425 (2000).

[Binnig87] G. Binnig, H. Rohrer, *Rev. Mod. Phys.* **59**, 615 (1987).

[Binnig82] G. Binnig, H. Rohrer, Ch. Gerber, E. Weibel, *Phys. Rev. Lett.* **49**, 57 (1982).

[Biolatti02] E. Biolatti, I. D'Amico, P. Zanardi, F. Rossi, *Phys. Rev. B* **65**, 075306 (2002).

[Bowen98] D. K. Bowen, B. K. Tanner, *High Resolution X-ray Diffractometry and Topography*, Taylor and Francis, London (1998).

[Brunner02] K. Brunner, *Rep. Prog. Phys.* **65**, 27 (2002).

[Campbell97] J. C. Campbell, D. L. Huffaker, H. Deng, D. G. Deppe, *Electron. Lett.* **33**, 1337 (1997).

[Capellini01] G. Capellini, M. De Seta, F. Evangelisti, *Appl. Phys. Lett.* **78**, 303 (2001).

[Carlsson94] N. Carlsson, W. Seifert, A. Petersson, P. Castrillo, M.-E. Pistol, L. Samuelson, *Appl. Phys. Lett.* **65**, 3093 (1994).

[Chu96] C. C. Chu, T. B. Ng, J. Han, G. C. Hua, R. L. Gunshor, E. Ho, E. L. Warlick, L. A. Kolodziejski, A. V. Nurmikko, *Appl. Phys. Lett.* **69**, 602 (1996).

[Constantino98] M. E. Constantino, M. A. Vidal, B. Salazar-Hernández, H. Navarro-Contreras, M. López-López, M. Meléndez, I. Hernández-Calderon, *J. Cryst. Growth* **193**, 301 (1998).

[Cullis96] A. G. Cullis, A. J. Pidduck, M. T. Emeny, *J. Cryst. Growth* **158**, 15 (1996).

[Daruka97] I. Daruka, A. L. Barabasi, *Phys. Rev. Lett.* **79**, 3708 (1997).

[Dhese92] K. Dhese, J. Goodwin, W.E. Hagston, J.E. Nicholls, J.J. Davies, B. Cockayne, P.J. Wright, *Semicond. Sci. Technol.* **7**, 1210 (1992).

[Dupré69] A. Dupré, *Théorie Méchanique de laChaleur*, Gauthier-Villard (1869)

[Efros96] Al. L. Efros, M. Rosen, M. Kuno, M. Nirmal, D. J. Norris, M. Bawendi, *Phys. Rev. B* **54**, 4843 (1996).

[Ehrlich66] G. Ehrlich, F.G. Hudda, *J. Chem. Phys.* **44**, 1039 (1966).

[Eigler90] D.M. Eigler, E.K. Schweizer, *Nature* **344**, 524 (1990).

[Elkinani94] I. Elkinani, J. Villian, *J. Phys. I* **4**, 949 (1994).

[Faschinger99] W. Faschinger, M. Ehinger, T. Schallenberg, M. Korn, *Appl. Phys. Lett.* **74**, 3404 (1999).

[Finley98] J. J. Finley, M. Skalitz, D. Heinrich, M. Arzberger, A. Zrenner, G. Böhm, G. Abstreiter, *Proceedings of 24th International Conference on the Physics of Semiconductors*, Jerusalem, Israel, D. Gershoni (ed.), World Scientific, Singapore (1994).

[Flack96] F. Flack, N. Samarth, V. Nikitin, P. A. Crowell, J. Shi, J. Levy, D. D. Awschalom, *Phys. Rev. B* **54**, R17312 (1996).

[Flissikowski04] T. Flissikowski, *PhD thesis* (Available online at http://edoc.hu-berlin.de/dissertationen/flissikowski-timur-2004-11-16/PDF/Flissikowski.pdf), Humboldt Universität, Berlin (2004).

[García97] J. M. García, G. Medeiros-Ribeiro, K. Schmidt, T. Ngo, J. L. Feng, A. Lorke, J. Kotthaus, P. M. Petroff, *Appl. Phys. Lett.***71**, 2014 (1997).

[Gerard92] J. M. Gerard, *Appl.Phys. Lett.* **61**, 2096 (1992).

[Gierz07] I. Gierz, *Master's Thesis,* Universität Würzburg (2007).

[Giessibl03] F. J. Giessibl, *Rev. Mod. Phys.* **75**, 949 (2003).

[Gindele99] F. Gindele, U. Woggon, W. Langbein, J.M. Hvam, K. Leonardi, D. Hommel, H. Selke, *Phys. Rev. B* **60**, 8773 (1999).

[Goede81] O. Goede, W. Heimbrodt, R. Muller *Phys. Status Solidi (b)*, **105** 543 (1981).

[Gong04] Q. Gong, P. Offermans, R. Nötzel, P. M. Koenraad, J. H. Wolter, *Appl. Phys. Lett.* **85**, 5697 (2004).

[Gonsalves90] D. Li, J. M. Gonsalves, N. Otsuka, J. Qiu, M. Kobayashi, R. L. Gunshor, *Appl. Phys. Lett.* **57**, 449 (1990).

[Graham04] T. C. M. Graham*, B. Urbaszek, X. Tang, C. Bradford, K. A. Prior, B. C. Cavenett, R. J. Warburton, *Phys.Status Solidi(c)* **1**, 755 (2004).

[Grillo95] D. C. Grillo, M. D. Ringle, G. C. Hua, J. Han, R. L. Gunshor, M. Hovinen, A. V. Nurmikko, *J. Vac. Sci. Technol. B* **13**, 720 (1995).

[Grinfeld86] M. A. Grinfeld, *Sov. Phys. Dokl.* **31**, 831 (1986).

[Gu05] Y. Gu, Igor L. Kuskovsky, M. van der Voort, G. F. Neumark, X. Zhou, M. C. Tamargo, *Phys. Rev. B* **71**, 045340 (2005).

[Guha93] S. Guha, H. Munekata, L. L. Chang, *J. Appl. Phys.* **73**, 2294 (1993).

[Guha90] S. Guha, A. Madhukar, K. C. Rajkumar, *Appl. Phys. Lett* **57**, 2110 (1990).

[Gunshor96] R.L. Gunshor,, J. Han, G.C. Hua, A.V. Nurmikko, H. Jeon, *J. Cryst. Growth* **159**, 1 (1996).

[Hanke07] T. Hanke, *Master's Thesis*, Universität Konstanz, (2007).

[Hartmann00] A. Hartmann, Y. Ducommun, E. Kapon, U. Hohenester, E. Molinari, *Phys. Rev. Lett.* **84**, 5648 (2000).

[Hatami98] F. Hatami, M. Grundmann, N. N. Ledentsov, F. Heinrichsdorff, R. Heitz, J. Böhrer, D. Bimberg, S. S. Ruvimov, P. Werner, V. M. Ustinov, P. S. Kop'ev, Z. I. Alferov, *Phys. Rev. B* **57**, 4635 (1998).

[Heimbrodt86] W. Heimbrodt, O. Goede, *Phys. Status Solidi (b)* **135,** 795 (1986).

[Heinrichsdorff97] F. Heinrichsdorff, M.-H. Mao, N. Kirstaedter, A. Krost, D. Bimberg, A. O. Kosogov, P. Werner, *Appl. Phys. Lett.* **71**, 22 (1997).

[Hernández-Calderon83] I. Hernández-Calderon, H. Höchst, *Phys. Rev. B* **27**, 4961 (1983).

[Herz97] K. Herz, T. Kümmell, G. Bacher, A. Forchel, B. Jobst, D. Hommel, G. Landwehr, *Phys. Rev. B* **56**, 15 261 (1997).

[Heun97] S. Heun, J. J. Paggel, L. Sobra, S. Rubini, A. Franciosi, J.-M. Bonard, J.-D. Ganiere, *Appl. Phys. Lett.* **70**, 237 (1997).

[Holloway90] H. Holloway, *J. Appl. Phys.* **67** 6229 (1990).

[Holý99] V. Holý, G. Springholtz, M. Pinczolits, G. Bauer, *Phys. Rev. Lett.* **83**, 356 (1999).

[Hommel97] D. Hommel, K. Leonardi, H. Heinki, H. Selke, K. Ohkawa, F. Gindele, U. Woggon, *Phys. Status Solidi B* **202**, 835 (1997).

[Huffaker98] D. L. Huffaker, G. Park, Z. Zou, O. B. Shchekin, D. G. Deppe, *Appl. Phys. Lett.* **73**, 2564 (1998).

[Hwang96] R. Q. Hwang, *Phys. Rev. Lett.***76**, 4757 (1996).

[Hwang91] R.Q. Hwang, J. Schröder, C. Günther, R.J. Behm, *Phys. Rev. Lett.* **67**, 3279 (1991).

[Hÿtch02] M.J. Hÿtch, E. Snoeck, R. Kilaas, *Ultramicroscopy* **74**, 131 (2002).

[Imamoglu99] A. Imamoglu, D. D. Awschalom, G. Burkard, D. P. DiVincenzo, D. Loss, M. Sherwin, A. Small, *Phys. Rev. Lett.* **83**, 4204 (1999).

[Ivanov98] S. V. Ivanov, A. A. Toropov, T. V. Shubina, S. V. Sorokin, A. V. Lebedev, I. V. Sedova, P. S. Kop'ev, G. R. Pozina, J. P. Bergman, B. Monemar, *J. Appl. Phys.* **83**, 3168 (1998).

[Jesson98] D. E. Jesson, *Morphological Organization in Epitaxial Growth and Removal,* Ed. Zhang, Lagally, World Scientific, Singapore (1998).

[Jones03] R. A. Jones, Jan M. Yarrison-Rice, L. M. Smith, Howard E. Jackson, M. Dobrowolska, J. K. Furdyna, *Phys. Rev. Lett.* **68**, 125333 (2003).

[Jonsdottir95] F. Jonsdottir, L. B. Freund, *Mech. Mater.* **20**, 337 (1995).

[Joyce04] B. A. Joyce, T. B. Joyce, *J. Crystal Growth* **264**, 605 (2004).

[Joyce01] P. B. Joyce, T. J. Krzyzewski, P. H. Steans, G. R. Bell, J. H. Neave, T. S. Jones, *Surf. Sci.* **492**, 345 (2001).

[Joyce97] B. A. Joyce, J. L. Sudijono, J. G. Belk, H. Yamaguchi, X. M. Zhang, H. T. Dobbs, A. Zangwill, D. D. Vvedensky, T. S. Jones, *Jpn. J. Appl. Phys.* **36**, 4111 (1997).

[Joyce86] B. A. Joyce, P. A. Dobson, J. H. Neave, K. Woodbridge, Jing Zhang, P. K. Larsen, B. Bolder, *Surf. Sci.* **168**, 423 (1986).

[Kegel01] I. Kegel, T.H. Metzger, A. Lorke, J. Peisl, J. Stangl, G. Bauer, K. Nordlund, W.V. Schoenfeld, P.M. Petroff, *Phys. Rev. B* **63**, 035318 (2001).

[Keim00] M. Keim, M. Korn, J. Seufert, G. Bacher, A. Forchel, G. Landwehr, S. Ivanov, S. Sorokin, A. A. Sitnikova, T. V. Shubina, A. Toropov, A. Waag, *J. Appl. Phys.* **88**, 7051 (2000).

[Kiessling06] T. Kiessling, G. V. Astakhov, A. V. Platonov, T. Slobodskyy, S. Mahapatra, W. Ossau, G. Schmidt, K. Brunner, L. W. Molenkamp, *Phys. Status Solidi (c)* **3**, 912 (2006).

[Kim00] C.S. Kim, M. Kim, J.K. Furdyna, M. Dobrowolska, S. Lee, H. Rho, L.M. Smith, H.E. Jackson, E.M. James, Y. Xin, N.D. Browning, *Phys. Rev. Lett* **85**, 1124 (2000).

[Kobayashi96] N. P. Kobayashi, T. R. Ramachandran, P. Chen, A. Madhukar, *Appl. Phys. Lett.* **68**, 3299 (1996).

[Korutcheva00] E. Korutcheva, A. M. Turiel, I. Markov, *Phys. Rev. B* **61**, 16890 (2000).

[Koshiba94] S. Koshiba, Y. Nakamura, M. Tsuchiya, H. Noge, H. Kano, Y. Nagamune, T. Noda, H. Sakaki, *J. Appl. Phys.* **76**, 4138 (1994).

[Kratzert02] P. R. Kratzert, *PhD thesis* (Available online at http://edoc.hu-berlin.de/dissertationen/kratzert-philipp-2002-07-03/PDF/Kratzert.pdf), Humboldt Universität, Berlin (2002).

[Kratzert01] P. R. Kratzert, M. Rabe, F. Henneberger, *Phys.Status. Solidi (b)* **224**, 179 (2001).

[Kratzert00] P. R. Kratzert, M. Rabe, F. Henneberger, *Appl. Surf. Sci.* **166**, 332 (2000).

[Krause05] B. Krause, T. H. Metzger, A. Rastelli, R. Songmuang, S. Kiravittaya, O. G. Schmidt, *Phys. Rev. B* **72**, 085339 (2005).

[Kruse07] C. Kruse, M. Gartner, A. Gust, D. Hommel, *Appl. Phys. Lett.* **90**, 221102 (2007).

[Kulakovskii99] V. D. Kulakovskii, G. Bacher, R. Weigand, T. Kümmell, A. Forchel, E. Borovitskaya, K. Leonardi, D. Hommel, *Phys. Rev. Lett.* **82**, 1780 (1999).

[Kumpf07] C. Kumpf, A. Stahl, I.Gierz, C. Schumacher, S. Mahapatra, F. Lochner, K. Brunner, G. Schmidt, L. W. Molenkamp, E.Umbach, *Phys. Status Solidi (c)* **4**, 3150 (2007).

[Kunkel90] R. Kunkel, B. Poelsema, L. K. Verheij, G. Comsa, *Phys. Rev. Lett.* **65**, 733 (1990).

[Kuo97] L. H. Kuo, K. Kimura, A. Ohtake, S. Miwa, T. Yasuda, T. Yao, *J. Vac. Sci. Technol. B* **15**, 1241 (1997).

[Kurtz02] E. Kurtz, B. Dal Don, M. Schmidt, H. Kalt, C. Klingshirn, D. Litvinov, A. Rosenauer, D. Gerthsen, *Thin Solid Films* 412, 89 (2002).

[Kurtz01] E. Kurtz, M. Schmidt, M. Baldauf, S. Wachter, M. Grün, H. Kalt, C. Klingshirn, D. Litvinov, A. Rosenauer, D. Gerthsen, *Appl. Phys. Lett.* **79**, 1118 (2001).

[Kurtz00] E. Kurtz, J. Shen, M. Schmidt, M. Grün, S. K. Hong, D. Litvinov, D. Gerthsen, T. Oka, T. Yao, C. Klingshirn, *Thin Solid Films* **367,** 68 (2000).

[Kuskovsky01] I. L. Kuskovsky, C. Tian, G. F. Neumark, J. E. Spanier, I. P. Herman, W.-C. Lin, S. P. Guo, M. C. Tamargo, *Phys. Rev. B* **63**, 155205 (2001).

[Lai2006] Y.J. Lai, Y.C. Lin, C.P. Fu, C.S. Yang, C.H. Chia, D.S. Chuu, W.K. Chen, M.C. Lee, W.C. Chou, M.C. Kuo, J.S. Wang, *J. Cryst. Growth* **286**, 338 (2006).

[Larsson06] M. Larsson, A. Elfving, W.-X. Ni, G. V. Hansson, P. O. Holtz, *Phys. Rev.B* **73,** 195319 (2006)

[Lee98] S. Lee, I. Daruka, C. S. Kim, A. L. Barabasi, J. L. Merz, J. K. Furdyna, *Phys. Rev. Lett.* **81**, 3479 (1998).

[Lee92] C. D. Lee, H. L. park, C. H. Chuang, S. K. Chang, *Phys. Rev. B* **45**, 4491 (1992).

[Lee87] D. Lee, A. Mysyrowicz, A.V. Nurmikko, B.J. Fitzpatrick, *Phys. Rev. Lett*. **58**, 1475 (1987).

[Leon95] R. Leon, S. Fafard, D. Leonard, J. L. Merz, P. M. Petroff, *Appl. Phys. Lett.* **67**, 521 (1995).

[Leonard93] D. Leonard, M. Krishnamurthy, C. M. Reaves, S. P. DenBaars, P. M. Petroff , *Appl. Phys. Lett.* **63,** 3203 (1993).

[Litvinov02] D. Litvinov, A. Rosenauer, D. Gerthsen, P. Kratzert, M. Rabe, F. Henneberger, *Appl. Phys. Lett.* **81**, 640 (2002).

[Litvinov01] D. Litvinov, A. Rosenauer, D. Gerthsen, H. Preis, K. Fuchs, S. Bauer, J. *Appl. Phys*. **89**, 3695 (2001).

[Litvinov00] D. Litvinov, A. Rosenauer, D. Gerthsen, N. N. Ledentsov, *Phys. Rev. B* **61**, 16819 (2000).

[Loss98] D. Loss, D. P. DiVincenzo, *Phys. Rev. A* **57**, 120 (1998).

[Lowisch99] M. Lowisch, M. Rabe, F. Kreller, F. Henneberger, *Appl. Phys. Lett.* **74**, 2489 (1999).

[Lundstrom99] T. Lundstrom, W. Schoenfeld, H. Lee, P. M. Petroff, *Science* **286**, 2312 (1999).

[Madhukar95] A. Madhukar, P. Chen, Q. Xie, A. Konkar, T. R. Ramachandran, N. P. Kobayashi, R. Viswanathan, *Low Dimensional Structures prepared by Epitaxial Growth or Regrowth on Patterned Substrates*, Ed. K. Eberl et al., Kluwer Academic Publishers, Amsterdam (1995).

[Maehashi00] K. Maehashi, N. Yasui, Y. Murase, A. Shikimi, H. Nakashima, *Appl.Surf. Sci* **166,** 322 (2000).

[Mahapatra06] S. Mahapatra, K. Brunner, C. Schumacher , T. Kiessling, G. V. Astakhov, U. Bass, E. Margapoti, W. Ossau , J. Geurts, L. Worschech, A. Forchel, L. W. Molenkamp, *Phys. Status Solidi (c)* **3,** 928 (2006).

[Maradudin80] A. A. Maradudin, R. F. Wallis, *Surf. Sci.* **91**, 423 (1980).

[Markov95] I. V. Markov, *Crystal Growth for Beginners*, *Fundamentals of Nucleation, Growth, and Epitaxy*, World Scientific, Singapore (1995)

[Márquez01] J. Márquez, L. Geelhaar, K. Jacobi, *Appl. Phys. Lett.* **78**, 2309 (2001).

[Martrou00] D. Martrou, N. Magnèa, *Thin Solid Films* **367***,* 48 (2000).

[Martrou99] D. Martrou, J. Eymery, N. Magnèa, *Phys. Rev. Lett.* **83**, 2366 (1999).

[Merz98] J.L. Merz, S. Lee, J.K. Furdyna, *J. Cryst. Growth* **184/185**, 228 (1998).

[Michely04] T. Michely, J. Krug, *Islands, Mounds and Atoms, Patterns and processes in Crystal Growth Far from Equilibrium*, Ed. Ertl et al., Springer-Verlag, Berlin Heidelberg (2004).

[Michler00] P. Michler, A. Kiraz, C. Becher, W. V. Schoenfeld, P. M. Petroff, L. Zhang, E. Hu, A. Imamoglu, *Science* **290**, 2282 (2000).

[Minne98] S.C. Minne, J.D. Adams, G. Yaralioglu, S.R. Manalis, A. Atalar, C.F. Quate, *Appl. Phys. Lett.* **73**, 1742 (1998).

[Mo90] Y.-W. Mo, D. E. Savage, B. S. Swartzentruber, M. G. Lagally, *Phys. Rev. Lett*. **65**, 1020 (1990).

[Möck01] P. Möck, T. Topuria, N. D. Browning, L. Titova, M. Dobrowolska, S. Lee, J. K. Furdyna, *J. Electron. Mater.* **30**, 748 (2001).

[Muraki92] K. Muraki, S. Fukatsu, Y. Shiraki, R. Ito, *Appl. Phys. Lett.* **61**, 557 (1992).

[Murray93] C. B. Murray, D. J. Norris, M. G. Bawendi, *J. Am. Chem. Soc.* **115**, 8706 (1993).

[Nirmal94] M. Nirmal, C. B. Murray, M. G. Bawendi, *Phys. Rev. B* **50**, 2293 (1994).

[Nötzel94] R. Nötzel, J. Temmyo, J. Tamamura, *Nature* **369**, 131 (1994).

[Nurmikko97] A. Nurmikko, R.L. Gunshor, *Semicond. Sci. Technol.* **12**, 1337 (1997).

[Ohishi00] M. Ohishi, H. Saito, M. Yoneta, T. Ichikawa, T. Fujimoto, *Jpn. J.Appl. Phys* **39**, 4584 (2000).

[Ohtake98] A. Ohtake, S. Miwa, L. Kuo, T. Yasuda, K. Kimura, C. Jin, T. Yao, *J. Cryst. Growth* **184/185**, 163 (1998).

[Orme98] C. Orme, M. D: Johnson, B. G. Orr, *Morphological Organization in Epitaxial Growth and Removal,* Ed. Zhang, Lagally, World Scientific, Singapore (1998).

[Orme94] C. Orme, M.D. Johnson, J.L. Sudijono, K.T. Leung, B.G. Orr, *Appl. Phys. Lett.* **64**, 860 (1994).

[Oswald06] S. Oswald , M. Zier, R. Reiche, K. Wetzig, *Surf. Interface Anal.* **38**, 590 (2006).

[Ouadjaout90] D. Ouadjaout, Y. Marfaing, *Phys. Rev. B* **41**, 12096 (1990).

[Passow02] T. Passow, K. Leonardi, H. Heinke, D. Hommel, D. Litvinov, A. Rosenauer, G. Gerthsen, J. Seufert, G. Bacher, A. Forchel, *J. Appl. Phys.* **92**, 6546 (2002).

[Passow01] T. Passow, H. Heinke, T. Schmidt, J. Falta, A. Stockmann, H. Selke, P. L. Ryder, K. Leonardi, D. Hommel, *Phys. Rev. B* **64**, 193311 (2001).

[Passow00] T. Passow, H. Heinke, J. Falta, K. Leonardi, D. Hommel, *Appl. Phys. Lett.* **77,** 3544 (2000).

[Patton03] B. Patton, W. Langbein, U. Woggon, *Phys. Rev. B* **68**, 125316 (2003).

[Phang94] Y.H. Phang, C. Teichert, M.G. Lagally, L.J. Peticolas, J.C. Bean, E. Kasper, *Phys. Rev. B* **50**, 14435 (1994).

[Peranio00] N. Peranio, A. Rosenauer, D. Gerthsen, S. V. Sorokin, I. V. Sedova, S. V. Ivanov, *Phys. Rev. B* **61**, 16015 (2000).

[Petruzello88] J. Petruzello, B. L. Greenberg, D. A. Cammack, R. Dalby, *J. Appl. Phys.* **63**, 2299 (1988).

[Perez-Paz05] M. N. Perez-Paz, X. Zhou, M.Muñoz, M. Sohel, H. Lu, F. Fernandez F.Jean-Mary D. L. Akins, M. C. Tamargo, *J. Vacuum Sci. Technol.B* **23**, 1236 (2005).

[Permogorov82] S. Permogorov, A. Reznitsky, S. Verbin, G. O. Müller, P. Fogel, M. Nikiforova, *Phys. Status Solidi (b)* **113**, 589 (1982).

[Phillips98] J. Phillips, K. Kamath, P. Bhattacharya, *Appl. Phys. Lett.* **72**, 2020 (1998).

[Phillips73] J.C. Phillips, *Bonds and Bands in Semiconductors*, Academic Press, New York (1973).

[Ponchet95] Ponchet, A., A. Le Corre, H. L'Haridon, B. Lambert, S. Salaün, *Appl. Phys. Lett.* **67**, 1850 (1995).

[Preis01] H. Preis, K. Fuchs, W. Gebhardt, *Phys. Status Solidi (b)* **224**, 527 (2001).

[Pryor98] C. Pryor, *Phys. Rev. B* **57**, 7190 (1998).

[Puls96] J. Puls, M. Rabe, H. J. Wünsche, F. Henneberger, *Phys. Rev. B* **60**, R16 303 (1999).

[Rabe98] M. Rabe, M. Lowisch, F. Henneberger, *J. Cryst. Growth* **184/185**, 248 (1998).

[Rabe98A] M. Rabe, *PhD thesis*, Humboldt Universität, Berlin (1998).

[Rastelli02] A. Rastelli, E. Müller, H. von Känel, *Appl. Phys. Lett.* **80**, 1438 (2002).

[Reed93] M. A. Reed, *Sci. Am.***268**, 118 (1993).

[Reed86] M. A. Reed, R. T. Bate, K. Bradshaw, W. M. Duncan, W. M. Frensley, J. W. Lee, D. H. Smith, *J. Vac. Sci. Technol. B* **4**, 358 (1986).

[Riley96] J. Riley, D. Wolfframm, D. Westwood, A. Evans, *J. Cryst. Growth* **160**, 193 (1996).

[Robin07] I. C. Robin, T. Aichele, C. Bougerol, R. Andre´, S. Tatarenko, E. Bellet-Amalric, B. Van Daele, G. Van Tendaloo, *Nanotechnology* **18**, 265701 (2007).

[Robin06] I. C. Robin, R. André, C. Bougerol, T. Aichele, S. Tatarenko, *Appl. Phys. Lett.* **88**, 233103 (2006).

[Robin05] I.C. Robin, R. Andre´, H. Mariette, S. Tatarenko, Le Si Dang, J.M. Ge´rard, E. Bellet-Amalric, *Physica E* **26**, 115 (2005).

[Robin04] I. C. Robin, R. André, Le Si Dang, H. Mariette, S. Tatarenko, J. M. Gérard, K. Kheng , F. Tinjod, M. Bartels, K. Lischka, D. Schikora, *Phys. Status Solidi (c)* **241**, 542 (2004).

[Royer28] L. Royer, *Bull. Soc. Fr. Mineralog. Crystallogr* .**51***,* 7 (1928).

[Santori04] C. Santori, D. Fattal, J. Vuckovic, G. S. Solomon, Y. Yamamoto, *New J. Phys.* **6**, 89 (2004).

[Santori02] C. Santori, D. Fattal, J. Vuckovic, G.S. Solomon, Y. Yamamoto, *Nature* **419**, 594 (2002).

[Santori01] C. Santori, M. Pelton, G. Solomon, Y. Dale, Y. Yamamoto, *Phys. Rev. Lett.* **86**, 1502 (2001).

[Schallenberg04] T. Schallenberg , C. Schumacher, K. Brunner, L. W. Molenkamp, *Phys. Status Solidi (b)* **241**, 564 (2004).

[Schikora00] D. Schikora, S. Schwedhelm, D. J. As, K. Lischka, D. Litvinov, A. Rosenauer, D. Gerthsen, M. Strassburg, A. Hoffmann, D. Bimberg, *Appl.Phys. Lett.* **76,** 418 (2000).

[Schwoebel66] R.L. Schwoebel, E.J. Shipsey, *J. Appl. Phys.* **37**, 3682 (1966).

[Seifert96] W. Seifert, N. Carlsson, M. Miller, M.-E. Pistol, L. Samuelson, L. R. Wallenberg, *Prog. Cryst. Growth Charact. Mater.* **33**, 423 (1996).

[Shchukin95] V. A. Shchukin, N. N. Ledentsov, P. S. Kop'ev, D. Bimberg, *Phys. Rev. Lett.* **75**, 2968 (1995).

[Shen98] A. Shen, H. Ohno, Y. Horikoshi, S.P. Guo, Y. Ohno, F. Matsukura, *Appl. Surf. Sci.*, **130–132**, 382 (1998).

[Shitara92] T. Shitara, D. D. Vvedensky, M. R. Wilby, J. Zhang, J. H. Neave, B. A. Joyce, *Phys. Rev. B.* **46**, 6815 (1992).

[Sikorski89] C. Sikorski, U. Merkt, *Phys. Rev. Lett.* **62**, 2164 (1989).

[Smathers98] J. B. Smathers, E. Kneedler, B. R. Bennett, B. T. Jonker, *Appl. Phys. Lett.* **72**, 1238 (1998).

[Songmuang03] R. Songmuang, S. Kiravittaya, O.G. Schmidt, *J. Cryst. Growth* **249**, 416 (2003).

[Sopanen95] M. Sopanen, H. Lipsanen, J. Ahopelto, *Appl. Phys. Lett.* **65**, 1662 (1995).

[Springholz01] G. Springholz, M. Pinczolits, V. Holy, S. Zerlauth, I. Vavra, G. Bauer, *Physica E* **9**, 149 (2001).

[Springholz00] G. Springholz, M. Pinczolits, P. Mayer, V. Holy, G. Bauer, H.H. Kang, L. Salamanca-Riba, *Phys. Rev. Lett*. **84**, 4669 (2000).

[Springholz98] G. Springholz, V. Holy, M. Pinczolits, G. Bauer, *Science* **282**, 734 (1998)

[Srolovitz89] *Acta Metall.* **37**, 621 (1989).

[Stangl04] J. Stangl, V. Holý, G. Bauer, *Rev. Mod. Phys.* **76**, 725 (2004).

[Strassburg00] M. Strassburg, Th. Deniozou, A. Hoffmann, R. Heitz, U. W. Pohl, D. Bimberg, D. Litvinov, A. Rosenause, D. Gerthsen, S. Schwedhelm, K. Lischka, D. Schikora, *Appl. Phys. Lett.* 76, 685 (2000).

[Steans99] P.H. Steans, J.H. Neave, J. Zhang, E.S. Tok, G.R. Bell, B.A. Joyce, T.S. Jones, *J. Cryst. Growth* **201/202**, 198 (1999).

[Stier99] O. Stier, M. Grundmann, D. Bimberg, *Phys. Rev. B* **59**, 5688 (1999).

[Stoldt00] C. R. Stoldt, K. J. Caspersen, M. C. Bartelt, C. J. Jenks, J. W. Evans, *Phys. Rev. Lett.* **85**, 800 (2000).

[Sugawara95] M. Sugawara, *Phys. Rev. B* **51**, 10743 (1995).

[Sutter00] P. Sutter, M. G. Lagally, *Phys. Rev. Lett.* **84**, 4637 (2000).

[Takagahara00] T. Takagahara, *Phys. Rev. B* **62**, 16840 (2000).

[Teichert02] C. Teichert, *Phys. Rep.* **365**, 335 (2002).

[Tersoff02] J. Tersoff, B. J. Spencer, A. Rastelli, H. von Känel, *Phys. Rev. Lett.* **89**, 196104 (2002).

[Tersoff98] J. Tersoff, *Phys. Rev. Lett.* **81**, 3183 (1998).

[Tersoff96] J. Tersoff, C. Teichert, M. G. Lagally, *Phys. Rev. Lett.* **76**, 1675 (1996).

[Tersoff95] J. Tersoff, Y. H. Phang, Z. Zhang, M. G. Lagally, *Phys. Rev. Lett.* **75**, 2730 (1995).

[Tersoff94] J. Tersoff, F. K. LeGoues, *Phys. Rev. Lett.* **72**, 3570 (1994).

[Thürmer95] K. Thürmer, R. Koch, M. Weber, K.H. Reider, *Phys. Rev. Lett.* **75**, 1767 (1995).

[Tinjod04] F. Tinjod, I.-C. Robin, R. André, K. Kheng, H. Mariette, *J. Alloys. Compd.* **371**, 63 (2004).

[Tinjod03] F. Tinjod, B. Gilles, S. Moehl, K. Kheng, H. Mariette, *Appl. Phys. Lett.* **82**, 4340 (2003).

[Tomiya95] S. Tomiya, E. Morita, M. Ukita, H. Okuyama, S. Itoh, K. Nakano, A. Ishibashi, *Appl. Phys. Lett.* **66**, 1208 (1995).

[Toropov06] A. A. Toropov, I. V. Sedova, O. G. Lyublinskaya, S. V. Sorokin, A. A. Sitnikova, S. V. Ivanov, J. P. Bergman, B. Monemar, F. Donatini, Le Si Dang, *Appl. Phys. Lett.* **89**, 123110 (2006).

[Toropov99] A. A. Toropov, S. V. Ivanov, T. V. Shubina, S. V. Sorokin, A. V. Lebedev, A. A. Sitnikova, P. S. Kop'ev, M. Willander, G. R. Pozina, J. P. Bergman, B. Monemar, *Jpn. J. Appl. Phys.* **38**, 566 (1999).

[Toyoshima93] H. Toyoshima, T. Niwa, J. Yamazaki, A. Okamoto, *Appl. Phys. Lett.* **63**, 821 (1993).

[Tromp00] R. M. Tromp, F. M. Ross, M. C. Reuter, *Phys. Rev. Lett.* **84**, 4641 (2000).

[Van Nostrand95] J.E. Van Nostrand, S.J. Chey, M.-A. Hasan, D.G. Cahill, J.E. Greene, *Phys. Rev. Lett.* **74**, 1127 (1995).

[Vegard21] L. Vegard, *Z. Phys. 5* **17**, (1921).

[Venables84] J. A. Venables, G. D. Spiller, M. Hanbucken, *Rep. Prog. Phys.* **47**, 399 (1984).

[Walther01] T. Walther, A. G. Cullis, D. J. Norris, M. Hopkinson, *Phys. Rev. Lett.* **86**, 2381 (2001).

[Wang00] L.G. Wang, P. Kratzer, M. Scheffler, *Jpn. J. Appl. Phys.* **39**, 429 (2000).

[Wang00A] N. Wang, K. K. Fung, I. K. Sou, *Appl. Phys. Lett.* **77**, 2846 (2000).

[Wang99] L.-W. Wang, J. Kim, A. Zunger, *Phys. Rev. B* **59**, 5678 (1999).

[Werner89] J. Werner, E. Kapon, N. G. Stoffel, E. Colas, S. A. Schwarz, N. Andreadakis, *Appl. Phys. Lett.* **55**, 540 (1989).

[Wolframm00] D. Wolfframm, D. A. Evans, D. I. Westwood, J. Riley, *J. Cryst. Growth* **216**, 119 (2000).

[Xie94] Q. Xie, P. Chen, A. Madhukar, *Appl. Phys. Lett.* **69**, 6565 (1994).

[Xin96] S.H. Xin, P.D. Wang, A. Yin, C. Kim, M. Dobrowolska, J.L. Merz, J.K. Furdyna, *Appl. Phys. Lett.* **69**, 3884 (1996).

[Yang98] C.S. Yang, D.Y. Hong, C.Y. Lin, W.C. Chou, C.S. Ro, W.Y. Uen, W.H. Lan, S.L. Tu, *J. Appl. Phys.* **83**, 2555 (1998).

[Yao88] T. Yao, M. Kato, J.J. Davies, H. Tanino, *J. Cryst. Growth* **86**, 552 (1988).

[Yao78] T. Yao, Y. Makita, S. Maekawa, *J. Cryst. Growth* **45,** 309 (1978).

[Yu96] P. Y. Yu, M. Cardona, *Fundamnetals of Semiconductors, Physics and Material Properties*, Springer Verlag, Berlin Heidelberg New York (1996).

[Yuan02] Z. Yuan, B. E. Kardynal, R. M. Stevenson, A. J. Shields, C. J. Lobo, K. Cooper, N. S. Beattie, D. A. Ritchie, M. Pepper, *Science* **295**, 102(2002).

[Zhang99] X.B. Zhang, S.K. Hark, *Appl. Phys. Lett.* **74**, 3857 (1999).

[Zhong04] Z. Zhong, G. Bauer, *Appl. Phys. Lett.* **84**, 1922 (2004).

[Zhu97] Z. Zhu, E. Kurtz, K. Arai, Y. F. Chen, D. N. Bagnall, P. Tomasini, F. Lu, T. Sekiguchi, T. Yao, T. Yasude, Y. Segawa, *Phys. Status Solidi B* **202**, 827 (1997).

[Zwiller01] V. Zwiller, H. Blom, P. Jonsson, N. Panev, S. Jeppesen, T. Tsegaye, E. Goobar, M-E Pistol, . Samuelson, G. Bjork, *Appl. Phys. Lett.* **78**, 2476 (2001).

Publications

---

1. Emanuela Margapoti, Lukas Worschech, **Suddhasatta Mahapatra**, Fabrizio M. Alves, V. Lopez-Richard, G. E. Marques, C. Bougerol, Karl Brunner, Alfred Forchel, "*Paramagnetic response of annealed nonmagnetic single quantum dots*" (Submitted).

2. **S. Mahapatra**, K. Brunner, C. Bougerol, "*Self-assembly of CdSe/ZnSe(001) quantum dot structures, mediated by a Tellurium cap layer* ", Appl. Phys. Lett. **91**, 153110 (2007).

3. **S. Mahapatra,** T. Kiessling**,** E. Margapoti, G. V. Astakhov, J. Renner**,** U. Bass**,** C. Bougerol, T. Schmidt, A. Bendounan **,** F. Schmitt, C. Schumacher, L. Worschech, W. Ossau**,** J. Geurts**,** L. W. Molenkamp, F. Reinert, A. Forchel, K. Brunner, "*CdSe/ZnSe heteroepitaxy: Aspects of growth and self organization of nanostructures"*, Phys. Status Solidi. (c) **4**, 3129 (2007).

4. E. Margapoti, L. Worschech, **S. Mahapatra**, T. Slobodskyy, A. Tribu, T. Aichele, K. Brunner, G. Schmidt, L. W. Molenkamp, R. André, K. Kheng, C. Bougerol, A. Forchel, *"Optical characterization of thermally annealed self-assembled ZnCdSe quantum dots"*, Phys. Status Solidi. (c) **4**, 3280 (2007).

5. T. Kiessling, G. V. Astakhov, A. V. Platonov, **S. Mahapatra**, T. Slobodskyy, W. Ossau, G. Schmidt, K. Brunner, L. W. Molenkamp, *"Optical studies of structural and magnetic anisotropies in epitaxial CdSe/ZnSe quantum dots"*, Phys. Status Solidi. (c) **4**, 3324 (2007).

6. C. Kumpf, A. Stahl, I. Gierz, C. Schumacher, **S. Mahapatra**, F. Lochner, K. Brunner, G. Schmidt, L. W. Molenkamp, E. Umbach, "*Structure and relaxation effects in thin semiconducting films and quantum dots"*,Phys. Status Solidi. (c) **4**, 3150 (2007).

7. J. Renner, L. Worschech, **S. Mahapatra**, K. Brunner, A. Forchel, *"Optical characterization of ZnSe/ZnMgSSe microdisks with embedded CdSe quantum dots"*, Phys. Status Solidi. (c) **4**, 3289 (2007).

8. Johannes Renner, Lukas Worschech, Alfred Forchel, **Suddhasatta Mahapatra**, Karl Brunner, *"Glass supported ZnSe microring strongly coupled to a single CdSe QD"* (Submitted).

9. E. Margapoti, L. Worschech, **S. Mahapatra**, K. Brunner, A. Forchel, Fabrizio M. Alves, V. Lopez-Richard, G. E. Marques, C. Bougerol, *"Negative Magneto-polarization in thermally annealed self assembled quantum dots"* , Phys. Rev. B (in press).

10. M. Ghali, R. Arians, T. Kümmell, G. Bacher, J. Wenisch, **S. Mahapatra**, K. Brunner, "*Spin injection into a single self-assembled quantum dot in a p-i-n II-VI/III-V structure"* Appl. Phys. Lett. **90**, 093110 (2007).

11. **S. Mahapatra**, E. Margapoti, L. Worschech, A. Forchel, K. Brunner, *"Amorphous-Te mediated self organization of CdSe/ZnSe nanostructures"* J. Cryst. Growth **301-302**, 293 (2007).

12. **S. Mahapatra**, T. Kiessling, E. Margapoti, G. V. Astakhov, W. Ossau, L. Worschech, A. Forchel, K. Brunner, *"Layer by Layer growth and island formation in CdSe/ZnSe heteroepitaxy"* J. Cryst. Growth **301-302**, 310 (2007).

13. Johannes Renner, Lukas Worschech, Alfred Forchel, **Suddhasatta Mahapatra**, Karl Brunner, *"CdSe quantum dot microdisk laser"* Appl. Phys. Lett. **89**, 231104 (2006).

14. J. Renner, L. Worschech, A. Forchel, **S. Mahapatra**, K. Brunner, *"Whispering gallery modes in high quality ZnSe/ZnMgSSe microdisks with CdSe quantum dots studied at room temperature"*, Appl. Phys. Lett. **89**, 091105 (2006).

15. **S. Mahapatra**, T. Kiessling, E. Margapoti, G. V. Astakhov, W. Ossau, L. Worschech, A. Forchel, and K. Brunner, *"Formation mechanism of CdSe quantum dots on ZnSe by low temperature epitaxy and in-situ annealing"* , Appl. Phys. Lett. **89**, 043102 (2006).

16. **S. Mahapatra**, K. Brunner , C. Schumacher, T. Kiessling G. V. Astakhov, U. Bass, E. Margapoti, W. Ossau, J. Geurts, L. Worschech, A. Forchel, L. W. Molenkamp, *"Comparative study of self assembled CdSe/ZnSe quantum dots grown by variants of conventional MBE"*, Phys. Status Solidi (c) **3**, 928 (2006).

17. A. V. Platonov , T. Kiessling , G. V. Astakhov , A. A. Maksimov, A. V. Larionov, D. R. Yakovlev, T. Slobodskyy, **S. Mahapatra**, W. Ossau, G. Schmidt, K. Brunner, M. Bayer, L. W. Molenkamp, *"Energy relaxation in CdSe/ZnSe quantum dots under the strong exciton-phonon coupling regime"* Phys. Status Solidi (c) **3**, 924 (2006).

18. T. Kiessling , G. V. Astakhov , A. V. Platonov, T. Slobodskyy, **S. Mahapatra**, W. Ossau, G. Schmidt, K. Brunner, L. W. Molenkamp, *"Optical anisotropy of CdSe/ZnSe quantum dots"*, Phys. Status Solidi (c) **3**, 912 (2006).

19. T. Kiessling, A. V. Platonov, G. V. Astakhov, T. Slobodskyy, **S. Mahapatra**, W. Ossau, G. Schmidt, K. Brunner, and L. W. Molenkamp, *"Anomalous in-plane magneto-optic anisotropy of self assembled quantum dots"*, Phys. Rev. B **74**, 041301(R) (2006).

20. G. V. Astakhov, T. Kiessling, A. V. Platonov, T. Slobodskyy, **S. Mahapatra**, W. Ossau, G. Schmidt, K. Brunner, and L. W. Molenkamp, *"Circular-to-linear and linear-to-circular conversion of optical polarization by semiconductor quantum dots"*, Phys. Rev. Lett. **96**, 027402 (2006).

21. J. Geurts, U. Bass, **S. Mahapatra**, K. Brunner, T. Muck, and V. Wagner, *"Vibration modes and interface abruptness of CdSe quantum dots, embedded either in BeTe or ZnSe"*, J. Phys. IV **132** 307 (2006).

22. **S. Mahapatra**, C. Schumacher, T. Kiessling, G.V. Astakhov, U. Bass, W. Ossau, J. Geurts and K. Brunner, *"CdSe/ZnSe Quantum Dots Formed by Low Temperature Epitaxy and In-Situ Annealing: Properties and Growth Optimization"* Acta. Phys. Pol. A, 108, 769 (2005).

Curriculum vitae

Suddhasatta Mahapatra,

born in Kharagpur, India, on 15th June, 1977.

Academics

Since 2003	Doctoral studies in the “Molekularstrahlepitaxie” workgroup (Prof. K. Brunner), of the “Experimentelle Physik 3” chair (Prof. L. W. Molenkamp), Julius-Maximilians-Universität, Würzburg, Germany.
2000-2003	Master of Science (Engg.) in Materials Science and Engineering, from Indian Institute of Science, Bangalore, India.
(1996-2000)	Bachelor of Science (Tech.) In Ceramic Technology from College of Ceramic Technology, University of Calcutta, Calcutta, India.
(1993-1995)	Higher Secondary Education, Hijli High School, Kharagpur, India.